Optically-detected NMR of defect sites in EuVO4
by Yongchen Sun

A thesis submitted in partial fulfillment of the requirements for the degree of Doctor of Philosophy in Physics
Montana State University

Abstract:
This thesis reports laser spectroscopic studies of stoichiometric EuVO4 and isomorphous compounds. Electronic and hyperfine stmctures have been used to study the electron-phonon coupling and the nature of the lattice defects.

Conventional absorption, fluorescence, and Raman scattering spectroscopy was used to study the Eu3+ energy levels of EuVO4, EuAsO4, Eu3+:YVO4, Eu3+:LuV04, Eu3+:YP04, and Eu3+TuPO4. Crystal field calculations were also carried out for these compounds. The Eu3+ 7F1 singlet levels in EuVO4 and EuAsO4 were found to exhibit Davydov splittings, a result of the ion-ion interaction in the stoichiometric compounds. The Eu3+ 7Fj 2 doublet levels all have anomalously small Lande g factor for the vanadates and EuAsO4, a result of the dynamic Jahn-Teller effect due to electron-phonon coupling.

EuVO4 had been found previously to have over 50 satellite lines in the 7F0 - 5Dq region, each line corresponding to a distinct defect site. Defect line maps were measured for two additional growths of EuVO4. Time-resolved fluorescence has been used to study the pathways of the energy migration among these sites. For example, the site at 515868 GHz was found to transfer its energy to other sites in 50 fls. Systematics of the rare earth spectra were considered, and a simple relationship between the energy levels and the lattice cell size of the host material has been suggested.

Spectral holebuming and optically-detected nuclear-magnetic-resonance (ODNMR) measurements have been used to study the hyperfine structure of the defect sites; each was found to possess a distinct hyperfine interaction. Ground state quadrupole interaction parameters (P, T|) are given for over 30 defect sites. A new holebuming mechanism -energy-transfer enhanced holebuming was proposed. The full angle-dependent ODNMR study of some of the defect sites yielded information about the ground state nuclear magnetic shielding parameters and the principal axes of the ground state quadrupole interaction. The site with 7Fq - 3D0 transition at 515868 GHz was found to have a quadrupole coordinate system tilted 10.7° and a very anisotropic nuclear magnetic moment, only 5% of the bare nucleus value in the defect x direction. This is the first time this kind of information is obtained for a defect site with no predetermined structural information. It should provide the basis for further theoretical calculations and the final determination of the lattice defect local structure.

OPTICALLY-DETECTED NMR OF DEFECT SITES IN $EuVO_4$

by

Yongchen Sun

A thesis submitted in partial fulfillment
of the requirements for the degree

of

Doctor of Philosophy

in

Physics

MONTANA STATE UNIVERSITY
Bozeman, Montana

November 1993

APPROVAL

of a thesis submitted by

Yongchen Sun

This thesis has been read by each member of the thesis committee and has been found to be satisfactory regarding content, English usage, format, citations, bibliographic style, and consistency, and is ready for submission to the College of Graduate Studies.

11 November 1993
Date

Rufus L Cone
Chairman, Graduate Committee

Approved for the Major Department

11-11-93
Date

Head, Major Department

Approved for the College of Graduate Studies

11/14/93
Date

Graduate Dean

STATEMENT OF PERMISSION TO USE

In presenting this thesis in partial fufillment of the requirements for a doctoral degree at Montana State University, I agree that the Library shall make it available to borrowers under rules of the Library. I further agree that coping of this thesis is allowable only for scholarly purposes, consistent with "fair use" as prescribed in the U.S. Copyright Law. Requests for extensive copying or reproduction of this thesis should be referred to University Microfilms International, 300 North Zeeb Road, Ann Arbor, Michigan 48106, to whom I have granted "the exclusive right to reproduce and distribute copies of the dissertation for sale in and from microform or electronic format, along with the right to reproduce and distribute my abstract in any format in whole or in part."

Signature 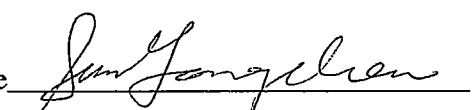

Date 11 November 93

ACKNOWLEDGEMENTS

The author wishes to thank a number of people, without whom the completion of this thesis would have been impossible. First and foremost, he wants to thank his advisor, Professor Rufus L. Cone, for his scientific guidance, inexhaustible ideas, patience, and encouragement. Thanks are also extended to Dr. M.J.M. Leask, with whom the author had wonderful collaboration in the laboratory, and to Dr. M.M. Abraham, who provided encouragement and many of the crystals studied in this thesis.

The author also wishes to acknowledge the technical assistance of Norman Williams and Erik Andersen, and the help he received from his fellow students: Raymond P. Jones, Randy W. Equall, Margaret Hall, and Guangming Wang. Last but not least, he wants to thank his wife and parents for their love and support over the years.

TABLE OF CONTENTS

TABLE OF CONTENTS---Continued

TABLE OF CONTENTS---Continued

LIST OF TABLES

LIST OF TABLES---Continued

Page

LIST OF FIGURES

Page

LIST OF FIGURES---Continued

Page

LIST OF FIGURES---Continued

Page

LIST OF FIGURES---Continued

Page

ABSTRACT

This thesis reports laser spectroscopic studies of stoichiometric $EuVO_4$ and isomorphous compounds. Electronic and hyperfine structures have been used to study the electron-phonon coupling and the nature of the lattice defects.

Conventional absorption, fluorescence, and Raman scattering spectroscopy was used to study the Eu^{3+} energy levels of $EuVO_4$, $EuAsO_4$, Eu^{3+}:YVO_4, Eu^{3+}:$LuVO_4$, Eu^{3+}:YPO_4, and Eu^{3+}:$LuPO_4$. Crystal field calculations were also carried out for these compounds. The Eu^{3+} $^7F_1$ singlet levels in $EuVO_4$ and $EuAsO_4$ were found to exhibit Davydov splittings, a result of the ion-ion interaction in the stoichiometric compounds. The Eu^{3+} $^7F_{1,2}$ doublet levels all have anomalously small Landé g factor for the vanadates and $EuAsO_4$, a result of the dynamic Jahn-Teller effect due to electron-phonon coupling.

$EuVO_4$ had been found previously to have over 50 satellite lines in the $^7F_0$ - $^5D_0$ region, each line corresponding to a distinct defect site. Defect line maps were measured for two additional growths of $EuVO_4$. Time-resolved fluorescence has been used to study the pathways of the energy migration among these sites. For example, the site at 515868 GHz was found to transfer its energy to other sites in 50 μs. Systematics of the rare earth spectra were considered, and a simple relationship between the energy levels and the lattice cell size of the host material has been suggested.

Spectral holeburning and optically-detected nuclear-magnetic-resonance (ODNMR) measurements have been used to study the hyperfine structure of the defect sites; each was found to possess a distinct hyperfine interaction. Ground state quadrupole interaction parameters (P, η) are given for over 30 defect sites. A new holeburning mechanism - energy-transfer enhanced holeburning was proposed. The full angle-dependent ODNMR study of some of the defect sites yielded information about the ground state nuclear magnetic shielding parameters and the principal axes of the ground state quadrupole interaction. The site with $^7F_0$ - $^5D_0$ transition at 515868 GHz was found to have a quadrupole coordinate system tilted 10.7° and a very anisotropic nuclear magnetic moment, only 5% of the bare nucleus value in the defect x direction. This is the first time this kind of information is obtained for a defect site with no predetermined structural information. It should provide the basis for further theoretical calculations and the final determination of the lattice defect local structure.

CHAPTER 1

INTRODUCTION

The rare earth vanadate family crystallize in the tetragonal zircon structure (D_{4h}^{19}), with the exception of $LaVO_4$ which crystallizes in the monoclinic monazite structure. The rare earth phosphates crystallize both in the zircon and in the monazite structures, with the heavier and smaller ions (Gd^{3+} to Lu^{3+}, including Y^{3+}) going to the former and lighter and larger ions (La^{3+} to Eu^{3+}) going to the latter. $EuAsO_4$ also has tetragonal zircon structure. A schematic representation of the tetragonal zircon structure is shown in Figure 1.1. The crystal *c*-axis is shown as the z axis. The *a* and *a'* axes, parallel to the natural crystal surfaces, are shown as x and y. The rare earth ions occupy sites with D_{2d} local symmetry. The two-fold axes of D_{2d} are parallel to (x', y', z'), where (x', y') are in the basal plane and at 45° to (*a*, *a*'), respectively.

The tetragonal zircon crystals have a high pressure phase at P ~ 1 GPa where they undergo a phase transition to the scheelite structure (C_{4h}), resulting in a more efficient packing of the coordination polyhedra (Jayaraman *et al.* 1987, Chen *et al.* 1992). The high pressure phase transition of Eu^{3+}:YVO_4 was studied using Raman scattering, and it was found that the scheelite structure was almost stable. When relieving the pressure to the atmosphere, the Raman scattering spectrum would not return to the zircon-type spectrum, the scheelite structure was retained. The electronic transition energies did not change dramatically since they were more sensitive to the local environment change and

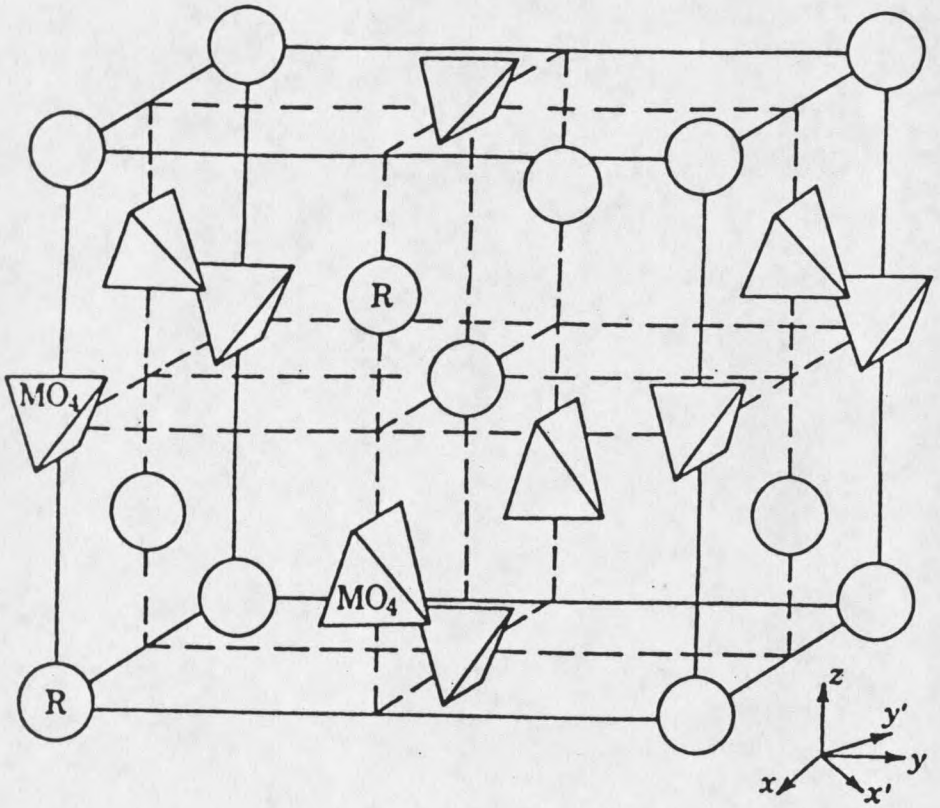

Figure 1.1 Schematic representation of the tetragonal zircon structure (D_{4h}^{19}) for RMO_4. (R ≡ rare earth, M ≡ V, As, or P). Two molecules per unit cell are indicated. (Wyckoff 1965, Elliott 1972)

relatively insensitive to the crystal structural change, but the Eu^{3+} $^5D_0$ lifetimes changed drastically in the two different phases (Chen *et al.* 1992).

The electronic structure of Eu^{3+} is simple compared to other trivalent rare earth ions. The ground state is always the $^7F_0$ state (a possible scenario is that $^7F_1$ was split so much by the crystal field that one of the three levels goes below $^7F_0$, but such a host has not been found yet). The $^7F_1$ state is usually 370 cm^{-1} above the ground state. The $^7F_2$ levels are around 1000 cm^{-1}. The ^7F_J levels extend up to about 5000 cm^{-1}. From then on, a large gap of about 12000 cm^{-1} occurs until the next level $^5D_0$ at ~ 17250 cm^{-1}. The $^5D_1$ levels are normally at ~19000 cm^{-1}, $^5D_2$ at 21400 cm^{-1}, and $^5D_3$ at 24000 cm^{-1}. $^5D_4$, $^5L_6$, and even higher levels are more mixed up and difficult to determine from experiments. The levels that we are most concerned with in this work are summarized in Figure 1.2.

Brecher *et al* (1967, 1968) studied the spectrum of Eu^{3+} in YVO_4 and YPO_4, and concluded that the crystal field parameter B_{20} had opposite signs for the two hosts. It was positive for Eu^{3+}:YPO_4, negative for Eu^{3+}:YVO_4. Other studies confirmed these observations. The lattice structures and the *a*/*c* ratios for these two hosts are not very different. The difference of B_{20} must come from the local oxygen coordinates. The crystal field seems to imply an oxygen octohedra elongated along the *c*-axis for YPO_4 and an octahedra pressed along the *c*-axis for YVO_4, but this is not confirmed by structural studies. An interesting observation by Brecher *et al* (1968) was that the general crystal field fit was much better for YPO_4 than for YVO_4. They attributed this phenomenon to the stronger covalency of the vanadates. We studied the polarized spectra of Eu^{3+} in $EuVO_4$, Eu^{3+}:YVO_4, Eu^{3+}:$LuVO_4$, Eu^{3+}:YPO_4, Eu^{3+}:$LuPO_4$, and $EuAsO_4$, and made crystal field calculations for each host. The general fit quality confirmed Brecher *et al*'s observation. These experiments and calculations will be presented in Chapter 2.

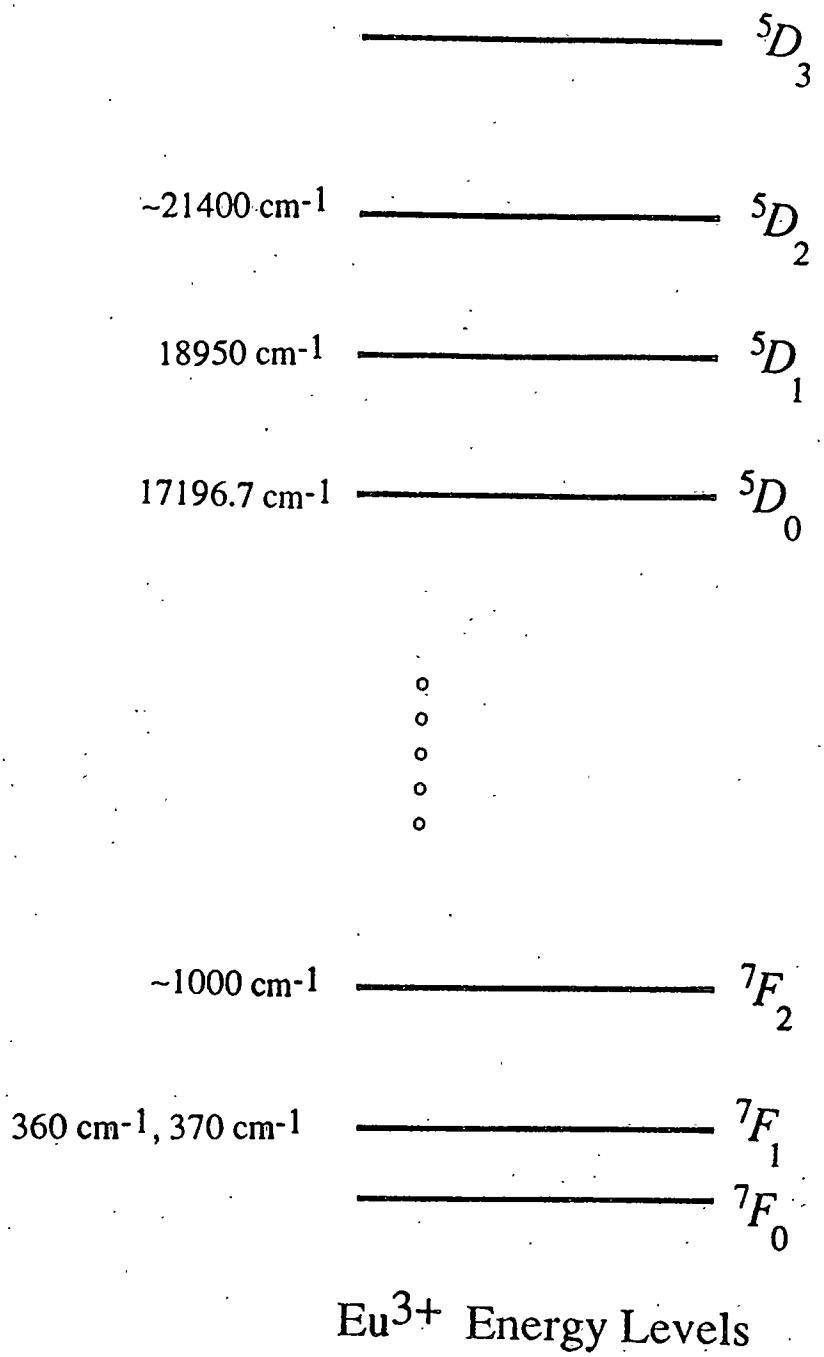

Figure 1.2 Simplified energy level diagram of an Eu^{3+} ion.

Various vanadate, arsenate, and phosphate crystals undergo cooperative Jahn-Teller (CJTE) structural phase transitions at low temperature (Gehring and Gehring, 1975). Depending on the specific material. the phase transitions can either be structural or magnetic or both. Most of the structural transitions were driven by the coupling between degenerate or near degenerate ground state electronic levels and optical or acoustic phonons, or macroscopic lattice strain. Because of the transparency of these crystals, the CJTE effect in these compounds were suitable for optical studies and the transition mechanisms are particularly well understood compared to other Jahn-Teller systems (spinels, etc.).

Since Eu^{3+} has an isolated J = 0 ground state with very little mixing with other levels, no phase transition is expected for europium compounds. But Zeeman experiments on the $^5D_0$ - $^7F_1$ transition showed anomalously small Landé g factors for $EuVO_4$, Eu^{3+}:YVO_4, Eu^{3+}:$LuVO_4$, and $EuAsO_4$. Electronic Raman scattering on the stoichiometric compounds confirmed this observation. The apparent quenching of the angular momentum is attributed to the dynamic Jahn-Teller effect (Ham 1965). The fluorescence and Zeeman experiment will be presented in Chapter 2. The Raman scattering experiments and the dynamic Jahn-Teller effect will be discussed in Chapter 3.

In the fluorescence spectrum of $^5D_0$ for $EuVO_4$ and $EuAsO_4$, another anomaly appears as the double peak of the $^5D_0$ to $^7F_1$ singlet transition. Higher temperature absorption experiments confirmed the splitting of the $^7F_1$ singlet level. The splitting of the singlet level in the stoichiometric compounds is proposed to be a Davydov splitting due to the exciton nature of the electronic states. The experiments leading to this conclusion will be presented in Chapter 2. The possible mechanism causing this splitting and other exciton phenomena will be discussed in Chapter 3 after the presentation of the dynamic Jahn-Teller interaction.

If a structural defect (impurity, vacancy, or interstitial) is present in a crystal, the active ions close to the defect will experience a different environment than in the ideal crystal. It can depart from the ideal environment by so much that numerous satellite spectral lines appear in the spectrum. Since there can be more than one active ion adjacent to the point defect and each one has a different environment, more than one defect site is present for each point defect. In a spectral region with many transitions, the different crystal fields associated with the various defect sites will give many transitions that overlap each other. The assignment of the spectral lines to the correct sites and transitions could be very difficult. The Eu^{3+} ion has the advantage that the ground state $^7F_0$ and the excited state $^5D_0$ are all isolated and are relatively insensitive to the crystal field, so that each spectral line in the $^7F_0$ - $^5D_0$ region will correspond to a distinctive environment; a one-to-one relationship can be established between the spectral line and the crystal environment.

Cone *et al.* (1984) studied the excitation spectrum of stoichiometric $EuVO_4$ in the $^7F_0$ - $^5D_0$ region and found more than 50 defect lines scattered over 50 cm^{-1}, corresponding to over 50 distinct defect sites. Later experiments on a dozen different growths of $EuVO_4$ found over 50 defect lines for each one of them (Robinson 1986, Cone *et al* 1988. Lazzouni 1988, Hansen 1990, Cone *et al* 1993). Stoichiometric $EuAsO_4$ was also studied by laser excitation (Robinson 1986, Cone *et al* 1988); a very "defective" spectrum was again found in the $^7F_0$ - $^5D_0$ region. Excitation spectra for two additional growths of $EuVO_4$ are given in Chapter 2. Because of the one-to-one relationship between the defect sites and the defect spectral lines, this kind of spectral map for the defect sites is very useful when other work is planned on the defect sites. We use the line labels from the spectra to label the defect sites. For example, when the property of line D is discussed, it is really the property of the site giving rise to the spectral line called line D.

Among all these defect lines, each has a distinctive fluorescence spectrum. In the $^5D_0$ - $^7F_1$ spectra, generally more than three spectral lines (expected) are observed; energy transfer among the defect sites must be responsible for the extra fluorescence lines.

Chapter 4 addresses the energy transfer dynamics among these sites. Time-resolved fluorescence is used to find the donor-acceptor relations among them; and to determine the $^7F_1$ levels of the donor. General systematics of the rare earth spectra in different hosts are considered in an attempt to interpret the ~50 cm^{-1} shifts for the relatively crystal-field-insensitive $^7F_0$ - $^5D_0$ transition. Energy transfer routes and lattice structures associated with defects will be discussed in the same chapter.

The europium nucleus has a spin of I = 5/2 and possesses a strong quadrupole moment. In a crystalline environment, nuclear quadrupole splittings occur for different spin states. Splitting schemes are different for different crystal environments. Holeburning (Erickson, 1977a) was used to study the hyperfine splittings of these defect sites (Cone *et al.* 1984, Robinson 1986, Cone *et al.* 1988, Lazzouni 1988, Hansen 1990, Cone *et al.* 1992). Very different quadrupole splittings were found for the different defect sites. Nuclear Zeeman holeburning experiments were also used to study the defect sites in an effort to find the principal directions of the nuclear quadrupole interaction axes, and they were found to be strongly tilted (*ibid.*). A related technique - optically-detected nuclear-magnetic-resonance (ODNMR) - was used to study the ground state of these defects (Hansen 1990, Cone *et al.* 1992). Because of the strong and anisotropic quenching of the ground state Eu^{3+} nuclear magnetic moment (Elliott 1957, Cone *et al.* 1992), more parameters have to be used to fit the experimental data. Using only the Zeeman data for a magnetic field either along the *a*- or *c*-axis was not enough to make a successful fit of the data, so the full angular dependence of the spectrum was measured.

In this work, the ODNMR technique is extensively used to study the hyperfine structure of the defect ground states in $EuVO_4$. The nuclear quadrupole Hamiltonian and the hyperfine splitting measurements for over 30 defect sites at zero field will be presented in Chapter 5, with extensive discussions of the results and their implications. A new holeburning mechanism will also be discussed.

In Chapter 6, we present the angle-dependent ODNMR experiments on some of the defect sites in $EuVO_4$. These experiments were carried out with full angle rotation of the crystal in a magnetic field. Magnetic site inequivalence in a D_{4h} crystal will be discussed. Euler angles are used to define the defect coordinate system relative to the crystal. A fitting program taking into account the site inequivalence and the anisotropic nuclear magnetic moment was written for processing the angle-dependent experimental data. After a brief account of the apparatus, we will give the angle-dependent ODNMR results on some of the defect sites.

CHAPTER 2

PRIMARY SPECTROSCOPY AND CRYSTAL FIELD ANALYSES

In this chapter, we will present the absorption and fluorescence experiments on the stoichiometric $EuVO_4$ and $EuAsO_4$ crystals and on the europium doped YVO_4, $LuVO_4$, YPO_4, and $LuPO_4$ crystals. $Eu(OH)_3$ and $EuPO_4$ were also studied for comparison. Defect line maps on the $^7F_0$ - $^5D_0$ transition of two new $EuVO_4$ crystals will also be presented.

Brecher *et al.* (1967, 1968) studied the polarized spectra of Eu^{3+}:YVO_4 and Eu^{3+}:YPO_4. Those experiments were carried out at liquid nitrogen temperature without time resolution. Grenet *et al.* (1977) studied europium doped $GdVO_4$, YVO_4, and $LuVO_4$, and made crystal field analyses for each situation. Their results will be discussed along with our analysis. We remeasured these spectra with time resolution, which has the advantage that at regions with many fluorescence peaks, the initial state can be distinguished by its lifetime signature. M. Bouzaoui (1991) carried out two-photon absorption experiments on the higher levels of Eu^{3+}:$LuPO_4$. Because of the different selection rules for one-photon and two-photon transitions, additional levels in the $^5D_2$ region were determined in 2-photon experiments. We used those data in our analysis.

The energy levels of $EuVO_4$ have been studied extensively by Cone *et al.*(1984), Lazzouni (1988), Hansen (1990), and Cone *et al.* (1993). Some of the results have been

used in this study. The $EuAsO_4$ spectra have been studied by Robinson (1986) and Cone *et al.* (1988).

Zeeman experiments were used to measure the splittings of the energy levels. In particular, we focussed our attention on the $^5D_0$-$^7F_1$ transition. This transition, in the vanadates and $EuAsO_4$, has been found to have smaller Landé g factors than that expected for pure electronic states.

Experiments

Absorption Experiments

White light absorption experiments were employed to measure the $^5D_2$ and $^5D_1$ levels of Eu^{3+}. The experimental setup is shown in Figure 2.1, together with the fluorescence setup. A 55 W tungsten halogen lamp was used as the light source. A 75 mm lens focused an image of the lamp filament onto the crystal, which was immersed in pumped liquid helium. The crystal was normally masked by shim brass to minimize the stray light. The light exiting from the crystal was collected and collimated by a 75 mm f/2.8 camera lens. The collimated light was then focused by a 200 mm f/3.5 camera lens onto the slit of a SPEX 14018 scanning double monochromator (referred to as the SPEX in later discussions). Regular Polaroid polarizers were used just after the collecting lens to select the polarization measured. A quarter-wave plate was placed before the 200 mm lens to scramble the polarization in the monochromator.

The monochromator scanning was controlled by computer generated TTL pulses. Fifty pulses move the spectrometer *down* by one wavenumber. Since the SPEX has a maximum scan rate of 130 cm^{-1}/s, the pulses were generated at a much lower rate (<<6.5 KHz) so that they would not overwhelm the SPEX control box. The light signal was detected by an EMI9558QB photomultiplier at the exit slit of the spectrometer. The

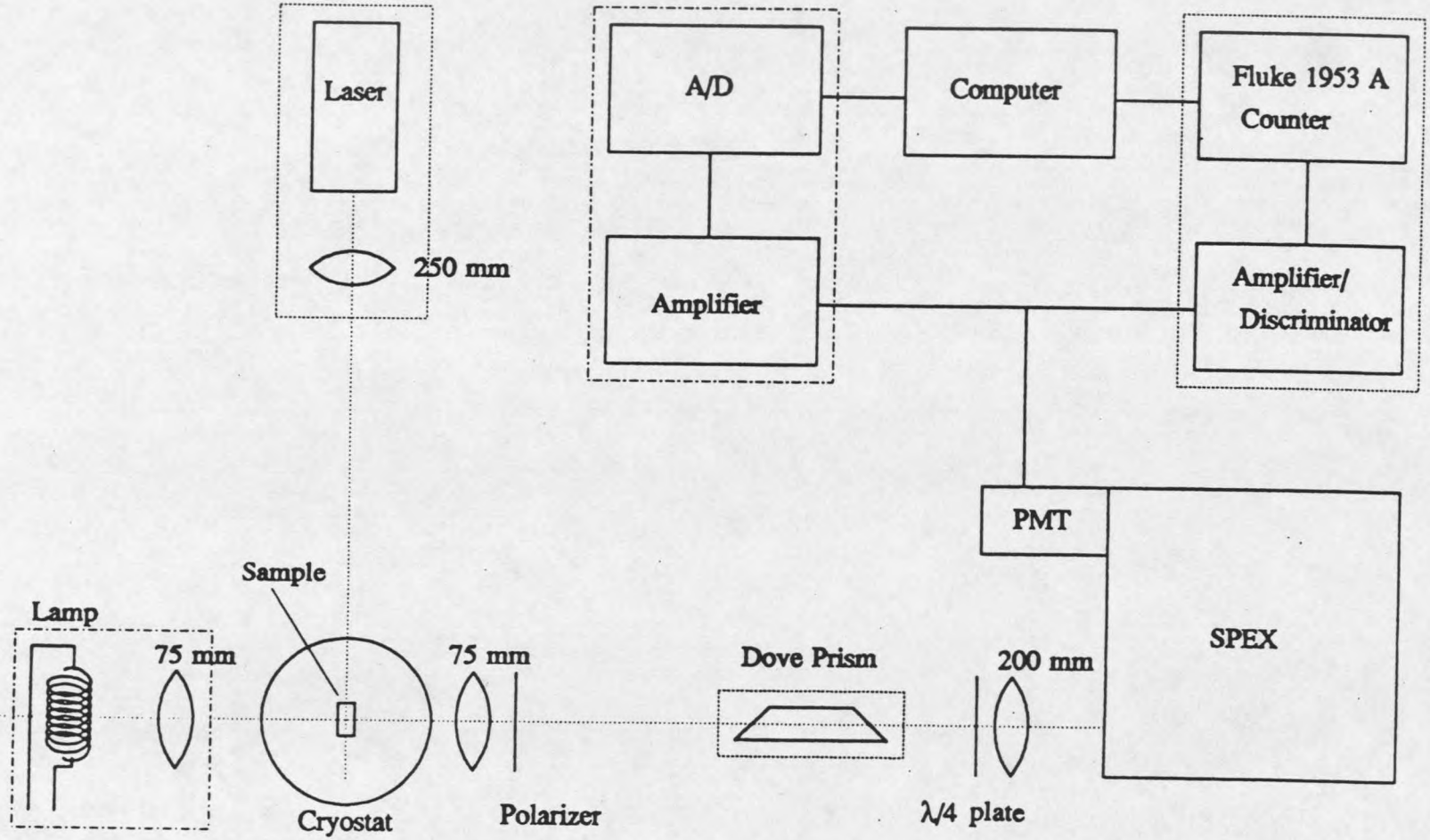

Figure 2.1 Experimental setup. Equipment blocked in dash-dotted lines was used only in absorption experiments. Those items blocked by dotted lines were used only in fluorescence experiments. Others are common to both.

output from the PMT was low-pass filtered and amplified by a Tektronix 7A22 amplifier, and then was fed to one channel of the DT2762 A/D converter. In the data acquisition process, the SPEX was set first and the light intensity was measured; then the spectrometer was scanned *down*, and the light intensity was measured again. An iron-neon hollow-cathode lamp was used to calibrate the SPEX.

The SPEX is most sensitive at around 19000 cm^{-1}. We had the best signal in the $^5D_1$ region, while that for the $^5D_2$ levels was weaker.

Fluorescence Experiments

In the fluorescence experiments, the laser was focused onto the samples by a 250 mm lens. When the laser frequency was tuned onto a transition peak, there would be fluorescence along the path of the laser beam. The fluorescence was collected at a 90° angle to the exciting beam direction. Otherwise, the collecting optics are identical to that used in the absorption experiments. A Dove prism was usually used between the 75 mm lens and the 200 mm lens to rotate the image of the fluorescence from the horizontal laser path to a vertical orientation so that most of the image can be focused onto the vertical monochromator entrance slit. This arrangement increased the signal by an order of magnitude in fluorescence experiments.

The output from the photomultiplier passed through a preamplifier and a discriminator before being converted to TTL pulses. These pulses were then sent to a GPIB-controlled Fluke 1953A counter/timer. Photon counting was the method of choice for fluorescence data. Monochromator scanning was the same as in the absorption experiment.

Laser Excitation

Sometimes, measuring energy levels by absorption is simply impossible due to the weak transition probability. However, the immeasurable amount of absorption may result in observable fluorescence that can be detected easily because of the higher sensitivity of a fluorescence experiment. The dependence of the fluorescence intensity upon the excitation frequency can serve as a good indication as to where the transition occurs, and how wide and strong it is. The spectra measured by monitoring the fluorescence while scanning the laser excitation frequency are called excitation spectra. This way of measuring absorption does not always provide the same spectra as those measured by absorption experiments, but in case of extremely weak absorption, this may be the only alternative.

In our mapping of the defect $^7F_0$ - $^5D_0$ spectra and in the measurement of the intrinsic $^7F_0$ - $^5D_0$ transition in a magnetic field, laser excitation spectroscopy was used. A Coherent 599/21 single frequency cw dye laser was used to excite these transitions. The laser can scan 30 GHz (1 cm^{-1}) at one time. To map out a 50 cm^{-1} range , many "pages" of 30 GHz spectra had to be assembled together.

Sample Temperature

Most of our experiments were carried out at pumped liquid helium temperature. This has the advantage that the phonon contributions to most of the transitions can be neglected. The results quoted in this thesis should all be at $T < 2$ K unless otherwise indicated.

Cryostats and Magnetic Fields

All our zero field experiments were carried out in a transverse access glass cryostat. In that dewar, the equipment layout was almost exactly like that shown in Figure 2.1.

The Zeeman experiments were carried out in a superconducting magnet dewar with an inner bore of about two inches. The magnetic field and supply current ratio was 1.00 kG/A. In this dewar, the layout changed a little in that the Dove prism was not used. Due to the axial access geometry, a mirror was used to send the light vertically into the dewar. The laser light was then reflected by a right angle prism to pass through the sample horizontally. A second prism sent the transmitted light out of the dewar for analysis in the absorption experiments. In fluorescence experiments, a third prism was used on the side to collect the fluorescence light for analysis. The fluorescence collection lens just outside of the dewar normally had a focal length of 330 mm.

Selection Rules

Group theory states that in order to have a dipole-allowed transition between an initial state represented by Γ_i and a final state represented by Γ_f, there must be an excitation mechanism represented by Γ_e so that $\Gamma_i \times \Gamma_e$ contains Γ_f, where Γ_e is the representation either for an electric- or a magnetic-dipole (Tinkham 1964, for example).

From the multiplication tables given by Koster *et al.*(1963), selection rules in any symmetry may be determined. For D_{2d} symmety, as laid out by Brecher et al (1967), and restated by others (Macfarlane and Shelby 1987, Hansen 1990), the selection rules are listed in Table 2.1.

The compatibility table for this symmetry shows

J=0: Γ_1.

J=1: Γ_2, Γ_5.

J=2: Γ_1, Γ_3, Γ_4, and Γ_5.

From the transition rules we can see that along the c axis, we see only the circularly polarized light originating from transitions with at least one doubly degenerate state as a terminal state, as would be expected since the *a* and *a'* axis should be equivalent.

Table 2.1. Selection rules in D_{2d} symmetry*.

	Γ_1	Γ_2	Γ_3	Γ_4	Γ_5
Γ_1		M σ		E π	E σ α M π α
Γ_2	M σ		E π		E σ α M π α
Γ_3		E π		M σ	E σ α M π α
Γ_4	E π		M σ		E σ α M π α
Γ_5	E σ α M π α	E σ α M π α	E σ α M π α	E σ α M π α	E π M σ

* In Eu^{3+}, all transitions for which $\Delta J \neq \pm 1$ obey electric-dipole selection rules. For $\Delta J = \pm 1$, magnetic-dipole rules are obeyed when $J = 0$ is one of the terminal states. Otherwise, the transition will be of mixed character.
E denotes electric-dipole; M, magnetic-dipole; π, electric vector parallel to *c*-axis; σ, electric vector perpendicular to the *c*-axis; α, circularly polarized around the *c*-axis.

Crystals

We have studied a range of europium-doped zircon-structured crystals of different Eu^{3+} concentrations. The stoichiometric $EuVO_4$ crystal we used most was grown in the Clarendon Laboratory of the University of Oxford by B. Wanklyn. It was colorless and about 1x1.5x3 mm^3 in size and was classified as growth A in Cone *et al.* (1993) and Hansen (1990). An $EuVO_4$ crystal classified as growth I by Cone *et al.* (1993) was studied using angle-dependent optically-detected nuclear-magnetic-resonance (see Chapter 4). Another growth of $EuVO_4$ crystals obtained from the University of Oxford were doped with 1% praseodymium; it also had a tint of brown color. Other $EuVO_4$ samples used were grown by Dr. M.M. Abraham of Oak Ridge National Laboratory on 22 Nov 1991; these crystals have a brownish color and are transparent. They have not

been studied before and will be called the ORNL crystals later in the text. The $EuAsO_4$ crystal was from the University of Oxford and was the largest of all the concentrated crystals (2 x 3 x 5 mm^3). The concentrated vanadate and arsenate crystals were studied by additional laser spectroscopy techniques, as described in later chapters.

All the dilute crystals were grown by Dr. M.M. Abraham. The phosphate crystals are usually thin (<0.3 mm) slabs about 1 mm wide and much longer parallel to the *c* direction (1-5 mm). They were colorless and transparent. The absorption peaks were very weak due to the low doping level and the small size of the crystals. It was only realistic to pass light through along the thin direction in absorption experiments. This resulted in extremely weak $^5D_1$ and $^5D_2$ absorption peaks. Higher doping crystals were used for verification of weak transitions.

The dilute vanadate crystals were transparent with light brownish color. They were usually square in the a-a' plane and much longer in the c-axis direction (1 to 5 mm). Well grown crystals have a distinctively pyramically tapered end. Because of the larger dimension, we were able to measure the $^5D_1$ and $^5D_2$ levels directly from absorption even for our most dilute crystals.

All the results quoted in this chapter for dilute crystals were measured for crystals with doping concentration lower than 1% unless otherwise indicated. Higher doping levels broaden the lines because the dopant ions distort the original lattice instead of just substituting for Y or Lu. The dopant ions can also form clusters to broaden the linewidth even more. For more detailed discussion about the broadening mechanism, see Chapter 4. All the crystals we used are listed in Table 2.2.

Table 2.2 Crystals studied

	Color	Size	Source	Date	Studies*
$EuVO_4$					
Growth A	colorless	1x1.5x3 mm^3	Oxford		A, F, O
Growth I	colorless	1x1x5 mm^3	Oxford		O
ORNL	light brown		Oak Ridge	11/22/ 91	A, F, O, LE
Pr doped	light brown		Oxford		LE
$EuAsO_4$	colorless	2x3x5 mm^3	Oxford		A, F
Eu:YVO_4 0.03% - 1%	light brown		Oak Ridge		A, F, LE
Eu:$LuVO_4$ 0.03% - 1%	light brown		Oak Ridge		A, F, LE
Eu:YPO_4 0.5%-100%	colorless		Oak Ridge		A, F, LE
Eu:$LuPO_4$ 0.5%, 5%	colorless		Oak Ridge		A, F, LE

* A: absorption, F: fluorescence, O: optically-detected nuclear magnetic resonance, LE: laser excitation.

General Results

^5D_J levels

The $^5D_2$ splits into 4 levels in D_{2d} symmetry: Γ_1, Γ_3, Γ_4, Γ_5. Transitions from the ground state are only allowed for Γ_4 and Γ_5; the other two transitions are forbidden.

The $^5D_1$ splits into 2 levels by a D_{2d} crystal field: Γ_2 and Γ_5. Transitions from the ground state correspond to $\Delta J = \pm 1$ with one of the terminal states having $J = 0$. Only magnetic-dipole transitions are allowed.

The $^7F_0$ to $^5D_0$ transition is both electric-dipole and magnetic-dipole forbidden. No transition should be observed.

In $EuVO_4$ and $EuAsO_4$, the allowed $^7F_0$ to $^5D_2$ absorption was very strong. Over-absorption occurred for crystals of less than 1 mm thickness. Numerous satellite transitions were also observed beside the two main transitions. For the dilute crystals, the intrinsic absorption could be observed but were very weak. Because of the larger crystal size, we saw stronger absorption in the vanadate crystals than in the phosphates for the same concentration. Absorption for the phosphate crystals was extremely weak but observable. Higher doping crystals had to be used to confirm the measurements in the more dilute crystals. We see a concentration effect when using crystals of different doping levels; the energy levels move up when the concentration is higher.

For the $^7F_0$ to $^5D_1$ transitions, the oscillator strength is considerably lower than for the $^7F_0$ to $^5D_2$ transitions. The absorption is nearly total in our concentrated crystals of about 1 mm thickness. Absorption can be seen in the dilute crystals, but is much weaker than the $^7F_0$ to $^5D_2$ transition. The energy levels had to be confirmed by laser excitation spectra in the phosphate crystals. Although only magnetic-dipole transitions should be allowed in this symmetry, forced electrical dipole transitions have been observed in the $^7F_0$ (Γ_1) to $^5D_1$ (Γ_5) transition. The electric-dipole transition and magnetic-dipole transition have about equal intensity. So this must be a very small breakdown of the transition rules since the electric-dipole transition is normally much stronger.

The $^5D_1$ splitting is exceptionally small for the concentrated crystals. It is 1.2 cm^{-1} for $EuAsO_4$, and 3.5 cm^{-1} for $EuVO_4$ at $T < 2$ K. But the signs of the splittings are different for these two crystals. The singlet Γ_2 is higher in $EuAsO_4$. The doublet Γ_5 is higher in $EuVO_4$. The dilute crystals we studied have larger splittings: > 10 cm^{-1}; but the phosphates split with the same sign as $EuAsO_4$, while the vanadates split with the same sign as $EuVO_4$ does.

No absorption can be observed for the $^7F_0$ to $^5D_0$ transiton for any of these crystals, as would be expected. However, this transition will be weakly allowed under a magnetic

field which admixes J = 1 states. The transition probability increases quadratically with a magnetic field (Otteson, 1984). All $^5D_0$ levels for these crystals were measured by laser excitation in a field. In a magnetic field, the $^5D_0$ level will move up by a very small amount relative to the ground state (Cone *et al.*, 1993), a negligible effect for the accuracy quoted here. A single frequency dye laser beam was directed on to the sample and the fluorescence from the sample was monitored. When the laser was tuned to the strongest fluorescence position, the laser frequency was measured by a home made wavemeter. This frequency is the $^7F_0$ to $^5D_0$ transition frequency. The conversion between the wavemeter reading and frequency can be found in Appendix I. The concentration-induced effect can also be observed for this transition. For example, the transition frequency was 17184.91 cm^{-1} for the 0.1% Eu^{3+}:YVO_4 sample , while it was 17185.10 cm^{-1} for the 1% concentration sample.

The ^5D_J data for these crystals can be found in Appendix II. Not listed in the Appendix is the $^7F_0$ to $^5D_0$ transition for $EuPO_4$ which occurs at 17264.1 cm^{-1}.

Room temperature absorption experiments were carried out on $EuVO_4$ for the ^7F_J (J = 0, 1, 2) to ^5D_J (J = 0, 1, 2) transitions. We were able to determine all the ^5D_J (J = 0, 1, 2) and ^7F_J (J = 0, 1, 2) levels. The characters of the energy levels were determined by the polarization of the spectra. The assignment of the levels is consistent with Cone *et al.* (1993). Unlike the $^7F_0$ to $^5D_1$ spectra, the $^7F_1$ to $^5D_1$ spectra are pure electrical-dipole in nature.

The missing levels in Eu^{3+}:$LuPO_4$ $^5D_2$ were measured at T = 12 K by M. Bouazaoui (1991) using two-photon absorption. The missing levels in $EuVO_4$ $^5D_2$, as well as the $^5D_3$ levels, were measured by Cone *et al.* (1993) under a field. These levels are also included in Appendix II.

^7F_J Levels

The ^7F_J levels were determined from fluorescence spectra originating from both the $^5D_0$ and $^5D_1$ levels. A pulsed N_2 laser-pumped dye laser was used to excite the $^5D_2$ (Γ_5) level. Due to the fast relaxation, fluorescence directly from this level could not be observed. Fluorescence came from the $^5D_2$ (Γ_3), $^5D_1$, and $^5D_0$ states, but the $^5D_2$ fluorescence was not used in our calculation of the ^7F_J levels partly because the $^5D_2$ (Γ_3) level was not well determined, partly because the fluorescence from this level had a very short lifetime (~ ns), making photon counting impractical.

Most of these experiments were carried out with the light incident along the *a*-axis of the crystal and the fluorescence was collected along the *a'*-axis. Measurements along the *c*-axis were not attempted although this would give a nice identification for transitions with a doubly degenerate terminal state. We had enough information for most of these transitions to assign them.

Fluorescence from the $^5D_1$ levels originated mostly from the lowest level at low temperature. In the vanadates, this is the Γ_2 singlet; in the phosphates, the Γ_5 doublet. Due to the small splittings in $EuVO_4$ and $EuAsO_4$, fluorescence can originate from both levels. The fluorescence lifetime from the lower level is normally around 20 μs.

Fluorescence from $^5D_0$ was usually very strong and had a long lifetime, typically 0.5 ms to 1 ms. The phosphates had longer lifetimes. Since the $^5D_0$ energies were measured very accurately, we used the $^5D_0$ fluorescence as much as possible.

When the $^5D_2$ is pumped, fluorescence can come from both the $^5D_1$ and $^5D_0$ levels. In some spectral regions, fluorescence lines from different sources can overlap. When this happens, the lifetime signature of the upper state can be used to identify the origin of the fluorescence lines. For example, we can measure a spectral region using a 20 μs gate to select the fluorescence of the first 20 μs after excitation. Then we can repeat the scan using a 1 ms or 2 ms gate in the same spectral region. By comparing the two spectra,

the relatively stronger lines in the first spectrum originate from $^5D_1$; while the other lines originate from $^5D_0$. Using this method, we identified some spectral lines from the $^5D_1$ state that were buried under the strong $^5D_0$ fluorescence lines in the spectrum taken without time resolution.

There were many defect fluorescence lines in the concentrated crystals when the $^5D_2$ was pumped. The identification of the intrinsic fluorescence was difficult. The defect lines are present even in the dilute crystals when the doping level exceeded 1 %. Without sacrificing too much signal signal, we used crystals with as low doping level as possible. This problem is more serious in the $^5D_0$ to $^7F_1$ spectrum. While the $^5D_0$ to $^7F_2$ spectrum is relatively clean. This does not mean that we are seeing the intrinsic transition always in $^5D_0$ - $^7F_2$. It is more of a result of the wide, lifetime limited linewidth and the large gap between the allowed transitions. If the defect transition frequency is not too far away from the intrinsic transition frequency (a few wavenumbers), then it may merge onto the intrinsic transition and increase the linewidth. The lineshape for the $^5D_0$ - $^7F_2$ (Γ_5) transition is very irregular, probably due to the defects. The strange lineshape in the $^5D_0$ - $^7F_2$ (Γ_4) transition has a different origin (see below). The fact that the intrinsic $^5D_0$ to $^7F_1$ transition is only magnetic-dipole allowed while the defect transitions are electric-dipole allowed may also contribute to the dirtier signal in this transition.

The fluorescence from $^5D_0$ has been observed all the way up to the $^5D_0$ to $^7F_6$ transition for the dilute vanadate crystals. It is observed only up to $^5D_0$ to $^7F_4$ in the phosphates. This differs from Brecher *et al.* (1967, 1968) in that they observed the $^5D_0$ to $^7F_6$ transition for Eu:YPO_4, but not for Eu:YVO_4. Failure to detect the $^5D_0$ to $^7F_6$ fluorescence in the phosphates in this work is probably due to the small size of the crystal.

The observed ^7F_J levels for all these crystals are listed in Appendix II.

The fluorescence with $^7F_2$ (Γ_4) as a terminal state always had a phonon side band associated with it on the lower energy side in the europium doped vanadates and $EuAsO_4$. For all the vanadate crystals, this band was about 20 cm^{-1} wide. It was a little narrower (10 cm^{-1}) for $EuAsO_4$. In Brecher *et al.*'s published spectra of Eu^{3+}:YVO_4 (1967), this band could also be seen. These bands had a strange shape as shown in Figure 2.2. The zero phonon line was not symmetric. This band was identified as a phonon side-band because in room temperature absorption experiments it was on the higher energy side of the zero-phonon line in $EuVO_4$ as shown in Figure 2.3. The line shape is not understood at this moment.

Results for Concentrated Crystals

$^7F_0$-$^5D_0$ Defect Spectra by Laser Excitation

Since one of the main concerns of this thesis is the defect sites in the concentrated $EuVO_4$, we will comment more on the spectra of these crystals. The $^7F_0$ to $^5D_2$ spectra reveal many satellite transitions besides the two main transitions. The two allowed intrinsic transitions all have total absorption for crystals less than 1 mm thick. The $^7F_0$ to $^5D_1$ absorption also shows some defect transitions. No absorption can be observed at all in the $^7F_0$ to $^5D_0$ transition region.

Defect $^7F_0$ - $^5D_0$ excitation spectra of many $EuVO_4$ crystals from different crystal growths have been published in Cone *et al.* (1993) and Hansen's thesis (1990). We measured the $^7F_0$ to $^5D_0$ defect spectra of the ORNL $EuVO_4$ crystals, and the Pr^{3+}:$EuVO_4$ crystal from the University of Oxford. These measurements are important for any optical study of the defects in these crystals, since they are used as maps when other high resolution work (ODNMR, etc.) on the defect sites are planned. These spectra were measured by scanning the Coherent 599/21 cw dye laser while monitoring

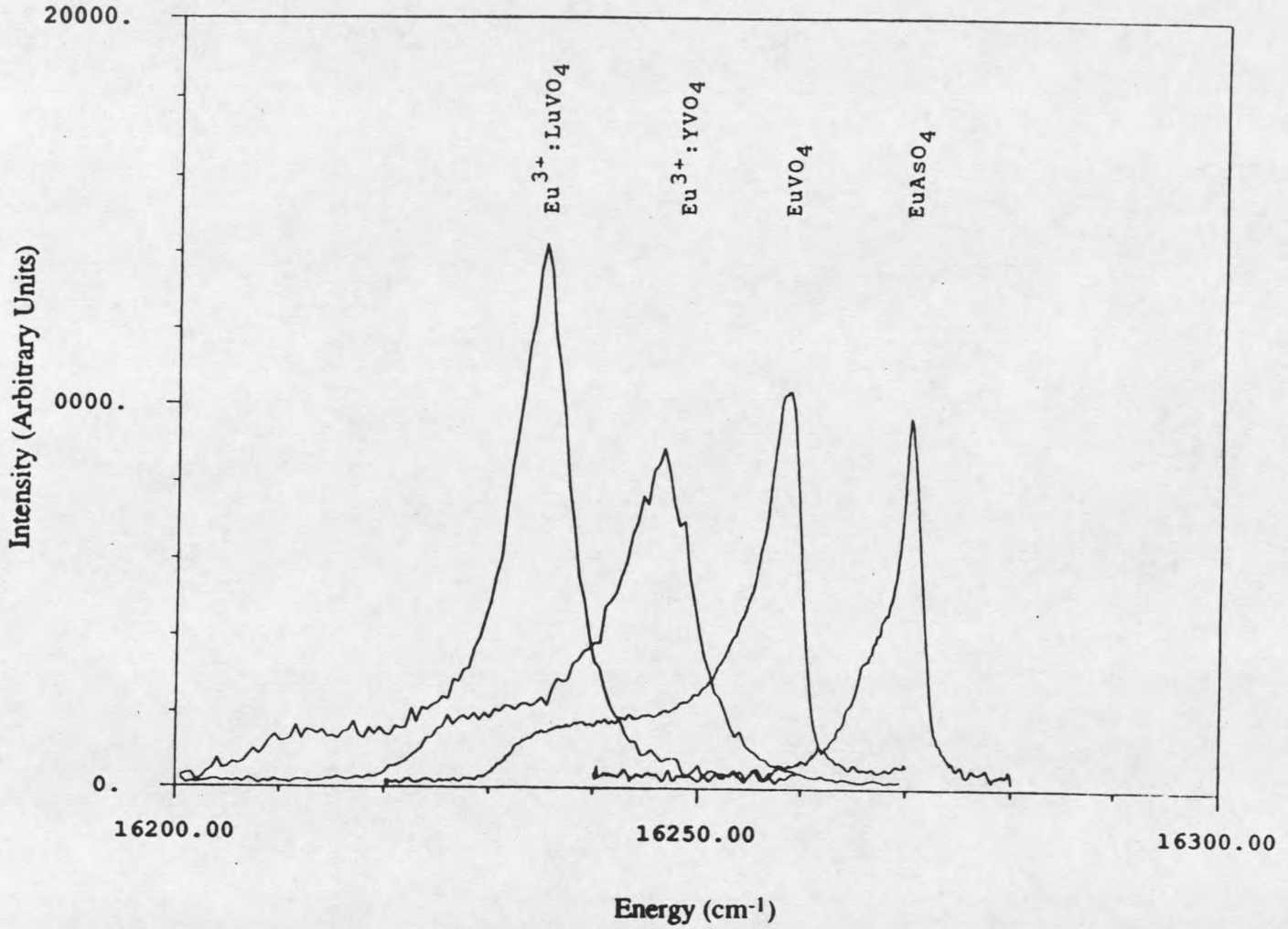

Figure 2.2 The $^5D_0$ - $^7F_2$ (Γ_4) spectrum for europium-doped vanadates and $EuAsO_4$ at 1.5 K.

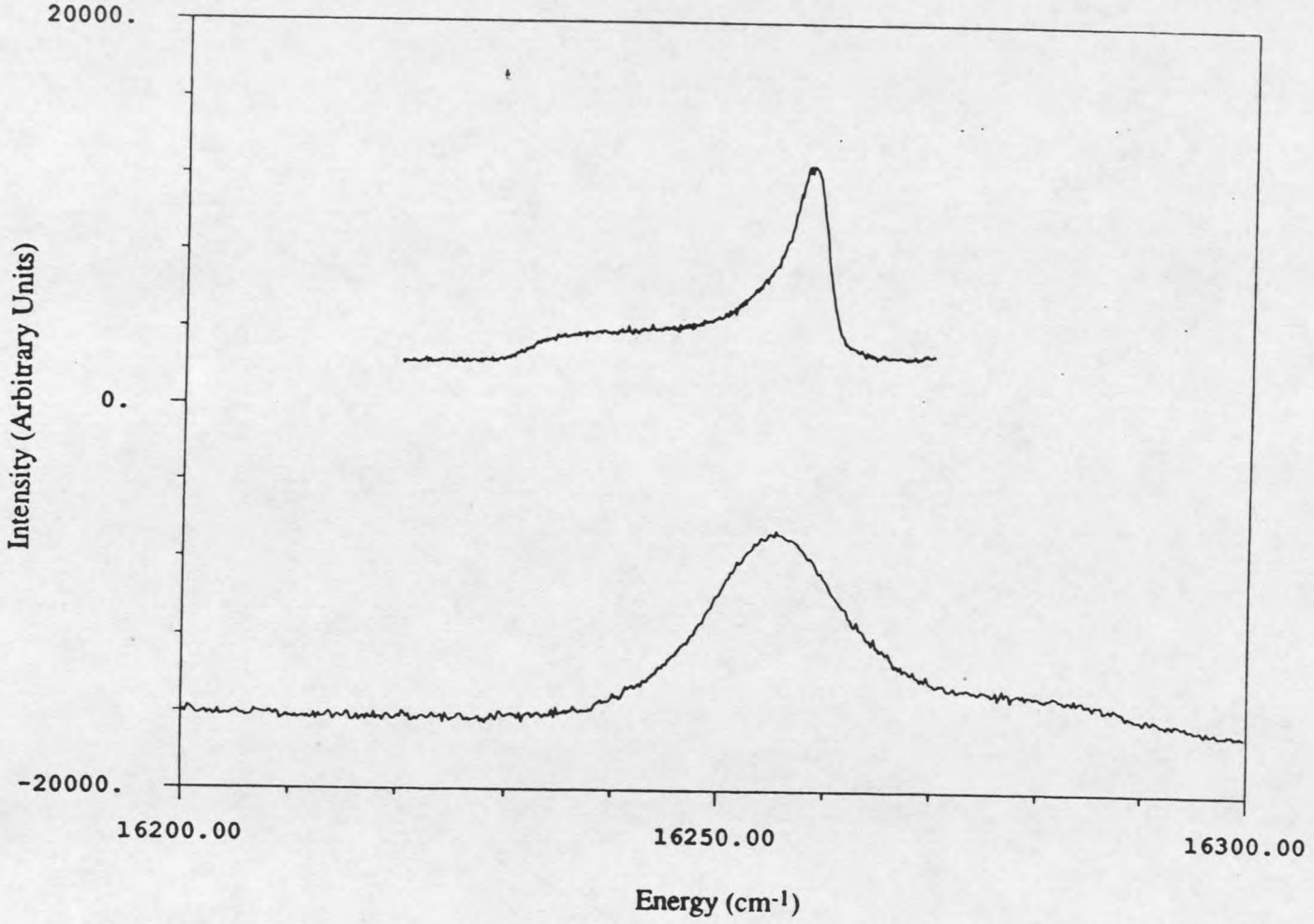

Figure 2.3 Comparison of the fluorescence and absorption spectra of the $EuVO_4$ $^7F_2$ (Γ_4) $\Leftrightarrow$ $^5D_0$ transition. Top line: fluorescence at 1.5 K. Bottom line: absorption at 300 K.

the fluorescence from the crystal. The fluorescence light was collected by an optical fiber bundle. Optical filter stacks (Corning 3-66) were used to select the $^5D_0$-$^7F_2$ fluorescence. The laser has a linewidth of about 1 MHz, and can scan a maximum of 30 GHz. So, the defect spectra given are assemblies of many small pieces. The final spectra were synthesized by computer from experimental linewidth and intensity data for the specific crystal. They resemble the real spectra well. These two spectra are given in Figures 2.4 to 2.7.

The ORNL crystals have a FWHM linewidth of about 2 GHz, while the Pr^{3+} doped crystals have a linewidth of about 5 GHz. The Pr^{3+} doped crystals have two weak high energy lines (516635, 516389 GHz) that appear in crystals grown with fluorine flux. Although this crystal was *not* grown with fluorine flux, it still could have fluorine contaminations in the crucible. These two lines are not as strong as in the growth I crystals (Cone *et al*, 1993).

Just as in other $EuVO_4$ crystals, the intrinsic $^7F_0$ to $^5D_0$ transition in the ORNL crystal grows quadratically in intensity with magnetic field. But it has a very strange shape, almost like a double humped feature at the top. It also exhibits holeburning (see Chapter 5) which is not typical of other crystal growths.

The intrinsic transition was observed at 17196.7 cm^{-1} in a magnetic field. It was identified as intrinsic because the transition intensity increases quadratically in a field. At a field of 55 kG, the absorption was about 50% for our crystal of about 1 mm thickness. Defect lines close to this region increase their intensity much more slowly since there is already a zero field transition mechanism due to lower symmetry. Higher energy defect lines do not enhance under a field. Directly below the intrinsic transition, there is a spectral region of about 20 GHz where no defect line was observed at all for any of the crystals. Even the base line seems to be much smoother than in other regions.

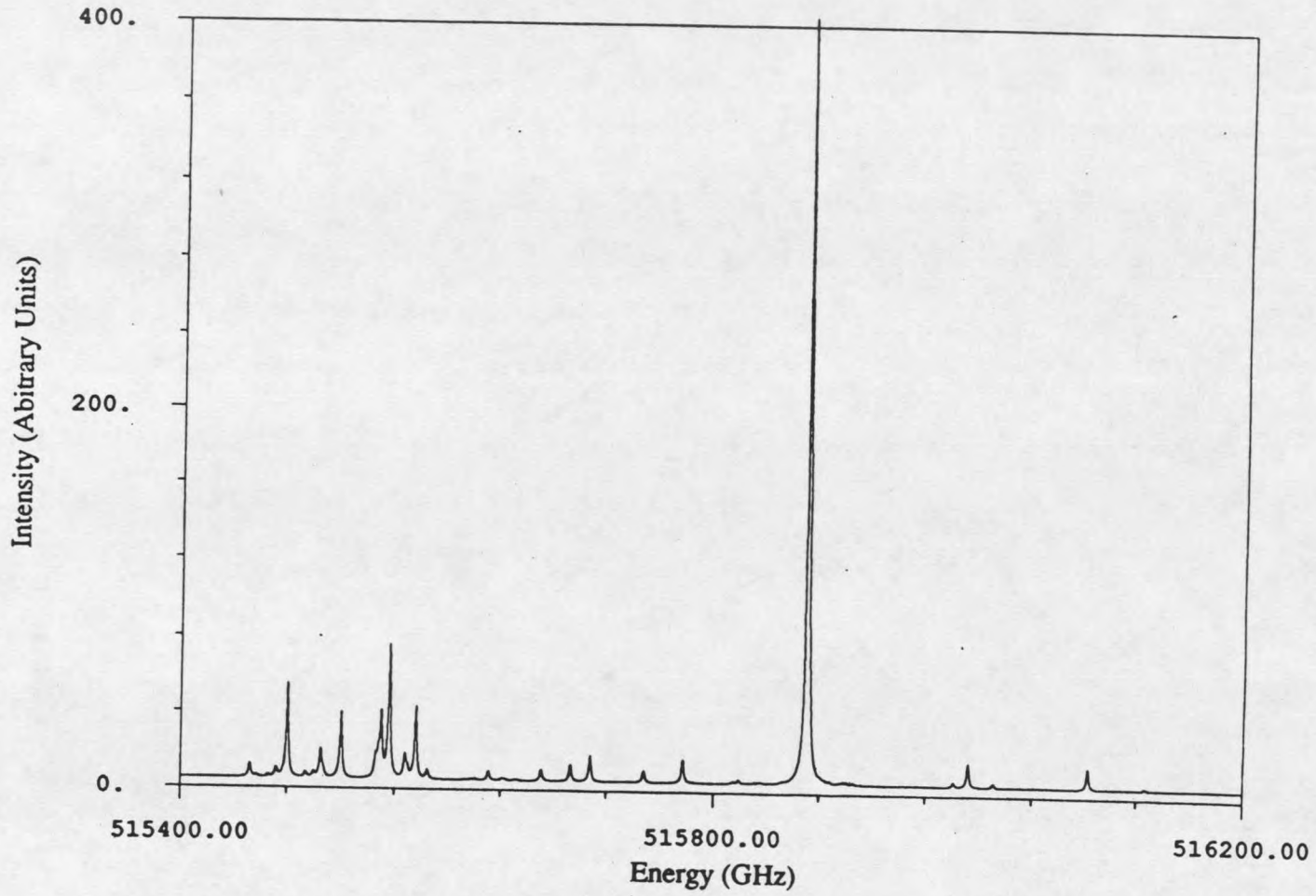

Figure 2.4 The $^7F_0$ - $^5D_0$ defect spectrum of the ORNL $EuVO_4$ crystal.

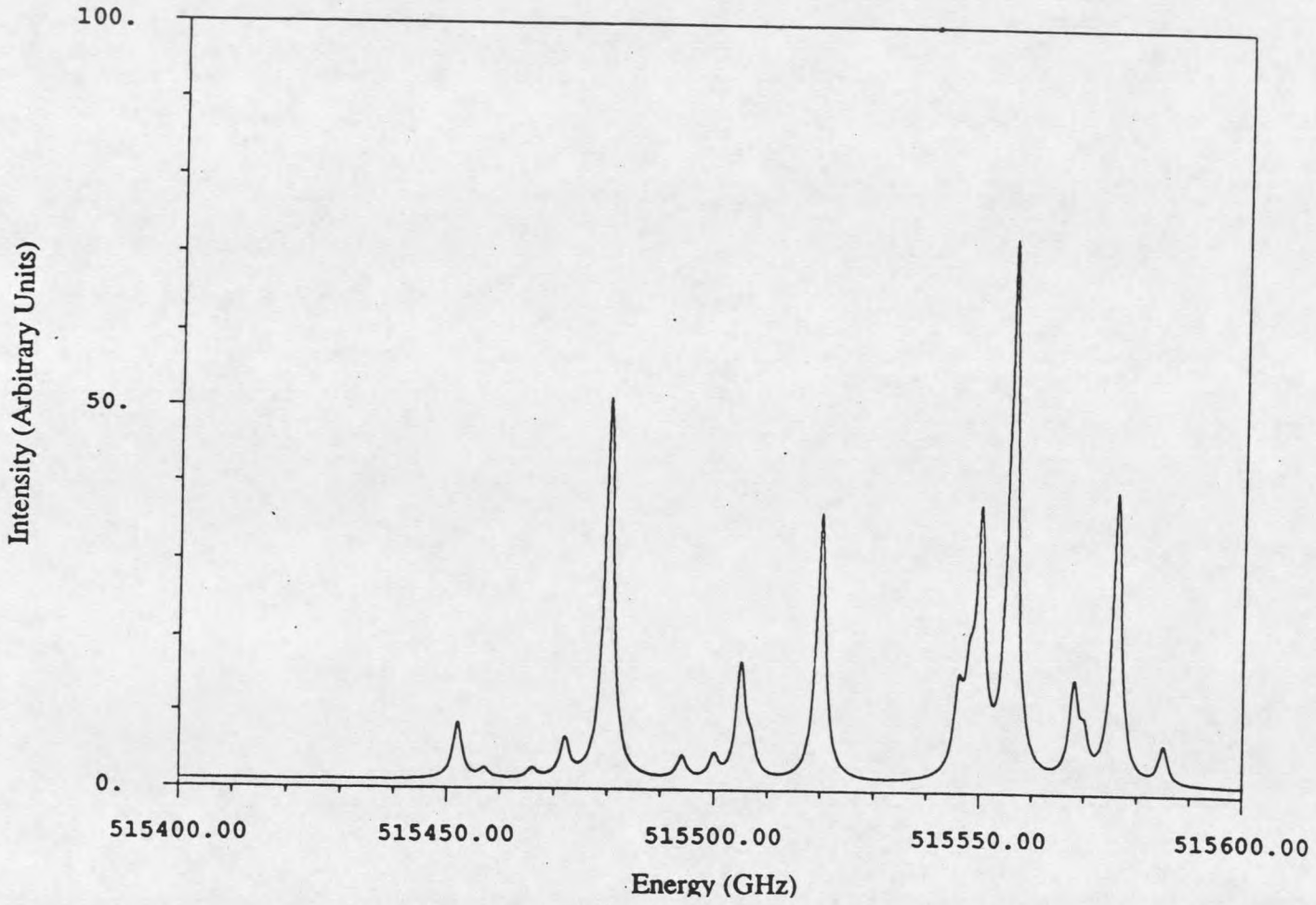

Figure 2.5 Expanded view of Figure 2.4 in the intrinsic site transition region for $EuVO_4$. The intrinsic site transition occurs at 515544 GHz or 17196.70 cm^{-1}.

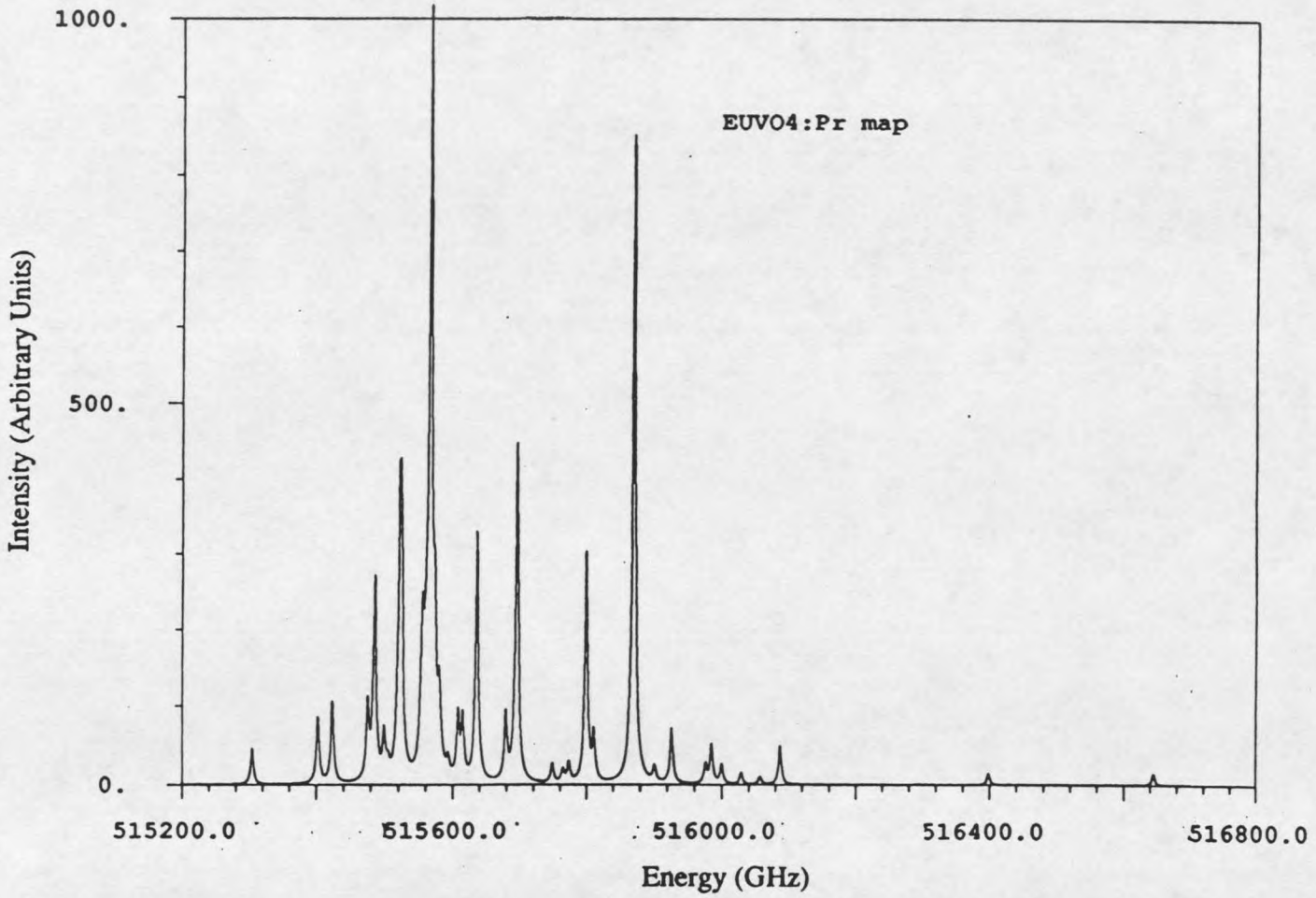

Figure 2.6. The $^7F_0$ - $^5D_0$ defect spectrum of the Pr^{3+} doped $EuVO_4$ crystal. Notice the two small lines at the higher end of the spectrum. They are typical of crystals grown with fluorine flux.

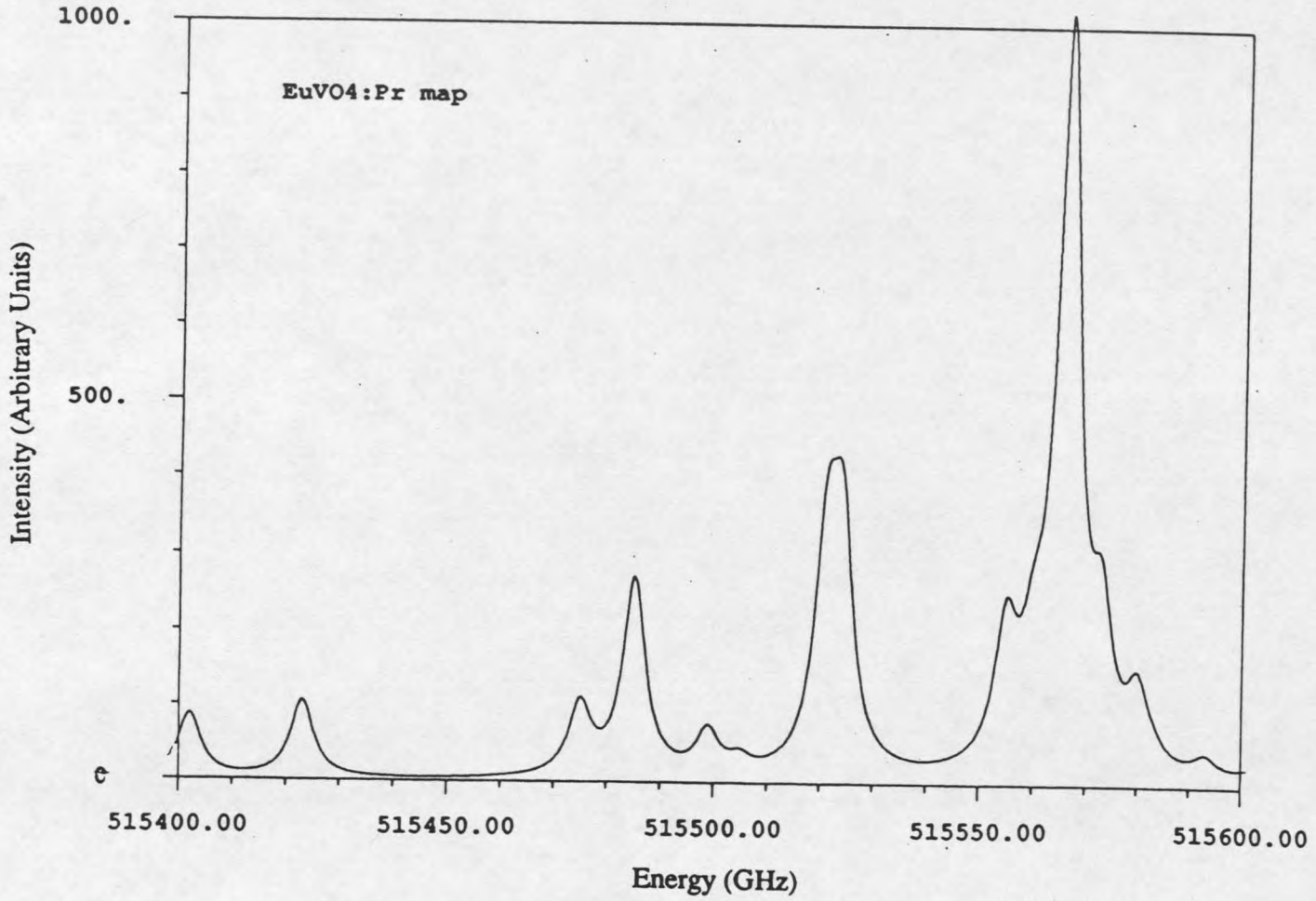

Figure 2.7 Expanded view of Figure 2.6 in the intrinsic transition region for $EuVO_4$.

Fluorescence

We have determined the ^7F_J (J = 1, 2) levels for the concentrated crystals by directly exciting the $^5D_0$ level under a field using a narrow band cw laser and pumping $^5D_1$ by a pulsed dye laser. These findings were confirmed by our Raman experiments (see Chapter 3). Since $^5D_0$ - $^7F_2$ only has two transitions allowed, the other two levels were determined from the $^5D_1$ - $^7F_2$ transiton. For the concentrated crystals, the fluorescence terminating to ^7F_J J>2 states were not assigned unambiguously due to the complexity of the defect transitions and the broad linewidths. The fluorescence to $^7F_3$ was very weak as noted be Brecher *et al.* (1967, 1968). No level was determined for $^7F_3$ in the concentrated crystals. Two $^7F_4$ levels were determined for $EuVO_4$.

We observed strong self quenching of the fluorescence in the concentrated crystals. At room temperature, no matter what frequency was pumped in the $^7F_0$ - ^5D_J transitions, no fluorescence was visible. At 77 K, there was weak fluorescence. The lifetimes were orders of magnitude shorter at higher temperature. For example, at liquid helium temperature, the $^5D_0$ lifetime is about 1 ms, the $^5D_1$ lifetime about 20 μs, and the $^5D_2$ lifetime about 100 ns. At 77 K, the $^5D_0$ lifetime is about 20 μs and the $^5D_1$ lifetime about 100 ns. No fluorescence from the $^5D_2$ level could be observed. At room temperature, even the $^5D_0$ transition lifetime is shorter than 1 μs.

When we pump the $^5D_2$ levels and observe the fluorescence in the $^5D_0$ - $^7F_1$ region, there are so many fluorescence lines that no intrinsic fluorescence could be identified. The envelope of the fluorescence spectrum changes dramatically when the laser frequency changes. Using a xenon lamp for excitation yielded a cleaner spectrum; the intrinsic fluorescence was recognizable, but there were still many other lines from defects (Cone and Leask, private communications). Experiments done by Jean-Claude Gacon and Bernard Jaquier in France have given similar spectra. Fluorescence from

direct pumping of $^5D_1$ also gave spectra with many defect lines, but these spectra are cleaner than those obtained by pumping $^5D_2$.

In a strong field, the intrinsic $^5D_0$ - $^7F_0$ transition intensity increases quadratically due to the small admixture of the $^7F_0$ and $^7F_1$ levels (Otteson 1984, Hansen 1990). When this transition is pumped directly using a narrow band laser, three spectral lines can be observed in the $^5D_0$ - $^7F_1$ region correponding to the expected transitions to the singlet and the split doublet. Typical spectra are shown in Figure 2.8 and Figure 2.9 for $EuVO_4$ and $EuAsO_4$, respectively. All the peaks present in the spectra seem to have a shoulder. This is more obvious in $EuAsO_4$. If we just use the strong peaks, the $EuAsO_4$ splitting is 7.2 cm^{-1}, the $EuVO_4$ splitting is 10.2 cm^{-1}. If the weaker peaks are used, then the $EuAsO_4$ splitting is 6.2 cm^{-1}, while the $EuVO_4$ splitting is 9.6 cm^{-1}. The singlet is the lower level in $EuVO_4$, while it is the higher level in $EuAsO_4$. For these spectra, we also observe:

(1) The doublet splits with Landé g factors of 1.30 ($EuVO_4$) and 1.40 ($EuAsO_4$) instead of 1.50. We made sure of the calibration of our magnet by using a Hall probe to calibrate it.

(2) The singlet peak is about twice as wide as the doublet peaks.

The anomalously small g factor suggested that these fluorescence lines might be from defects with tilted principal axes, but if they were, we should have been able to see this kind of fluorescence when that defect site was excited directly. We examined the spectra of all the defect lines around the intrinsic transition; none of them had similar fluorescence. Only one weak line 1 GHz above the intrinsic line in the Growth A crystal gave similar fluorescence spectrum but shifted up by a wavenumber, and with similar splittings.

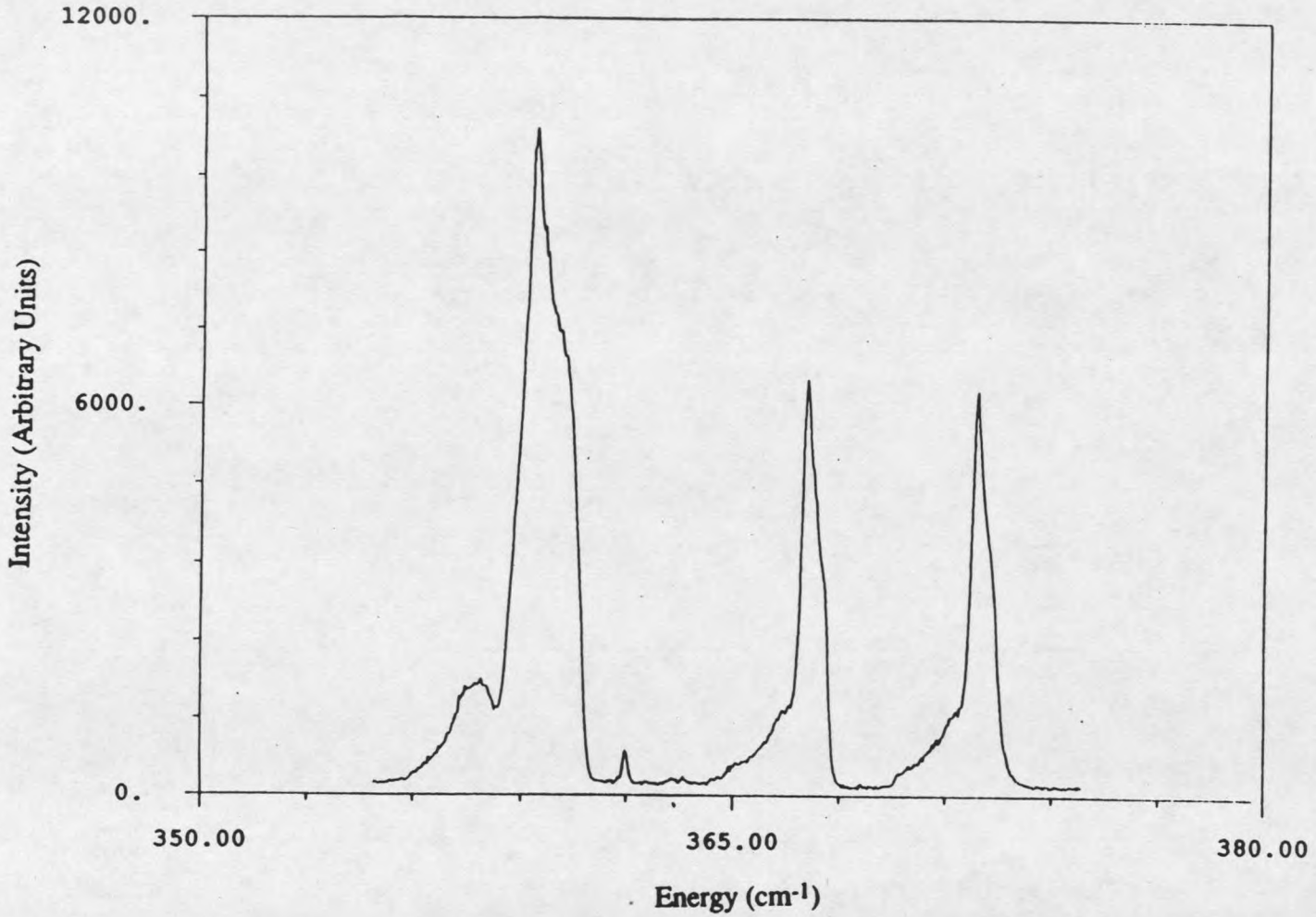

Figure 2.8 The $^7F_1$ energy levels of $EuVO_4$ as measured by $^5D_0$ - $^7F_1$ fluorescence, in a field of 40.0 kG. The lower peak is the singlet. The two higher ones are the doublet split by the magnetic field.

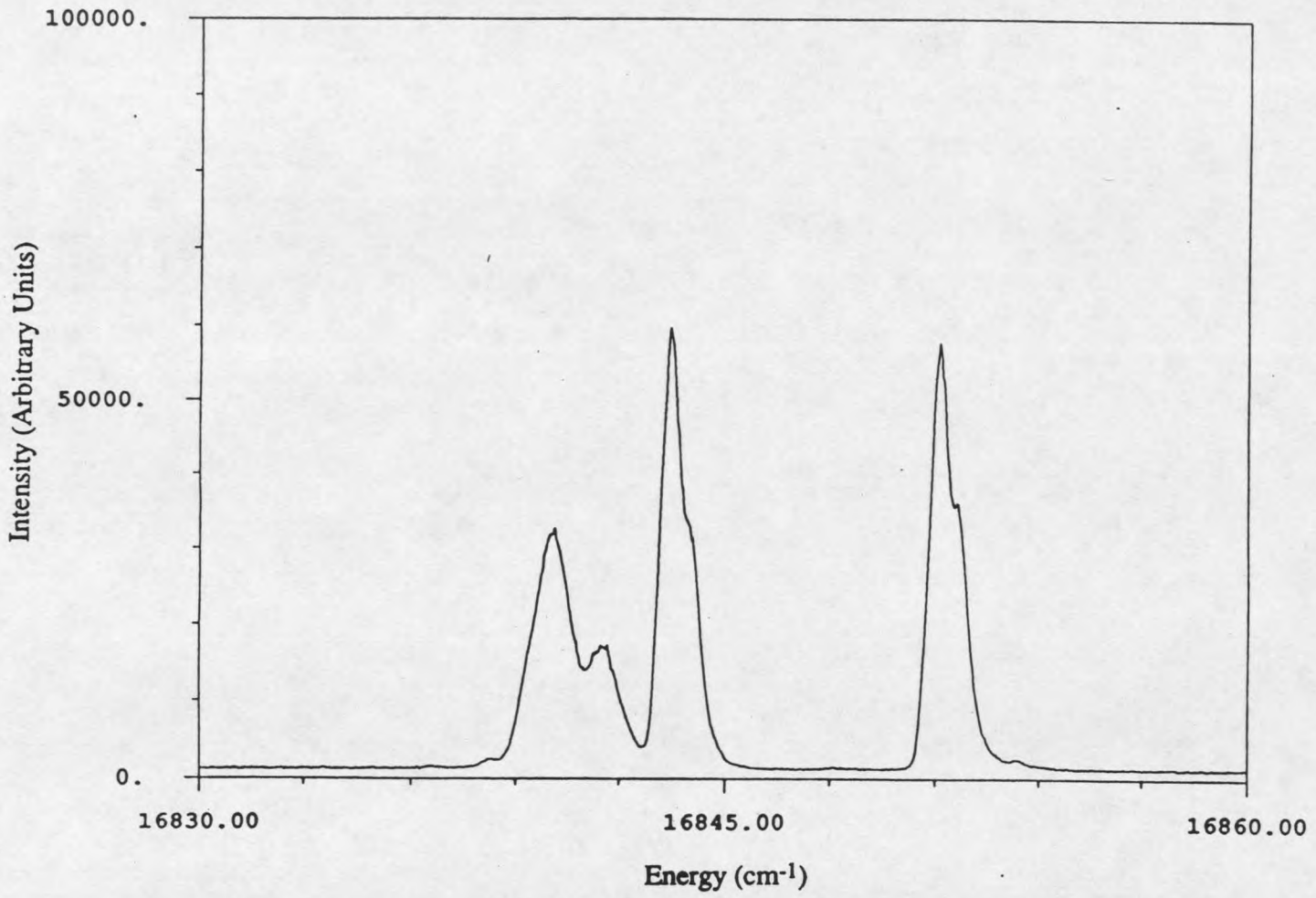

Figure 2.9 The $^5D_0$ - $^7F_1$ spectrum of $EuAsO_4$ in a field of 59.0 kG. The $^5D_0$ level at 17215.30 cm^{-1} is pumped directly by a single frequency laser.

The alignment of the crystal was verified by measuring the Zeeman splitting of the $^5D_1$ absorption. It gave a g factor of 1.5. So we concluded that we must be seeing intrinsic fluorescence, and that the smaller g factor had a more fundamental origin.

The $EuVO_4$ $^7F_1$ splitting at room temperature is about 5 cm^{-1}, while at about 100 K, this splitting is about 10 cm^{-1}. At liquid helium temperature, this splitting is also 10 cm^{-1}. The $^5D_1$ level splitting is about 2.6 cm^{-1} at room temperature, while it is 3.5 cm^{-1} at temperatures below 100 K. The doublet of $^7F_1$ stays about the same level relative to the ground state (370 cm^{-1}), while other levels go to higher energies with increasing temperature. This phenomenon also happens in Eu^{3+}:YVO_4.

$^7F_1$ - ^5D_J Transitions

One of the ways to determine if we were seeing the real intrinsic fluorescence is to do higher temperature absorption experiments. At high enough temperature, the $^7F_1$ levels have enough thermal population that absorption starting from these levels will be observed. This temperature was found to be just above liquid nitrogen temperature. We estimate it to be at 100 K.

Both the $^7F_1$ - $^5D_0$ and $^7F_1$ - $^5D_1$ transitions have been observed. The $EuVO_4$ absorption spectrum for $^7F_1$- $^5D_0$ transition is shown in Figure 2.10. The spectra for the $^7F_1$ - $^5D_1$ transition is shown in Figure 2.11, and the spectra for the same transition in $EuAsO_4$ is shown in Figure 2.12. The $^7F_1$ - $^5D_1$ transition could be observed at slightly lower temperature due to the stronger electric-dipole transition moment. The result at near liquid nitrogen temperature gave about the same $^7F_1$ splittings as obtained in the lower temperature fluorescence experiment, confirming that we were seeing the intrinsic transitions. But the normally unexpected result of these experiments was the double peaks related to the $^7F_1$ singlet transition. Both the $^7F_1$ (Γ_2) - $^5D_0$ and $^7F_1$ (Γ_2) - $^5D_1$ (Γ_5) transitions gave the same double humped feature implying this splitting came from

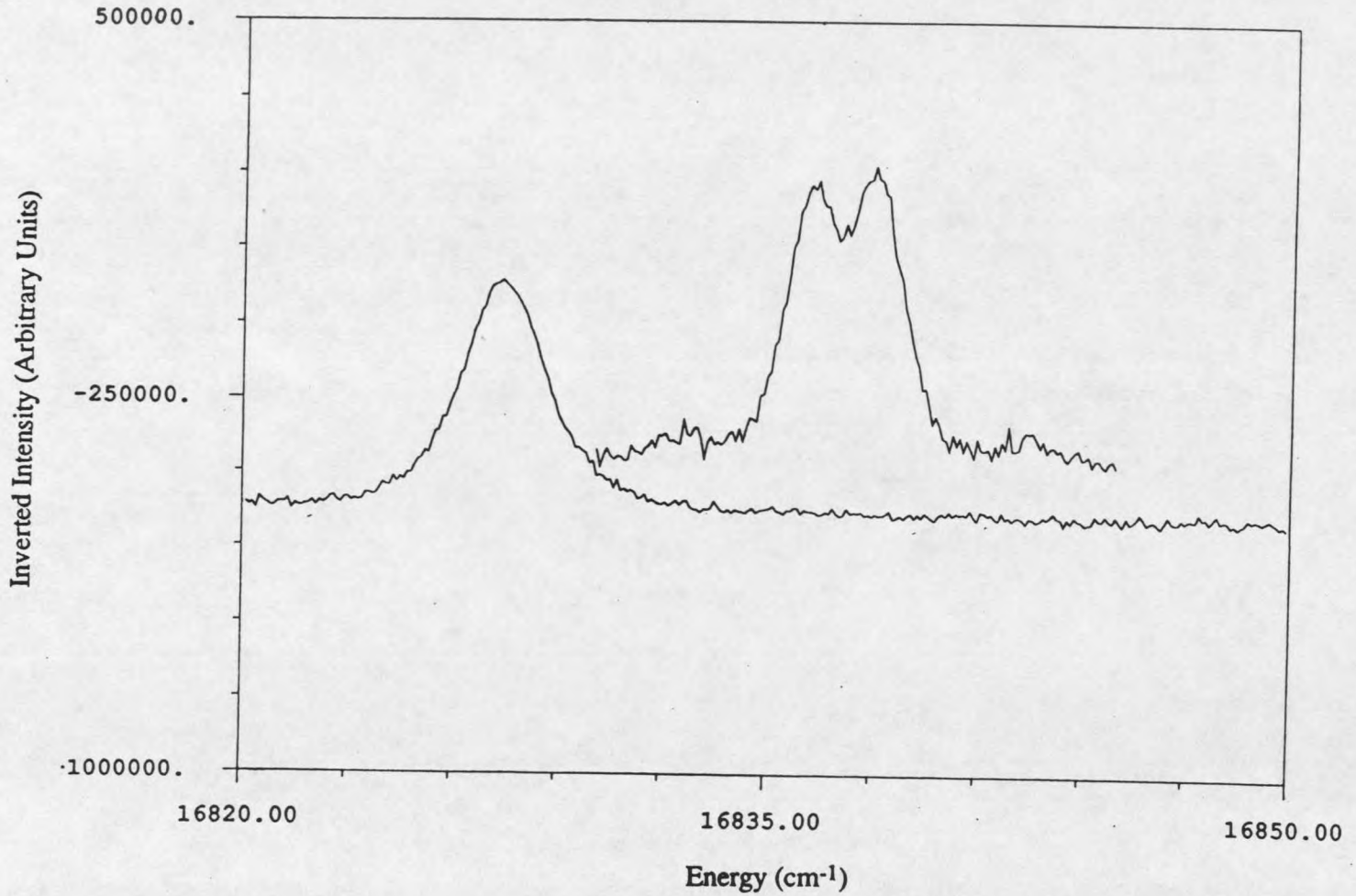

Figure 2.10 Polarized $EuVO_4$ $^7F_1$ - $^5D_0$ absorption spectra at T ≈ 100 K. The upper trace with the double humped feature is taken with σ polarization. The lower trace is taken with π polarization.

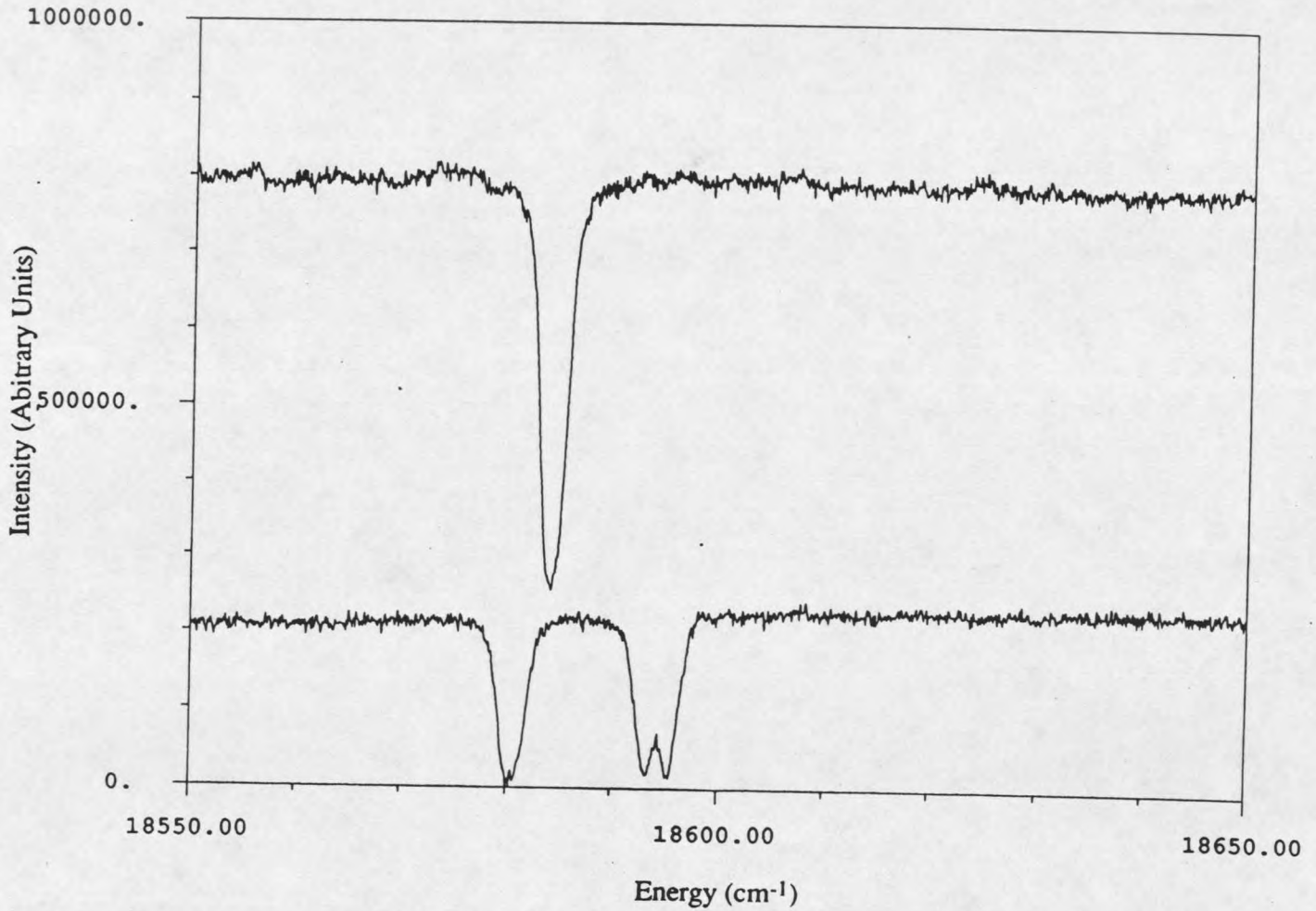

Figure 2.11 Polarized $EuVO_4$ $^7F_1$ - $^5D_1$ absorption spectra at T ≈ 100 K. Upper trace taken with π polarization, lower trace taken with σ polarization.

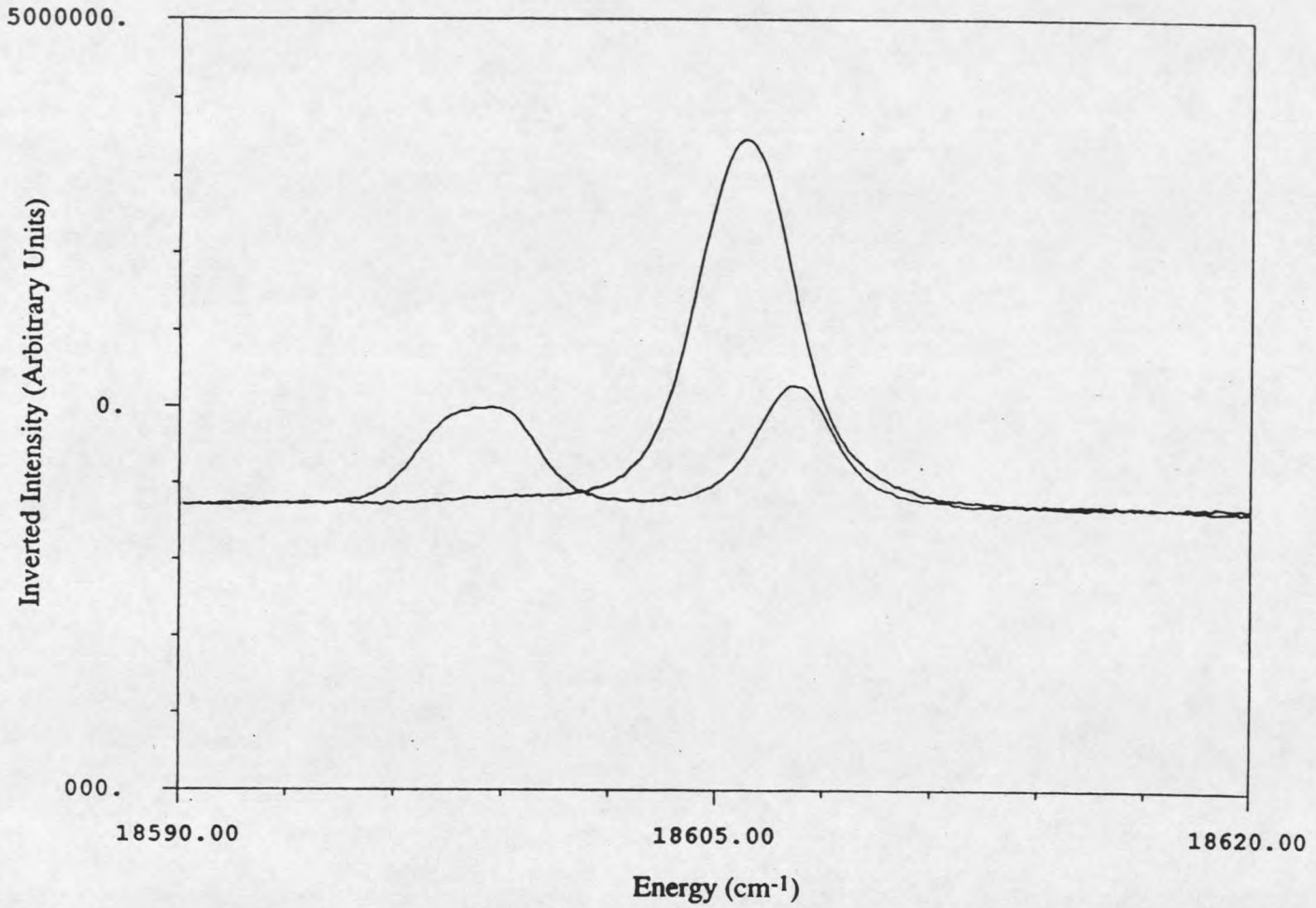

Figure 2.12 Polarized $EuAsO_4$ $^7F_1$ - $^5D_1$ absorption spectra at T ≈ 100 K. The stronger peak is in π polarization.

the $^7F_1$ (Γ_2) level. The identity of the $^7F_1$ - $^5D_0$ transitions is not uncertain, since the order of the J = 1 levels is known. For the $^7F_1$ - $^5D_1$ transitions, only three peaks are expected because the Γ_2 - Γ_2 transition is not allowed for either magnetic-dipole or electrical dipole transitions. For $EuVO_4$, the two lower frequency peaks originate from the $^7F_1$ (Γ_5) level and terminate on both of the $^5D_1$ levels, while the double peaked transition corresponds to $^7F_1$ (Γ_2) - $^5D_1$ (Γ_5). Because of the differences in the splittings of $^7F_1$ and $^5D_1$ levels, no confusion should occur here. For $EuAsO_4$, due to the different sign of the splittings, the upper two peaks are due to the transitions originating from the $^7F_1$ (Γ_5) level.

We attribute this double humped feature of the $^7F_1$ singlet to Davydov splitting. It will be treated more thoroughly in Chapter 3.

Zeeman Experiments

The $^7F_0$-^5D_J Transitions

Zeeman experiments were carried out by Hansen (1993) and Cone *et al.* (1993) on the $^7F_0$ - $^5D_0$, $^7F_0$ - $^5D_1$, $^7F_0$ - $^5D_2$, and $^7F_0$ - $^5D_3$ transitions of $EuVO_4$. The experiments on $^7F_0$ - $^5D_1$ have been repeated in this work; the results confirmed the original measurements. Hansen also analyzed the $^7F_0$ - $^5D_0$, $^7F_0$ - $^5D_1$, and $^7F_0$ - $^5D_2$ data and found that all of the Zeeman splittings are within theoretical predictions. The $^7F_0$ - $^5D_3$ transition was not fully analyzed, but preliminary analysis of the B || c indicated that the Landé g factor was about 1.45 (Hansen, 1990).

As Dr. M.J.M. Leask pointed out (private communications), there was only one unknown parameter in the description of the $^5D_3$ levels. If we write the Hamiltonian in a matrix form in the space spanned by J = 3, there will be only two off diagonal elements. The 7 x 7 matrix is

$$\begin{bmatrix} A & 0 & 0 & 0 & E & 0 & 0 \\ 0 & B & 0 & 0 & 0 & F & 0 \\ 0 & 0 & C & 0 & 0 & 0 & E \\ 0 & 0 & 0 & D & 0 & 0 & 0 \\ E & 0 & 0 & 0 & C & 0 & 0 \\ 0 & F & 0 & 0 & 0 & B & 0 \\ 0 & 0 & E & 0 & 0 & 0 & A \end{bmatrix}$$

From the zero field data of Hansen (1990) as quoted in Appendix II, we can easily determine that B = 24288.8 cm^{-1}, D = 24271.8 cm^{-1}, and F = ±28.7 cm^{-1} from the Γ_1 ($M_J = 0$) and Γ_3 and Γ_4 levels (mixed $M_J = \pm 2$). The other two levels at 24271.9 cm^{-1} and 24312.4 cm^{-1} are given by the eigenvalues of the 2x2 matrix:

$$\begin{bmatrix} A & E \\ E & C \end{bmatrix},$$

so obviously we can not determine all three parameters just from the zero field data. Using the Zeeman data with B ∥ c, we were able to find, assuming g = 1.5, that

A = 24284.5 cm^{-1}, C = 24299.7 cm^{-1}, and E = ±18.71 cm^{-1}.

The signs of E and F could not be determined just from these data. When these parameters were used to fit the B ⊥ c data, however, it was found that only negative values of E and F allow good fit of the data, while other combinations of the signs gave fittings that did not remotely resemble the real data. The fits for these two directions are shown in Figures 2.13 and 2.14.

The $^5D_1$ and $^5D_2$ levels of Eu^{3+}:$LuVO_4$ were also studied in a field. All those levels exhibited the expected Zeeman splitting behavior.

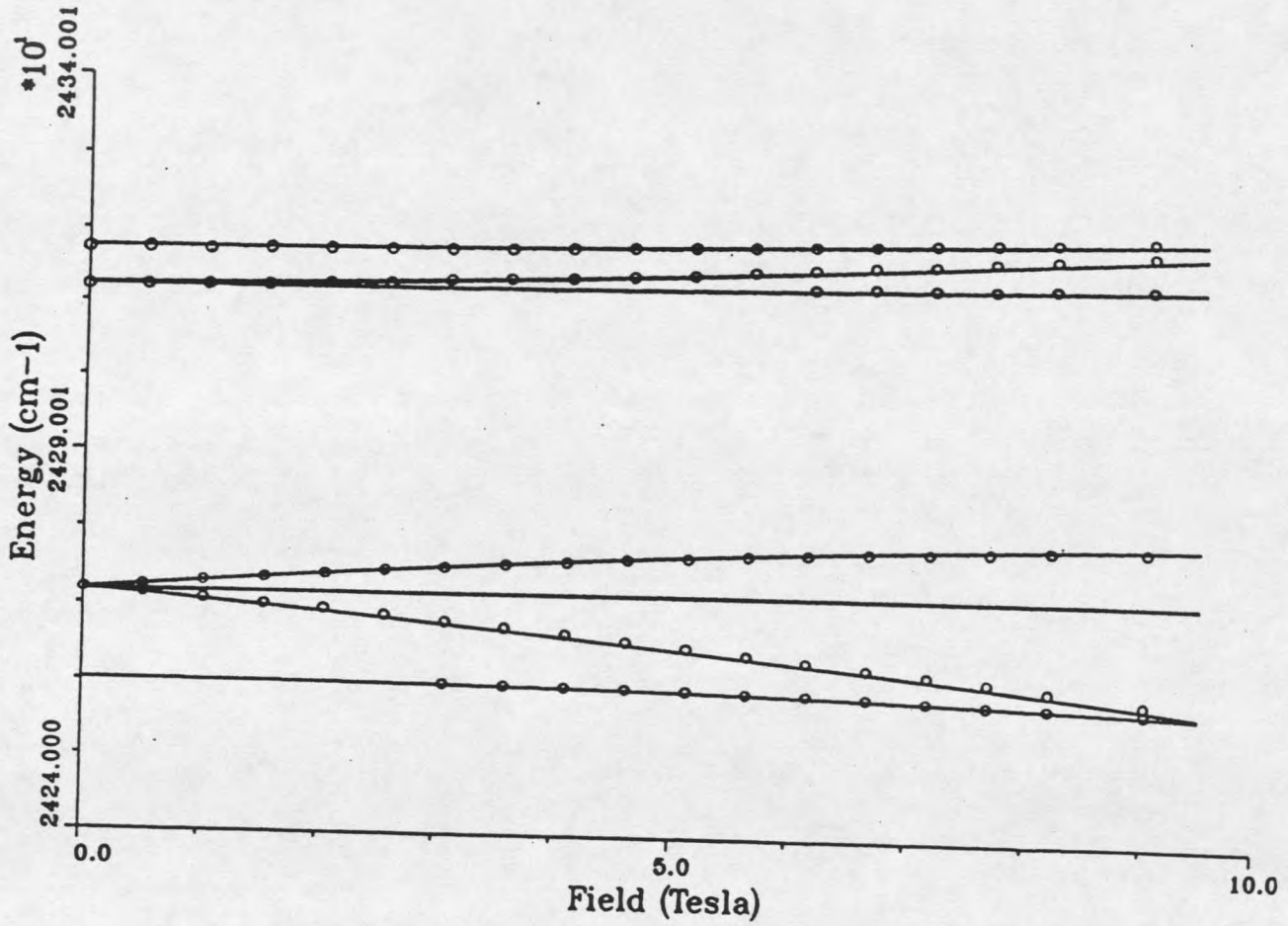

Figure 2.13 The $^5D_3$ spectra of $EuVO_4$ in a field parallel to the *c*-axis. The solid curves are the fit using the parameters given in section 2.6.1; the data were taken by Hansen (1990).

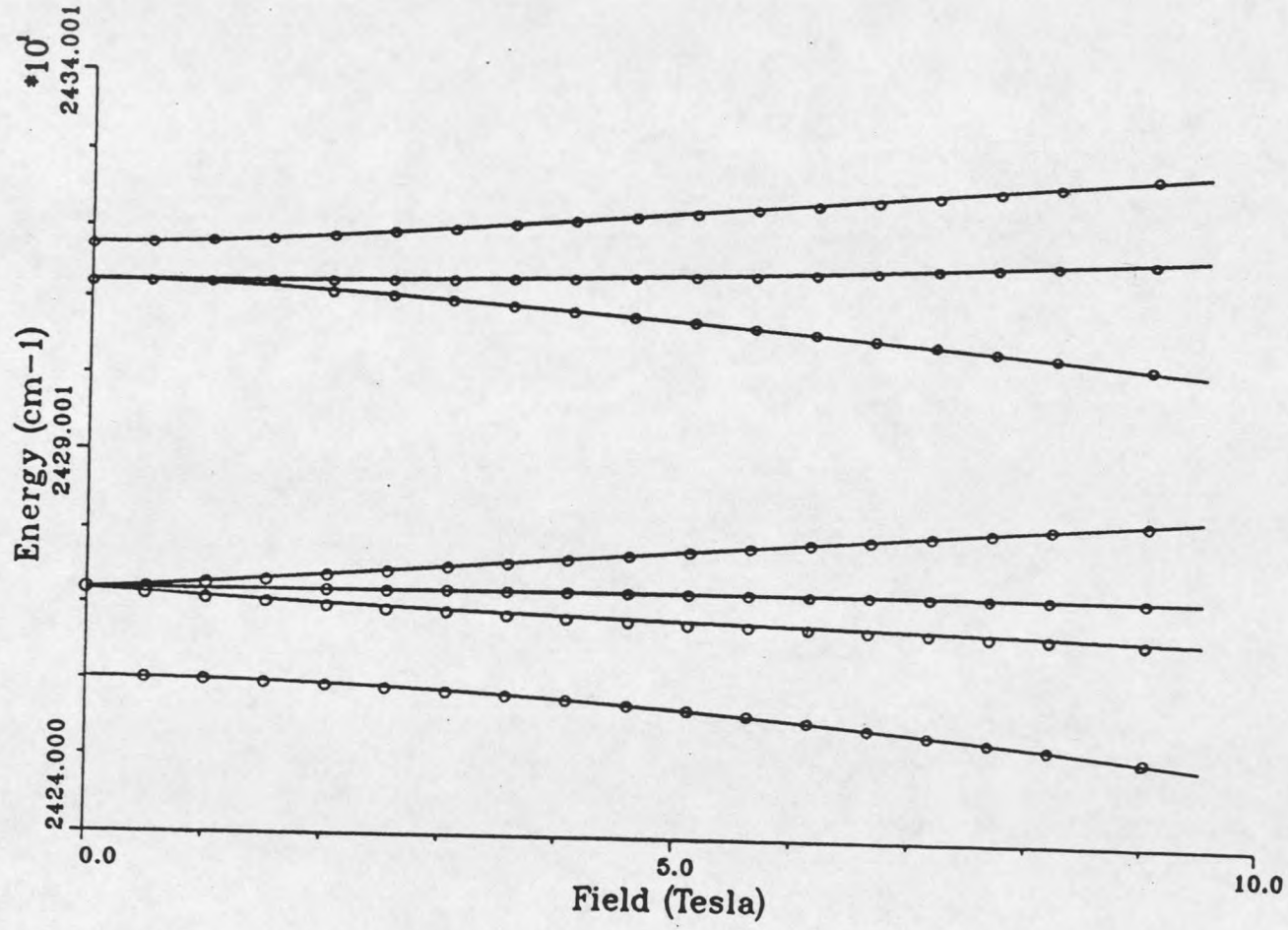

Figure 2.14 The $^5D_3$ spectra of $EuVO_4$ in a field perpendicular to the *c*-axis. The solid curves are the fit using the same parameters as those for Figure 2.13; the data were taken by Hansen (1990).

$^5D_0$ - ^7F_J Transitions

We have measured the Zeeman effect of the $^5D_0$ - $^7F_1$ fluorescence lines for $EuAsO_4$, $EuVO_4$, Eu:YVO_4, Eu:$LuVO_4$, Eu:YPO_4, and Eu:$LuPO_4$. $Eu(OH)_3$ was also studied for comparison. The intrinsic $^5D_0$ level was directly pumped by a cw laser in a field for all the crystals except Eu:YVO_4 and Eu:$LuVO_4$. The splittings in $Eu(OH)_3$, Eu:YPO_4, and Eu:$LuPO_4$ all had the right splitting behavior (g = 1.5), while the vanadates and $EuAsO_4$ did not split enough in a magnetic field.

For ^7F_J levels, because L = S, we expect to see g = 1.50. When the magnetic field is applied along the *c* direction, we expect the total splitting of the $^7F_1$ doublet to be 0.140 cm^{-1}/kG. But measurement of the splittings indicated that g = 1.40 for $EuAsO_4$, 1.30 for $EuVO_4$. Splittings for Eu^{3+}:YVO_4 and Eu^{3+}:$LuVO_4$ were even smaller. The splittings for these crystals with a magnetic field of 55.0 kG along the *c* direction are listed in Table 2.3. The Zeeman spectrum for $EuAsO_4$ is shown in Figure 2.15.

Table 2.3 Splittings at a field of 55 kG along the *c* direction (Expect 7.70 cm^{-1}, for Jz = ±1, g = 1.50, $\mu_B g = 0.070\ cm^{-1}/kG$)

Crystals	$^7F_1$	$^7F_2$	$^5D_1$	$^5D_2$	$^5D_3$
$EuVO_4$	6.8	6.0	7.7	7.7	g = 1.5
$EuAsO_4$	7.2				
Eu:YPO_4	7.7				
Eu:$LuPO_4$	7.7				
Eu:YVO_4	6.7	6.2			
Eu:$LuVO_4$	6.5	6.3	7.7	7.7	
$Eu(OH)_3$	7.70	15.4			

** Except in the $Eu(OH)_3$ case, all $^7F_2$ splittings are not well determined because of the large linewidths. The observable $^7F_2$ doublet in C_{3h} symmetry is $J_z = \pm 2$, instead of $J_z = \pm 1$ for the 4-fold axis case.

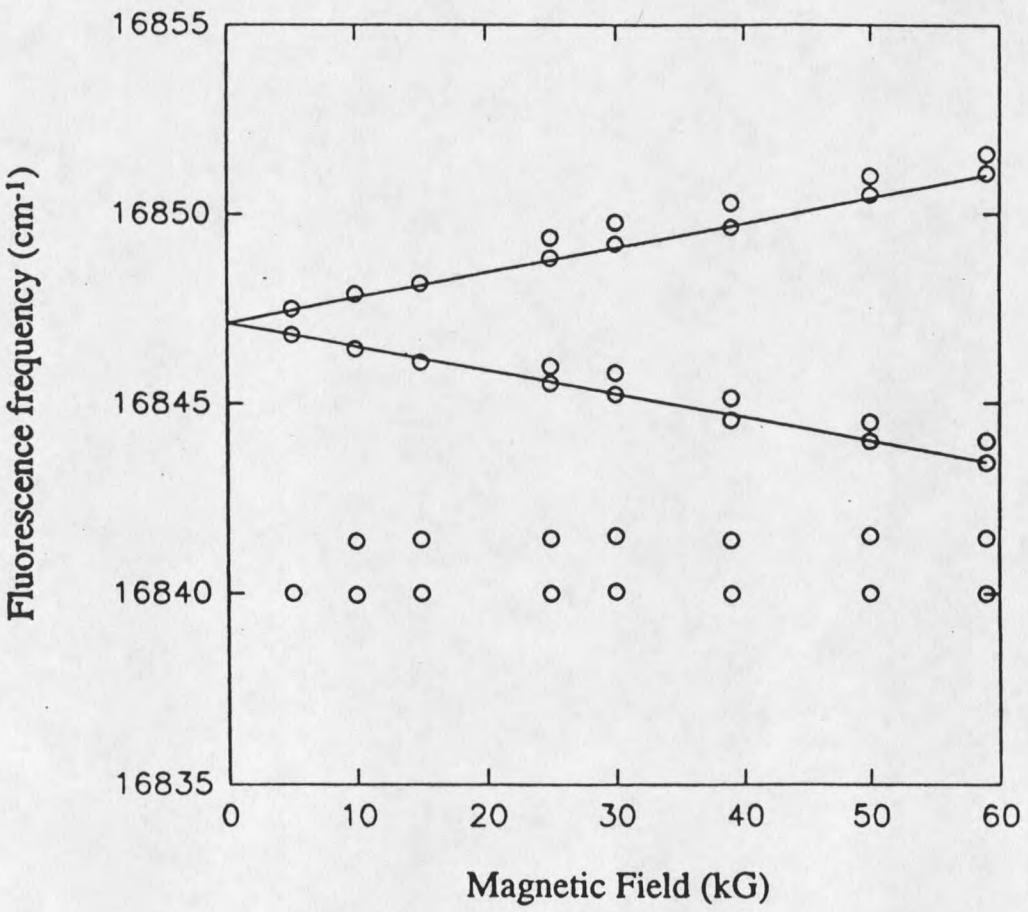

Figure 2.15 Zeeman spectra of the $^5D_0$ - $^7F_1$ transition in $EuAsO_4$.

The $^5D_0$ - $^7F_2$ (Γ_5) transitions in these crystals were also studied. The transition peaks are very wide even for the very dilute crystals (0.1 %). For concentrated crystals, not only are the peaks wide, extra fluorescence lines from defects are also present. These fluorescence lines overlap the intrinsic fluorescence, making the identification virtually impossible. From what we measured, however, the g factor for these levels is about the same size as that of the $^7F_1$ levels. The measurement of these levels by Raman scattering will be discussed in Chapter 3.

For $Eu(OH)_3$, the observable $^5D_0$ - $^7F_2$ doublet peak belongs to $J_z = \pm 2$. The splitting in a field therefore doubles the splitting we observed in the zircon structured crystals. At a field of 55.0 kG along the *c* direction, the splitting was 15.4 cm^{-1}, giving a g factor of 1.50.

We did Zeeman experiments on the $^5D_0$ to $^7F_1$ transitions with the magnetic field along the *a*-axis in $EuVO_4$. When the magnetic field is along the *a*-axis, the level splittings will be quadratic. One of the doublet levels will not move, while the other one will go up as the singlet will go down according to the formula

$$\Delta = \pm\left(\sqrt{\frac{E_{01}^{\,2}}{4} + (g\mu_B H)^2} - \frac{E_{01}}{2}\right)$$

where Δ is the shift of the levels while E_{01} is the energy gap between the singlet and doublet levels of $^7F_1$ at zero field; g is the Landé factor, and μ_B is the Bohr magneton, and H is the magnetic field.

This quadratic equation depends not only on the magnetic field, but also on the gap between the doublet and the singlet. The larger the gap, the less sensitive it is to the magnetic field. In the extreme case that the gap is small and the field is strong, it will approach linear splitting again.

In our Zeeman spectrum with H along the *c*-axis, the splitting at a field of 55.0 kG was 1.25 cm^{-1}. From the spectrum when the field was along the *c* direction, two

numbers could be used for the zero field splitting E_{01}. If we use the gap as 10.2 cm^{-1} we would expect 1.29 cm^{-1} for this field which is not far off. If we use 9.6 cm^{-1} then we would expect the splitting to be 1.43 cm^{-1}, which means we were seeing too small a splitting. There is some difficulty here because of the Davydov splitting (see Chapter 3).

We suspected that these splittings might not be linear when the field was along the *c*-axis since the electronic levels might couple to an Γ_1^+ phonon nearby at 377 cm^{-1}, so that anti-crossing might occur, but experiments in magnetic fields up to 80 kG confirmed that the splittings were linear within experimental accuracy. The splittings for all these crystals at 55.0 kG are listed in Table 2.3.

Crystal Field Analysis

For crystal field analysis, we used a computer program written by Hanna Crosswhite of Argonne National Laboratory. The Hamiltonian is

$$H = H_F + H_{CF}$$

The free ion part of the Hamiltonian is

$$H_F = \sum_{k=0,2,4,6} F^k(nf,nf)f_k + \zeta_{4f}A_{so} + \alpha L(L+1) + \beta G(G_2) + \gamma F(R_7) + \sum_{i=2,3,4.6,7,8} T^i t_i + \sum_{k=0,2,4} M^k m_k + \sum_{k=2,4.6} P^k p_k$$

where F^k, ζ_{4f}, α, β, γ, T^i, M^k, and P^k are parameters and their associated terms are operators. H_{CF} reperesents the crystal field interactions. In D_{2d} symmetry,

$$H_{CF} = \sum_{k,q} B_{kq}C_{kq} = B_{20}C_{20} + B_{40}C_{40} + \mathrm{Re}\,B_{44}(C_{44} + C_{4-4}) + B_{60}C_{60} + \mathrm{Re}B_{66}(C_{66} + C_{6-6})$$

We were able to fit the energy levels listed in Appendix II with the crystal field parameters listed in Table 2.4. The calculated levels are listed beside the observed levels in Appendix II. In Table 2.4, we also listed crystal field calculations by other workers for the vanadate crystals studied here and results for other Eu^{3+} crystals to illustrate the trend of the crystal field parameters.

Table 2.4 Fitted crystal field parameters in vanadates and phosphates.

	B_{20} (cm^{-1})	B_{40} (cm^{-1})	B_{60} (cm^{-1})	B_{44} (cm^{-1})	B_{64} (cm^{-1})
Eu^{3+}:YVO_4	-161.8	579.7	-922.5	-904	60
(Brecher *et al.*, 1967)	-122.0	403.2	-961.6	-701.7	39.6
(Grenet *et al.*, 1977)	-141	481	-956	-720	-19
Eu^{3+}:$LuVO_4$ (0.5%)	-309.4	459.7	-1330	-947	301
(Grenet *et al.*, 1977)	-247	408	-757	-994	-78
Eu^{3+}:YPO_4 (0.5%)	302	274.4	-870.8	-798.1	-174.6
(Brecher *et al.*, 1968)	293.2	400	-524.8	-707.2	-559
(Karayianis *et al.*, 1976)	362	125	-785	-757	-67
Eu^{3+}:$LuPO_4$ (0.5%)	185.8	387.2	-841.8	-849.3	-136.5
$EuVO_4$	~ -62	366	-1376	-662	742
Eu^{3+}:$GdVO_4$ (Grenet *et al.*, 1977)	-66	404	-985	-729	-25

From these parameters, we can see that the vanadates have negative B_{20}, while the phosphates have positive B_{20}. This should indicate a big difference in the arrangement of the 8 nearest neighbor oxygen ions around the rare earth ion. Also, the B_{44} and B_{64} parameters have same signs in the phosphate crystals while they have opposite sign in the vanadates. Only the relative signs are important for the B_{44} and B_{64} parameters in the

fittings of the zero field data. But as we have shown earlier in the calculations of the $^5D_3$ Zeeman splittings, there should be only one choice for the signs of these parameters.

Focussing our attention on the analysis of $EuVO_4$, we note the difficulty of carrying out a fit when only a few ^7F_J levels have been identified. We obtained complete data for ^5D_J up to J = 3, but we only have ^7F_J data up to J = 2. Two more levels are known in the J = 4 multiplets.

The $^7F_1$ splitting is 10.2 cm^{-1} for $EuVO_4$ and about 7.7 cm^{-1} for $EuAsO_4$ though they have opposite signs. If B_{20} is calculated just from the $^7F_1$ splittings, it should be -34 cm^{-1} for $EuVO_4$ and 23 cm^{-1} for $EuAsO_4$. Crystal field calculations including other levels make this parameter somewhat larger for $EuVO_4$. If we look at the variation of B_{20} among the vanadates, we observe that this parameter gets smaller with larger lattice cells. The B_{20} of Grenet *et al.* (1977) for Eu^{3+}:$GdVO_4$ falls in the gap between $EuVO_4$ and YVO_4.

CHAPTER 3

JAHN-TELLER EFFECTS AND ION-ION INTERACTIONS

Introduction

Zircon structured rare earth compounds are known to have strong Jahn-Teller interactions. In fact, many of them undergo cooperative Jahn-Teller structural phase transitions at low temperature. The compounds $DyVO_4$, $TmVO_4$, $TbVO_4$, $DyAsO_4$, and $DyPO_4$ are just some of the examples. In this chapter, we will demonstrate that even in europium compounds, the Jahn-Teller effect plays an important role. This suggests that the Jahn-Teller effect is a very common phenomenon. Its contribution to the energy level structure is important. Due to the complexity of the spectra of other ions, it is often difficult to distinguish the exact contribution of this effect from other processes. The simplicity of the spectra and well defined wavefunctions of europium compounds make a good testing ground for studying this interaction.

Unlike in dilute crystals, where active ions are surrounded by other kinds of non-active ions, the active ions are surrounded by like ions in stoichiometric compounds. The excitation is not necessarily localized anymore. Since the excitation embraces a large volume in the crystal, it is not adequate to describe the excitation of stoichiometric compounds using the simple single ion picture. Group theory-wise, using the simple local site point group to describe the excitation is oversimplified, the whole space group

must be used to describe the excitation. In these compounds, new phenomena arises from ion-ion interaction. Energy bands have dispersion throughout the Brillouin zone. Due to multiple, equivalent ions in one unit cell, Davydov splittings may result (Davydov 1971 and Cone and Meltzer 1987). Such effects were first observed for rare earths in $GdCl_3$ (Meltzer and Moos 1972) and $Tb(OH)_3$ (Cone and Meltzer 1975).

In tetragonal zircon crystals, there are two rare earth ions per unit cell that are related by inversion symmetry, resulting in two exciton branches with opposite parities. The energy difference between these branches at $\mathbf{k} = 0$ is called a Davydov splitting and has been observed in one of the low-lying states of $TbVO_4$ with a gap of 17 cm^{-1} (Ergun *et al.* 1976). A splitting of 2.3 cm^{-1} has also been observed for a doublet excited state at 23 cm^{-1} in $HoVO_4$ (Battison *et al.* 1977 and Aminov 1981). The low-lying PrF_3 levels also show Davydov splittings of up to 4 cm^{-1} (Dahl and Schaack 1984, 1986). We will show that $EuVO_4$ and $EuAsO_4$ are the first examples of europium compounds that have both Davydov splittings and Jahn-Teller effects. Davydov splittings can be observed even at higher than liquid nitrogen temperature.

As we have shown in the last chapter, the $^7F_1$ levels of stoichiometric $EuVO_4$ and $EuAsO_4$, and europium doped YVO_4 and $LuVO_4$ crystals do not have the expected Zeeman splitting behavior for pure electronic states, the measured Landé g factor is smaller than that expected for pure ^7F_J states. Equipment calibration has been ruled out as the cause for such phenomena since we have measured the splittings of the ^5D_J levels in the same setup and the ^5D_J levels have the correct splitting factors.

In the dilute samples, most of the dopant ions substitute into the original lattice at the Y or Lu sites. Although there still might be clusters of Eu^{3+} ions formed so that defect transitions may occur, the main transitions should be from isolated ions. Fluorescence experiments show that the splitting factor is also too small for the dilute vanadate crystals, implying that the smaller than normal g factor should be considered an

intrinsic property of the host. For the stoichiometric compounds, efforts were taken to search for a possible defect site that gave the observed fluorescence. No such site was found. Doubts still exist about observation of the intrinsic fluorescence. Non-resonant Raman scattering experiments discussed in this chapter provides an independent technique that measures the intrinsic energy levels directly from the ground state.

Raman Scattering Selection rules

Raman scattering is a two-photon process. The first photon excites the ion to a virtual state, then it will relax back to a third level radiatively. The Stokes photon energy should be the exciting energy minus the energy of the third energy level. The allowed scattering symmetry is determined by its related second order susceptibility in the crystal. For crystals with D_{4h} symmetry, the allowed light scattering symmetries and the 2nd order susceptibilities related to them are listed in Table 3.1 (Hayes and Loudon 1978).

Table 3.1 Allowed scattering symmetries and their related second-order susceptibilities for groups D_{4h} (first label) and D_{2d} (second label).

Γ_1^+,Γ_1

$$\begin{bmatrix} a & & \\ & a & \\ & & b \end{bmatrix}$$

Γ_2^+,Γ_2

$$\begin{bmatrix} & -c & \\ c & & \\ & & \end{bmatrix}$$

Γ_3^+,Γ_4

$$\begin{bmatrix} d & & \\ & -d & \\ & & \end{bmatrix}$$

Γ_4^+,Γ_3

$$\begin{bmatrix} & e & \\ e & & \\ & & \end{bmatrix}$$

Γ_5^+,Γ_5

$$\begin{bmatrix} & & f \\ g & & \end{bmatrix} \begin{bmatrix} & & \\ & & f \\ & g & \end{bmatrix}$$

For a rare earth ion at D_{2d} symmetry, the selection rules are exactly the same as for D_{4h} except for the Γ_3^+ and Γ_4^+ case. For the local D_{2d} symmetry, the 2-fold axes are actually 45° from the crystal *a* and *a'* axes (see Chapter 1 and Elliott 1972). This has the effect that Γ_3 in D_{2d} symmetry corresponds to Γ_4^+ in D_{4h}, while Γ_4 corresponds to Γ_3^+ in D_{4h}.

The general susceptibility breaks down into transition operators of various symmetries. For phonon scattering, the ground state is always Γ_1^+, so the excited state symmetry is the same as that needed for the transition operator. Similarly, in europium compounds, the ground state $^7F_0$ always has Γ_1 symmetry, so it takes a transition operator of the same symmetry as the excited state to induce a Raman transition.

In the zircon structure, there are 36 branches of phonons according to Miller *et al.* (1968) and Elliott (1972). Due to differences in the choices of the axes, Γ_3^+ and Γ_4^+ are interchanged in those two papers. Using Elliott's convention, where the x and y axes are chosen so that they coincide with the crystal surfaces, the 36 branches can be classified as

$$\Gamma_{36} = (2\Gamma_1^+ + 2\Gamma_4^-) + (\Gamma_4^+ + \Gamma_1^-) + (\Gamma_2^+ + \Gamma_3^-)$$
$$+ (4\Gamma_3^- + 4\Gamma_2^-) + (5\Gamma_5^+ + 5\Gamma_5^+)$$

In all these, only $\mathbf{k} = 0$ even parity phonons will be observed. There are thirteen even parity phonons; all but the Γ_2^+ phonon should be Raman active. The Γ_2^+ phonon cannot be observed because vibrational scattering requires that the transition operator have symmetric second order susceptibility (Hayes and Loudon, 1978) while the second order susceptibility related to it is anti-symmetric in D_{4h}. So, only 12 phonon modes should be seen in a Raman spectrum for the zircon crystals.

Suppose we have a Raman scattering setup for a tetragonal crystal as illustrated in Figure 3.1. The pumping light is incident either along the *y* or *z* axis. The scattered light will be observed along the *x* axis. If we express the scattering geometry by the common

notation, e.g. $z(xz)y$, in which the directions of propagation of incident and scattered light are specified by the letters before and after the bracket and the polarization properties of the light by the letters inside the bracket, then we can determine what kind of scattering we would see in each geometry. These are summarized in Table 3.2.

It is easy to see that when light is incident along the c-axis, all Raman active transitions could be observed.

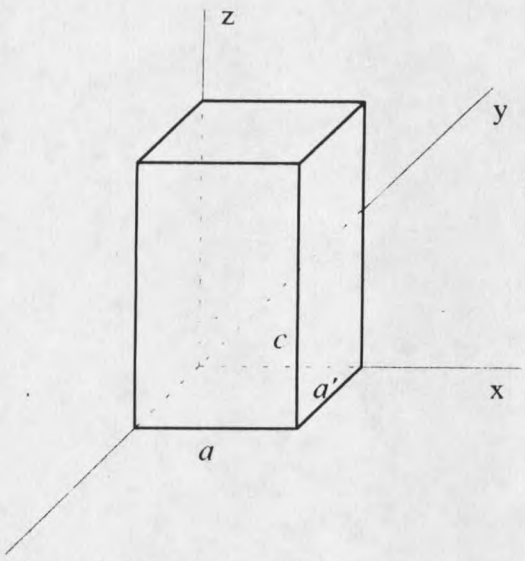

Figure 3.1 Raman scattering of a tetragonal crystal

Table 3.2 Scattering geometry and allowed excitations

Scattering Geometry	Allowed Scattering symmetry	Scattering Geometry	Allowed Scattering symmetry
$y(zz)x$	Γ_1	$z(yy)x$	Γ_1, Γ_3
$y(zy)x$	Γ_5	$z(yz)x$	Γ_5
$y(xz)x$	Γ_5	$z(xy)x$	Γ_4, Γ_2 (electronic)
$y(xy)x$	Γ_4, Γ_2 (electronic)	$z(xz)x$	Γ_5

Raman Scattering Experiments

Phonon Scattering

The experiments were carried out using a 514.5 nm Argon ion laser beam. The laser beam was first filtered using a prism setup to filter out the plasma lines. The laser power was about 150 mW entering the cryostat. The collecting optics were exactly like those

in the fluorescence experiments with the exception that the photomultiplier in the Raman experiments was an actively cooled RCA31034A-02 tube. The operating temperature was about -20 °C. This PMT has an extremely low dark count rate at the operating temperature, suitable for applications with very weak signal.

When the laser was incident onto the sample, the laser frequency was in the phonon sideband absorption of the $^5D_1$ levels (~19000 cm^{-1}). Visible fluorescence could be observed for the concentrated crystals: an orange streak was evident along the path of the light. This was helpful for the alignment of the optics. Care was taken to minimize scattering from the physical imperfections of the crystal (cracks, spots, etc.) to reduce the stray light entering the monochromator. For experiments at liquid nitrogen temperature, the fluorescence was difficult to see due to the self quenching of the crystal. A streak of the same color as the laser could still be seen due to the macroscopic imperfections in the crystal. This streak was used for the alignment. The dilute crystals still fluoresced at that temperature.

Raman scattering measurements on the phonon lines of $EuVO_4$, $EuAsO_4$, Eu^{3+}:YVO_4, and Eu^{3+}:$LuVO_4$ were carried out. Compared to electronic Raman scattering, the scattering signal was normally very strong, and measurement of these levels did not require special effort. The observed phonon energies are listed in Table 3.3. All the energies listed were measured at liquid nitrogen temperature except in $EuAsO_4$ which is measured at liquid helium temperature. The resolution was 1 cm^{-1}. It took one second or less to count the signal for each data point.

Figure 3.2 is the typical Raman scattering spectrum in $EuAsO_4$. The Γ_1^+ phonon at 398 cm^{-1} is asymmetric and wide (>10 cm^{-1}). The dip at 460 cm^{-1} was due to the absorption of the Eu^{3+} $^5D_1$ levels. The fluorescence from this level to $^7F_1$ was also observed together with the Raman scattering signal. Figure 3.3 is the Raman scattering spectrum of the lower phonon frequency region of $EuVO_4$. The Γ_1^+ phonon at 377 cm^{-1}

Table 3.3 Phonon frequencies (cm^{-1}) of the vanadates measured at 77 K.

$EuAsO_4$ phonon frequencies were measured at liquid helium temperature.

Not all frequencies for $TmVO_4$ were measured due to experimental geometry.

Crystal	Γ_1^+	Γ_5^+	Γ_3^+	Γ_3^+	Γ_5^+	Γ_1^+	Γ_4^+	Γ_3^+	Γ_5^+	Γ_5^+	Γ_3^+	Γ_5^+
YVO_4	894	841.7	818.8	489.2		381.2	259.2	269.5	263.5	162.5	158	150.8
(Elliott)	894	842	819	490		382	260	270	264	163	157	-------
$EuVO_4$	877.8	821.2	780.1	477.8		377	243.2	-----	258.5	153.8	123.3	113.4
$LuVO_4$	903.8	849	828.5	493		379.5	254.5		260	156.7	114.7	104.2
$TmVO_4$	898	842	821	499?		381.5			260	157.5		
$EuAsO_4$	880.5	822	852	466	427	398	235		237.3	161	130.5	110

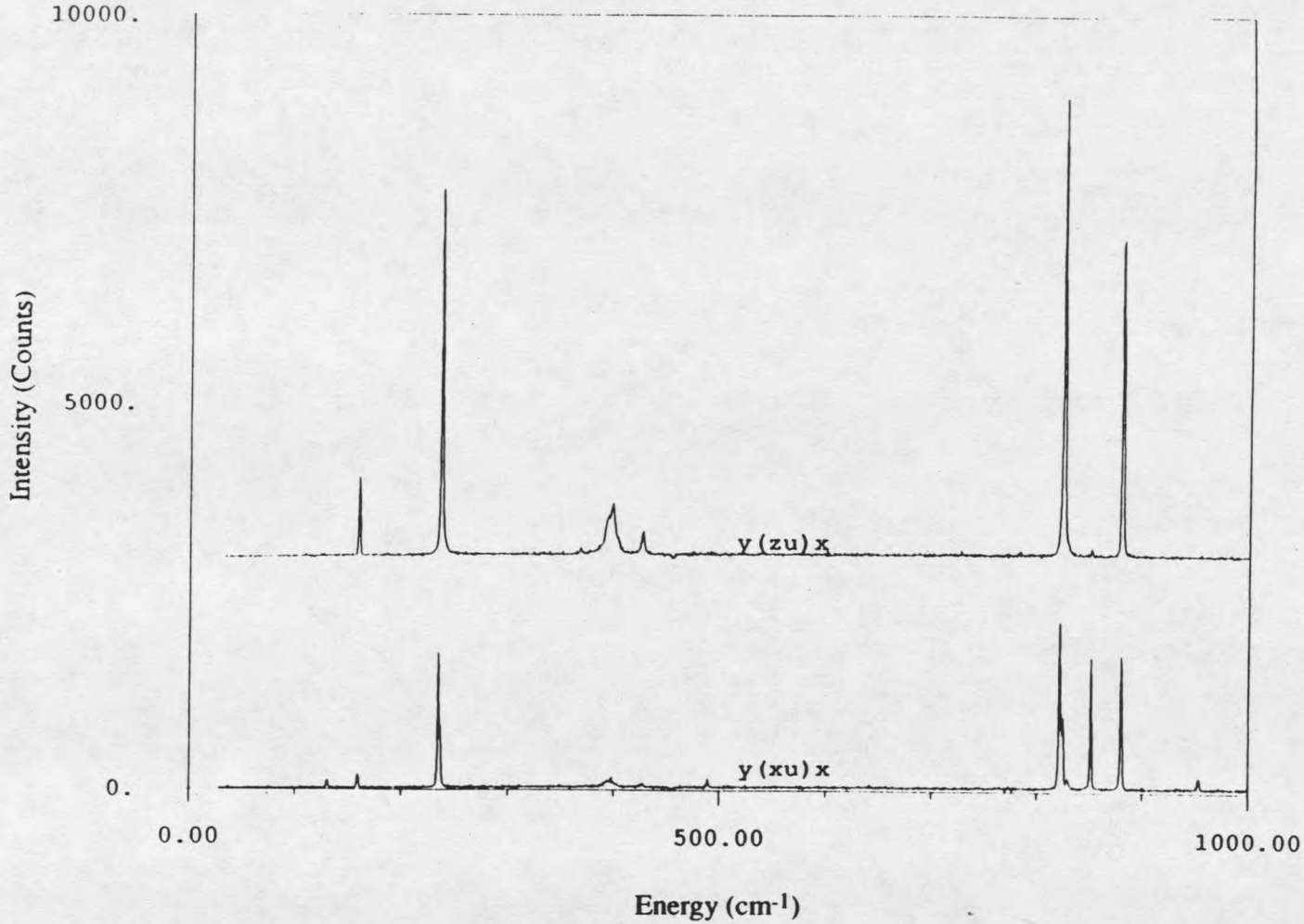

Figure 3.2 Raman scattering spectrum of $EuAsO_4$ at T = 1.5 K. Letter *u* in the brackets means the scattered light was collected without polarization discrimination.

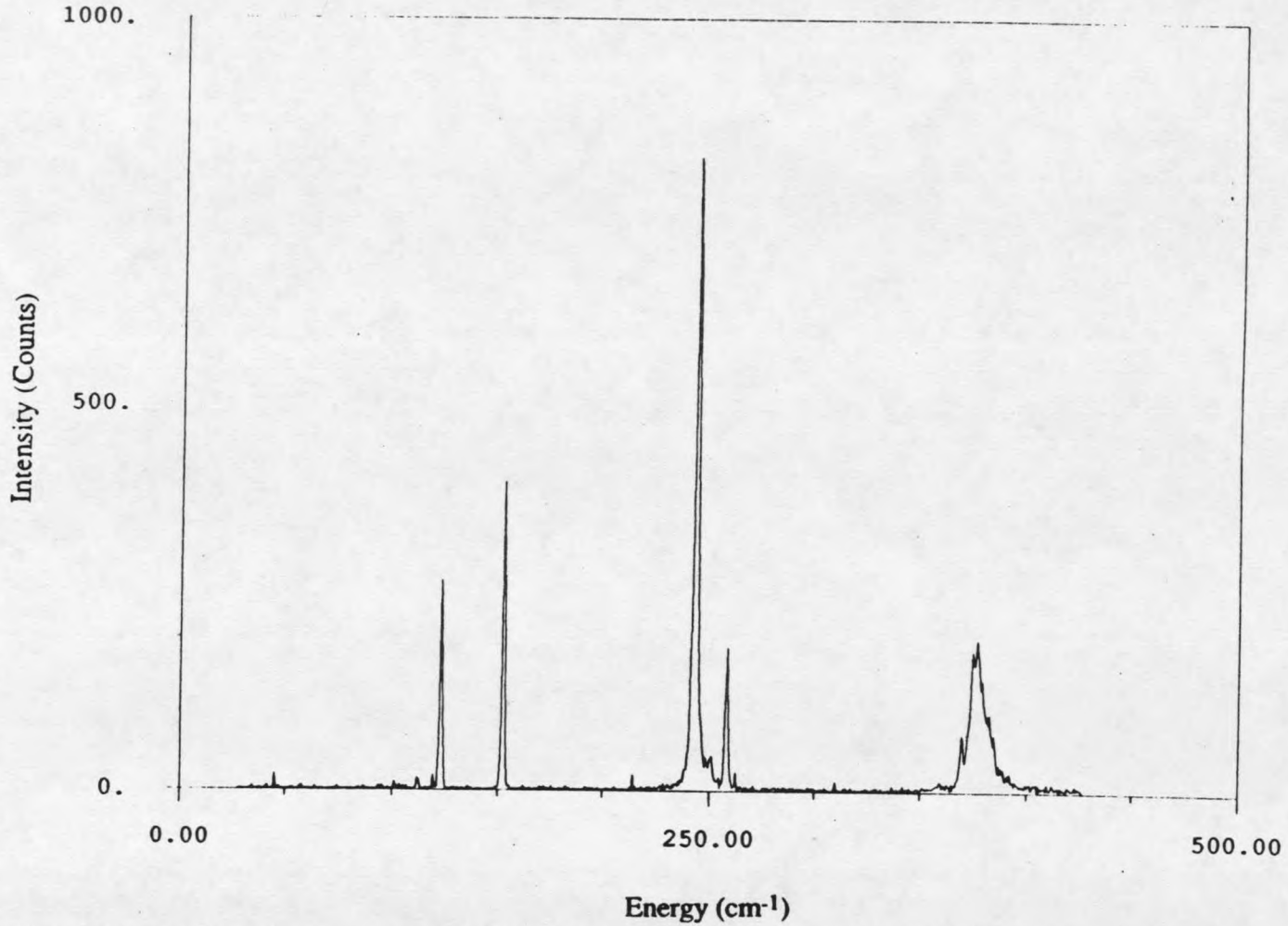

Figure 3.3 Raman scattering spectrum of $EUVO_4$ in the lower frequency region. The scattering geometry was $z(yu)x$. Collection was not polarization discriminated.

is also very wide. Raman scattering of 0.5%Eu^{3+}:$LuVO_4$ was also carried out. The Γ_1^+ phonon also showed a wide peak.

In contrast to all these, the Γ_1^+ phonon at 381.2 cm^{-1} in the 0.1%Eu^{3+}:YVO_4 spectrum is no different from other phonon scattering peaks. To illustrate the difference between the Γ_1^+ phonons, a plot of the Γ_1^+ scattering peaks of both $EuVO_4$ and 0.1%Eu^{3+}:YVO_4 is shown in Figure 3.4. This lineshape difference in different crystals is not understood, but we want to note that Eu^{3+}:YVO_4 is the only system where the Eu^{3+} $^7F_1$ (Γ_5) electronic level is very close to the phonon level. The electronic level is at 380.0 as determined from the fluorescence experiments.

Electronic Raman Scattering

Electronic Raman scattering has been observed in $EuVO_4$ and $EuAsO_4$. Since it was much weaker than vibrational scattering, longer time was needed to do the experiments. No electronic Raman signal was observed for the dilute crystals due to the low concentration of active ions. Unlike the case of phonon scattering where Γ_2 scattering is forbidden, it is allowed in electronic Raman scattering, so that both of the $^7F_1$ levels should be observable. Both of the $^7F_1$ levels were observed. The $^7F_1$ scattering peaks were very sharp. With 0.5 cm^{-1} resolution used on the monochromator, the linewidth was still slit-limited. Scattering from $^7F_2$ was also observed, but the peaks were much wider (several wavenumbers), just like what we observed in the fluorescence experiments. The linewidths of these levels are probably lifetime limited due to fast relaxation.

The $^7F_1$ levels measured by Raman scattering for the concentrated crystals roughly match those measured by fluorescence experiments, as we expected. The zero field spectra are shown in Figure 3.5 for $EuVO_4$ and Figure 3.6 for $EuAsO_4$. Only single peaks were observed in the spectra. The measured $^7F_1$ levels were at 360.3 cm^{-1} (Γ_2) and 369.9 cm^{-1} (Γ_5) for $EuVO_4$. They were at 367.7 cm^{-1} (Γ_5) and 375.4 cm^{-1} (Γ_2) for $EuAsO_4$.

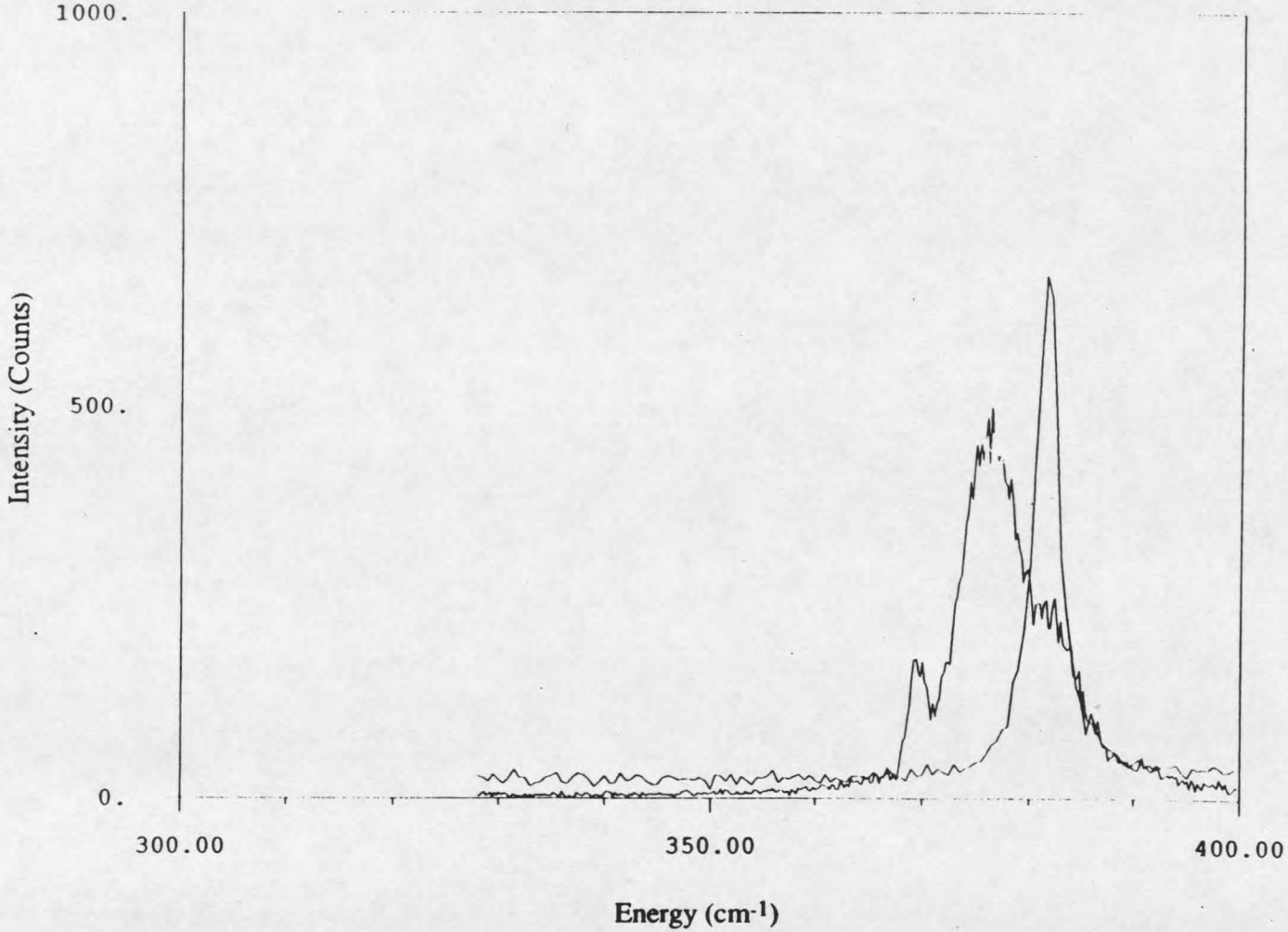

Figure 3.4 Comparison of the $EuVO_4$ and 0.1%Eu^{3+}:YVO_4 Γ_1^+ phonon scattering spectrum. The sharp peak is for YVO_4.

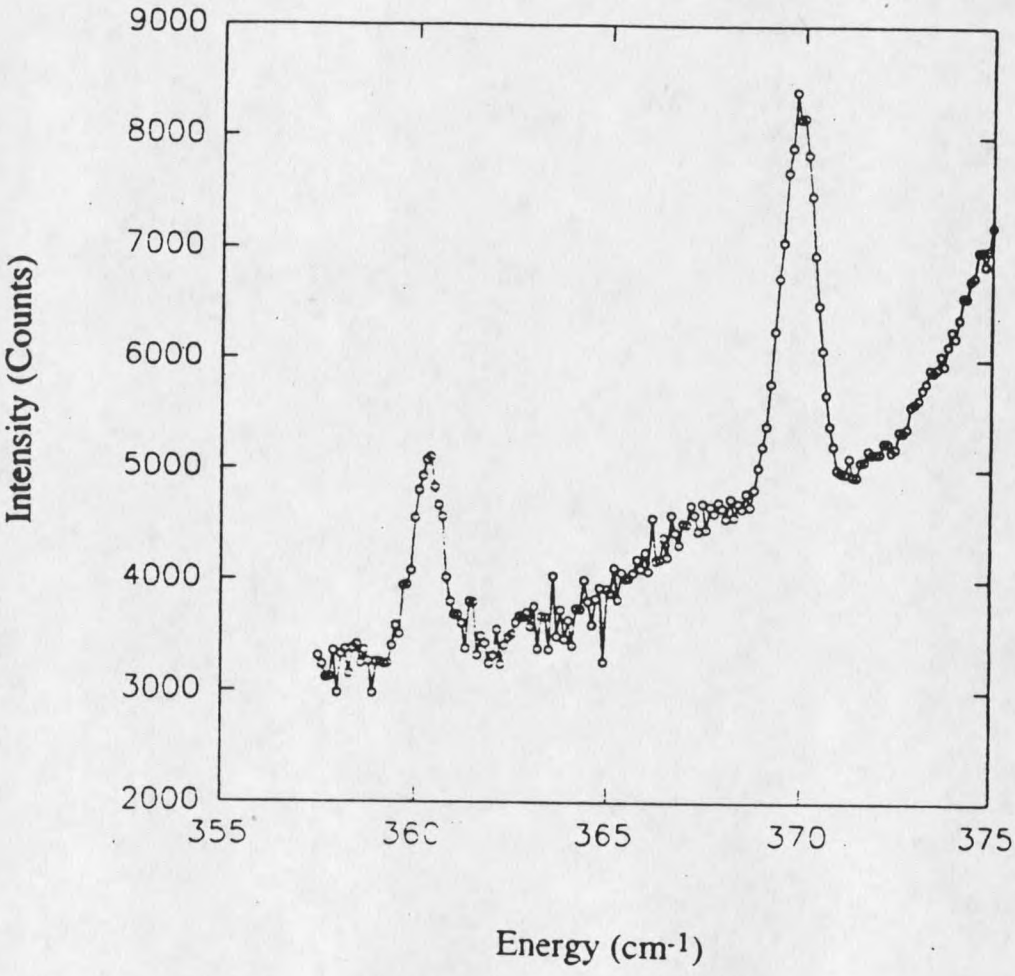

Figure 3.5 Electronic Raman Scattering spectrum for $EuVO_4$ $^7F_1$ levels. The strong phonon peak can still be seen due to polarization leakage.

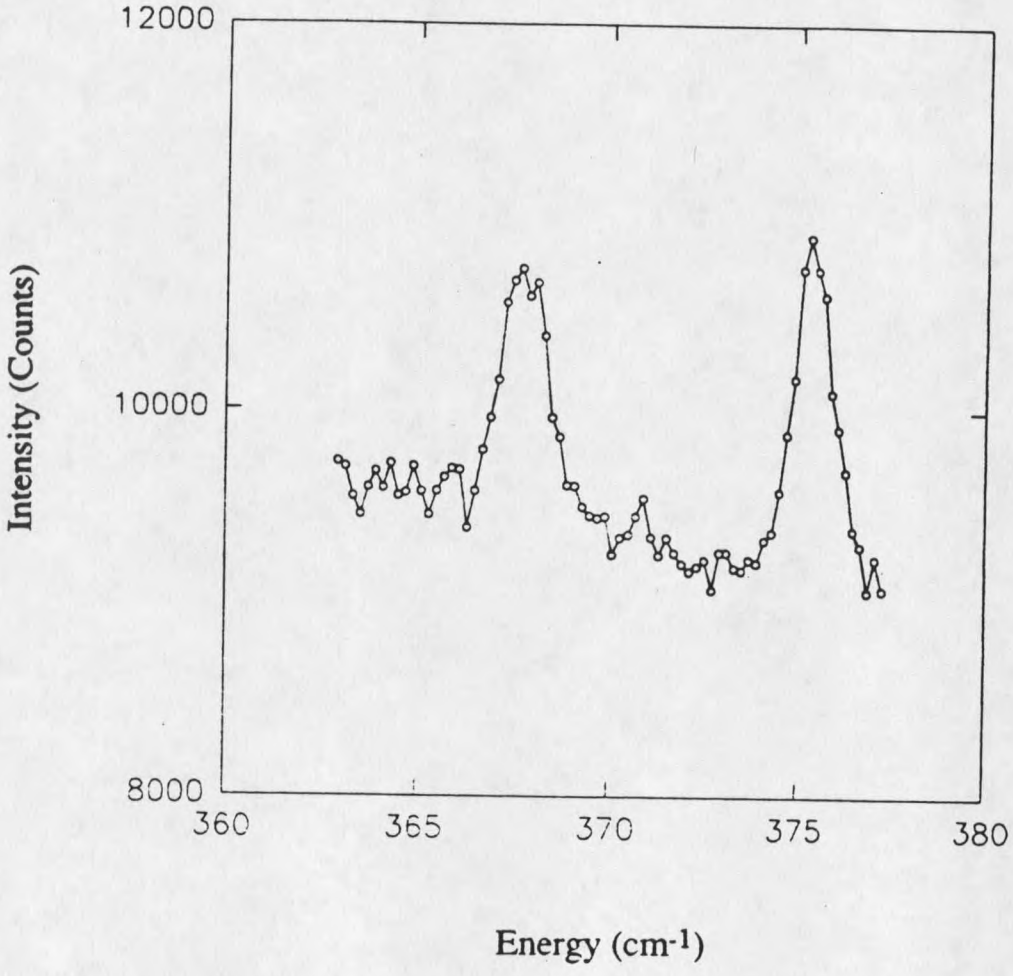

Figure 3.6 Electronic Raman scattering spectrum for $EuAsO_4$ $^7F_1$ levels. Vertical scale is number of photons.

Only 3 levels in $^7F_2$ were observed. The highest Γ_3 level was not seen in either crystal. The doublet was observed at the position determined by fluorescence experiments. The Γ_1 level was also observed. This level in $EuAsO_4$ was 1.5 cm^{-1} above the doublet. The observed Γ_4 level, however, did not match that determined by fluorescence experiments in either $EuVO_4$ or $EuAsO_4$. Both of them are about 10 cm^{-1} higher than the values determined by fluorescence experiments. That level had been determined to be at 936.8 cm^{-1} by fluorescence for $EuVO_4$, but Raman scattering showed that it was at 946.1 cm^{-1}. In $EuAsO_4$, it had been determined to be at 944 cm^{-1} by fluorescence, while it was determined to be at 953.3 cm^{-1} from Raman scattering. The interpretation of the descrepancy will be discussed in section 3.5. The Raman scattering determined levels are summarized in Table 3.4.

Table 3.4 Energy levels in $EuVO_4$ and $EuAsO_4$ as determined by Raman scattering.

$EuVO_4$ Energy Levels (cm^{-1})			$EuAsO_4$ Energy Levels (cm^{-1})		
$^7F_1$	Γ_1	360.3	$^7F_1$	Γ_1	367.7
	Γ_2	369.9			375.4
$^7F_2$	Γ_4	946.1	$^7F_2$	Γ_4	953.3
	Γ_1	993.1		Γ_5	1033.5
	Γ_5	1044.1		Γ_1	1035.
	Γ_3	not observed		Γ_3	not observed

Zeeman Experiments

In the fluorescence experiments (Chapter 2), we found that in the vanadates and in $EuAsO_4$, the Eu^{3+} $^7F_1$ and $^7F_2$ doublets did not split with the expected Landé g factor. Zeeman Raman experiments were carried out to confirm this observation unambiguously.

Zeeman experiments can be done with the magnetic field along either the c or a direction. When it is along a, the splitting will be quadratic, making it difficult to determine the g factor. But when the experiment is done with the magnetic field along c, the splitting is linear; the determination of the g factor will be straight-forward.

For the Zeeman experiments, a small split-pair superconducting magnet was used. It was designed by Harry Jones of the Clarendon Laboratory, the University of Oxford. The magnet has a bore of 8 mm. Four holes of 4 mm in diameter on the sides provide radial optical access to the sample. At the center of the magnet, the ratio of field to the current supply is 0.800 kG/A as calculated by Harry Jones and also calibrated by a BHA921 axial Hall probe (serial #12182). The power supply has a maximum output of 68 A. Because of the split-pair geometry, the field strength profile along the center line is saddle-shaped. Care was taken to put the sample at the center of the magnet. Otherwise, the field might be stronger than that predicted by the field/current ratio for the center.

As shown in Figure 3.3, the $EuVO_4$ Γ_1^+ phonon at 377 cm^{-1} is 10 cm^{-1} wide, much broader than other lines. Its lineshape is not symmetric as shown on the expanded scale of Figure 3.4. The Γ_5 electronic line around 370 cm^{-1} is on its low energy wing. To see a reasonable Zeeman spectrum, we had to choose a geometry so that the phonon line was suppressed and the electronic line could be seen.

Of all the scattering geometries listed in Table 3.1, Γ_1 scattering occurs for only two. There are four geometries where Γ_5 scattering is allowed. Since the Γ_1^+ phonon is much stronger than the Γ_5 electronic line, a choice was made among these four that would best serve the purpose of maximizing the electronic scattering signal and minimizing the phonon scattering signal in that region. For $EuVO_4$, the $z(xz)x$ geometry was used, because in the other geometries, imperfection of the incident light polarization might still be a problem. For example, when the light is incident along y, in $y(zy)x$ and $y(xz)x$ geometries, only Γ_5 scattering is allowed. But Γ_1 scattering is allowed in $y(zz)x$ geometry,

where only one letter is different in polarization (as indicated in the bracket) from the other two Γ_5 allowed geometries, so that polarization selection is effective only on either the incident side, or the collecting side of the crystal, but not on both. When the light is incident along *c*, $z(y\bar{z})x$ and $z(xz)x$ also allow only Γ_5 scattering, but the first geometry is only different from the Γ_1 allowed geometry $z(yy)x$ by the polarization on the collecting side. We chose the $z(xz)x$ geometry for the $EuVO_4$ $^7F_1$ (Γ_5) scattering.

Since it was neccesary to do the experiment with the magnetic field along *c*, optical access to the crystal inside the small magnet was more difficult in this geometry, but it did have the advantage that no Dove prism was needed in the collection optics. A 2 mm x 2 mm right angle prism was used to send the light verticallly through the crystal. Ideally, the transmitted light should be collected and sent out of the dewar, but even without doing this, reasonable signal was observed. The $EuVO_4$ $^7F_1$ (Γ_5) level was measured this way. The measured Zeeman spectra for $EuVO_4$ are given in Figure 3.7 and Figure 3.8. The splittings for both the $^7F_1$ and $^7F_2$ levels are 6.0 cm^{-1} in a field of 50.0 kG, implying a g factor of 1.29 instead of the normally expected 1.50.

For $EuAsO_4$, the Γ_1^+ phonon line was also very strong and much wider than other phonon lines, but it was at 398 cm^{-1}, about 30 cm^{-1} above the 367.7 cm^{-1} Γ_5 electronic line. Since the dicrimination against the phonon line was not a concern for $EuAsO_4$ electronic scattering, the $EuAsO_4$ scattering experiments were all done in the $y(xz)x$ geometry. The Zeeman split spectra at 50.0 kG for both the $^7F_1$ and $^7F_2$ doublets of $EuAsO_4$ are shown in Figure 3.9 and Figure 3.10. In both cases, the splitting was 6.5 cm^{-1}, implying a g factor of 1.40. All these values precisely confirmed our measurements from the Zeeman fluorescence experiments.

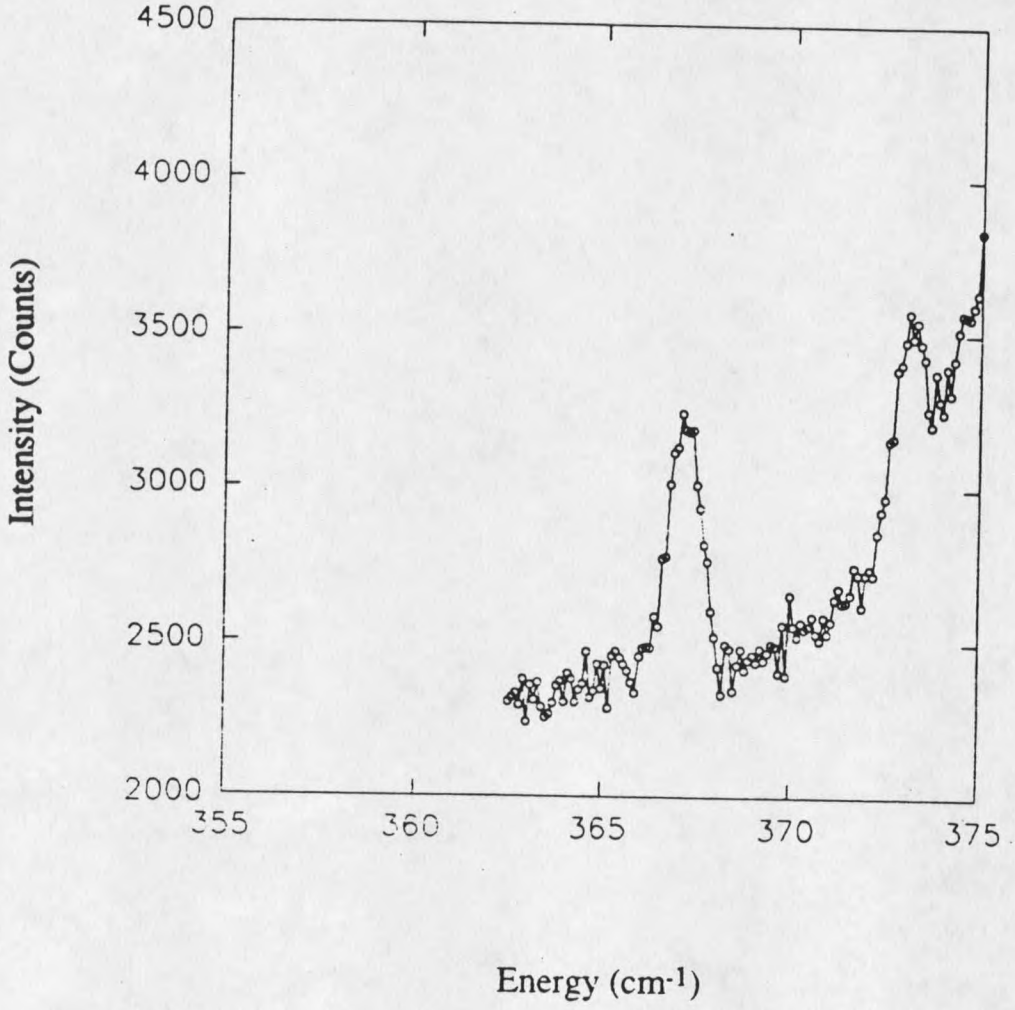

Figure 3.7 Raman scattering spectrum of $EuVO_4$ $^7F_1$ (Γ_5) in a field of 50.0 kG along the *c*-axis.

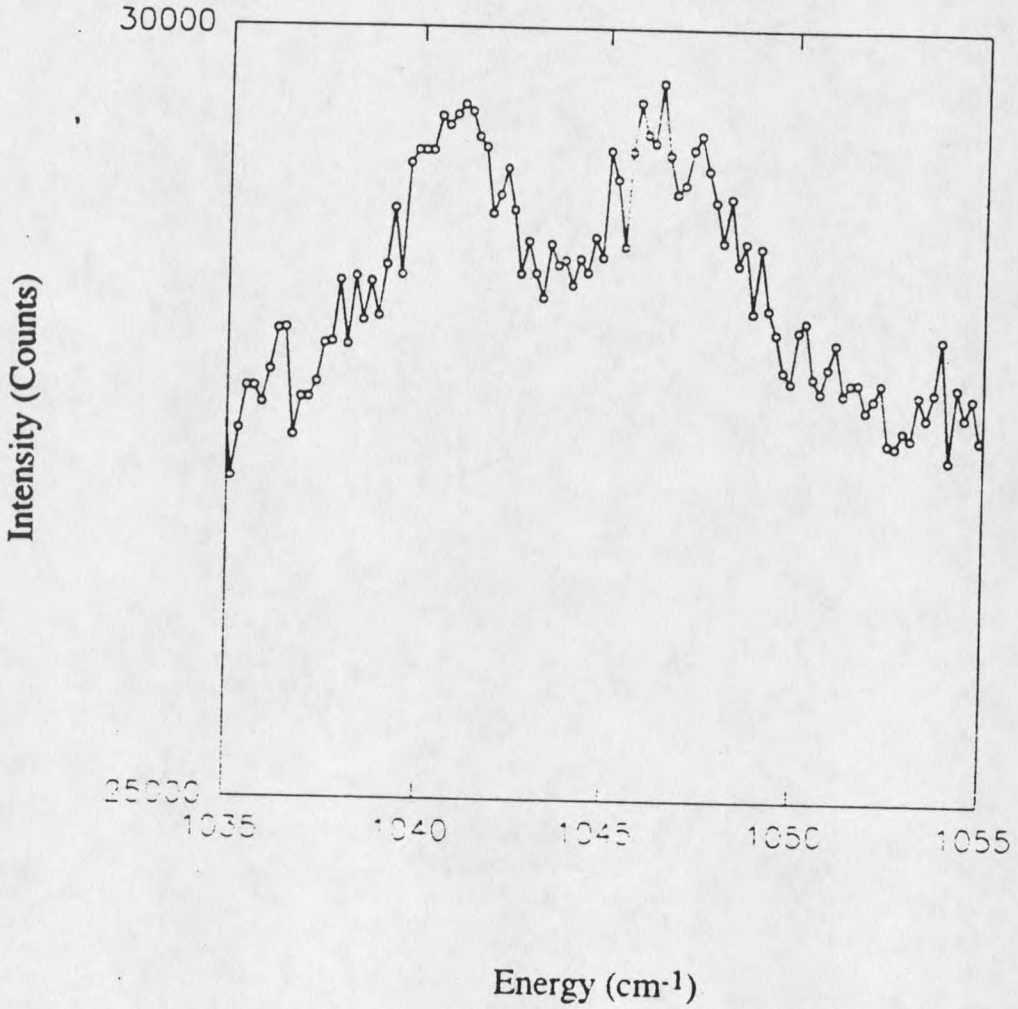

Figure 3.8 Raman scattering spectrum of $EuVO_4$ $^7F_2$ (Γ_5) in a field of 50.0 kG along the *c*-axis.

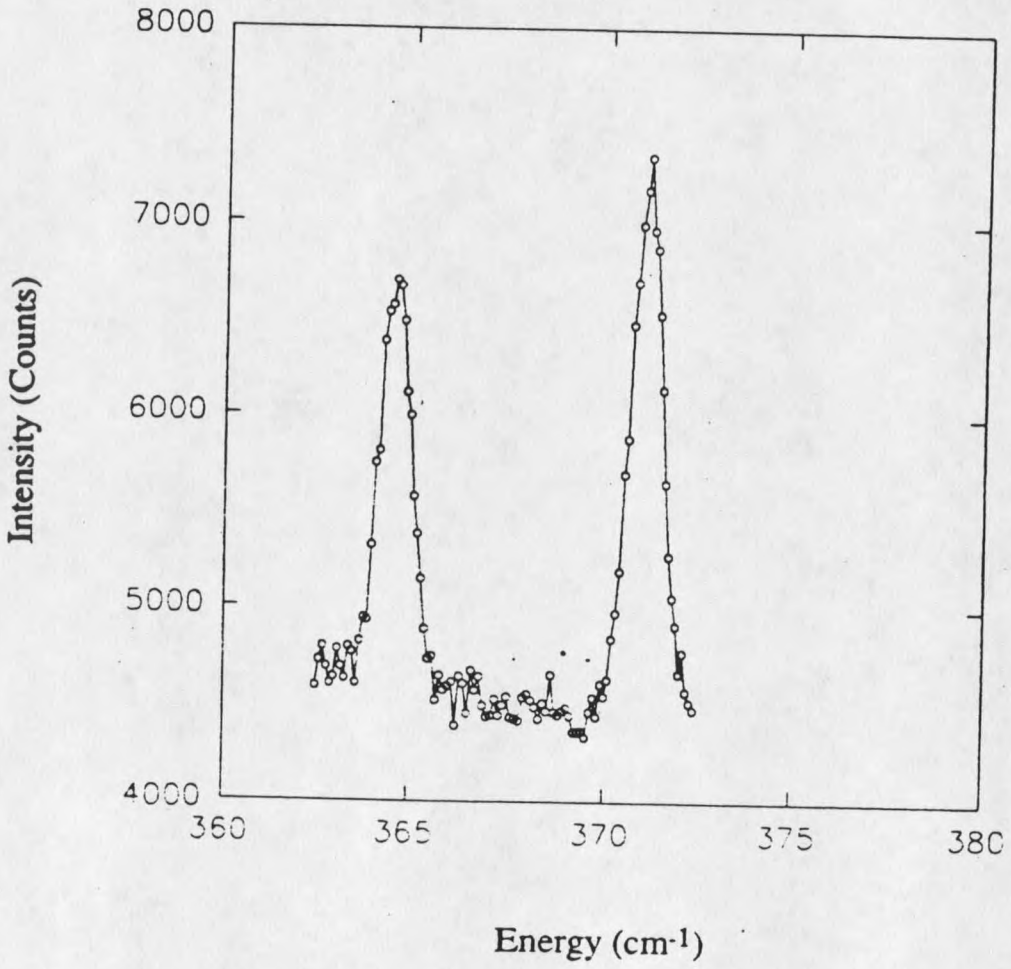

Figure 3.9 Raman scattering spectrum of $EuAsO_4$ $^7F_1$ (Γ_5) in a field of 50.0 kGalong the *c*-axis.

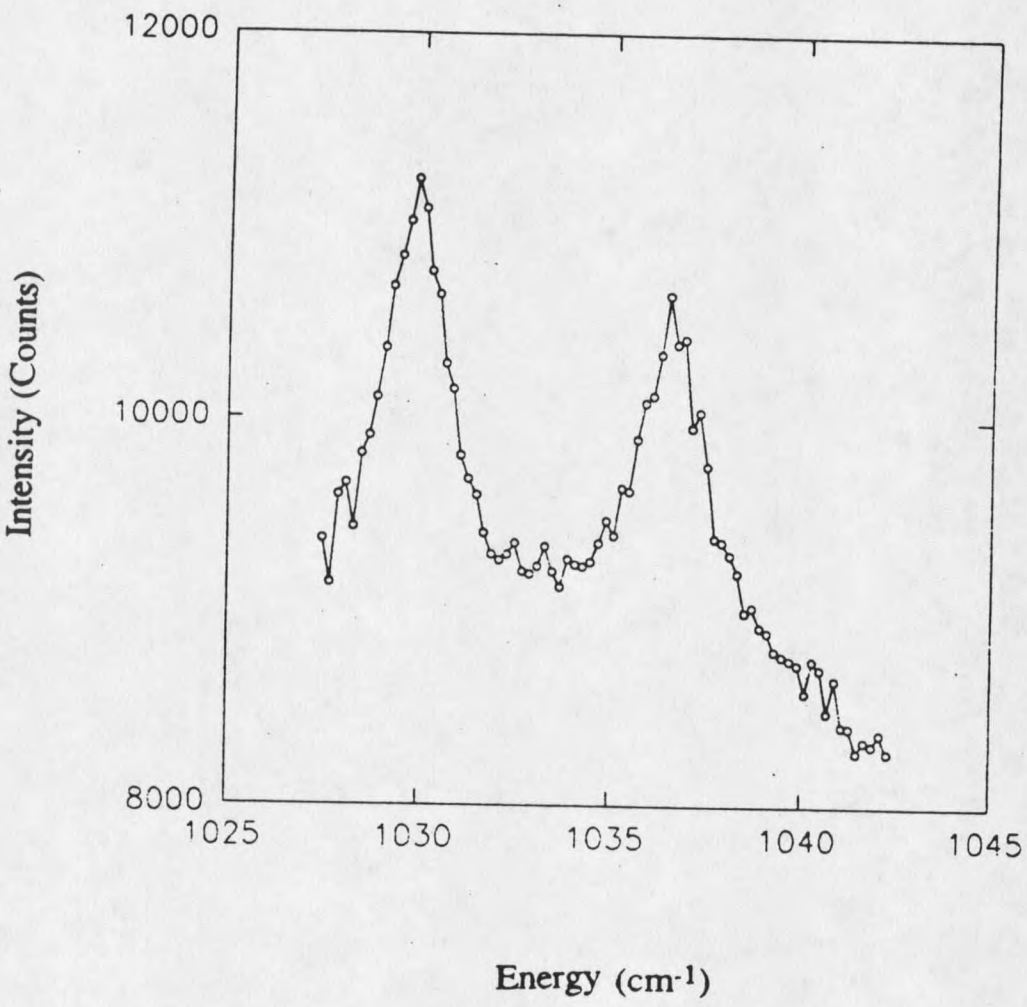

Figure 3.10 Raman scattering spectrum of $EuAsO_4$ $^7F_2$ (Γ_5) in a field of 50.0 kG along the *c*-axis.

The Jahn-Teller Effects

The Jahn-Teller Theorem

The Jahn-Teller theorem (Jahn and Teller, 1937) states that, for systems with electronic degeneracy (except Kramers degeneracy and other accidental degeneracies), there will be at least one kind of distortion that linearly couples to the degenerate state and makes it unstable. (A linear molecule is an exception).

This theorem was originally proven by exhausting all possibilities in the 32 point groups. The possible distortions that can act on a certain degeneracy represented by $\mathcal{D}$ should be contained in the symmetric self product of $\mathcal{D}$. For an ion at D_{2d} symmetry, the doublet can only interact with

$$[\Gamma_5^2] = \Gamma_1 + \Gamma_3 + \Gamma_4$$

The Γ_1 coupling will not lift the degeneracy of the doublet. It will move both branches in the same direction. Zircon structure rare earth compounds show couplings to both to the Γ_3 ($DyVO_4$) and Γ_4 ($TbVO_4$) phonons, and these couplings have resulted in static distortion of the lattice at low temperature (Gehring and Gehring, 1975).

The Jahn-Teller theorem is essentially an existence theorem which just states that there must be this kind of coupling, but it does not predict how strong this coupling will be and what consequences it may have in a spectrum. If this coupling is strong enough, it may result in a static distortion, as happens in $DyVO_4$. Another possibility is that this coupling is not strong enough for a distortion of the crystal itself to occur, but the old device of using a static field to describe the environment the ion "sees" is not valid anymore. This latter scenerio is probably much more common than the first one and results in the so-called dynamic Jahn-Teller effect (Ham 1965, Ham 1968, Abragam and

Bleaney 1971, Ham 1972, and Gehring and Gehring 1975). The most prominent manifestation of this effect is the reduction in the spin-orbit coupling and the apparent reduction of orbital angular momentum, or Ham quenching (Ham 1965).

Ham Quenching

Ham (1965, 1967) treated the dynamic Jahn-Teller effect in a triplet Γ_4 ground state system in O or T_d symmetry. In a tetragonal system, it is different since the tetragonal crystal field will split the triplet into a singlet and a doublet level. But as we shall see below, this problem can still be solved much the same way.

The correspondence between the O representations and D_{2d} representations is

$\Gamma_4^o = \Gamma_2^t + \Gamma_5^t$

$\Gamma_3^o = \Gamma_1^t + \Gamma_3^t$

where the superscript 'o' indicates O group representation and 't' represents a D_{2d}, or tetragonal group representation. We will treat our tetragonal problem like a cubic system with tetragonal distortion.

For the tetragonal field that is relevant to ^7F_J which is represented by Γ_4 in the O group, the basis functions are

$$Y_{20} \Rightarrow \frac{1}{2}(3z^2 - r^2)$$

$$Y_{22} + Y_{2\text{-}2} \Rightarrow \frac{\sqrt{3}}{2}(x^2 - y^2)$$

These are the basis functions for the doublet Γ_3 in the O group. We can write the whole Hamiltonian for the interaction of the electronic triplet with the doublet phonon state as

$$\mathcal{H} = E_0\Im + (1/2\mu)[P_\theta^2 + P_\varepsilon^2 + \mu^2\omega^2(Q_\theta^2 + Q_\varepsilon^2)]\Im + V[Q_\theta\Theta + Q_\varepsilon\mathcal{E}] + \frac{B_{20}}{5}\Theta,$$

where Q_θ and Q_ε are the generalized coordinates of the doublet phonon and P_θ and P_ε are their conjugate momenta, μ is the effective mass of the mode and ω its angular frequency; V is the Jahn-Teller coupling coefficient; and the matrices $\Im$, Θ, and $\mathcal{E}$ are, respectively, the unit matrix and

$$\Theta = \begin{bmatrix} \frac{1}{2} & & \\ & \frac{1}{2} & \\ & & -1 \end{bmatrix}, \qquad \mathcal{E} = \begin{bmatrix} \frac{\sqrt{3}}{2} & & \\ & -\frac{\sqrt{3}}{2} & \\ & & 0 \end{bmatrix}$$

as given by Koster *et al.* (1963) and Ham (1965, 1972).

The energy of the degenerate state in the symmetrical configuration is E_0. For simplicity we assume that the electronic states $\psi_i(\tau)$ are independent of Q, and we ignore coupling to other electronic states. B_{20} is the crystal field parameter.

In this Hamiltonian, all matrices commute, so that all of them can be brought into diagonalization simultaneously. The Jahn-Teller interaction and the crystal field interaction will not mix. Accordingly, the vibronic eigenfunction will be the product of the electronic wavefunction and the two dimensional harmonic oscillator, the equilibrium position of which is

$$Q_{\theta i} = -Ve_{i\theta}\ /\mu\omega^2, \qquad Q_{\varepsilon i} = -Ve_{i\varepsilon}/\mu\omega^2,$$

where $e_{i\theta}$ or $e_{i\varepsilon}$ is the appropriate diagonal component of the matrix Θ and $\mathcal{E}$. The potential energy of the oscillator at the equilibrium position is lower than E_0 by the Jahn-Teller energy E_{JT}, which in this case is given by $E_{JT} = V^2/2\mu\omega^2$. We therefore have

$$\Psi_{in}(\mathbf{Q},\tau) = \psi_i(\tau)F_{n\theta}(Q_\theta + Ve_{i\theta}\ /\mu\omega^2)F_{n\varepsilon}(Q_\varepsilon + Ve_{i\varepsilon}/\mu\omega^2),$$

where $i = \xi, \eta, \zeta$, the electronic functions of the triplet state and the corresponding energy

$$E_{in} = E_0 + e_{i\theta} \quad B_{20}/5 - (V^2/2\mu\omega^2) + (n_\theta + n_\varepsilon + 1)\hbar\omega,$$

$$n_\theta, n_\varepsilon = 0, 1, 2, 3, \ldots,$$

where $F_n(y)$ is the standard harmonic oscillator function.

We should note that the perturbation represented by Θ will not distort the tetragonal doublet. This is the branch that goes to Γ_1 in the tetragonal structure.

The vibronic spectrum stays the same as in the absence of the Jahn-Teller interaction, except for the displacement $-V^2/2\mu\omega^2$, common to all states. However, the equilibrium position for the displaced oscillator is different for the three electronic functions $\psi_i(\tau)$ corresponding to $i = \xi, \eta, \zeta$. As this separation increases in proportion to $V/\mu\omega^2$, the region of overlap between corresponding oscillator states associated with different electronic functions is diminished, and the matrix elements of such states fall accordingly.

Matrix elements of various operators between the vibronic eigenstates can be evaluated explicitly. In the vibronic ground state, the diagonal matrix elements should not be affected, while the nondiagonal matrix elements will be modified by the Jahn-Teller states. The orbital angular momentum is a nondiagonal operator, and

$$L_x = \begin{bmatrix} & -i \\ i & \end{bmatrix} \qquad L_z = \begin{bmatrix} & -i \\ i & \end{bmatrix} \qquad L_z = \begin{bmatrix} -i & \\ & i \end{bmatrix}.$$

The angular momentum will be modified by a quenching factor of

$$\exp(-3E_{JT}/2\hbar\omega)$$

according to Ham's calculation (Ham 1965, 1972). This reduction of the orbital angular momentum and other interactions is called *Ham quenching*.

We can also treat this problem in the space spanned by the doublet electronic state using a formalism similar to pseudospin. According to the Jahn-Teller theorem, only Γ_3 or

Γ_4 can be coupled linearly to the doublet in a tetragonal crystal. Since this is one-dimensional, we can write the Hamiltonian as

$$H = E_0 + 1/2\mu[P^2 + \mu\omega^2 Q^2] + VQS_z$$

where Q and P are the coordinate and its conjugate momentum. E_0 is the energy at the equilibrium position. V is the Jahn-Teller coupling coefficient, and

$$S_z = \begin{bmatrix} 1 & \\ & -1 \end{bmatrix}$$

in the space spanned by the doublet. Very similarly to the coupling of a doublet to an electronic triplet in the O group treated above, this Hamiltonian can also be solved exactly, for which we have

$$E_n = E_0 - V^2/2\mu\omega^2 + (n+1)\hbar\omega$$

$$\Psi_{in}(Q,\tau) = \psi_i(\tau)\, F_n(Q + e_{is}\, V/\mu\omega^2)$$

$$n = 0, 1, 2, 3, \ldots,$$

where i is the label for the electronic functions and e_{is} is the appropriate diagonal matrix element of S_z. All calculations are very similar to the problem treated above. Since we have

$$L_z = \begin{bmatrix} & 1 \\ 1 & \end{bmatrix},$$

the reduction factor for it is

$$\exp(-2E_{JT}/\hbar\omega)$$

The two different treatments led to different expressions for the reduction factor. In the first treatment, a triplet is influenced by a tetragonal field and is coupled to Γ_1^t and Γ_3^+ at the same time. In the second treatment, only the tetragonal doublet was considered and only Γ_3^t or Γ_4^t is considered. The point in deriving these expressions is not to give an expression for any quantitative calculation of the reduction factor, since none of the

parameters are known, but rather to prove that this kind of coupling can indeed induce the reduction of the orbital angular momentum.

Ham Quenching in Europium Compounds

Since the spin operators should be diagonal in the above treatment, the reduction factor for spin should be 1. For the ^7F_J system, the g_J factor has significant contributions from the orbital and spin part because L = 3 and S = 3. For g_J = 1.5, the contribution from spin is 1 and the contribution from the orbital part is 0.5.

In $EuVO_4$, both the $^7F_1$ and $^7F_2$ levels split with a g factor of 1.29. In $EuAsO_4$, the g factor is 1.40. From the measurement of the $^7F_1$ splittings, Eu:YVO_4 and Eu:$LuVO_4$ have g factors of 1.30 and 1.27, respectively.

If only the orbital part is reduced by the Jahn-Teller effect, then the reduction factor ranges from 0.54 to 0.6 for the vanadates, and it is 0.8 in $EuAsO_4$. The reduction is too large to be explained by the covalency of the lattice, since rare earth salts are typical ionic crystals. Besides, the europium doped phosphates gave the correct splitting factors. The reduction here must come from the dynamic Jahn-Teller effect.

A reduction factor of 0.6 would mean that the power in the expression for the reduction factor is around -0.5. It is difficult to estimate what the Jahn-Teller energy is. In the crystal field calculations of the last chapter, the fitted energy levels always seem to be higher than the measured ones. It is attempting to say that maybe this is due to the displacement by the Jahn-Teller energy. But in reality it probably is more due to the fact that free-ion parameters from Eu^{3+}:$LaCl_3$ energy levels were used in the crystal field calculations. On the other hand, if this really is due to the Jahn-Teller energy displacement of several wavenumbers, that would mean that the phonon coupled to the doublet may be tens of wavenumbers (3 or 4 times of E_{JT}, several cm^{-1} from crystal field calculation) in energy which was not seen in the phonon scattering spectrum. It is far more probable that

the phonon frequency is under a wavenumber and the lowering of the energy is not observable.

Ion-ion Interaction and Davydov Splittings

As we have discussed in Chapter 2, in the stoichiometric compounds, all Eu^{3+} $^5D_0$ - $^7F_1$ transitions seem to have double peaked features as shown in Figure 2.8 and Figure 2.9. The double peaked structure in these transitions is far more pronounced in transitions associated with Γ_2; it is 1.4 cm^{-1} for $EuAsO_4$, 0.8 cm^{-1} for $EuVO_4$. The structure in the transitions related to Γ_5 is more subtle and needs high resolution to be resolved, the gap is 0.3 -0.4 cm^{-1}. In higher temperature absorption experiments, the Γ_5 transition is broad enough that no structure can be seen. But the Γ_2 transitions still show double peaks with about equal intensity as shown in figures 2.10 through 2.12. In $EuVO_4$, the Γ_2 gap is larger at 100 K than at 1.5 K. In $EuAsO_4$, the gap is similar at 100 K and 1.5 K. The energy levels determined by different methods and at different temperatures are summarized in Table 3.5. The letters s and w indicate stronger or weaker transitions.

Table 3.5 $^7F_1$ levels measured by different method in the stoichiometric europium compounds.

$EuVO_4$ levels				$EuAsO_4$ levels			
	Raman	Fluores.	Ab. at 100 K		Raman	Fluores.	Ab. at 100 K
Γ_5	369.9	369.9(w)	368.7	Γ_2	375.4	374.2(s)	375.4
		369.6(s)				372.8(w)	374.2
Γ_2	360.3	360.3(w)	359.3	Γ_5	367.7	367.0(s)	367.7
		359.5(s)	357.2			366.6(w)	

In the dilute crystals, this kind of spectrum was not seen. The fluorescence spectra were just as expected from the normal single-ion picture. This indicates that the double peaked feature of the transitions must be from ion-ion interactions.

In the absorption experiments, both exciton branches of $^7F_1$ should be equally thermal-populated. Transitions from these excitons start from both branches and go to the opposite parity branches of the $^5D_1$ and $^5D_0$ states. Two equal-intensity peaks can be seen. In the fluorescence experiments, the $^5D_0$ population is from the photo-excitation of the ground state electrons. Ground state has only even parity by definition. So that only one exciton branch (odd) in $^5D_0$ will be excited. The fluorescence from this level to $^7F_1$ should also occur only to one branch of the exciton (even). Processes other than normal optical transitions may break the rigorous selection rules, but one branch should still be stronger than the other, and that is what was observed in the fluorescence experiments.

From Table 3.4, we can see that energy levels measured by different methods do not match each other exactly, although they are roughly at the same positions and the zero-field splittings are similar. In $EuVO_4$, the Raman scattering determined level positions seem to match the positions determined by the weaker peaks in the fluorescence experiments. In $EuAsO_4$, none of the levels match.

The discrepancies of the energies determined by different methods can be explained by exciton band transitions. Since Raman scattering should only measure the energy level of the even branch, and the $^5D_0$ - $^7F_1$ fluorescence also should see the transition of the even parity branch, then the energy determined by the stronger fluorescence transition and that determined by Raman scattering should be from the same branch. It is obvious that all Raman measured energy is higher than those measured by fluorescence experiments. Since Raman scattering measures only zone center transitions, while fluorescence measures a zone-averaged transition, this implies that the exciton has a smaller energy at the zone boundary. This seems to be true for both crystals.

If we consider the exciton band structure, it can also explain the discrepancy in the $^7F_2$ (Γ_4) measurements. In this case, energy levels measure by Raman scattering seem to be 10 cm^{-1} higher than the fluorescence measured energy. This could also mean that the zone center energy is 10 cm^{-1} higher than the zone edge energy.

CHAPTER 4

DEFECT STRUCTURE AND DYNAMICS

This chapter deals with two seemingly unrelated subjects: (a) the relationship of the energy levels with the crystal structure cell size and (b) the time-resolved fluorescence results when the $^7F_0$ - $^5D_0$ defect transitions were pumped directly. We put these two subjects together in an attempt to determine the local lattice structures around the defects and the possible energy migration routes among Eu^{3+} ions at the various sites. The relationship between the energy levels of a guest ion and the unit cell size of the host crystal will be discussed.

Cone *et al.* (1984) and Cone *et al.* (1993) studied the defect $^7F_0$ - $^5D_0$ spectra of $EuVO_4$ crystals of over a dozen different growths and found around 50 defect lines in each one of them. Similar spectra were given for two additional growths of crystals in Chapter 2. Holeburning studies of all these sites determined that the sites with higher energy than the intrinsic site had more distorted local environments than those sites close to the intrinsic site in energy. Those sites with energy close to the intrinsic site had near axial environments ($\eta \approx 0$, see Chapter 5).

We shall first consider the systematics of the rare earth spectra generally, together with absorption spectra for Eu^{3+}:YPO_4 with different Eu^{3+} concentrations. Time-resolved fluorescence spectra and lifetimes will be presented next. Then the possible defect structures and their correlation with the energy migration dynamics will be discussed.

Systematics of Rare Earth Ion Spectra

When a rare earth ion is incorporated into a crystalline environment, the most dramatic difference of its spectra from the gaseous state can be described by a so-called crystal field interaction arising from neighboring ligand ions. The originally spin-orbit split J levels are split again by the crystal field, but the crystal field can only split an isolated J level, its baricenter should not be dramatically changed. The energy levels in a crystalline environment always have lower baricenters than those for the same ion in the gaseous state. Baricenters for the same ion in different hosts also vary. Comparing the spectra of different ions in one specific crystal, one finds that if one ion has higher energy baricenters, other ions have higher baricenters in that crystal, too. So the characteristics of the crystal modify the Slater integrals. The modifications are similar for different ions in the same crystal. By comparing the spectra of the same ion in different crystalline hosts, the modification of the Slater integrals by different crystals can be estimated.

Two main theories were developed to explain the shifts of the Slater integrals in different hosts, and the shift from the gaseous state to the solid state. One was proposed by Jørgensen (1962; 1971) and was called the nephelauxetic - cloud expanding - effect. It attributes the reduction of the Slater integrals to the covalency of the crystal, and the consequent reduction in the two-electron interaction operator $\langle r_{12}^{-1} \rangle$. The second theory was proposed by Morrison *et al.* (1967) and attributed the reduction in the Slater integrals to the dielectric constant of the crystal environment. Newman (1972) calculated the magnitude of the reduction predicted by these theories for Pr^{3+} in anhydrous chloride ($LaCl_3$) and concluded that covalency for this material had too small an effect to explain the observed shift, while the dielectric constant theory predicted a shift of the right order of magnitude.

The ions in the lanthanides (including yttrium) have very similar chemical properties, but rare earth crystals have different lattice constant, thus different cell volumes. The effective radius of a cation in a crystal is directly proportional to the cell size of the crystal. In the rare earth tetragonal zircons, it was found empirically to be as directly proportional to the cubic root of the cell size (a^2c for a tetragonal crystal) (Alfred 1984). The ionic radii of the lanthanides decrease from 1.313 Å (La^{3+}) to 1.117 Å (Lu^{3+}). Yttrium falls between holmium and erbium, but is closer to holmium. For two crystal lattice cells of the same structure, the cation-anion distance should be longer for a large unit cell, shorter for a small unit cell. The long cation-anion distance means a smaller dielectric constant. For ions in the two different lattices, the ion in the larger unit cell should have larger Slater integrals. For crystals with different anions, the heavier anion influences the cation much more. For the same cell size, the cation will experience a larger dielectric constant in case of the heavier anion. Thus the energy levels change.

Most ions have a degenerate ground state in the gaseous state. When they are doped into a crystalline environment, this degenerate level is normally split. When one compares the energy level baricenters of a certain ion in different crystals, one has to take into account of the splitting of the ground state: the baricenter of the lowest J manifold has to be used instead of the lowest level. For ions that have many levels mixed in the low energy region, this can be very difficult.

The Eu^{3+} ion provides a special case where the ground state has J = 0, so that it will not move much in a crystalline environment; the shift due to the admixture with the $^7F_1$ levels is usually within 1 cm^{-1}. The $^5D_0$ state, which also has J = 0, should not be moved much by the crystal field either; shifts of $^5D_0$ due to admixture with other levels are even smaller. With these properties, the difference in the $^7F_0$ - $^5D_0$ transitions in different crystals can be used as an indicator of the modifications of the Slater integrals.

Morrison and Leavitt (1982) compiled the rare earth energy levels in many different hosts. Comparison of the Eu^{3+} $^5D_0$ levels in different hosts can be easily made using these tables. We summarize the $^7F_0$ - $^5D_0$ energy for some representative hosts in Table 4.1.

Table 4.1 Eu^{3+} $^7F_0$ - $^5D_0$ energy in different hosts

CaF_2 (G1 center)	17430 cm^{-1}	$Eu(OH)_3$	17225 cm^{-1}
LaF_3	19293 cm^{-1}	$EuAsO_4$	17215 cm^{-1}
EuF_3	17290 cm^{-1}	$EuVO_4$	17196.7 cm^{-1}
$LaCl_3$	17267.35 cm^{-1}	Y_2O_2S	17143.3 cm^{-1}

Ions in Hosts with Different Anions

It is obvious from Table 5.1 that the Eu^{3+} $^5D_0$ level decreases in the following sequence:

CaF_2, LaF_3, $LaCl_3$, $Eu(OH)_3$, YPO_4, YVO_4, Y_2O_2S,...

According to Jørgensen (1971), the general order for Slater integrals in different anions is

Gaseous > F^- > H_2O > Cl^- > Br^- > I^- > O^{--},

implying that the weight and the valence of the the anion all play important roles in the determination of the energy levels.

Baumert *et al.* (1975) studied the concentration effect of an anion on the energy levels of the dopant ions. The $^4I_{9/2}$ - $^4S_{3/2}$ energy of Nd^{3+}:$La(Cl_{1-x}Br_x)_3$ was studied with various x values. $LaCl_3$ has a smaller cell than $LaBr_3$, but the energy levels are higher in $LaCl_3$. By doping Br^- into the $LaCl_3$ lattice, defect lines appear due to the Br^- distortion. But the main line from the $LaCl_3$ lattice also changes. Instead of going down toward the Nd^{3+}:$LaBr_3$ transition frequency which is lower, the transition

frequency goes up. Doping Cl^- into the $LaBr_3$ lattice makes the main transition lower in energy. It was estimated that a $LaCl_3$ lattice made with $LaBr_3$ lattice constants would make this transition increase by 18 cm^{-1}.

This can be explained by the correlation between the cell size and the energy levels. When Br^- is doped into the $LaCl_3$ lattice, it will replace some of the 9 Cl^- ions around the rare earth ion. Normally, for the same cell size, the Br^- lattice would have a larger dielectric constant, and hence lower energy levels. But in $LaCl_3$, Br^- substitution enlarges the original cell by so much that the effective dielectric constant is actually smaller after the Br^- substitution. The reverse is true for Cl^- doped into the $LaBr_3$ crystal.

Ions in Hosts with Same Anions

Aside from the shifts for hosts with different anions - which are dramatic from one anion to another, shifts also occur in hosts with the same anion, and the same structure but with different cations. Hosts with similar chemical formulas but different crystal structures can have very different dielectric constants, and so different spectra. For example, $EuPO_4$ and $Eu:YPO_4$ have different structures. The $^5D_0$ level of $EuPO_4$ is at 19264.1 cm^{-1}; the $^5D_0$ of $Eu^{3+}:YPO_4$ is at 19201.2 cm^{-1}.

It was noted during this work that the Eu^{3+} $^7F_0$ - $^5D_0$ energy level baricenters are directly related to the cell size of the hosts, or the ionic radius of the host ion. For example, the Eu^{3+} $^5D_0$ level in $EuVO_4$, $Eu^{3+}:YVO_4$ and $Eu^{3+}:LuVO_4$ were found at 17196.7 cm^{-1}, 17184.9 cm^{-1}, and 17176.71 cm^{-1}, respectively, a difference of 20 cm^{-1} across only half of the lanthanide series. The $Eu^{3+}:YPO_4$ and $Eu^{3+}:LuPO_4$ energy levels (Appendix II) also show that larger host cells imply larger Slater integrals for the guest ion.

The same statement can be made when comparing the spectra of Pr^{3+}:$Y(OH)_3$ and $Pr(OH)_3$ (Chirico, 1979 and Boger 1987), those of Tb^{3+}:$Y(OH)_3$ and $Tb(OH)_3$ (Scott, 1970), of Gd^{3+}:$LaCl_3$ and $GdCl_3$ (Schwiesow, 1968), and the series of Er^{3+}:$Y(OH)_3$, $Er(OH)_3$, and Er^{3+}:$Tb(OH)_3$ (Cone 1972). The energy levels of Eu^{3+} in the C_{4V} centers in CaF_2, SrF_2, and BaF_2 (Silversmith and Macfarlane 1992) also confirm this trend.

The most interesting of these is the comparison of the Er^{3+}:$Y(OH)_3$ and $Er(OH)_3$ spectra (Cone 1972) because yttrium and erbium have very similar ionic radius (Alfred 1982). The energy levels in the visible range are all lowered in $Er(OH)_3$ by a small amount (~ 1 cm^{-1}) compared to those of Er:$Y(OH)_3$. The lower lying infrared levels of the two crystals are very similar. The baricenters are also very close.

The unpublished spectra for Ho^{3+}:$LiYF_4$ and $LiHoF_4$ from this lab show that the differences of most lines for the two crystals are within the linewidths of the spectra. The holmium ionic radius is the closest one to the yttrium ionic radius in the rare earth series.

All these phenomena can be explained by the change of the dielectric constants when the crystal cell sizes are different. Larger cells imply smaller dielectric constants.

The direct relation of the energy levels to the lattice size was confirmed by Baumert *et al.* (1975) who studied the pressure dependence of the $^4P_{9/2}$ - $^2P_{1/2}$ transition in Nd^{3+}:$LaCl_3$. They found that the transition energy decreases with pressure applied parallel and perpendicular to the *c*-axis.

$\Delta E_{\parallel}(^2P_{1/2}) = -0.85$ cm^{-1}/kbar

$\Delta E_{\perp}(^2P_{1/2}) = -0.3$ cm^{-1}/kbar,

Concentration Effect of the Active Ions

We studied the effect of changing Eu^{3+} doping concentration for several host materials. In Chapter 2, the effect of concentration for Eu^{3+}:YVO_4 was noted; the Eu^{3+}:$LuPO_4$ energy levels also show concentration induced shifts. We summarize the energy levels of these two crystals for several concentrations in the table below.

Table 4.2 Energy levels of Eu^{3+} doped YVO_4 and $LuPO_4$.

	$^5D_0$ (Γ_1) (cm^{-1})	$^5D_2$ (Γ_5) (cm^{-1})	$^5D_2$ (Γ_2) (cm^{-1})
0.1%Eu^{3+}:YVO_4	17184.91		
1%Eu^{3+}:YVO_4	17185.10		
0.5%Eu^{3+}:$LuPO_4$	17186.42	21406.8	21452.6
5%Eu^{3+}:$LuPO_4$	17187.11	21409.2	21454.1

It is easy to see that the energy levels move up with the doping level as expected since the europium ionic radius is larger than that of either yttrium or lutetium. When there are more europium ions, the cell will become larger than the real YVO_4 or $LuPO_4$ cells.

For Eu^{3+}:YPO_4, this effect was studied up to much higher concentrations. Crystals of 0.5%, 5%, 10%, 25%, 40%, and 50% europium concentration were used. Since 75%Eu^{3+}:YPO_4 and pure $EuPO_4$ crystals have a monoclinic structure, their energy levels cannot be compared directly with the others. The $^5D_1$ and $^5D_2$ absorption spectra were taken for these crystals at T = 1.5 K. The results are shown in Figure 4.1 and Figure 4.2. The energy levels increase linearly with concentrations up through 50%. Somewhere between 50% and 75% concentration the system begins to crystallize in the monoclinic structure, and the energy levels are typical of the low symmetry where no degenerate level exists. Besides the increase in the energy, the linewidths also are very broad (~5 cm^{-1}) at higher concentrations because of the disordered lattice. The europium dopant goes into the YPO_4 lattice and forms $Y_{1-x}Eu_xVO_4$ tetragonal lattices.

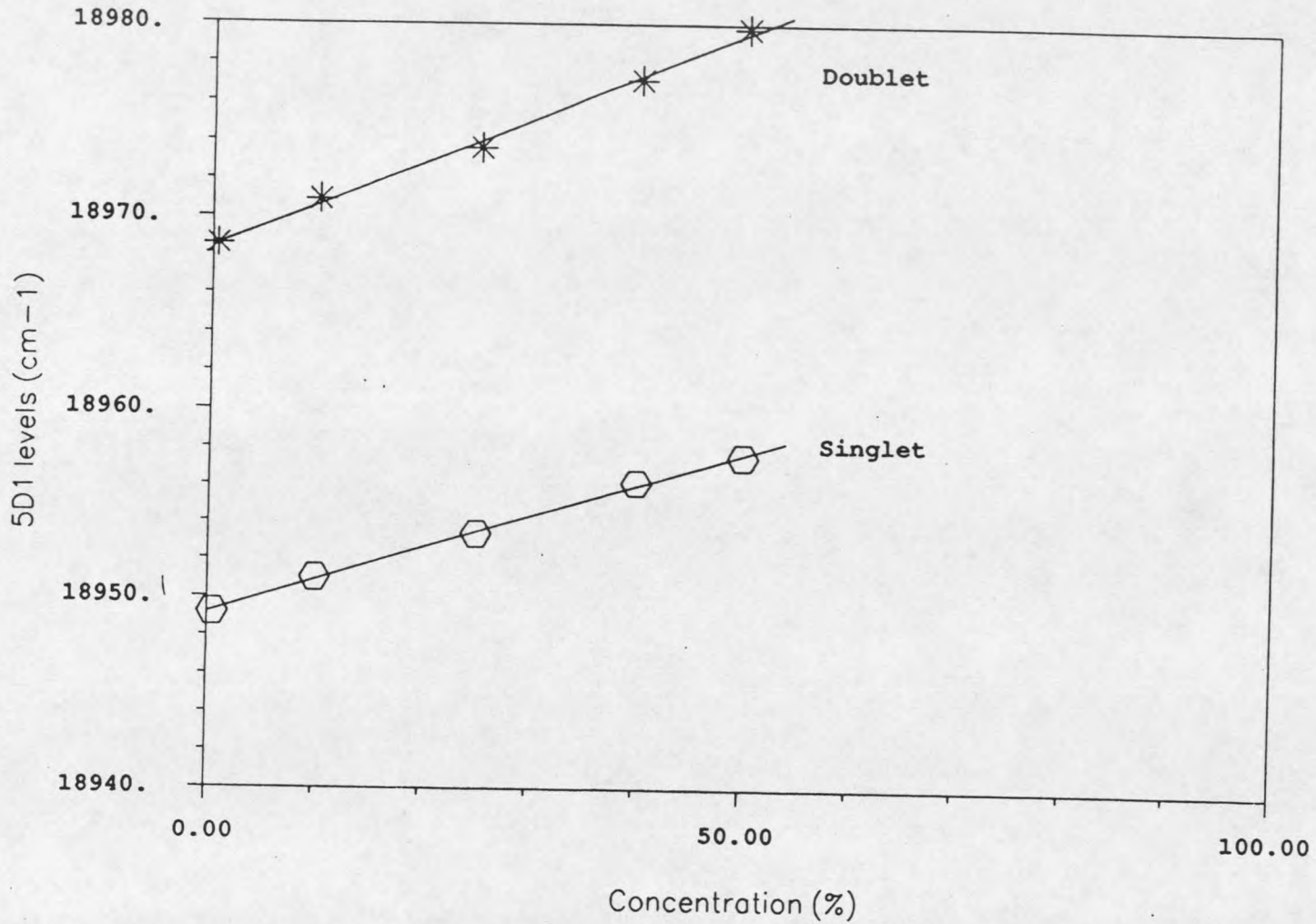

Figure 4.1 The variation of the Eu^{3+} $^5D_1$ levels with the europium concentration in Eu:YPO_4. Crystals with more than fifty percent of europium crystalize in the monozite structure.

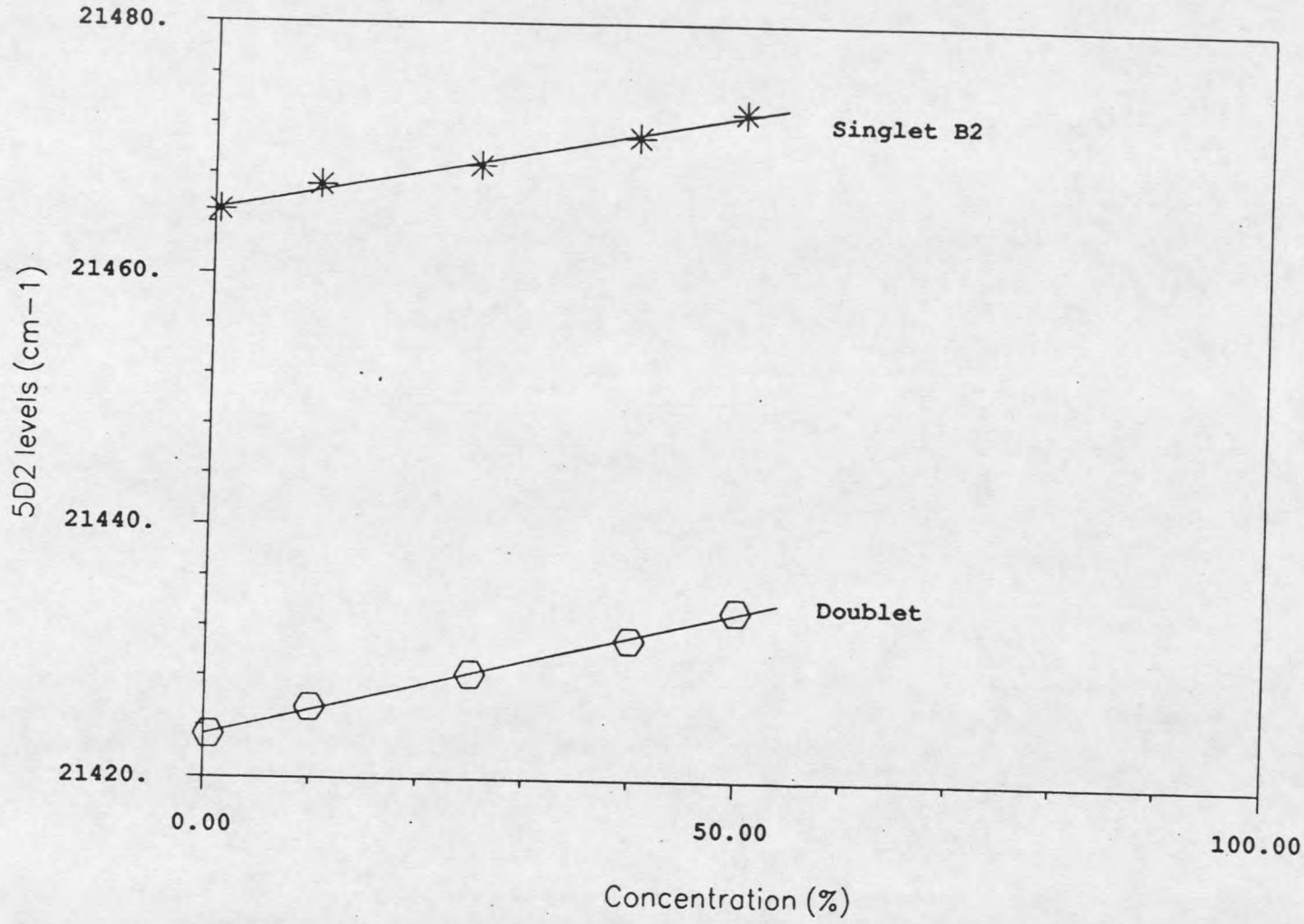

Figure 4.2 The variation of the Eu^{3+} $^5D_2$ levels with the europium concentration in Eu:YPO_4 .

As the Eu^{3+} ions are larger than Y^{3+} ions, the mixed lattices are larger than the real YPO_4 lattice. So the energy levels increase.

In all the cases discussed above, the dopant ions have larger ionic radii than the host ion, so the energy levels increase with the doping level. For the opposite case of La^{3+} compounds, we would expect the energy levels to shift down as the concentration gets higher.

Temperature Effect

When the temperature changes, the volume of the crystal changes, and so do the lattice constants. Due to the lattice changes, the energy levels vary. In most cases, the energy levels move up with temperature as would be expected. The energy levels of $EuVO_4$ and Eu^{3+}:YVO_4 listed in Appendix II certainly fit into this picture. The change for the ^5D_J levels from T = 1.5 K to room temperature is about 6~7 cm^{-1}.

Defect Site Fluorescence

Defect Site Fluorescence without Time Resolution

As mentioned in Chapter 2, when the $EuVO_4$ $^5D_2$ (Γ_5) level was excited, a very complicated spectrum was obtained in the $^5D_0$ - $^7F_1$ region. No obvious structure could be distinguished from the spectrum as a whole. The envelope of the observed lines also changed when the laser frequency was changed or when different crystals were used. The sensitivity of the defect spectra to the pumping frequency was probably due to the strong absorption and large linewidths of the defect $^5D_2$ levels, so when the frequency was changed, different defect sites might be excited directly within the intrinsic transition lineshape. Exciting the $^5D_1$ levels gave a cleaner fluorescence spectrum, but defect transitions could still be seen.

The exciton nature of the excitation played an important role in the fluorescence when the $^5D_2$ level was pumped. We showed in Chapter 2 that there were at least 50 different defect sites present in these $EuVO_4$ crystals. For intrinsic $^5D_2$ levels, only Γ_4 and Γ_5 could be excited directly, but neither of them was the lowest level in this manifold. The lowest level $^5D_2$ (Γ_3) was 35 cm^{-1} below Γ_5 - the lowest level with an allowed transition from the ground state. The excitation of the Γ_5 level moved through the crystal as an exciton. Because the exciton encompasses a large volume in the crystal, it may easily include a defect site, even when the defect number population is very small. But a defect site will act as a trap for the exciton; then the excitation cannot be treated as an exciton any more. When the defect has a lower energy than the intrinsic site, the transfer of energy from the exciton to the defect will be a favorable process. In $EuVO_4$ $^5D_2$, almost all defects have at least one energy level lower than the excitation because the excitation is not on the lowest level in that manifold. For that reason we see many defect lines, while the intrinsic fluorescence is totally buried.

Pumping $^5D_1$ gave a cleaner fluorescence spectrum in the $^5D_0$ - $^7F_1$ region; the intrinsic transition could be seen, although there were still defect fluorescence lines. This was due to the fact that the $^5D_1$ levels do not split very much and also the lowest level was excited directly. The defects may still act as traps, but the probability of transferring energy to the defect sites was much smaller than for $^5D_2$.

When the intrinsic $^5D_0$ level was pumped directly in a field, very clean spectra were obtained, especially in a strong field as shown in Chapter 2. This was due to the fact that most defect sites had higher energies than the intrinsic site. Even for the few sites that had lower energy, the energy difference was very small. The transfer of energy happened slowly enough that the intrinsic fluorescence was the main signal observed. There were some weak fluorescence lines around the intrinsic transitions, with their origins in the very few lower energy sites, as will be discussed below.

In the $^7F_0$ - $^5D_0$ defect spectra, the spectral lines can be classified into three categories: (a) the two groups of lines within 2 cm^{-1} each side of the intrinsic site transition at 17196.70 cm^{-1}; (b) all the lines that are higher than type a in energy; and (c) those lower than all above. There are very few lines in category c. Typical fluorescence spectra when these lines were pumped by a narrow band laser are given in Figure 4.3.

Spectrum (a) in this graph was obtained by cw pumping of line A of the growth A crystal at 515868 GHz. Two kinds of lines appear in this spectrum: the strong lines between 16820 cm^{-1} and 16840 cm^{-1}, and weak lines scattered over a wider region of 100 cm^{-1}.

Spectrum (b) is the fluorescence when the intrinsic $^7F_0$ - $^5D_0$ transition was pumped directly in a field of 55.0 kG along the *c* direction. Three strong lines were observed. The two lines at lower frequency were due to the split $^7F_1$ doublet. The upper line was the transition to the $^7F_1$ singlet. Extrapolating to zero field, the Γ_2 and Γ_5 levels were 10 cm^{-1} apart. When groups of lines immediately above the intrinsic transition were pumped, they gave three line patterns that usually fell between 16820 and 16840 cm^{-1} and were very close to the intrinsic fluorescence. When the group of lines immediately under the intrinsic transition were pumped, most of them gave three line fluorescence patterns similar to those in the upper group. However, a few of them gave complicated fluorescence patterns. One of them is shown as spectrum (c) in Figure 4.3; it was taken when the line at 515510 GHz was pumped. Pumping lines even lower in energy gave spectra similar to spectrum (c).

Time-resolved fluorescence

The many lines present in a $^5D_0$ - $^7F_1$ spectrum when one of the defect $^5D_0$ lines was pumped must be from multiple sites. Since only one site was pumped, other sites must have been receiving energy through a process called energy transfer or energy

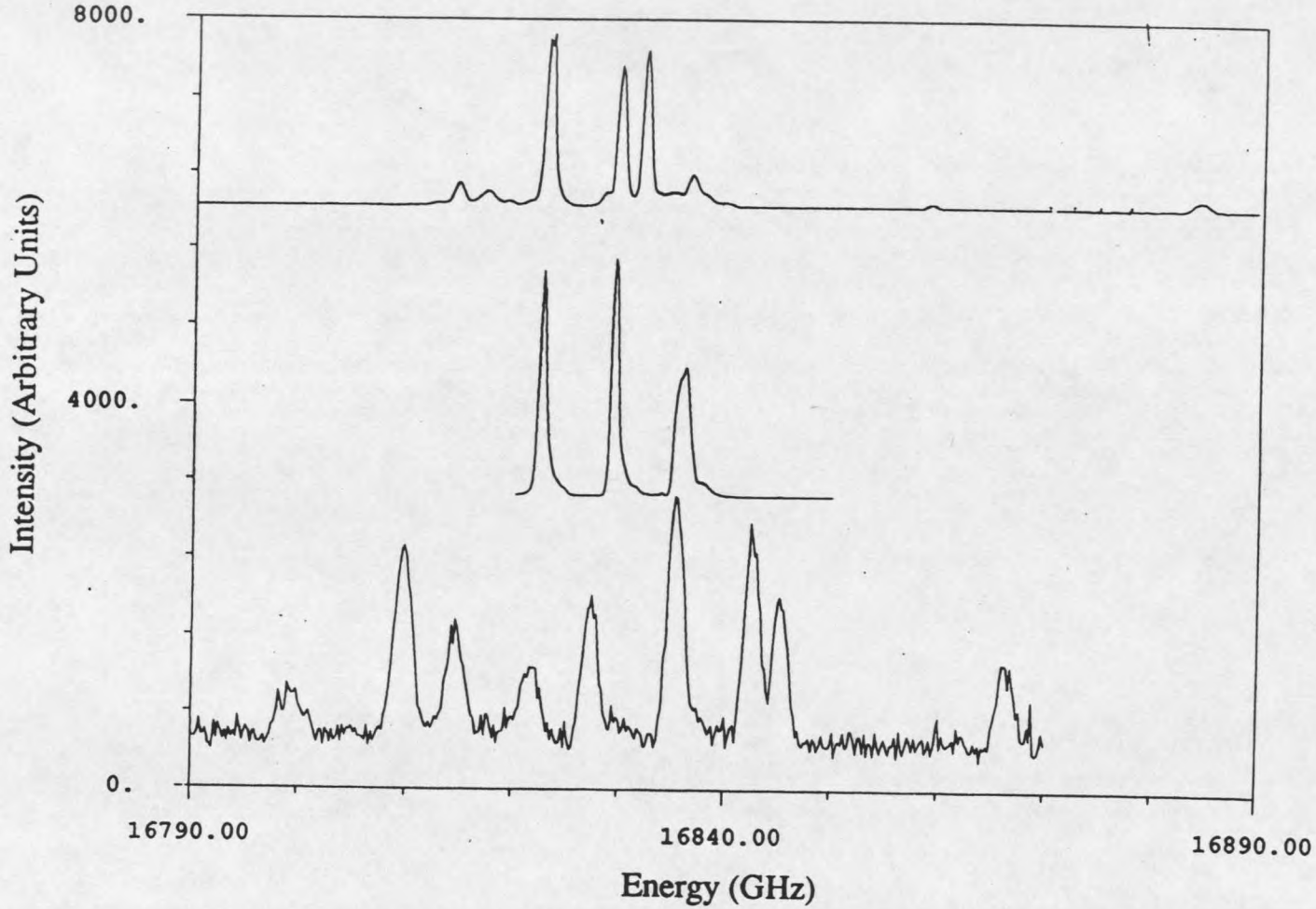

Figure 4.3 The $^5D_0$ - $^7F_1$ fluorescence spectra when different $^5D_0$ defect lines were excited. See text for details.

migration. To isolate the fluorescence from the site being pumped, time-resolved fluorescence was used. Figure 4.4 shows the time-resolved spectra when line A of growth A (515868 GHz) was pumped in $EuVO_4$. These spectra were taken with 50 μs gates using various delays. In the first 50 μs, two strong lines could be seen at the lower end and one at the upper end of the spectrum. Numerous small peaks were in the region between 16820 - 16840 cm^{-1}. In the second 50 μs, the strong peaks of the first 50 μs spectrum grew weaker while those weak lines in the first 50 μs became stronger. In the third and fourth 50 μs intervals, all the fluorescence peaks were decaying, but the originally strong peaks were decaying much faster. Measuring the decay constant showed that three lines marked "A" decayed with a lifetime shorter than 50 μs. Those lines between 16820 cm^{-1} and 16840 cm^{-1} decayed with a time constant of several hundred microseconds. It is obvious that those fast "A" lines came from the site being pumped and that the slow lines originated from the acceptor sites. Comparing these spectra with spectrum (a) in Figure 4.3 which was obtained by cw pumping of the same site, we can see that the site being pumped transferred at least 90% of its energy to other sites with a consequent reduction of its own fluorescent emission and its lifetime.

Figure 4.5 shows another example of the time-resolved spectra. The upper trace is the spectrum when the site at 515979 GHz was pumped cw, while the lower line is the fluorescence when only the first 10 μs was monitored. Even in the first 10 μs after the 5 ns excitation pulse, the acceptor site already had a fluorescence intensity comparable to that from the site that was pumped directly. In the cw-pumped spectrum, the fluorescence from the pumped site was almost unseen due to the rapid energy transfer. The time-resolved fluorescence spectrum was obtained by an total of 50 laser shots per point, averaging less than 1 photon per shot for the fluorescence of the site that was pumped.

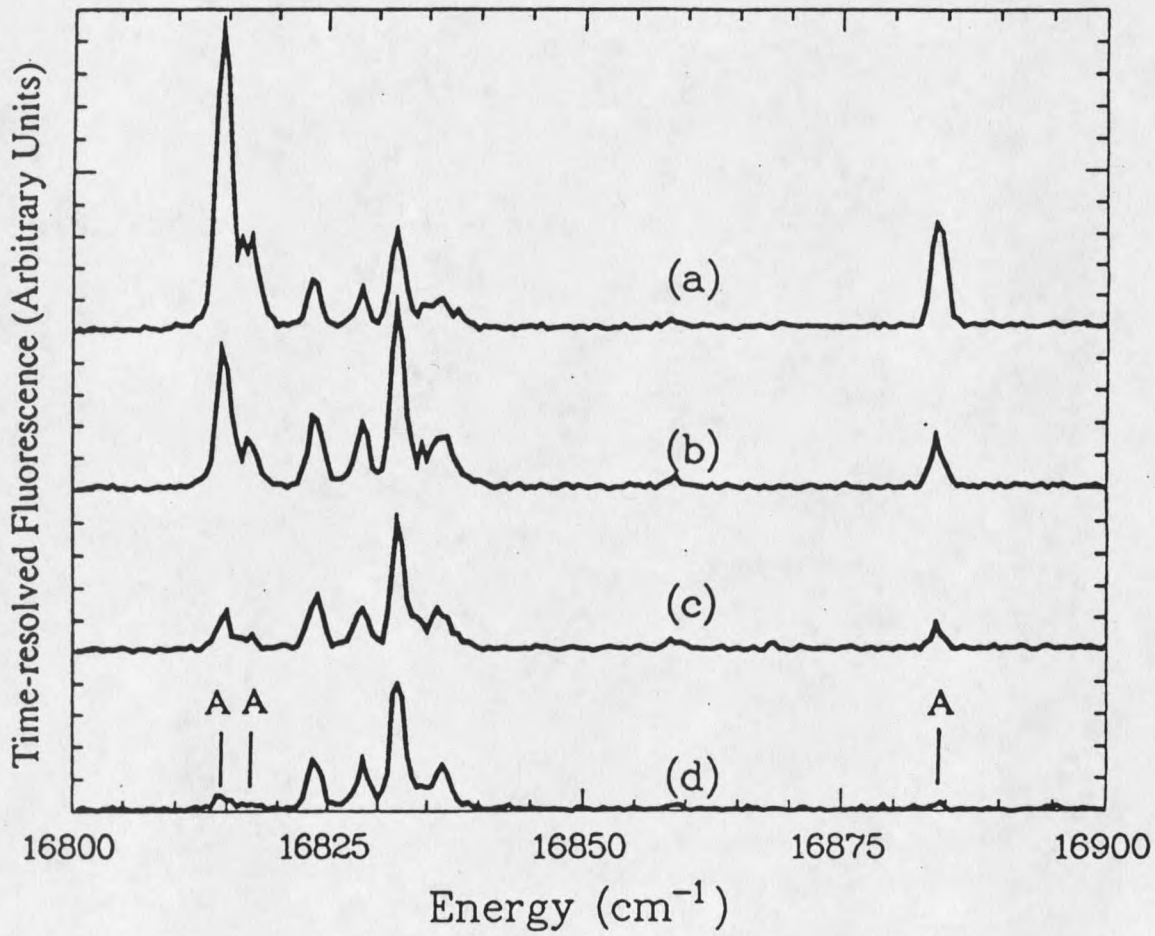

Figure 4.4 Time resolved $^5D_0$ - $^7F_1$ fluorescence spectra when pumping the 515868 GHz defect line in $EuVO_4$. Peaks labeled A originate from this site directly; all others from energy transfer. (a) the first 50 μs after the excitation, (b) the second 50 μs after the excitation, (c) the third 50 μs after the excitation, and (d) the fourth 50 μs after the excitation.

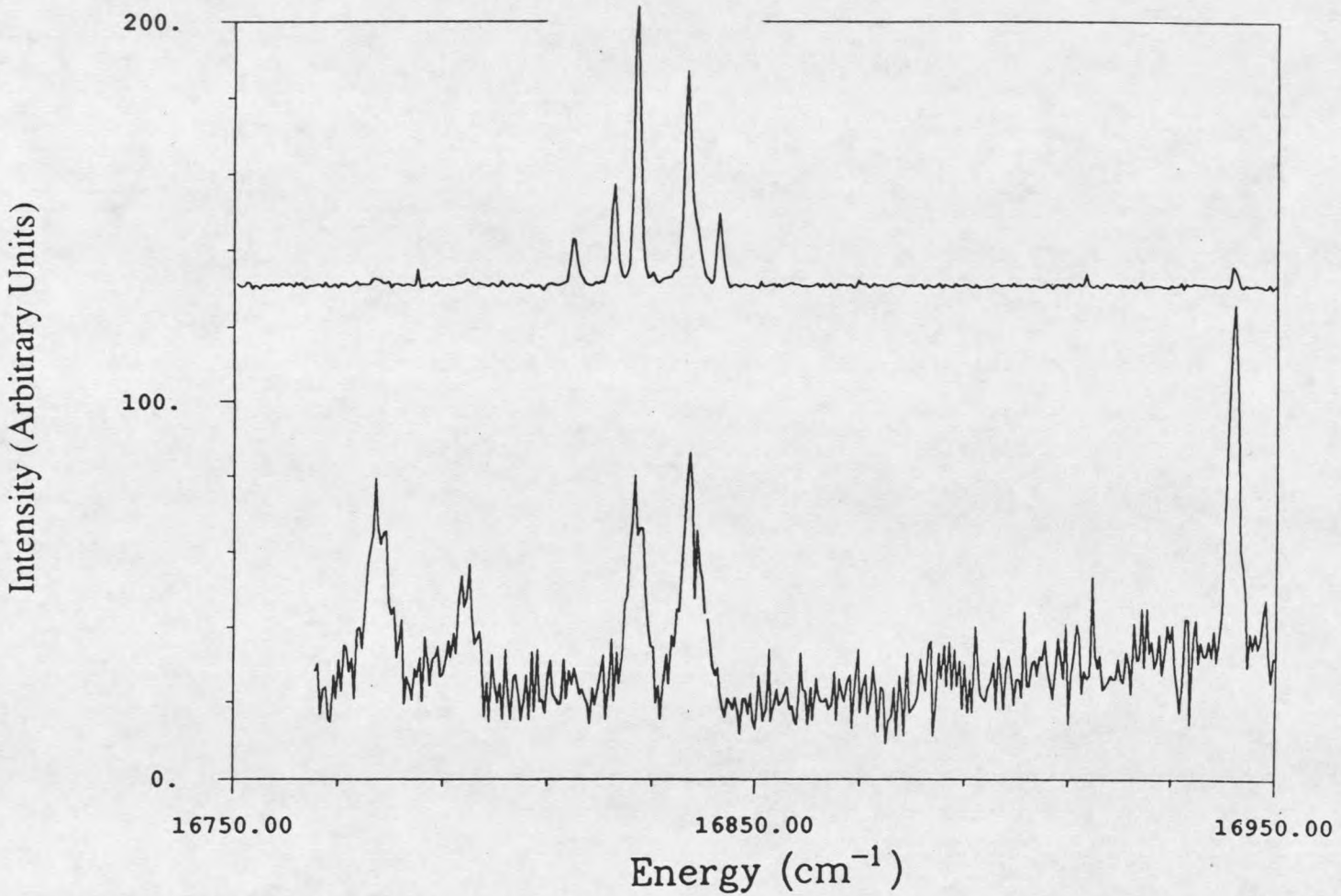

Figure 4.5 The $^5D_0$ - $^7F_1$ fluorescence spectra of the site at 515979 GHz in $EuVO_4$. The upper spectrum was taken when this was excited by a cw laser. The lower spectrum was taken within 10 μs after the excitation. The vertical scale is only for the time-resolved spectrum. The cw spectrum was scaled down to fit into the graph.

Discussion

From the time-resolved fluorescence spectra shown in Figure 4.4 and Figure 4.5 and others, we can see that when the higher energy lines were pumped, the fluorescence lines from the pumped site were usually widely spaced and were very weak or almost indiscernible in a spectrum recorded without time resolution. The fluorescence lines from the acceptor sites were usually strong and were in the region between 16820 to 16840 cm^{-1}, very close to the intrinsic site fluorescence lines.

From our discussions of the relation between the energy levels and the cell sizes, we can see that the higher energy lines must come from some sites that have smaller local dielectric constants. A vacancy will give such an environment, or an impurity with smaller ionic radius than Eu^{3+} may deform the lattice in such a way that the neighboring cells have larger than normal size or smaller than normal local dielectric constant. Due to this defect, the Eu^{3+} ions in neighboring cells will have higher energy than the intrinsic site. Those ions that are further away from this vacancy or impurity will have lower energy than those close to it, but still higher than the intrinsic site energy. The nearest neighbor ions are responsible for the lines that were classified as group B in the last section, while the next-nearest or more distant neighbors are responsible for the lines that constitute the upper half of group (a). One single lattice defect in the crystal can be responsible for more than one defect Eu^{3+} site.

On the other hand, if an interstitial ion is present in the lattice, the neighboring lattice will deform in such a way that the dielectric constant at the neighboring europium site is larger than the intrinsic site. It is common knowledge that an interstitial is more difficult to form than a vacancy, which is probably the reason that fewer defect lines were observed at the lower side of the intrinsic transition.

We noted in Chapter 1 that high pressure causes these crystals to undergo a phase transition to the more efficiently packed Scheelite structure (Jayaraman *et al* 1987). On releasing the pressure, the Scheelite structure is retained. It is possible that there might be some domains of this crystal structure that can cause some of the defect lines.

In the growth I $EuVO_4$ crystal, lines #39, #40, and #41 appear at 516389 GHz, 516415 GHz, and 516635 GHz. These are thought to be related to the presence of fluorine in the growing flux. If that is true, the fluorine ion may replace an oxygen ion in the VO_4^- tetrahedra and be charge compensated in some way or perhaps be correlated with divalent europium possibly present in the crystal. As discussed earlier in this chapter, there are large differences in the energy level baricenters for a fluoride crystal and oxide crystal. A fluoride lattice has much higher energy, which is probably the reason that these lines are at least 23 cm^{-1} higher than the intrinsic fluorescence.

Time-resolved fluorescence shows that when any of the higher energy sites were pumped, they tended to give energy to less distorted sites (with fluorescence lines in the narrow region close to the intrinsic site fluorescence). This suggests to the following migration route for excitation. Those sites that are nearest neighbors of a vacancy or of an impurity with smaller ionic radius than europium, have higher energies than the intrinsic site. They transfer their energy to the next-nearest neighbor sites that are even farther from the defect; these sites have lower energy. Depending on the specific site, the energy may or may not reach the intrinsic site before being lost to heat or radiative relaxation. The acceptor sites far enough from the defect have energy levels and local environments similar to that of the intrinsic site, and the fluorescence spectrum was also similar. They had very small overall splittings, corresponding to a small B_{20} with perhaps a small B_{22} being added.

For the defect sites lower than the intrinsic site in energy, the lattice defect's nearest neighbors have the lowest energy while the groups of lines just under the intrinsic

transition are due to the more distant neighbors. When the lattice defect's nearest neighbors were pumped, they could not transfer the energy away due to the unfavorable energy mismatch. But there might be other Eu^{3+} ions that were similar distances from the defect and had energies similar to or lower than the excited ion; transfer between these ions could occur.

When the lines close to the intrinsic line but below it were excited, some of them showed 3 line patterns close to the intrinsic site fluorescence, which was probably due to sites far from the lattice defect. Another possibility is that those lines are due to the nearest neighbors of impurities with ionic radii very similar to but slightly larger than europium. In this case, even the nearest neighbors are not distorted very much and they have similar but lower energies than the intrinsic site and similar $^5D_0$ - $^7F_1$ fluorescence patterns.

Spectrum (c) in Figure 4.3 apparently arose when a site more distant than the nearest neighbor of a defect was excited. The energy transferred to several more distorted sites that had widely spaced $^5D_0$ - $^7F_1$ fluorescence patterns. There were usually weak lines in the region between 16820 and 16840 cm^{-1}, just the opposite of the spectra represented by spectrum (a).

CHAPTER 5

SPECTRAL HOLEBURNING AND ODNMR

Holeburning experiments have been used for studying the hyperfine structures of rare earth ions since Erickson (1977a) demonstrated holeburning by optical pumping of the hyperfine levels of Pr^{3+}:LaF_3. Optically-detected nuclear-magnetic-resonance (ODNMR) was demonstrated on that system in the same year (Erickson, 1977b). The use of holeburning to investigate the defect sites in stoichiometric $EuVO_4$ started with Cone *et al.* (1984). Since the initial work on $EuVO_4$, holeburning and hyperfine interactions have played a central role in studying the defect structure in $EuVO_4$ and $EuAsO_4$. Robinson (1986) used holeburning to study the defect sites in $EuAsO_4$ and developed the method of using the Zeeman spectra with the magnetic field along the *c* and *a* directions to find the direction of the defect z-axis in the crystal coordinates. Lazzouni (1988) studied more defect sites in $EuVO_4$ by nuclear Zeeman holeburning with a focus on the high energy defect lines in the growth I crystals. Hansen (1990) studied the defect sites of many different growths of $EuVO_4$, using both holeburning and ODNMR. Some of his data will be discussed along with our results.

In this chapter, we first introduce the nuclear quadrupole Hamiltonian of an Eu^{3+} system. The holeburning and ODNMR mechanisms will be discussed after that. The experimental setup and zero-field ODNMR data will then be presented. Angle-dependent ODNMR will be the topic of Chapter 6.

The Nuclear Quadrupole Hamiltonian

General Treatment

We will follow Macfarlane and Shelby (1987) in the treatment of the general Hamiltonian. The Hamiltonian beyond the free-ion and crystal field contributions can be described as

$$H = H_{HF} + H_Q + H_Z + {}_z. \tag{5.1}$$

Included here are the magnetic hyperfine interaction, the nuclear quadrupole interaction, the electronic Zeeman interaction, and the nuclear Zeeman interaction. Explicitly,

$$H_{HF} = 2\,\mu_B \hbar \gamma_N \langle r^{-3} \rangle \mathbf{N} \cdot \mathbf{I}, \tag{5.2}$$

where $2\,\mu_B \langle r^{-3} \rangle \mathbf{N}$ is the field at the nucleus from the 4f electrons (Abragam and Bleaney, 1970), $\langle r^{-3} \rangle$ is the expectation value of the inverse cube electron-nuclear distance, γ_N is the nuclear gyromagnetic ratio, and μ_B is the Bohr magneton. Within one LSJ state

$$H_{HF} = A_J \mathbf{I} \cdot \mathbf{J} \tag{5.3}$$

where $A_J = 2\,\mu_B \hbar \gamma_N \langle r^{-3} \rangle \langle J \| N \| J \rangle$. (5.4)

The quadrupole interaction has the form

$$H_Q = P[(I_z'^2 - I(I+1)/3) + (\eta/3)(I_x'^2 - I_y'^2)], \tag{5.5}$$

where the prime is for the pure quadrupole interaction as opposed to the tensor Λ and its related pseudoquadrupole interaction as described below. The nuclear Zeeman interaction is

$$H_z = -\hbar \gamma_N \mathbf{H} \cdot \mathbf{I}, \tag{5.6}$$

and the electronic Zeeman interaction is given by

$$H_Z = g_J \mu_B \mathbf{H} \cdot \mathbf{J} \tag{5.7}$$

where g_J is the Landé g factor.

For an electronic singlet, especially for the J = 0 states in Eu^{3+}, H_{HF} and H_Z vanish in first order; the hyperfine and electronic Zeeman effect appear in the Hamiltonian in second order, and the Hamiltonian can be written as (Teplov, 1968)

$$H_{eff} = - g_J^2 \mu_B^2 \mathbf{H} \cdot \Lambda \cdot \mathbf{H} - (2 A_J g_J \mu_B \mathbf{H} \cdot \Lambda \cdot \mathbf{I} - H_Z) - (A_J \mathbf{I} \cdot \Lambda \cdot \mathbf{I} + H_Q)$$
$$= - g_J^2 \mu_B^2 \mathbf{H} \cdot \Lambda \cdot \mathbf{H} + H_Z' + H_Q' \qquad (5.8)$$

where the tensor

$$\Lambda_{ij} = \sum_n \frac{<0|J_i|n><n|J_j|0>}{E_n - E_0} \qquad (5.9)$$

with |0> being the level to which H_{eff} applies, |n> being the other crystal field levels. The effective nuclear Zeeman interaction will be

$$H_Z' = - \hbar [\gamma_x H_x I_x + \gamma_y I_y I_y + \gamma_z H_z I_z] \qquad (5.10)$$

and

$$\gamma_i = \gamma_N + 2 A_J g_J \mu_B A_J \Lambda_{ii} / \hbar . \qquad (5.11)$$

The term $A_J^2 \mathbf{I} \cdot \Lambda \cdot \mathbf{I}$ in H_Q' is the second order magnetic hyperfine interaction, or the pseudoquadrupole interaction (Baker and Bleaney, 1958). It can be written as

$$H_{pq} = D_{pq}[I_z^2 - I(I + 1)/3] + E_{pq} (I_x^2 - I_y^2) \qquad (5.12)$$

with

$$D_{pq} = A_J^2 [(\Lambda_{xx} + \Lambda_{yy})/2 - \Lambda_{zz}]$$

and

$$E_{pq} = A_J^2 (\Lambda_{yy} - \Lambda_{xx})/2. \qquad (5.13)$$

In combining the pseudoquadrupole and pure quadrupole into one effective Hamiltonian, one must bear in mind that the axes (x, y, z) of the Λ tensor and the axes (x', y', z') of H_Q may not coincide in low symmetry situations. Diagonalization of the two will result in some new principal axes x", y", and z". Now the effective Hamiltonian can be written as

$$H_Q' = D[I_{z''}^2 - I(I + 1)/3] + E_{pq} (I_{x''}^2 - I_{y''}^2) \qquad (5.14)$$

In Eu^{3+}, the pseudoquadrupole interaction is very small compared to the pure quadrupole interaction, so the principal axis directions of the effective Hamiltonian should be similar to the pure quadrupole interaction. We will use (x, y, z) to denote the principal axes of the total quadrupole interaction just for convenience.

Quadrupole Interaction

Eq. (5.5) may be rewritten as

$$H_Q = P[I_z^2 - I(I+1)/3 + \eta/3(I_x^2 - I_y^2)] \quad (5.15)$$

where P is the quadrupole interaction constant and η is the quadrupole asymmetry parameter. Or alternatively

$$H_Q = D[I_z^2 - I(I+1)/3] + E[(I_x^2 - I_y^2)] \quad (5.16)$$

Obviously, P = D, and η = 3E/D. A treatment of the quadrupole interaction from first principles can be found in Weissbluth (1978), Cone (1986), or Hansen (1990). An expression showing the relation of the quadrupole interaction with the electric field gradient (EFG) can be written as

$$H_Q = \frac{3eQ}{4I(2I-1)}[\langle V_{zz} \rangle (I_z^2 - \frac{I(I+1)}{3}) + \frac{\langle V_{xx} - V_{yy} \rangle}{3}(I_x^2 - I_y^2)] \quad (5.17)$$

with the EFG subject to $\nabla^2 V = 0$.

In Elliott's original work (1957), it was concluded that the main contribution to the ground state quadrupole interaction should come from the second order polarization of the 4f electrons due to the coupling of the ground state to the J = 2 states, and that the contributions from the lattice were small. Judd, Lovejoy, and Shirley (1962) modified this conclusion by realizing that the closed electron shell actually amplifies the field gradient of the lattice, the so-called Steinheimer anti-shielding. Later work by Edmonds (1963) and Blok and Shirley (1966) discussed the quadrupole and shielding effects of Eu^{3+} in the framework of rare earth ions in general.

The lattice contribution is given by

$$P_{latt} = -\frac{3Q(1-\gamma_\infty)B_{20}}{2I(2I-1)(1-\sigma_2)<r^2>_{4f}}, \qquad (5.18)$$

where Q is the quadrupole moment of the nucleus (0.95 barn for ^{151}Eu, and 2.42 barn for ^{153}Eu), γ_∞ is the antishielding factor which is normally around -80 for rare earths, and σ_2 is the associated shielding parameter for $<r^2>$ in a host. It is usually a function of the particular electronic states being considered, though mostly it is around 0.57. B_{20} is the crystal field parameter as defined in Chapter 2.

The electronic contribution from the second order mixing of the J = 2 and J = 0 states is given by (Hansen 1990, Cone 1986)

$$P_{4f} = \frac{3e^2QB_{20}}{2I(2I-1)}<r^{-3}>(1-R_Q)\frac{|<^7F_2|C_{20}|^7F_0>|^2}{E_{20}-E_{00}} \qquad (5.19)$$

where $(1-R_Q)$ is the shielding factor for $<r^{-3}>$. The matrix element $|<^7F_2|C_{20}|^7F_0>|$ = +0.10487 for the ^5D_J states using intermediate coupling (Erickson, 1986). It is 0.2309 for pure ^7F_J or 0.20242 for ^7F_J in intermediate coupling. Because of the difference in this parameter and the relative magnitude of $(E_{20} - E_{00})$ in ^5D_J and ^7F_J, this term is 16 times larger in $^7F_0$ than in $^5D_0$.

For the nonaxial component, in both the lattice and electronic contributions, we have (Cone, 1986)

$$\eta = \sqrt{6}\,B_{22}/B_{20} \qquad (5.20)$$

The pseudoquadrupole interaction is given by eq. (5.13). For a number of the defect sites, it makes a noticeable contribution.

Nuclear Magnetic Shielding

Elliott (1957) pointed out that the Eu^{3+} nucleus was almost totally shielded in the electronic ground state by the induced magnetic moments of the 4f electrons. The Eu^{3+} $^7F_1$ levels are only 300 - 400 cm^{-1} above the ground state. The admixture of these levels with the ground state results in a cancellation or "quenching" of the nuclear Zeeman interaction. If we consider eqs.(5.4) and (5.9) up to the J = 1 levels, and write the effective nuclear magnetic moment as $\mu_{eff} = (1-\alpha_i)\hbar I\gamma_N$, then

$$\alpha_i = \frac{-4\mu_B^2\langle r^{-3}\rangle\langle {}^7F_0|L_i + 2S_i|{}^7F_1(\Gamma)\rangle\langle {}^7F_1(\Gamma)|N_i|{}^7F_0\rangle}{\Delta_\Gamma}. \tag{5.21}$$

where Γ is the symmetry of the $^7F_1$ level to which the ground state couples when the magnetic field is along the *i* direction. Δ_Γ is the energy of the Γ symmetry component of $^7F_1$. Without J mixing

$$\alpha_i = 40\ \mu_B^2 \langle r^{-3}\rangle/3\Delta_\Gamma \tag{5.22}$$

Δ_Γ is in cm^{-1}, and $\langle r^{-3}\rangle = 49.6$ $Å^{-3}$ for Eu^{3+}, so that

$$\alpha_i = 290/\Delta_\Gamma \tag{5.23}$$

or,

$$\sum 1/\alpha_i = \sum \Delta_\Gamma/290 \approx 3.77 \text{ to } 3.93,$$

assuming the baricenter for $^7F_1$ is 365 - 380 cm^{-1}. At low symmetry, for a certain direction *i* that is the principal direction for the tensor $\underline{\alpha}$, Γ may not be unique, we should consider all the $^7F_1$ levels that can couple to the ground state when the magnetic field is along *i*. But the sum $\sum 1/\alpha_i$ should still be close to 4.

The Holeburning Process

Basic Mechanism

In trivalent rare earth ions, the most common holeburning mechanism is through the optical pumping of the nuclear hyperfine level reservoir via fluorescence branching between different hyperfine levels (Erickson, 1977), though in some cases the reservoir could be superhyperfine or transferred hyperfine (Macfarlane *et al.* 1981, G.K Liu 1988, Manson *et al*, 1992). In Eu^{3+}, the nucleus has a spin of 5/2, so at zero field there are three Kramers doublet hyperfine levels associated with each electronic state. The quadupole splittings of Eu^{3+} are normally tens of megahertz. The optical transition linewidth due to inhomogeneous broadening is several Ghz. At low temperature, the phonon contribution to the homogeneous linewidth is negligible, so the homogeneous linewidth is smaller than the hyperfine splittings. A narrow band (1~2 MHz) laser only excites one transition between the ground state and the excited state hyperfine levels for one subset of ions that have similar environments. When the ions relax back from the excited state, they do not always come back to the original hyperfine level. Those that do come back will be excited again and have another chance for branching. This is called optical pumping. The holeburning process for one such subset of ions is shown in Figure 5.1. Because of the long spin-lattice relaxation time, the optically pumped hyperfine level will have a depleted population, while the other two levels will have excess population. When a weak laser is used to probe the vicinity of the original laser frequency, no absorption occurs at the frequencies corresponding to the transitions originating from the depleted level. Spectral holes are said to be burnt. At the frequencies corresponding to transitions originating from the hyperfine levels with excess population, stronger than normal absorption will result in the so-called antiholes. The

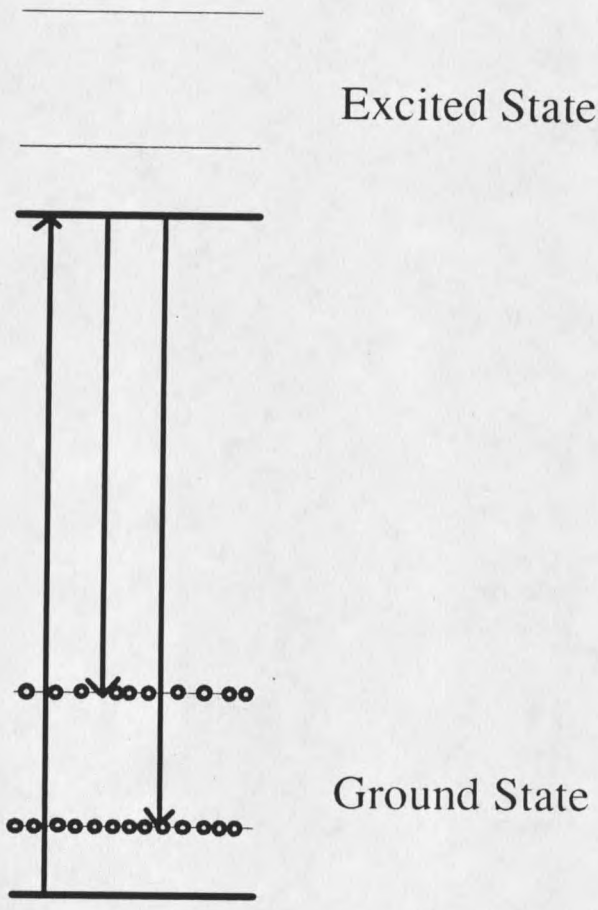

Figure 5.1 The holeburning process for an I = 5/2 system with singlet electronic states. Only one subset of ions is shown. The laser frequency corresponds to the energy between the highlighted excited state and ground state levels. Because of the long spin-lattice relaxation time and optical fluorescence branching, the highlighted ground state hyperfine level population gets depleted. The other two have excess population. Transitions starting from the highlighted level will have holes. Those from the other two levels will exhibit antiholes.

relative strength of the holes and antiholes depend totally on the degree of admixtures of the nuclear spin $|I_z>$ states. The long lifetime of the hole (minutes to hours) makes it easy to record the holeburning spectrum and makes holeburning an extremely useful technique to study the hyperfine structure, especially the excited state structure which is difficult to obtain by other techniques.

In the Eu^{3+} compounds studied so far, the inhomogeneous linewidth is broader than the homogeneous linewidth and the nuclear hyperfine splittings by several orders of magnitude, so more than one subset of ions will be excited by a single laser frequency. For an I = 5/2 system, actually 9 subsets of ions will be excited. A detailed discussion of all the possible transitions and hole patterns can be found in Macfarlane and Shelby's review article (1987). The conclusion is: there will be seven holes in a holeburning spectrum - one main hole and three auxiliary holes (side-holes) on each side of the main hole. The frequency differences between the side-holes and the main hole correspond to the hyperfine splittings of the excited state. There also will be 42 antiholes - 21 on each side of the main hole, or 6 around each hole (main hole or side-hole). The frequency differences between these antiholes and their related hole correspond to the ground state hyperfine splittings.

There are two naturally stable isotopes of europium (^{151}Eu, ^{153}Eu), with roughly equal abundance (47.82%, 52.12%, respectively). Their nuclear quadrupole moments and nuclear magnetic moments differ, so that each of these isotopes will display a distinct hole and antihole pattern, resulting in a total of 6 side-holes and 42 anti-holes on *each side* of the main hole, though the number observed may be much fewer due to accidental degeneracy and hole-antihole cancellations.

Axial Sites

Sites with axial symmetry are characterized by essentially pure $|I_z>$ nuclear eigenstates, where $I_z = \pm 1/2, \pm 3/2, \pm 5/2$ for $I = 5/2$. For such a site, the fluorescence branching and the corresponding holeburning process are either forbidden or very slow. Even if fluorescence branching or some other process makes holeburning possible (see the discussion about the energy-transfer enhanced holeburning later in this chapter), and population depletion occurs to a degree, the strongest transitions are still $\Delta I_z = 0$, so very weak side holes or no side holes should be observed in a holeburning spectrum. For antiholes, because of the $\Delta I_z = 0$ nature of the transitions, we will see only the differences between the ground state and the excited state splittings. Thus in practice, there are usually only 6 antiholes, 3 on each side of the main hole for one isotope. If the excited and ground state splittings are similar and of the same sign, the antiholes on each side of the main hole may not be resolvable, so that only two unresolved groups of antiholes will appear in the spectrum. This kind of holeburning spectrum was observed for many of the defect sites close to the intrinsic site in energy in $EuVO_4$ and provides important evidence that they are nearly axial. Silversmith and Macfarlane's holeburning study of Eu^{3+} ions at the C_{4v} centers in the fluorides gave other examples of well resolved spectra for these sites (Silversmith and Macfarlane 1992).

Non-axial Sites

For ions at non-axial sites, the different nuclear hyperfine levels involve appreciable admixtures of the nuclear $|I_z>$ spin states. For these sites, almost any optical transition between the ground state and excited state hyperfine levels is consistent with the selection rule $\Delta I_z = 0$. There will be strong side holes and numerous antiholes. The most typical of these for $EuVO_4$ can be found in Cone *et al.* (1984) and Cone *et al.*

(1988). The compounds $Eu^{3+}:Y_2SiO_5$ (Yano *et al* 1991) and $Eu^{3+}:YAlO_3$ (Shelby and Macfarlane 1981) also showed similar looking spectra.

The holeburning spectrum of a nonaxial site provides a good method to determine the excited state hyperfine splittings, but it is generally more difficult to determine the ground state splittings from the antihole patterns because of the large number of antiholes and the many different possible transitions to which they could be assigned. Unresolved antiholes or cancellations of side-hole and antihole due to accidental degeneracy can also confuse the picture. Fortunately, the technique of optically-detected nuclear-magnetic-resonance (ODNMR) provides a complementary method to holeburning experiments and makes unambiguous identifications of the ground state splittings or even the excited state splittings.

Optically-Detected Nuclear-Magnetic-Resonance (ODNMR)

The ODNMR technique takes advantage of the high sensitivity of optical spectroscopy and the accuracy of RF techniques to measure the nuclear hyperfine splittings. Its accuracy is limited only by the inhomogeneous linewidth of the nuclear transition or the linewidth of the RF source, but not by the laser frequency jitter, so it can make the determination of the hyperfine splittings at least an order of magnitude more precisely than holeburning.

The basic mechanism for ODNMR starts with holeburning. First we burn a hole at a fixed frequency, so one of the nuclear levels will have a depleted population due to the holeburning process. An RF magnetic field is then applied to the sample. When the RF frequency is in resonance with a nuclear transition, it modifies the level populations, and the degree of holeburning will change. If this is a *ground* state resonance, because of the transition, the depleted hyperfine level gains population from other levels, and this results in a decrease in the hole depth or an increase in the absorption and fluorescence signal.

If this is an *excited* state resonance, it results in stronger branching of the hyperfine transitions, an increase of the holeburning signal, and a decrease of the absorption or fluorescence signal. Figure 5.2 is an example of an ODNMR spectrum showing both the ground state and excited state resonances. This spectrum was taken when holeburning line Q of the growth A $EuVO_4$ crystal at 515554 GHz. It has slow but steady holeburning. During the experiment, the holeburning was kept at about 80% depth of the original excitation profile. Because of the slow holeburning process, it takes about a minute to burn to this depth. The slow holeburning also accounts for the asymmetric lineshape. More detailed discussion of this spectrum is given in section 5.4.

Excited state resonances are generally more difficult to observe than the ground state resonances since extra care is required to control the degree of holeburning in the experimental conditions. If the holeburning is already to the baseline, then the faster fluorescence branching is not going to show any signal.

Experimental Setup

The holeburning experiments were carried out the same way as described in Otteson's thesis (1984), the only difference being the use of a newer computer (Microvax II) instead of the PDP-11 used in that work. The A/D converters were the same. Experimental timing was controlled by the real-time clock in the present work. A hole was burnt by fixing the laser frequency. The hole pattern was probed by lowering the laser power through the A/O modulator and scanning the laser frequency across the region of interest. Absorption was too weak to observe directly for any of the defect sites in $EuVO_4$. The holeburning spectrum was monitored via fluorescence; an optical fiber bundle was used to collect the fluorescent light from the side of the crystal at 90

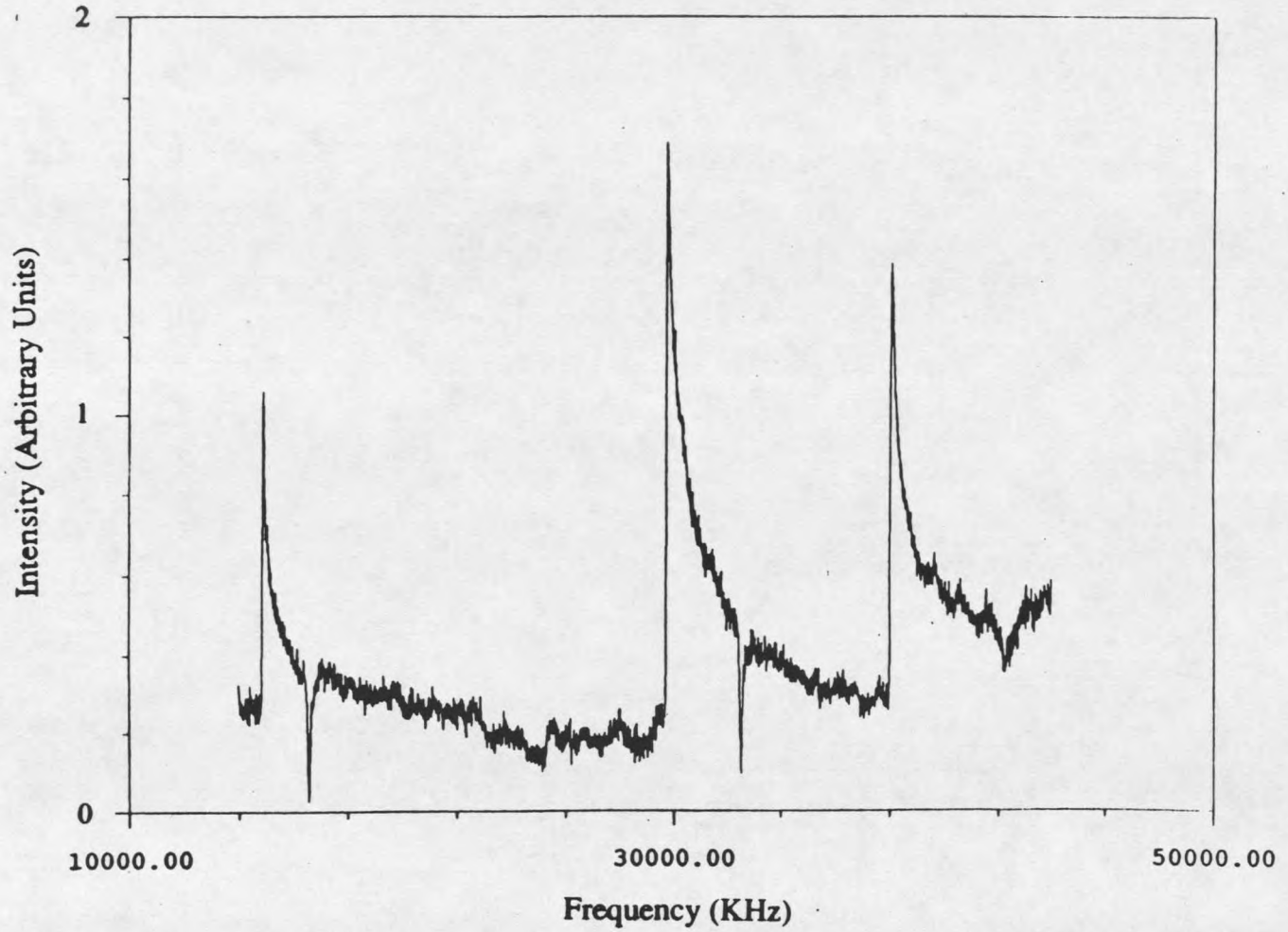

Figure 5.2 Zero field ODNMR spectrum for line Q of the growth A $EuVO_4$ crystal, showing large signals due to ground state resonances and smaller signals of opposite polarity due to excited state resonances.

degrees to the incident laser direction. This burn-and-read cycle was repeated until the desired signal to noise ratio was obtained.

For the ODNMR experiments, a 5-turn coil with approximately 5 mm diameter made of 20 AWG or 22 AWG magnet wire was used. The coil was connected to the center conductors of the incoming and outgoing coaxial cables carrying the RF. Capacitors were used between each turn of the coil and the ground of the coax. The design priority was to match capacitors with the coil inductance so that the coil acted like a transmission line for all frequencies. Theoretically the match required C = 11 pf, but it was found that capacitors from 11 pf to 22 pf all worked well in the frequency range of 5 MHz to 80 MHz.

The zero field experiments were carried out in a transverse-access glass cryostat. Signal detection was the same as in the holeburning experiments. A block diagram of the experimental setup is shown in Figure 5.3. A 514.5 nm Ar^+ laser was used to pump the Coherent 599/21 dye laser. The dye laser beam was tuned to the right wavelength (measured by the wavemeter, Appendix I) and sent to the sample, site-selectively exciting an optical transition and causing holeburning. The fluorescence was picked up by an optical fiber bundle and sent to the MacPherson 218 monochromator to filter out the background light. The monochromator was tuned to the $^5D_0$ - $^7F_2$ wavelength. A stack of 3-66 Corning glass filters were placed between the fiber and the monochromator slit to prevent the stray laser beam from overwhelming the signal even after the monochromator discrimination. The signal was then amplified by a Tektronix 7A22 amplifier and sent to the A/D converter for data acquisition. The computer-controlled PTS500 radio frequency (RF) synthesizer output was sent to the coil after being amplified by the ENI 411LA RF power amplifier. After going through the coil, the RF power was dumped into a 50 Ω dummy load immersed in an oil bath; the 50 Ω load was important for the RF circuit to act as a transmission line. The RF was tuned to a specific

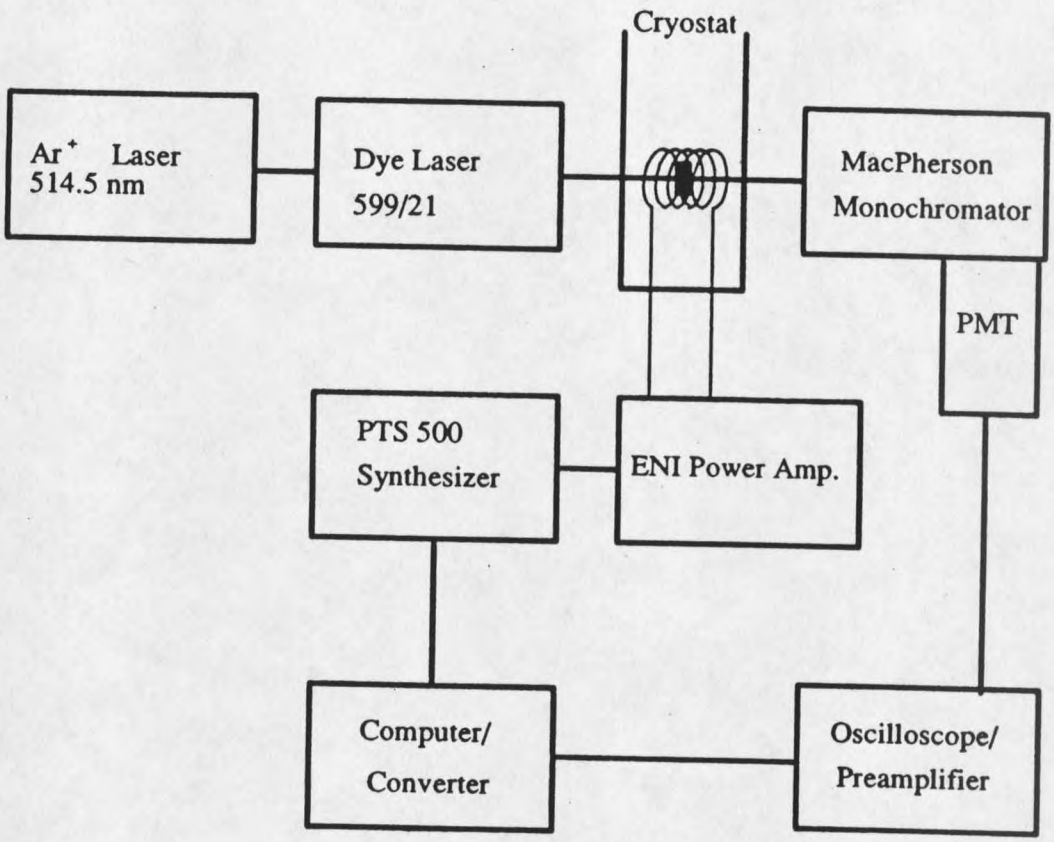

Figure 5.3 Block diagram of the ODNMR experimental setup.

frequency, then the fluorescence intensity was recorded with 200 samples of the signal made during a time interval of about 17 ms - the period of the power line frequency. When the RF was tuned to a new frequency, the fluorescence intensity was recorded again.

Even when the laser frequency was supposed to be fixed, the 599/21 dye laser scan control box still generated weak scan drive signals. Although they were not applied to the dye laser directly, they still caused laser frequency drift synchronized with the scan drive frequency. The scanning was adjusted to the lowest rate (T = 625 sec) to minimize the influence of this noise during experiments.

Zero Field Results

Zero field experiments were carried out with the RF field applied along either the *a*-axis or the *c*-axis. When along *a*, the RF field induces $\Delta I_z = \pm 1$ transitions. It will induce only $\Delta I_z = 0$ transitions when along the *c*-axis. For the very low symmetry sites that we studied, none of the nuclear levels was a pure spin state anymore, so most of the transitions could be observed in both geometries.

The growth A crystal was studied with the RF field along the *a*-axis. The results are summarized in Table 5.1. The ORNL crystal was studied with the RF field along the *c*-axis. The results are summarized in Table 5.2. The quadrupole parameters were calculated using the algorithm laid out in Lazzouni (1988) Chapter 9 and Hansen (1990) Chapter 7.

Figure 5.2 showed a typical ODNMR data set. This spectrum was taken on line Q of the growth A crystal. The upward peaks indicate stronger fluorescence (and absorption) due to the ground state resonances, while those toward smaller intensities are due to the excited state resonances. The resonances due to the two different

Table 5.1 $^7F_0$ ODNMR peaks and quadrupole parameters for defect sites of the growth A crystal of $EuVO_4$.

Line#	λ meter reading	Freq. (GHz)	ODNMR peaks (MHz) ^{151}Eu & ^{153} Eu	|P| (MHz)	η	Line# in ORNL crystal
E	1.08967	516081	14.08 23.81 37.88 36.08 61.66	6.12 15.82	0.386 0.371	50
D	1.089454	515979	15.84 26.32 42.16 39.86 66.24	6.784 17.07	0.408 0.408	48
C	1.08939	515948	19.74 21.61 41.35 49.45 55.87	6.02 15.47	0.891 0.854	
B	1.08928	515896	15.36 27.73 39.44 71.41	7.05 18.14	0.293 0.289	
A	1.089220	515868	13.53 24.08 37.66 34.76 60.93	6.135 15.56	0.315 0.337	39
F	1.08911	515816	15.78 25.21 41.00 39.86 64.68	6.543 16.74	0.457 0.438	34
G	1.08910	515811	15.97 26.22 42.07 40.36 67.44	6.772 17.37	0.423 0.401	33
H	1.08896	515745	14.62 26.38 41.01 37.62 67.93	6.70 17.26	0.294 0.293	
I	1.08895	515740	14.90 22.47 37.44 37.99 57.80	5.89 15.13	0.526 0.516	
K	1.08885	515693	15.08 26.85 41.95 38.68 68.24	6.84 17.41	0.314 0.328	
L	1.08884	515688	14.27 28.55 36.44	7.13	0.00	
M	1.08878	515658	13.75 15.96 29.72 35.23 40.14	4.396 11.09	0.823 0.844	28
O	1.088594	515571	16.13 32.25 41.28	8.06	0.00	
Q	1.088556	515554	14.90 29.80 38.06 {16.56 32.56 42.22} Resonances for $^5D_0$	7.45 19.03 8.162	0.00 0 0.115	
X	1.088455	515505	29.33 30.84 37.97	???		
Z	1.088394	515477	14.76 29.50 37.72 75.34	7.38 18.84	0.00 0.03	

Table 5.2 $^7F_0$ ODNMR peaks and quadrupole parameters for defect sites in the ORNL crystal of $EuVO_4$. The experiments were done with the RF field along the *c*-axis. This geometry forbids any transition for the axial sites and is the reason that no resonance was observed in this geometry for the sites close to the intrinsic site in energy. Line 11 and line 15 were measured with the RF field along the *a*-axis.

line#	λ meter reading	freq. (GHz)	ODNMR peaks ^{151}Eu &^{153}Eu (MHz)	|P| (MHz)	η	line# in growth A
11	1.088485	515520	10.77 21.52 27.15 54.28	5.381 13.57	0.027 0.017	
15	1.088556	515554	14.90 29.80 38.06	7.45 19.03	0.00	Q
19	1.088624	515586	15.74 17.65 40.11	4.894	0.8629	
22	1.088705	515624	17.305 43.79 30.99 48.29	7.887	0.3056	
23	1.088722	515632	15.91 31.30 47.20	7.846	0.113	
28	1.088795	515667	13.79 16.00	4.407	0.823	M
29	1.088847	515691	15.77 28.20 43.95 39.16	7.177	0.308	
30	1.088875	515705	23.07 33.16 56.20 58.51 83.91	8.771 22.205	0.581 0.5836	
32	1.089023	515775	18.500 25.23 43.68 48.95 65.158	6.739 17.48	0.6405 0.6677	
33	1.089090	515806	15.83 26.17	6.7518	0.4150	G
34	1.089097	515810	15.743 25.207	6.5397	0.4548	F
39	1.089220	515868	13.55 24.11 37.65 34.79 60.96	6.1429 15.57	0.3152 0.3374	A
48	1.089454	515979	15.85 26.34	6.7895	0.4084	D
49	1.089510	516005	15.66 16.20 31.88 39.85 41.66 81.57	4.562 11.71	0.9585 0.9458	
50	1.089676	516084	14.07 23.80 37.90 36.11 61.71	6.117 15.83	0.3855 0.3719	E

isotopes can be identified by the quadrupole moment ratio since the resonances of ^{153}Eu should be about 2.55 times as high in frequency as the resonances of ^{151}Eu. Because of the pseudoquadrupole effect, this ratio may not always be the same for different defect lines, but the discrepancy should be small.

The absorption lineshape is clearly asymmetric, with long quasi-exponential tails on the high frequency side of the resonances. This is due to the experimental procedure rather than the characteristics of the hyperfine interaction. A separate series of experiments established that the direction of the frequency sweep determines whether the quasi-exponential tail is to the low or high frequency compared to the peak (absorption) frequency (Hansen 1990, Cone *et al.* 1993). In Figure 5.2, the sweep was from low to high frequency, and the explanation for this asymmetry is as follows: After the resonance, the holeburning takes time to burn back to its original depth, the time it takes depending on the holeburning rate. Even when the RF is tuned off any resonance, the signal still remains stronger for some time interval than the original holeburned fluorescence.

Figure 5.4 is an example of the real lineshape of a nuclear transition. It was taken with 2 KHz steps for the ^{151}Eu "1/2 - 3/2" transition for line D of growth A $EuVO_4$. It was obtained by turning on the RF, taking data, then turning off the RF and waiting for the holeburning to reach its original depth. Data acquisition was then resumed. It was very similar to the "smash and grab" method described in Cone *et al.* (1992) and Hansen's thesis. Since this way of data acquisition takes much more time but is no more accurate than the tailed data, we took data with the tails in real experiments and used the frequency of the peaks. For most sites that holeburnt easily, the tails were not very long. Figure 5.2 was just an extreme case due to the slow holeburning for this site.

The defect lines at the higher energy side of the $^7F_0$ - $^5D_0$ defect spectrum generally burn very easily, while lines close to the intrinsic site transition are difficult to burn.

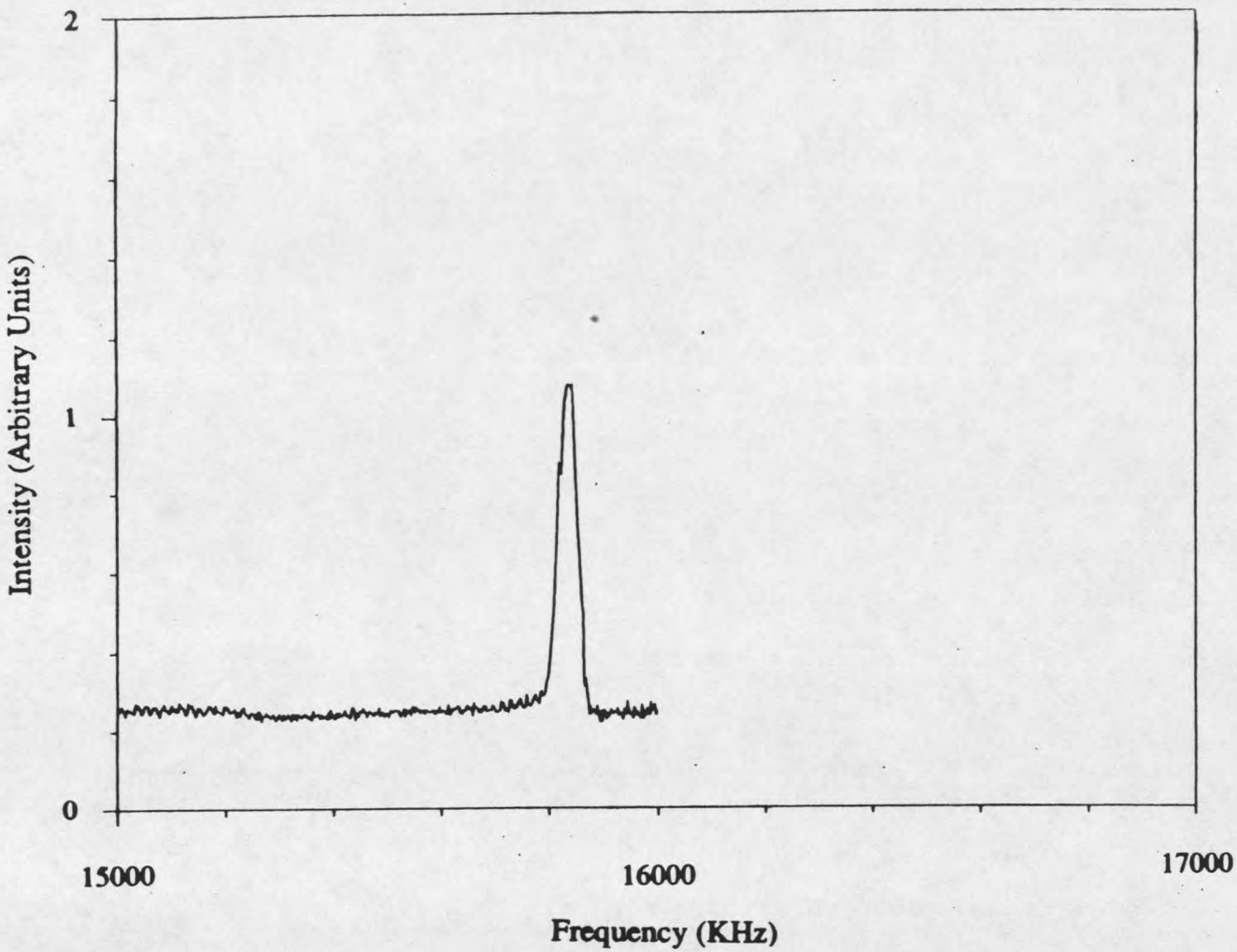

Figure 5.4 Inhomogeneous lineshape of the ^{151}Eu "1/2 to 3/2" nuclear hyperfine transition for line D in the growth A $EuVO_4$ crystal.

Since fluorescence branching causes holeburning, lack of holeburning means that very little or no branching occurs for the sites close to the intrinsic site in energy and that those sites have axial-like nuclear states. For the sites that did show some holeburning, like those corresponding to lines L, O, Q, and Z in the growth A crystal, and lines 11 and 15 in the ORNL crystal (see Table 5.1 and 5.2 for line positions), the asymmetry parameter η was zero within experimental error. We expect that those lines that did not show holeburning at all have more exact axial quadrupole parameters and very small P's. As an example of intrinsic site holeburning and long hole lifetime, we show in Figure 5.5 the excitation spectrum of the intrinsic $^7F_0$ - $^5D_0$ transition for Eu^{3+}:YPO_4 in a field of 55 kG along the *c*-axis. The magnetic field makes the $^7F_0$-$^5D_0$ transition weakly allowed. This line showed very weak holeburning, but once the hole was burnt, it would stay for a long time. No ODNMR was attempted on this crystal. In this spectrum four spectral holes were seen; each one was burnt with the laser sitting at one frequency for several minutes. The last hole was burnt about a hour after the first, but no obvious difference in the hole depth can be observed among them. The magnetic field was maintained at 55 kG in this time interval.

Many defect lines in $EuVO_4$ were found to have exactly the same energy in crystals of different growths. They are almost certainly due to the same kind of defects, since in much greater detail, they also exhibit exactly the same ODNMR patterns. Identical spectra were obtained for lines E and 50, for lines D and 48, for lines A and 39, for lines F and 34, for lines G and 33, for lines M and 28, and for line Q and 15. The lines labeled with a letter were for the growth A crystal, while those labeled by a number were for the ORNL crystal (see tables 5.1 and 5.2 for positions). This suggests that when particular statements are made for these defect lines, such as the relationship between the optical transition energy and crystal field and the quadrupole parameters, there is no need to

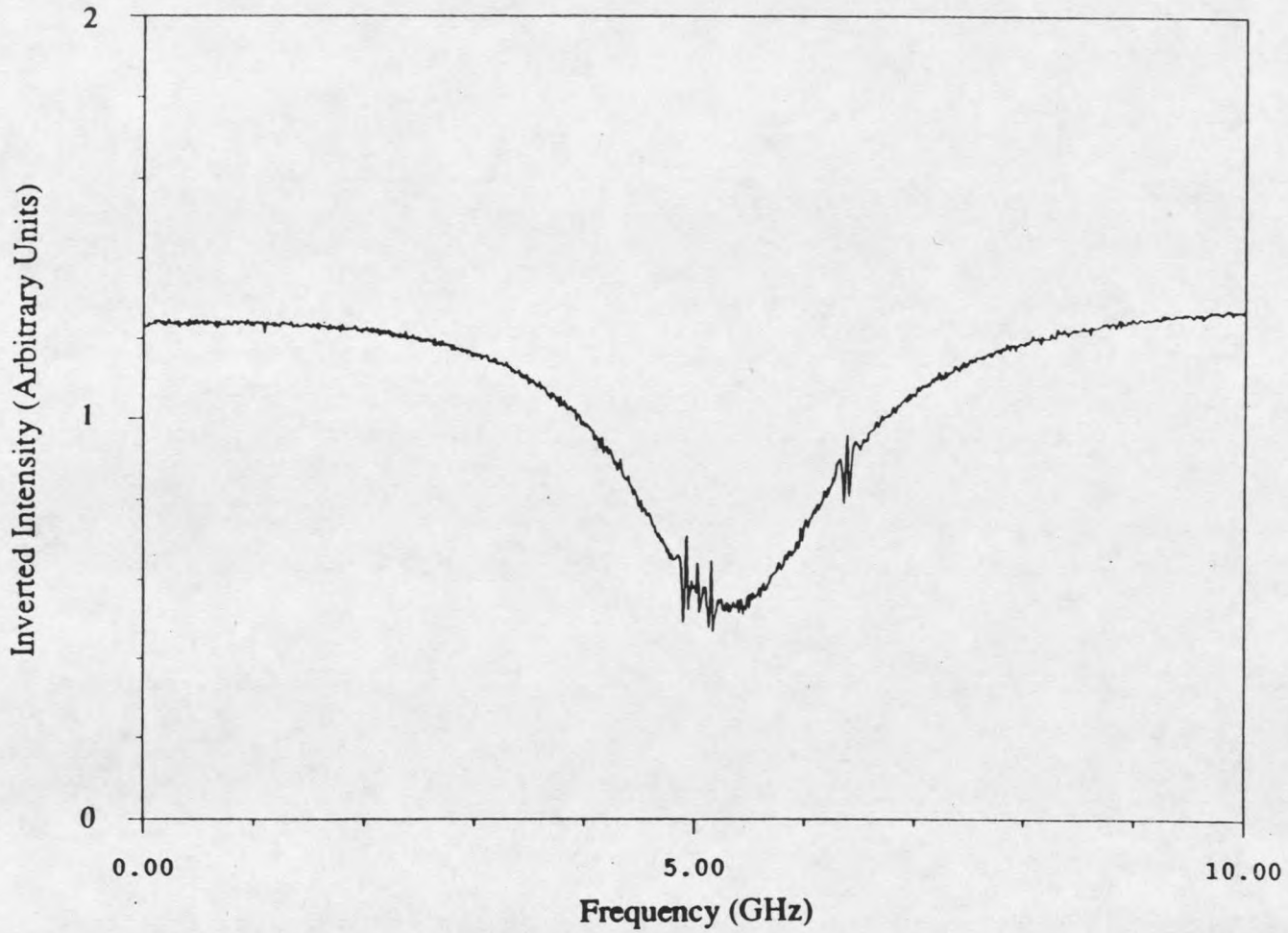

Figure 5.5 Excitation profile of the $^7F_0$ - $^5D_0$ intrinsic transition for 0.5%Eu^{3+}:YPO_4, in a magnetic field of 55 kG, showing long-lived holes in the intrinsic transition.

make separate statements for different crystals, but on the other hand, the dynamics might be different for the same site in different crystals due to different site abundances.

In different growths of crystals, defect lines from different origins might have the same energy accidentally. Line 29 in the ORNL crystal and line K in the growth A crystal are within 2 GHz in energy, close to the resolution of the wavemeter and comparable to the inhomogeneous transition linewidth, but they have different ODNMR spectra, indicating different origins. This dramatically testifies to the sensitivity of this technique.

Different crystals showed different inhomogeneous nuclear transition linewidths which were themselves transition frequency dependent. For example, the "1/2-3/2" transitions had smaller linewidths than the "3/2-5/2" transitions, and the ^{151}Eu transitions had smaller linewidths than the ^{153}Eu transitions. For the ^{151}Eu "1/2-3/2" transition, the FWHM linewidth was 40 KHz for the growth A crystal, 80 KHz for the ORNL crystals, and 100 KHz for the growth I crystals. They seemed to be related to the optical inhomogeneous linewidths. The typical $^7F_0$ - $^5D_0$ defect transition linewidths were < 1 GHz for the growth A crystal, 2 GHz for the ORNL crystal, and > 5 GHz for the growth I crystal.

The linewidth of the nuclear transition limits the effectiveness of the Zeeman experiments since splittings on this order may not be resolvable. That was why we did our experiments on the growth A crystal as often as possible. The *a-a'* plane data described in Chapter 6 were all taken on the ORNL crystals. The growth I crystal was used to study the high energy lines that were thought to be related to the fluorine presence in the crystal growing flux. The Zeeman experiments will be discussed in Chapter 6.

We wish to point out that the interpretation of the spectrum of line D (Line #44 in Growth A as Hansen (1990) called it) was different from that of Hansen's thesis. For

this line, ODNMR peaks were observed at 15.84, 26.32, 42.16, 39.86, and 66.24 MHz. The first three peaks belong to ^{151}Eu and the last two belong to ^{153}Eu. The last peak for ^{153}Eu was not observed due to the weak response of the RF coil at that frequency. The ratio of P for these two isotopes was 2.516, close to published numbers. Hansen incorrectly interpreted the spectrum by assuming that there was an accidental degeneracy at the 26.32 MHz peak, thus the 26.32, 39.86, and 66.24 peaks were assigned to ^{153}Eu. This led him to calculate P = 6.78, η = 0.41 for ^{151}Eu and P = 10.44, η = 0.52 for ^{153}Eu, suggesting a very large pseudo-quadrupole moment. This spectrum was very deceptive because the sum of the second and fourth peaks was 66.18 MHz, very close to the peak at 66.24 MHz.

The absorption polarizations of lines K and L differ from those of the lines nearby in energy (see Table 5.1 for line positions). They have σ polarization while other lines are not very polarized. Line K burns readily while line L burns very slowly. This is consistent with the fact that line L has $\eta = 0$.

There are 3 strong defect lines in the higher end of the $^7F_0$ - $^5D_0$ spectrum in the growth I crystal (Cone *et al.* 1993). We list the ODNMR results on these lines in Table 5.3.

Last, the zero field ODNMR of $EuPO_4$ yielded five peaks at 19.55, 26.46, 45.97, 52.44, and 68.29 MHz, implying P = 7.077 MHz and η = 0.649 for ^{151}Eu and P = 18.40 MHz and η = 0.692 for ^{153}Eu.

Table 5.3 Comparison of the $^7F_0$ ODNMR results of the high energy lines in the growth I crystal. All P's listed are in absolute magnitude.

line #	Freq. (GHz)	This work	Hansen (1993)	Comments
39	516389	P = 7.113 η = 0.436	P = 4.40 η = 0.47	a
40	516415	P = 5.86 η = 0.18 P = 14.84 η = 0.20	Same	
41	516635	P = 5.77 η = 0 P = 14.59 η = 0.07	P = 3.27 η = 1.0 P = 8.34 η = 1.0	b

a. Origin of the discrepancy is not clear, but the Zeeman experiment in Chapter 6 seems to confirm the interpretation of the present work.

b. It is difficult to decide which interpretation is correct for this line, four peaks at 11.56, 23.12, 29.35 and 58.33 MHz were observed. They can be interpreted either as the only 4 allowed transitions for an axial system or as the 6 transitions for an η = 1 system with the lower transitions degenerate. We prefer the first explanation because for ^{153}Eu, if η = 1.0, another peak should appear at 28.98 MHz and should be detected since the 29.35 MHz transition had a linewidth of about 200 KHz. That it was not observed meant an η = 0 system. Although the parameter η was not zero in the excited state, this kind of site was observed before in Eu^{3+}:$YAlO_3$ where η = 0.56 for the excited state, and η = 0 for the ground state. Hansen (1990) did Zeeman splittings on $^7F_0$ of this line along the *c*-axis and observed 4 peaks for the lowest transition (only two are supposed to be observed for a real axial system); however, this also happened in Eu^{3+}:$YAlO_3$.

Discussions

Energy-Transfer Enhanced Holeburning

In perfectly axial systems, no nuclear spin state admixture should occur in either the ground states or the excited states, and the holeburning process should be forbidden. However, holeburning was observed for many compounds with axial symmetry, most notably the C_{3V} and C_{4V} centers in CaF_2 and other isomorphous compounds (Silversmith *et al.* 1986, Silversmith and Macfarlane 1992). Especially for the C_{4V} centers, the holeburning was very strong, yet the holeburning mechanism was not well understood. We propose here a holeburning mechanism that may be as important as fluorescence branching in some of these axial sites.

First we wish to make the following observations regarding the $^7F_0$ - $^5D_0$ transition at the defect sites of $EuVO_4$:

(1) All sites that are difficult to burn display hole lifetimes that are longer than those for easy to burn sites. This is an indication that such sites have much weaker interactions with the environment.

(2) All higher energy defect sites burn more readily than sites that are energetically close to the intrinsic site, and they usually display beautiful well-resolved holeburning spectra. However, ODNMR spectra on these higher energy sites rarely display any excited state resonances. On the contrary, ODNMR spectra on sites energetically close to the intrinsic sites sometimes display both excited and ground state resonances simultaneously.

(3) As discussed in Chapter 4, time-resolved fluorescence experiments showed that the higher energy sites had very strong energy transfer to other sites with lower energy.

(4) The same defect lines in different crystals show different holeburning rates. In the ORNL samples, even the intrinsic line exhibits holeburning.

From the time-resolved fluorescence experiments (see Chapter 4) we knew that those high energy sites transferred their energy to other sites. Many high energy sites had transfer times of only about 10 μs as opposed to the typical intrinsic fluorescence lifetime of ~0.5 ms. That suggested that the dominant $^5D_0$-$^7F_0$ decay mechanism for the high energy sites was phonon-assisted energy transfer, rather than radiative processes. For these high energy ions, this cross-relaxation avoids all questions regarding the hyperfine selection rules governing the original optical excitation process. Although fluorescence branching may still play a small role in these holeburning processes, it appears to be much less important than phonon-assisted energy transfer. The fact that line A burnt slower than line D might be a testament on the different energy-transfer rates (50 μs vs. 10 μs) rather than the difference in the degrees of admixture between different hyperfine states ($\eta = 0.315$ vs. $\eta = 0.408$).

If fluorescence branching has only a diminished role compared to energy transfer, it will be very difficult to observe the excited state resonance through ODNMR experiments because the energy transfer process will not respond to the RF radiation very much; this is consistent with observation (2). For those lines that are close to the intrinsic transition, no energy transfer to other sites was observed in the time-resolved fluorescence experiments; it is not surprising that holeburning occurs very slowly for those sites if energy transfer is the pumping mechanism for non-axial sites.

When fluorescence branching is the main mechanism for holeburning, ODNMR should be able to detect the excited state resonances. For 0.01%Pr^{3+}:Y_2SiO_5 (Equall, Sun, Cone, and Macfarlane, unpublished), holeburning was readily observed, but the majority of ions were at normal yttrium sites and were very isolated as a consequence of the low Pr^{3+} concentration. The possibility of energy transfer was low, and the

holeburning process was mostly due to fluorescence branching. Even when the holes were burned very deeply in the ODNMR experiments on Pr^{3+}:Y_2SiO_5, excited states resonance peaks were observed (small but recognizable); these peaks were verified and characterized through photon-echo nuclear double resonance (PENDOR) experiments.

The C_{4V} centers in CaF_2 showed strong holeburning, but ODNMR experiments to observe the excited state resonances were not successful (Silversmith and Macfarlane 1992), a good indication that fluorescence branching was not the main holeburning mechanism. It might be enhanced by the energy transfer process. For the C_{3V} centers in CaF_2, the holeburning was slow, which could mean a slower transfer rate, with fluorescence branching playing a more important role in the holeburning process. Excited state ODNMR signals were observed, implying that fluorescence branching was responding to the RF radiation (Silversmith *et al.* 1986).

The different holeburning rates for the same site in different growths of crystals can also be explained by the transfer rate. Although the same defect site should have exactly the same local environment in different crystals, there may be different defect types and defect abundances for different growths. This macroscopic environment may not influence the optical transition frequency, but it may affect the phonon processes, especially low energy phonon processes that involve long ranges; thus, the energy transfer rates for the same site in different crystals may not be the same, and thus the different holeburning rates in different growths of crystals.

Quadrupole Moment Ratio

From eq.(5.13), the pseudoquadrupole effect influences the two isotopes of europium differently because of their different nuclear magnetic moments. Since ^{151}Eu has a smaller quadrupole moment and a larger magnetic moment, the pseudoquadrupole effect not only affects the absolute magnitude of P for ^{151}Eu more than for the other

isotope, it also affects the ratio between the P's even more. For this reason, workers use this ratio as an indicator of the importance of the pseudoquadrupole effect. In ^5D_J, the J = 1 level is farther away from J = 0 than in ^7F_J; hence, the pseudoquadrupole effect is much smaller for the $^5D_0$ state and generally considered negligible.

A number of authors have published the ratio between the real quadrupole moments Q of the two abundant isotopes based on ODNMR experiments. They are listed in Table 5.4, together with the results of this work and those measured by other methods.

Table 5.4 Europium quadrupole moment ratios

host	Ratio	method	reference
	2.5445 ± 0.0194	Atomic beam	Sanders and Woodgate (1960)
	2.5835 ± 0.0191	ENDOR	Baker and Williams (1962)
	2.55 ± 0.34	Optical HFS	Krebs and Winkler (1960)
	2.517 ± 0.24	Hollow-cathode discharge	Muller *et al* (1965)
CaF_2 C_{3V} ($^5D_0$)	2.553±0.001	ODNMR	Silversmith *et al.* (1986) Silversmith and Macfarlane (1992)
$LiYF_4$ ($^7F_0$)	2.564±0.005	ODNMR	Sharma & Erickson, corrected for pseudoquadrupole effect
$YAlO_3$ ($^5D_0$)	2.5812±0.0016	ODNMR	Erickson and Sharma (1981)
CaF_2 C_{4V}($^7F_0$)	2.73	ODNMR	Silversmith and Macfarlane (1992)
BaF_2 C_{4V}($^7F_0$)	2.75	ODNMR	Silversmith and Macfarlane (1992)
Line Q ($^5D_0$)	2.5495	ODNMR	This work
$EuVO_4$ defect $^7F_0$'s	2.551±0.006*	ODNMR	This work (Average)

* The ratio for the ground state of the defect sites range from 2.483 to 2.594. The value 2.551 ± 0.006 is the average with standard deviation. Most sites have the ratio very close to 2.551.

The published values are not compatible with each other. Most noticable are the values for C_{4V} centers in CaF_2 and BaF_2; they are considerably larger than in other crystals. Silversmith and Macfarlane (1992) noticed this discrepancy and calculated the

pseudoquadrupole effect from the spectroscopic data of the $^7F_1$ levels. With the allowance for pseudoquadrupole interaction, the ratios were 2.64 and 2.91, respectively, even farther from other results for BaF_2. The ground state quadrupole interaction for these crystals was probably unduly sensitive to the pseudoquadrupole interactions because of the small pure quadrupole interactions, but in any case it showed that there must be some other mechanism that contributed. Of course the shielding and anti-shielding parameters could be changed to fit the data; even different ionic radii and shielding factors can be assumed for the two isotopes, but the real mechanism still seemed unclear. These two crystals, CaF_2 and BaF_2, have extremely similar structures, suggesting that there must be a common mechanism that dominates the pseudoquadrupole interaction, making these ratios similar for both crystals (2.73, 2.75), even though both results are far from other measurements. The Hamiltonian we gave at the beginning of this chapter may not be complete enough to describe the Eu^{3+} quadrupole interaction. On the other hand, if energy transfer was the holeburning mechanism, then the spectra giving the $^7F_{1,2}$ levels might be improperly assigned, making the analysis invalid. From Chapter 4, we know that the energy level baricenters are high in these crystals compared with others. But the $^7F_1$ levels given in that paper (Silversmith and Macfarlane, 1992) were extremely low. They were 352, 360, and 350 cm^{-1} in CaF_2, SrF_2, and BaF_2, respectively. This almost automatically means that either the emission they observed was not from the correct sites, or more likely, the calibration was off.

Asymmetry Parameters

Apart from the quadrupole moment ratio discussed above, different E_{pq}'s (eq.(5.13)) make η different for the two isotopes. This effect is very obvious in the ground states of many sites in $EuVO_4$. The high precision ODNMR data allowed us to calculate η to an

accuracy not achievable just from holeburning spectra. Angle dependent ODNMR (see Chapter 6) made it possible to determine the magnetic shielding parameters to around 1%, so comparison can be made there also.

For line A, $\eta = 0.315$ and 0.337 for ^{151}Eu and ^{153}Eu, respectively. Nuclear Zeeman data in Chapter 6 show that the nuclear magnetic moment for that site is anisotropic, so E_{pq} is not zero, and different η's result.

For Line D, $\eta = 0.408$ and 0.408 for ^{151}Eu and ^{153}Eu, respectively. Nuclear Zeeman experiments show that the magnetic moments in the x and y directions are very similar; thus, E_{pq} is very small. The similar η's are the result of this small E_{pq}.

For most other sites, the η's are different for the two isotopes. The η for ^{151}Eu can be either smaller or larger than η for ^{153}Eu, so the pseudoquadrupole interaction is a small but important process in the ground state.

For the non-axial part of the quadrupole interaction, in both the lattice and the electronic parts, we have $\eta = 3E/P = \sqrt{6}\,B_{22}/B_{20}$, which implies the same η for the excited and ground states. But generally, for low symmetry crystals, we have *different* η's for the excited and ground states. This is most notable in Eu^{3+}:$YAlO_3$ (Erickson 1981, Erickson 1986, and Macfarlane 1981), where in the excited state, $\eta = 0.56$, while in the ground state a dramatic cancellation occurs and $\eta = 0$. In $EuVO_4$, there are several sites for which both the ground state and the excited state splittings are known, and all show different asymmetry parameters in the two different states. These sites and their asymmetry parameters are summarized in Table 5.5.

Table 5.5 Nuclear quadrupole asymmetry parameters for $^7F_0$ and $^5D_0$ states of $EuVO_4$.

lines	$\eta(^5D_0)$	$\eta(^7F_0)$	reference
line D	0.81	0.408	This work, Cone *et al.* 1984
line A	0.64	0.315	This work
line Q	0.115	0.00	This work
line # 39	0.85 or 0.13	0.436	Lazzouni (1988), Hansen (1990), This work
Line #41	0.44	0. or 1	Lazzouni (1988), Hansen (1990), This work

Erickson (1986) noted this discrepancy of η in the ground and excited states for Eu^{3+}:$YAlO_3$ and attributed this qualitatively to the possible differences in the directions in the principal axes of the ground state and excited state nuclear quadrupole interactions. This is consistent with the results for line D, for which we show that these directions are different (see 6.3). But it is not clear how the quadrupole interactions can be this dramatically different when theory predicts that η should be the same for lattice and electronic contributions.

Electronic vs. Lattice Contributions in the Ground State

As mentioned in the discussions of the nuclear quadrupole Hamiltonian, since the $^5D_2$ levels are 4200 cm^{-1} away from $^5D_0$, the 4f contribution to the quadrupole interaction of $^5D_0$ is negligible; the lattice term dominates. Once the sign of the crystal field parameter B_{20} is known, then P in $^5D_0$ has the opposite sign. Although the sign of P in $^5D_0$ can be determined easily, the sign of the ground state P is controversial. It was believed that the P_{4f} contribution was always considerably smaller than the lattice contribution in the ground state (Erickson 1986, Hansen 1990), but recent experiments showed that the two contributions have comparable magnitudes and opposite signs (Silversmith *et al.* 1986, Silversmith and Macfarlane 1992). The holeburning study of

Eu^{3+} in the C_{4v} centers of the fluoride series by Silversmith and Macfarlane (1992) provided an explicit determination of the signs of P in both the excited and the ground states. Very small P values were found in the ground states of the fluorides with either the same or the opposite sign as the excited state P , depending on the specific crystal. This meant that the electronic contribution has about the same magnitude as the lattice contribution and the opposite sign. The ratio P_{latt}/P_{4f} was -1.19, -0.88, and -0.82 for CaF_2, SrF_2, and BaF_2, respectively. These values contradict Erickson's value of P_{latt}/P_{4f} = -2.03, or Hansen's calculation (P_{latt}/P_{4f} = -3). Erickson's value is potentially wrong since he did not determine the sign of the ground state splittings explicitly; if a different sign was assumed for the ground state P, P_{latt}/P_{4f} would be -0.67, which is not unreasonable compared to the fluoride numbers. For most of the $EuVO_4$ sites we studied, the excited P's are not available. The signs of the ground state splittings were not determined. Even so, some interesting comparisons can be made from the existing data. For line Q of growth A (Table 5.1), |P| = 7.450 MHz for the ^{151}Eu ground state, and |P| = 8.162 MHz for $^5D_0$. If the same signs are assumed, then P_{latt}/P_{4f} = -11.5. If the signs are assumed to be opposite, then P_{latt}/P_{4f} = -0.52. Either way, the ratio is out of the range of published data. The same situation also occurs in line A of growth A, where |P| = 6.135 MHz in the ground state and |P| = 6.84 MHz in the excited state. The ratio should be similar to that of line Q. From these facts, it seems possible that in the ground state the absolute magnitude of the quadrupole interaction might exceed that for the excited state. This kind of site has not been found yet, but there is no reason that the excited state must always have a larger quadrupole interaction.

If the current theory for the Eu^{3+} quadrupole interactions is correct, only when the shielding and anti-shielding factors change by a large amount even for crystals with isomorphous structures can we explain these changes of the relative contributions of the electronic and lattice contributions. But if the shielding factors cannot be changed that

much by the crystal environment, then the current theory must be defective and needs to be modified to explain the experimental data.

Correlation of P and B_{20}

From eq. (5.20), the ratio P_{latt}/B_{20} should be a constant for any crystal since γ_∞ cannot be changed too much (~ -80 for all rare earths). The only parameter left to change is $(1 - \sigma_2)\langle r^2 \rangle$. For $^7F_0$, because of the addition of the electronic and lattice contributions, more parameters come into play. But for the $^5D_0$ state, this ratio should not change by too much, but published values of P and B_{20} do not correlate very well. For example, the fluoride C_{3V} centers have very large B_{20}, but the $^5D_0$ P's are not exceptionally large. The Eu^{3+}:CaF_2 C_{3V} site has a P value similar to that for Eu^{3+}:$YAlO_3$, but their B_{20}'s are very different. The Eu^{3+}:CdF_2 C_{3V} and Eu^{3+}:CaF_2 C_{4V} sites have similar P's; again their B_{20}'s are very different. Some of the published ^{151}Eu data for different crystals are listed in Table 5.6.

For the ground state, except for the C_{4v} centers in CaF_2 and related fluorides, there are no extremely high or low P's. Most of them are between 6 and 8 MHz. Especially interesting are values for the $EuVO_4$ defect sites listed in the tables 5.1 and 5.2. These sites should have very different environments but the P's do not change much. Except in some extreme cases, most η's are around 0.3 ~ 0.4. This raises the question as to what is causing the similar P's when the local environments should be dramatically different.

Table 5.6 Comparison of quadrupole splittings and crystal field. P's without a sign in front are listed only in absolute magnitude.

host	P ($^7F_0$)	η ($^7F_0$)	P ($^5D_0$)	η ($^5D_0$)	B_{20} (cm^{-1})	$^7F_1$ splittings
$YAlO_3$	11.50	0	-22.715	0.56	610[a]	
$LiYF_4$	6.539	0.05			-600	
$KEu(WO_4)_2$	8	0.34 0.42	19	0.12		
CaF_2 C_{3V}	+8.21	0	-22.23	0	~1500	
CdF_2 C_{3V}	+7.85	0	-12.9	0	~1100	
Line D	6.784	0.408	10.2	0.86	unknown but < 600	
EuP_5O_{14}	6.38	0.59	8.0	0.59		
CaF_2 C_{4v}	-2.42		-13		~490	147
SrF_2 C_{4v}	+0.89		-6.5		~350	106
BaF_2 C_{4v}	+0.975		-4.5		~220	67
$Eu(OH)_3$			4.5		211	101

[a]Calculated from Erickson and Sharma (1981)'s numbers and consistent with numbers from other hosts listed in Morrison and Leavitt.

From the poor correlation of the $^5D_0$ P's and the crystal field parameters, it seems that the quadrupole interaction for Eu^{3+} is not well understood. The simple formula describing the $^5D_0$ state quadrupole interaction is not adequate. Although Silversmith and Macfarlane (1992) gave the first self-consistent study of the ground state splittings of Eu^{3+} in the C_{4V} centers of the fluorides, we disagree with them in saying that the poor correlation for sites with large crystal field splittings is just because they cannot be treated as typical rare earth sites where crystal field is only a small perturbation. More elaborate study of Eu^{3+} ions has to be made to properly address this problem.

CHAPTER 6

ANGLE-DEPENDENT ODNMR OF THE DEFECT SITES IN $EuVO_4$

In 1957, Elliott predicted the strong and anisotropic quenching of the nuclear magnetic moment in the ground state of Eu^{3+}. It was not until 1981 that this prediction was confirmed when the ground state splittings of Eu^{3+}:$YAlO_3$ were measured by Shelby and Macfarlane (1981), and Erickson and Sharma (1981) using the ODNMR technique. Anisotropic quenching of the nuclear magnetic moment in the Eu^{3+} ground state has also been observed in $LiYF_4$ (Sharma and Erickson 1985), the C_{3V} centers in CaF_2 and CdF_2 (Silversmith *et al* 1986), and the C_{4V} centers in CaF_2, SrF_2, and BaF_2 (Silversmith and Macfarlane 1992). Only Eu^{3+}:$YAlO_3$ was studied with full angular rotation. Part of the reason for the relatively scarce data is requirement of a stronger field to observe the splittings because of the quenching of the nuclear magnetic moment. The design of a rotating apparatus is not trivial.

Contrary to Eu^{3+} where the ground state nuclear magnetic moment is quenched due to the coupling with the $^7F_1$ state, the Pr^{3+} ion has an enhanced ground state nuclear magnetic moment due to the coupling of the ground electronic singlet with the low-lying electronic states, so it is much more sensitive to the magnetic field. A 100 Gauss magnetic field can split the transitions by several megahertz, so ordinary Helmholtz coils can be used to study these effects, making Pr^{3+} a very popular ion for this kind of experiment. The study of the nuclear Zeeman effect has been carried out on the hosts YAG (Shelby et al 1983), $LiYF_4$ (Sharma and Erickson 1980), YPO_4 (Shelby *et al.*

1984), LaF_3 (Macfarlane and Shelby 1981, Mitsunaga *et al* 1985), and $YAlO_3$ (Erickson 1979, Erickson 1981, Mitsunaga *et al* 1985). The Zeeman experiments with full angular rotation were carried out on Pr^{3+}:$YAlO_3$ and Pr^{3+}:LaF_3. This kind of study yielded information on the principal axis directions of the nuclear quadrupole interaction.

The series of experiments on $EuVO_4$ (Cone et al 1984, Robinson 1986, Cone et al 1988, Lazzouni 1988, Hansen 1990, Hansen 1992) focused on the nuclear Zeeman holeburning experiments for the $^5D_0$ state. Unlike other studies where the active ion is in the intrinsic site of the host crystal, there is no predetermined structural information for these defect sites. The purpose of the $EuVO_4$ work was to find the direction of the defect principal axes in the crystal coordinates. ODNMR experiments (Hansen 1990, Cone *et al.* 1992) were used to study the ground state splittings, but since there were more parameters to fit for the $^7F_1$ levels, no unique fit was realized from those experiments. Strong quenching of the ground state nuclear magnetic moment was observed for several sites, however, indicating that the nuclear magnetic shielding factors $1-\alpha_i$ are important.

In this work, full angle-dependent ODNMR data will be exploited to extract information on the anisotropic nuclear magnetic shielding factors and the directions of the principal quadrupole interaction axes for some of the defect sites in $EuVO_4$. To obtain that data, a sample holding system was built to rotate the sample relative to the magnetic field in the superconducting magnet. The experimental procedure will be described and the results of the experiments will be presented in this chapter. But first, we will discuss the possible spectra for defect sites in an tetragonal crystal using symmetry arguments.

ODNMR of a Defect System in a D_{4h} Crystal

Symmetry Consequences

In a D_{4h}^{19} system, the rare earth ions occupy D_{2d} local symmetry sites. This means that through D_{2d} transformations, the ions will be in exactly the same kind of environment. Through D_{4h} transformations, all directions of the crystal should go back to their original orientation. Since D_{4h} is equivalent to the product of D_{2d} and inversion, the D_{4h} transformation will at most leave a D_{2d} site in the orientation related to the original orientation by inversion symmetry. Two sites related by inversion symmetry are equivalent in a magnetic field, so all the D_{2d} sites in a D_{4h} crystal are magnetically-equivalent.

For a defect site, the local symmetry will most probably be C_1, corresponding to no symmetry at all. For a C_1 symmetry local site, the D_{4h} transformation will generate 16 sites as illustrated in Figure 6.1. Following the logic used for the intrinsic sites, 8 magnetically-inequivalent defect sites will be present in a D_{4h} crystal. Even for a higher symmetry site, the same argument can be applied if none of its axes coincides with the D_{4h} axis.

A magnetic field applied in an arbitrary direction in the crystal will have a different orientation in each of the magnetically-inequivalent sites, but the orientations are related by simple transformations. Suppose we use Euler angles α, β, γ to define the local coordinates of a defect site relative to the original crystal coordinates; there are two ways to define these angles. We will use the quantum mechanics convention (see Appendix III), and three steps are needed to reach the final conditions.

1. To start with, let the two sets of axes coincide. We rotate the defect axis set by α around the z-axis.

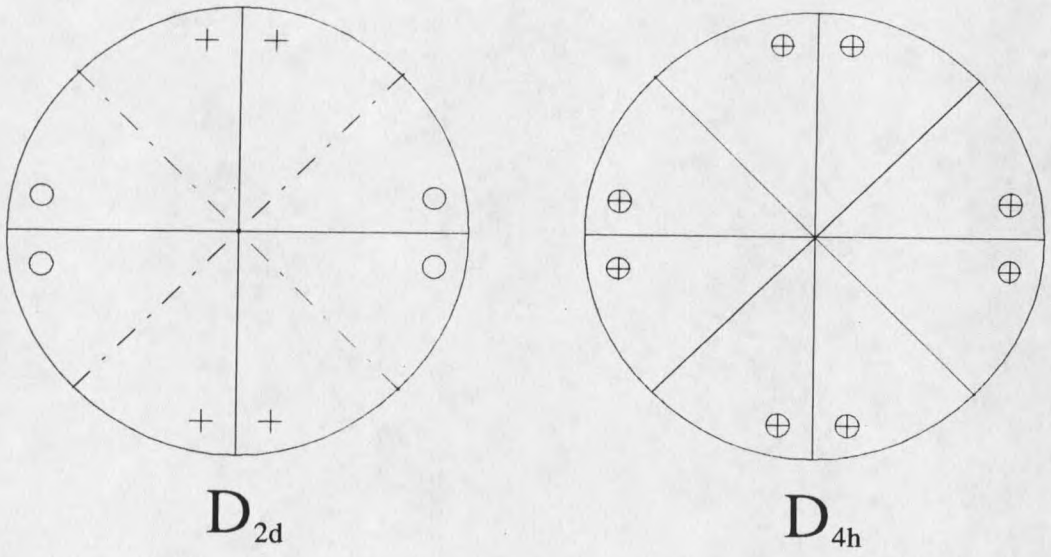

Figure 6.1. Stereographic projections of the D_{2d} and D_{4h} groups. $D_{4h} = D_{2d} \times i$.

2. Then we rotate the defect axis set around its intermediate y-axis by β to have the defect z-axis reach its final position.

3. We rotate the new defect axis set around the defect z-axis by γ to reach the final position for the defect axis set.

All these operations were done in the counterclockwise direction, looking inward toward the origin.

Because the i operation does not add new information, we only use half of the elements of the group D_{4h} to generate our 8 coordinate sets. Since also $D_{4h} = C_{4v} \times i$, we will use the C_{4v} operations to generate these sites. Four of them are described in Euler angles by

(1) (α, β, γ) (2) $(\pi/2+\alpha, \beta, \gamma)$ (3) $(\pi+\alpha, \beta, \gamma)$ (4) $(3\pi/2+\alpha, \beta, \gamma)$

which are connected by the C_4 operation. The other sites can be generated through the operation of the vertical mirror planes:

(5) $(-\alpha, \beta, -\gamma)$ (6) $(\pi/2-\alpha, \beta, -\gamma)$ (7)$(\pi-\alpha, \beta, -\gamma)$ (8) $(3\pi/2-\alpha, \beta, -\gamma)$.

If the experiment is done so that the magnetic field is in the *c-a* plane, only 4 inequivalent sites will be seen. They are 1 and 5, 2 and 6, 3 and 7, and 4 and 8. On the other hand, if the experiment is done with the magnetic field in the *a-a'* plane, 4 different inequivalent site combinations will be seen. They are 1 and 3, 2 and 4, 5 and 7, and 6 and 8. In the special case that the magnetic field is along the *c*-axis of the crystal, all eight sites should be equivalent.

Another special case is when the magnetic field is along the *a*-axis, only two inequivalent sites will be seen, they are 1, 3, 5, and 7; and 2, 4, 6 and 8. If the experiment is done with the magnetic field in the 45° plane that bisects the *c-a* and *c-a'* planes, also only 4 inequivalent site combinations may be observed. If $\alpha = \gamma = 0$, or one of them is 90°, the defect coordinates are tilted only in the crystal c-a plane. Experiments done with the magnetic field in the *c-a* plane should see only 3 site combinations, while experiments done with the magnetic field in the *a-a'* plane will see only two.

Matrix Solving Algorithm

From last chapter, the nuclear Hamiltonian can be written as

$$H = P[(I_z^2 - I(I+1)/3) + \eta/3(I_x^2 - I_y^2)] - \gamma\hbar\,\mathbf{H}\cdot(1 - \underline{\alpha})\cdot\mathbf{I}. \qquad (6.1)$$

From this expression, a 6×6 complex matrix must be solved to calculate all six energy levels in a field for each site orientation. An explicit expression for this Hermitian matrix can be found in Cone *et al.* (1988). The original expression was used for $^5D_0$ where the nuclear magnetic moment quenching as described in the last chapter was a small correction. However, strong and anisotropic quenching of the nuclear magnetic moment occurs in $^7F_0$. We therefore need to make the following changes:

$$k\cos\theta \Rightarrow k(1-\alpha_z)\cos\theta \qquad (6.2)$$

where $k = 1/2\ g_I\ \mu_N H$, and

$$k \sin\theta\ e^{i\phi} \Rightarrow k(1-\alpha_x) \sin\theta \cos\phi + i\, k(1-\alpha_y) \sin\theta \sin\phi. \tag{6.3}$$

If we define

$$\begin{aligned} K_x &= k(1-\alpha_x) \sin\theta \cos\phi \\ K_y &= k(1-\alpha_y) \sin\theta \sin\phi \\ K_z &= k(1-\alpha_z)\cos\theta, \end{aligned} \tag{6.4}$$

then the real part of the Hamiltonian can be written as

$$\mathrm{Re} = \begin{bmatrix} \frac{10}{3}P+5K_z & \sqrt{5}K_x & \frac{\sqrt{10}}{3}\eta P & 0 & 0 & 0 \\ \sqrt{5}K_x & -\frac{2}{3}P+3K_z & 2\sqrt{2}K_x & \sqrt{2}\eta P & 0 & 0 \\ \frac{\sqrt{10}}{3}\eta P & 2\sqrt{2}K_x & -\frac{8}{3}P+K_z & 3K_x & \sqrt{2}\eta P & 0 \\ 0 & \sqrt{2}\eta P & 3K_x & -\frac{8}{3}P+K_z & 2\sqrt{2}K_x & \frac{\sqrt{10}}{3}\eta P \\ 0 & 0 & \sqrt{2}\eta P & 2\sqrt{2}K_x & -\frac{2}{3}P+3K_z & \sqrt{5}K_x \\ 0 & 0 & 0 & \frac{\sqrt{10}}{3}\eta P & \sqrt{5}K_x & \frac{10}{3}P+5K_z \end{bmatrix} \tag{6.5}$$

The imaginary part of it is

$$\mathrm{Im} = \begin{bmatrix} 0 & \sqrt{5}K_y & 0 & 0 & 0 & 0 \\ -\sqrt{5}K_y & 0 & 2\sqrt{2}K_y & 0 & 0 & 0 \\ 0 & -2\sqrt{2}K_y & 0 & 3K_y & 0 & 0 \\ 0 & 0 & -3K_y & 0 & 2\sqrt{2}K_y & 0 \\ 0 & 0 & 0 & -2\sqrt{2}K_y & 0 & \sqrt{5}K_y \\ 0 & 0 & 0 & 0 & -\sqrt{5}K_y & 0 \end{bmatrix} \tag{6.6}$$

The algorithm used for solving this Hermitian matrix was from "Numerical Recipes" by Press *et al.* (1986). Diagonalization of an n × n Hermitian matrix Re + *i*Im is equivalent to a 2n × 2n real problem, i.e.

$$[\mathrm{Re} + i\,\mathrm{Im}]\cdot(u + iv) = \lambda\,(u + iv) \tag{6.7}$$

is equivalent to

$$\begin{bmatrix} \mathrm{Re} & -\mathrm{Im} \\ \mathrm{Im} & \mathrm{Re} \end{bmatrix}\begin{bmatrix} u \\ v \end{bmatrix} = \lambda\begin{bmatrix} u \\ v \end{bmatrix} \tag{6.8}$$

The only difference is that the eigenvalues will appear twice. These may be sorted out easily with the repeated values only counted once.

Fitting of Experimental Data

Since the experimental data with the magnetic field in the *c-a* plane or the *a-a'* plane normally have four sets of lines from sites related by symmetry, only one set of Euler angles are needed to fit the data. The nuclear magnetic moment is generally anisotropic; three more parameters thus are added to the Hamiltonian, making a total of six. The values of P and η can be calculated from zero field data directly; they are not adjustable parameters in the anglular fit. The bare nucleus NMR frequency is 10.559 MHz/kG for ^{151}Eu and 4.6627 MHz/kG for ^{153}Eu (Evans *et al.* 1965, Boyd 1966).

Normally, the ^{151}Eu "1/2 - 3/2" transition Zeeman data with the magnetic field in the *c-a* plane were used in the initial analyses because of the better signal in this frequency region and the stronger magnetic moment of ^{151}Eu. The magnetic field value was chosen large enough to resolve all the splittings but small enough so that the Zeeman components from different zero-field levels did not cross. This situation is shown in Figure 6.2.

In the fitting program, the computer generates a series of six eigenvalues by solving the 6 x 6 complex matrix for the Hamiltonian. We call these eigenvalues d1, d3, d5, d7,

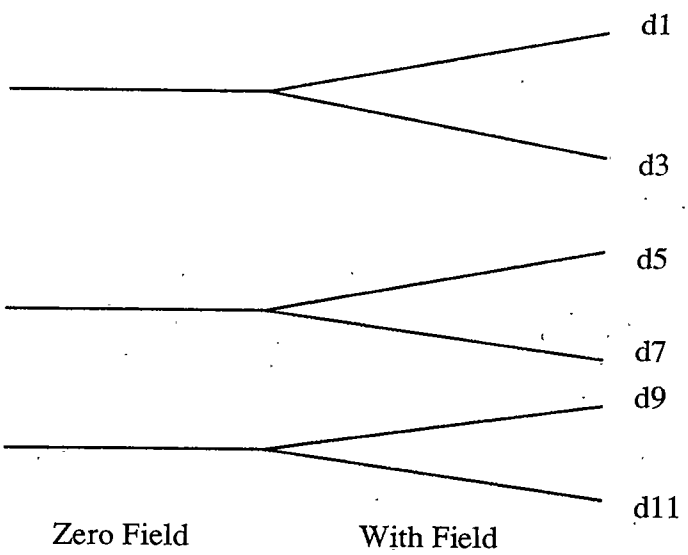

Figure 6.2 The splitting scheme of the nuclear hyperfine levels.

d9, and d11, according to their magnitudes. Only odd number labels were used because each eigenvalue appeared twice when the 12 x 12 real matrix was solved. The eigenvalues d1 and d3 are the split levels of "5/2", d5 and d7 those of "3/2", d9 and d11 those of "1/2". If only the "1/2 - 3/2" transitions are considered, there will be four transitions. The lowest one will be d7 - d9, and the highest one will be d5 - d11, but it is ambiguous to assign the two inner transitions because for different directions these two transitions may change their relative magnitudes by a large amount. For example, when the magnetic field is along the *c*-axis, d5 - d9 will be the higher energy transition, while when the field is along *a*, d7 - d11 will be the stronger transition. Both assignments were used in our fitting. Other evidence was used to determine the correct interpretation of the data in the rare case that both assignments yielded good fits.

Another ambiguity occurs because only the absolute magnitude of the magnetic moment influences the measured transition frequencies, so that $1-\alpha_i$ and $\alpha_i - 1$ will give

the same fit. If $|1-\alpha_i|$ is determined to be 0.5, we have to make a choice whether α_i is 0.5 or 1.5, that is not always obvious. Other evidence has to be used to determine if any of the three α_i's should be smaller or larger than 1. As we discussed in the last chapter, the sum of the inverse of the α_i's should be close to 4. Different combinations for the α_i's may be tried to decide if any of the α_i's needs to be larger than 1.

A nonlinear fitting program based on the routine MRQMIN from Press et al. (1986) was written to fit the experimental data. This program is given in Appendix IV. MRQMIN was modified to take up to 16 groups of data based on different functions simultaneously. Unfortunately, we do not have an analytical form for the transition frequencies at different angles, so for each angle and field, we have to diagonalize the whole matrix and calculate the eigenvalues and the corresponding transition frequencies between eigenvectors. The routine FDF calculates the transition frequencies and their Jacobian relative to the parameters (α, β, γ, and α_x, α_y, α_z). It uses the routine JACOBI to diagonalize the 12 x 12 matrix generated by routine MATRIX according to eq. (6.5) and (6.6). The routine TRANS transforms an arbitrary direction defined by (θ, ϕ) in the crystal coordinates into a direction in the defect coordinate system defined by (α. β, γ), through the transformation matrix generated by the routine EULER following the procedures described in Appendix III. The eigenvalue output from JACOBI was sorted by EIGSRT to arrange them according to their magnitudes. Transition frequencies can then be calculated.

Angular dependent ODNMR data for low symmetry defect sites are usually confusing at first glance. To use this program, we have to assign the input frequencies according to their origins on the different sites and assign them to the right transitions. It is not always obvious how to assign the data to particular sites, but some general rules were developed. As an example, for data taken with field in the *c-a* plane, if two

transitions merge into one when the field is along the *a*-axis, then they are from two sites related by a C_2 operation.

Normally we supplied the data on only one or two transitions and let the computer do a fit. The fit usually gave clues as to the origins of other transitions. Additional data were added for the final fitting.

Experimental Setup

For the Zeeman experiments, the basic optical requirements were the same as the zero field experiments. Because of the strong quenching of the ground state nuclear magnetic moment, a relatively strong magnetic field (~ 2000 G) had to be used to split the nuclear states. Since it was not very practical to use a Helmholtz coil to generate several kilogauss in a large space that would accommodate the dewar tail, all the Zeeman experiments were carried out in an axial access superconducting magnet dewar with an inner bore of 2" in diameter and an access window of 1½" diameter.

To relate the Zeeman data to the local coordinate system at any given defect site, we designed a system for rotating the single crystal sample relative to the magnetic field. The gear system is shown in Figure 6.3. A 3/8 inch stainless steel tube was used to support this system. A piece of 1/8 inch stainless steel tubing was used to drive the 1:1 Nylon bevel gears. The 1/8" tubing was accessible at the top of the magnet dewar, so that we could tell how many degrees the sample was rotated. The sample holder was made of Teflon, and it had three stepped cylindrical sections, 1/4", 3/16", and 1/8" in diameter. The 1/4" section rotated in a hole on the wall of the system (see Figure 6.3) and was large enough to allow light collection along the axis via an optical fiber bundle. The mid section had the RF coil around it. It was usually drilled through from the sides

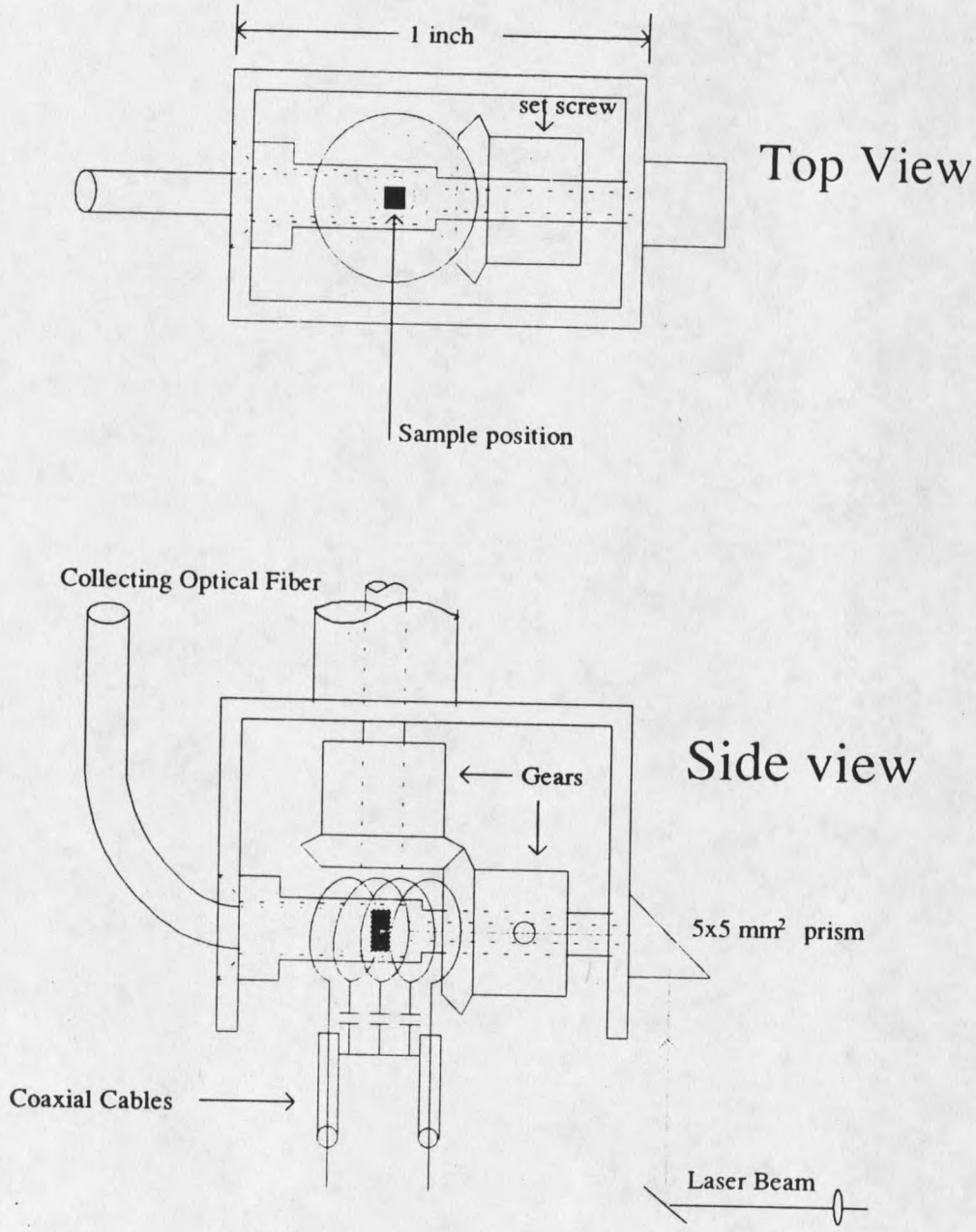

Figure 6.3 Diagram of the rotating gear system showing both the top view and the side view. For clarity, the coaxial cables are drawn downwards rather than upwards beside the stainless steel tubes.

so that it could hold the sample in the coil; the drill size depending on the size of the sample. For experiments with the magnetic field in the *a-a'* plane, however, the sample was put into the holder along its axis from the ends. The two larger sections had an inside diameter slightly larger than 1/8", so that the optical fiber bundle could reach the sample. The thinnest part of the sample holder was used as the shaft for the secondary bevel gear so that when the gear turned, the shaft turned, and the sample would be turned. This section had a 1/16" inside diameter so that the laser beam could pass through to the sample. A 5 mm × 5 mm right angle prism just outside of the thin part of the sample holder was used to direct the laser light onto the sample. The fluorescence light was picked up by the optical fiber directly at the sample and sent to the analyzing equipment outside. The lower part of the optical fiber was contained in a stainless steel tube with epoxy, and the tube and the optical fiber were bent while the epoxy was still wet. The ends were then cut to length and polished to 1/4 micron grit size.

Angle-Dependent ODNMR Results

From the consideration of geometry, we know that a single transition peak at zero field will split into 4 lines in a field. Since all crystallographically equivalent sites also should be magnetically equivalent for a field along the *c*-axis, only 4 resonance peaks should be seen for one zero field resonance peak if the magnetic field is along *c*. Figures 6.4 and 6.5 are the examples of the zero field and field-split spectra of the ^{151}Eu "1/2-3/2" transition of line D with a 2.0 kG magnetic field applied parallel to the *c*-axis.

Due to the magnetic inequivalence of the defect sites, there are a total of 8 inequivalent sites in a D_{4h} system for an arbitrary magnetic field direction. When the field is along an arbitrary direction in the *c-a* or *a-a'* plane, however, only 4 inequivalent

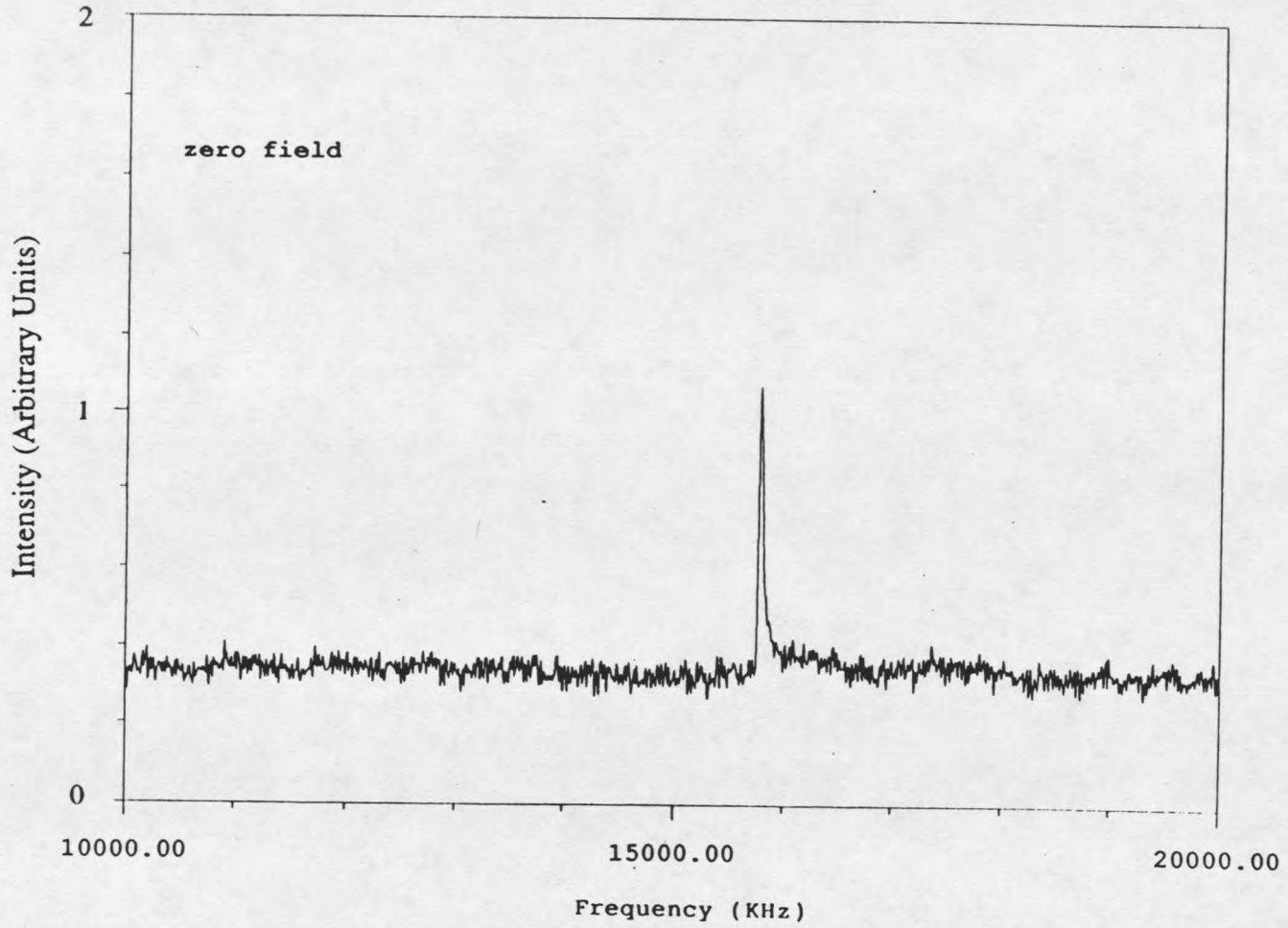

Figure 6.4 The ODNMR spectrum of the ^{151}Eu "1/2 to 3/2" transition for line D in $EuVO_4$.

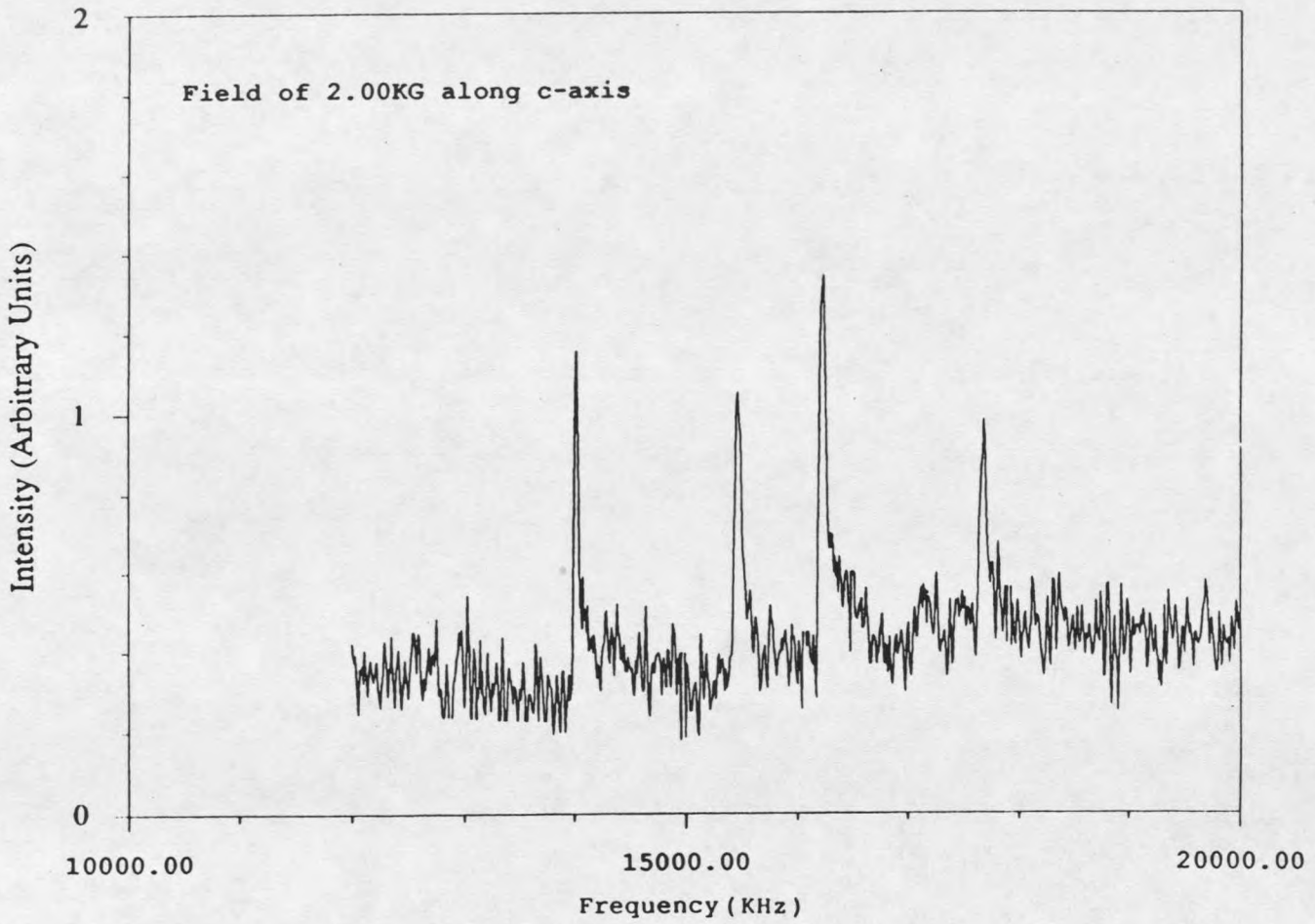

Figure 6.5 The ODNMR spectrum of the ^{151}Eu "1/2 to 3/2" transition for line D with a magnetic field of 2 kG along the *c*-axis in $EuVO_4$.

sites should be observed. Sixteen peaks are expected in place of one zero field peak. Figures 6.6 and 6.7 show the same transition for line D with magnetic fields of 2.0 kG at 31° and 60° from the *c* axis in the *c*-*a* plane.

When the field is along the *a*-axis, only two inequivalent sites are expected. Figure 6.8 is an example of this spectrum showing 8 split lines for the single peak at zero field.

We will discuss our angle dependent ODNMR results site by site. In the parenthesis after the line label, the first number is the ratio of the He-Ne and dye laser wavelengths, the second is the corresponding optical transition frequency for this site.

Line D (1.089454, 515979 GHz)

This site had been extensively studied; it was called line 30 in the original paper (Cone *et al.* 1984) and line #44 in Hansen's thesis (1990). In the present work, it is also called line 48 of the ORNL crystal. The $^5D_0$ quadrupole parameters were published as P = 10.2 MHz and η = 0.81 for ^{151}Eu. The ground state $^7F_0$ values were P = 4.6 and 10.42 MHz for the two different isotopes (Cone *et al.* 1984). Hansen's $^7F_0$ results based on ODNMR of this site yielded P = 6.76 MHz and η = 0.41 for ^{151}Eu; P = 10.4 MHz and η = 0.81 for ^{153}Eu. Hansen's ^{151}Eu result is confirmed in the present work, but the ^{153}Eu result was different, probably due to an incorrect interpretation of the ODNMR spectrum as discussed in the last chapter.

This line was very easy to burn; the holeburning would reach the base line (corresponding to zero fluorescence intensity) in a very short time. Time-resolved fluorescence on this site showed that energy-transfer enhanced holeburning was the main holeburning mechanism, so it was not possible to observe an excited state ODNMR signal. Since fluorescence branching was not the dominating mechanism for holeburning, nuclear resonance in the excited state would not affect the energy transfer process very much.

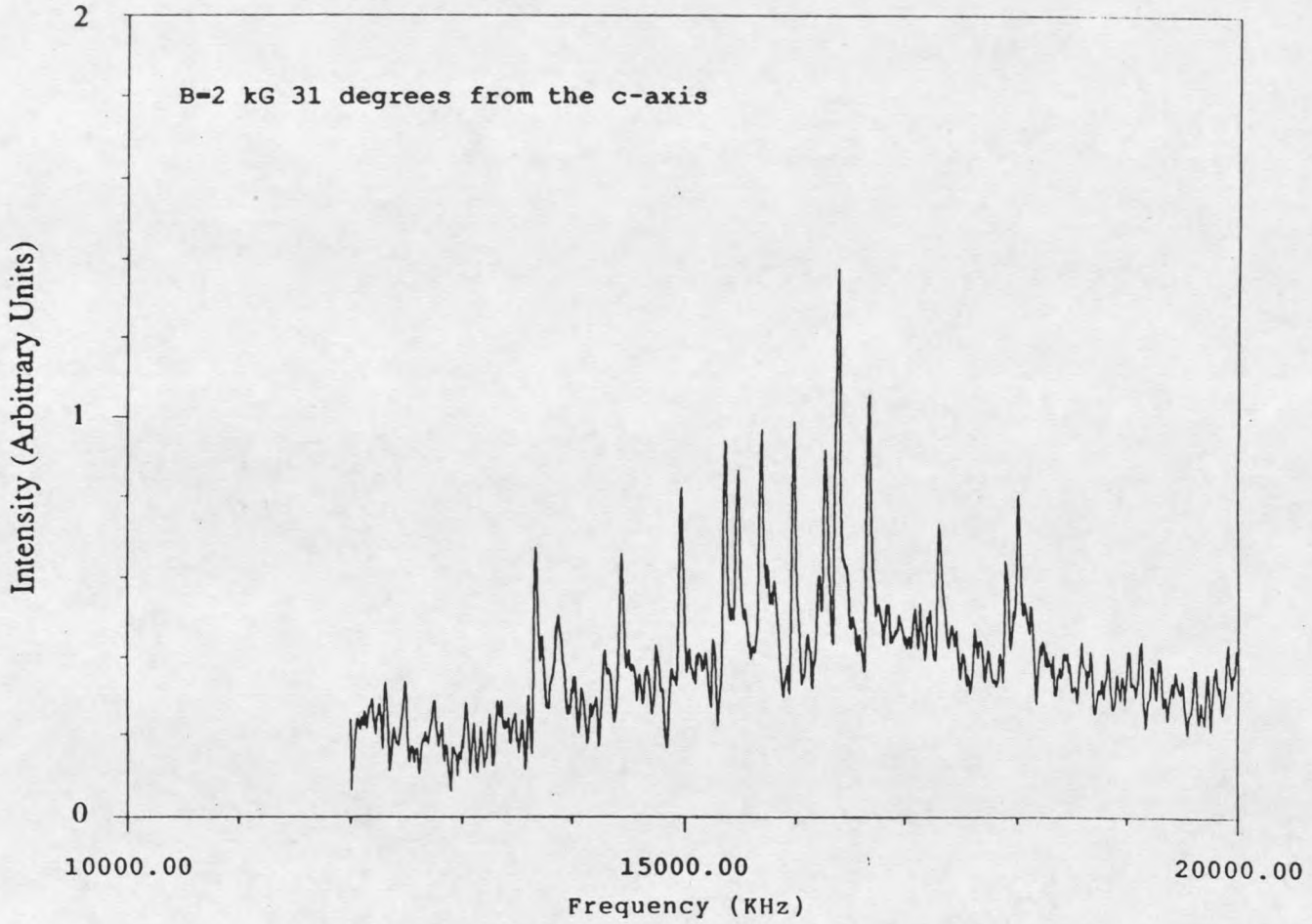

Figure 6.6 The ODNMR spectrum of the ^{151}Eu "1/2 to 3/2" transition for line D with a magnetic field of 2 kG at 31 degrees from the *c*-axis in the *c*-*a* plane in $EuVO_4$.

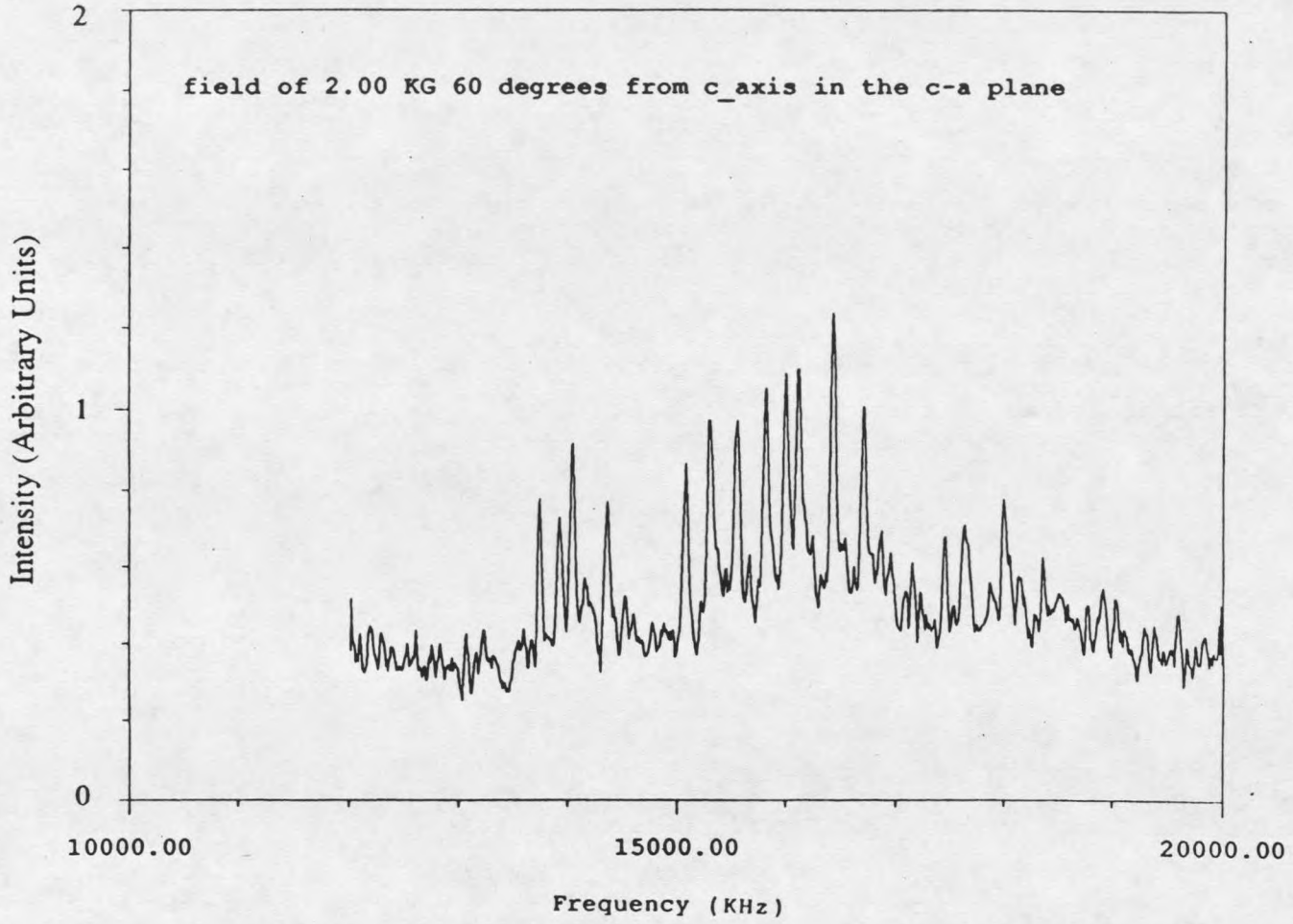

Figure 6.7 The ODNMR spectrum of the ^{151}Eu "1/2 to 3/2" transition for line D with a magnetic field of 2 kG at 60 degees from the *c*-axis in the *c*-*a* plane in $EuVO_4$.

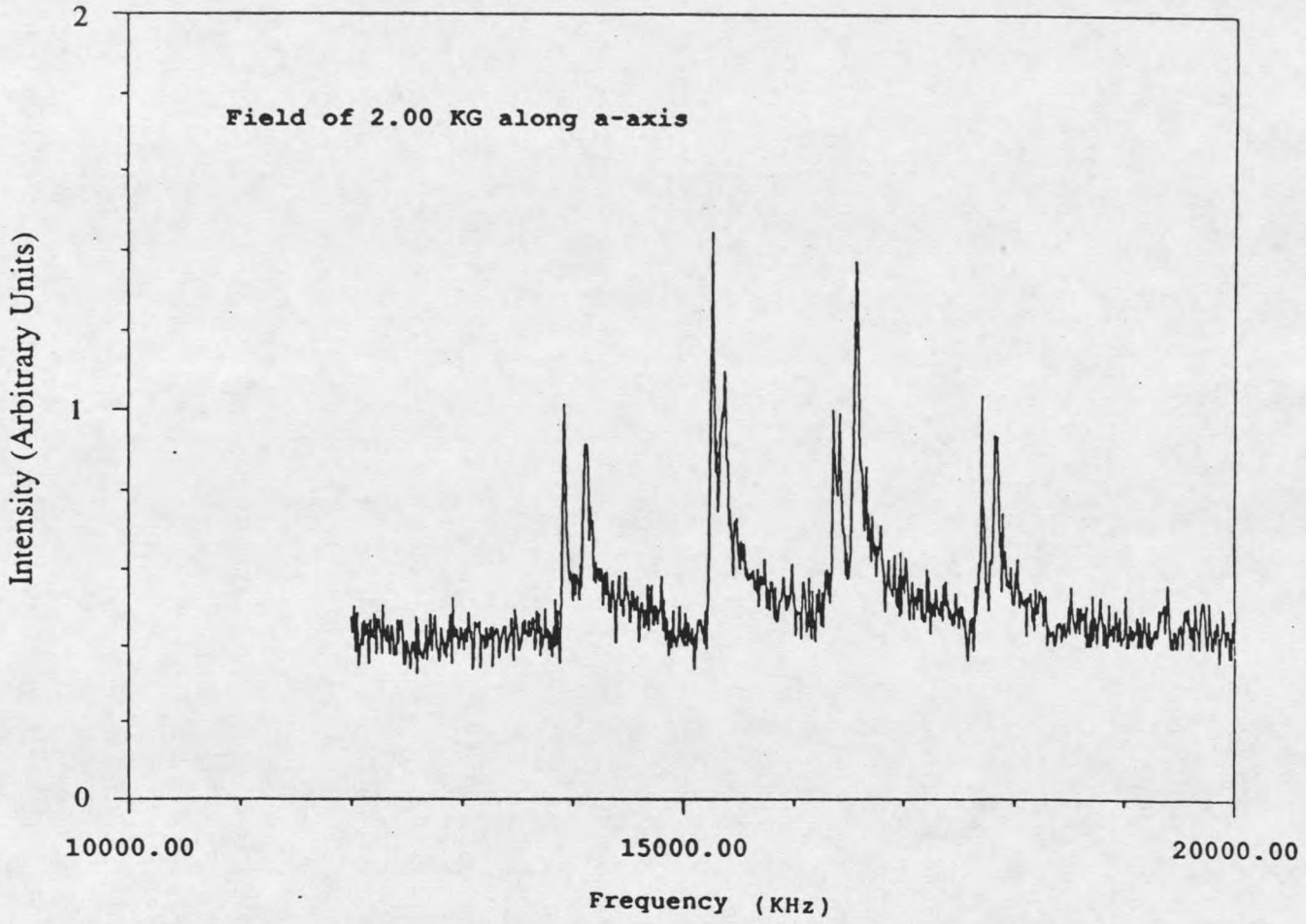

Figure 6.8 The ODNMR spectrum of the ^{151}Eu "1/2 to 3/2" transition for line D with a magnetic field of 2 kG along the *a*-axis in $EuVO_4$.

The representative ODNMR spectra with the magnetic field in the *c-a* plane are shown in figures 6.4 to 6.8. The ODNMR spectra with the magnetic field in the *c-a* plane were taken using the growth A crystal, while the *a-a'* plane spectra were taken using the ORNL crystal. They are shown in Figure 6.9 and Figure 6.10. The fit to the experimental data showed that the nuclear quadrupole z-axis is pointing 28.2° away from the *c*-axis in the *c-a* plane, the x and y axes are determined by rotating the intermediate coordinates by 50° around the defect *c*-axis. The nuclear magnetic tensor was very isotropic: $|1 - \alpha_x| = 0.389$, $|1 - \alpha_y| = 0.394$, and $|1 - \alpha_z| = 0.415$. This set of parameters also fit the linear Zeeman ODNMR spectrum measured by Hansen (1990, Figure 9.7) very well. Due to the arbitrariness in assigning the inner two transitions, another set of parameters were generated by the fitting program. They were:

$\alpha = 45°$, $\beta = 70°$, $\gamma = 70°$; $\alpha_x = 0.58$, $\alpha_y = 0.72$, and $\alpha_z = 0.39$.

This set of parameters fit the "1/2 - 3/2" transition data. The fitting quality was similar to that of the first set of parameters. They even fit the *a-a'* data, but the predictions using this set of parameters for the overall linear Zeeman effect did not match Hansen's data. So the fit with $\alpha = 28.2°$ should be the correct interpretation of the data.

From our discussion about the sum of the inverse of the nuclear shielding parameters, the value should be close to 4. If we assume all α_i's are smaller than 1, we have 1/0.611 + 1/0.606 + 1/0.585 = 4.996, which is far from the number 4, but if we change α_z to 1.415, then the sum will be 3.99. Since the quenched magnetic moment is similar in absolute magnitude in different directions, it is not clear which of the nuclear shielding parameters should be over 1, but one of them has to be. Time-resolved fluorescence showed that the $^7F_1$ levels for this site were at 268, 416, and 434 cm^{-1}. Using these levels directly without considering admixture of different levels did not yield the right shielding parameters. But since there is a level lower than 290, it is conceivable that the direction most strongly coupled to that level will have the shielding factor larger

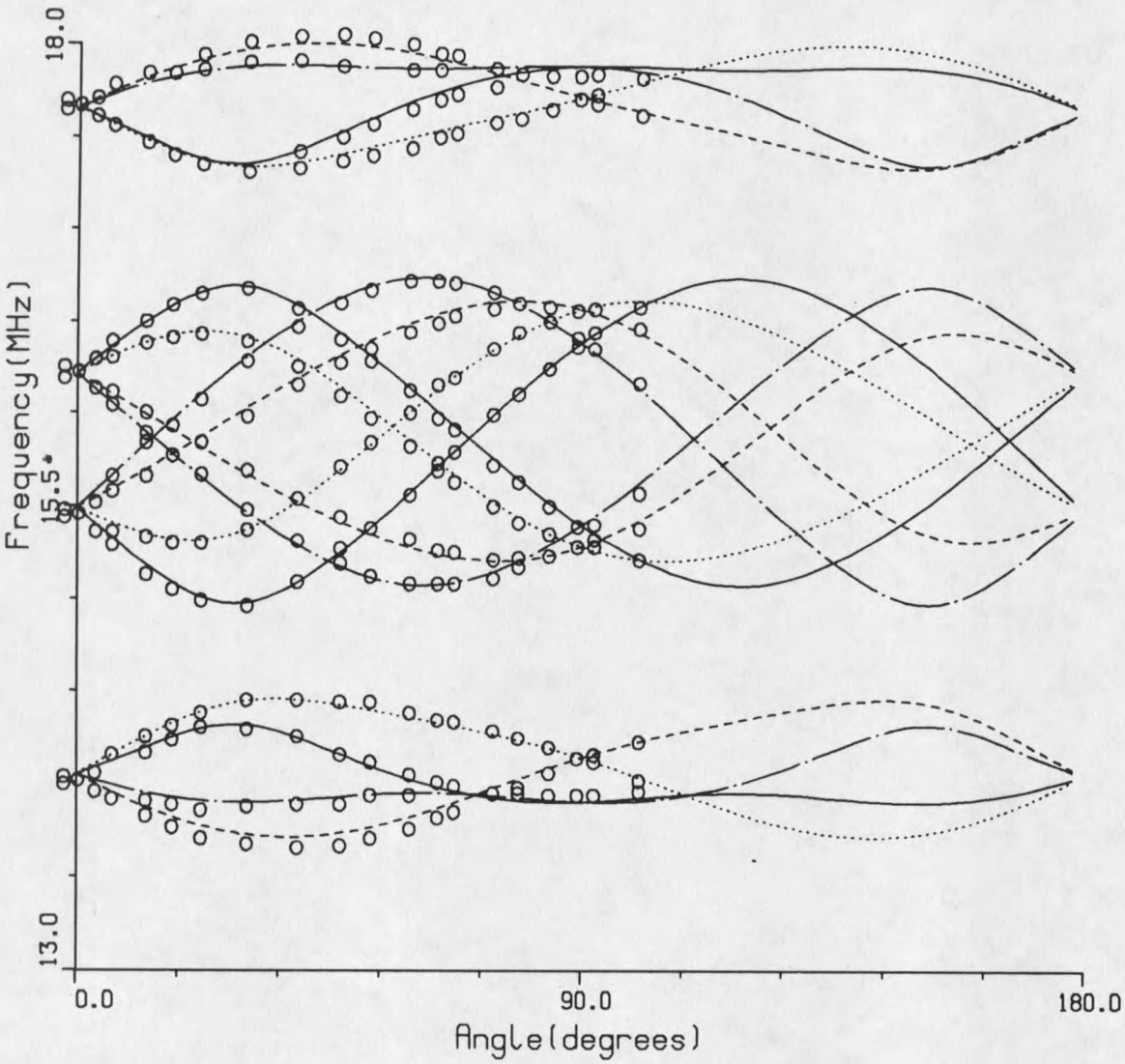

Figure 6.9 Constant field (H = 2.00 kG) angle-dependent ODNMR spectra on line D (515979 GHz) of $EuVO_4$. The angle is between the magnetic field and the crystal *c*-axis in the *c*-*a* plane. This spectrum is for the nominally 1/2 to 3/2 transition of ^{151}Eu. The circles are data points while the curves are theoretical fits. Curves of the same type arise from a single site orientation.

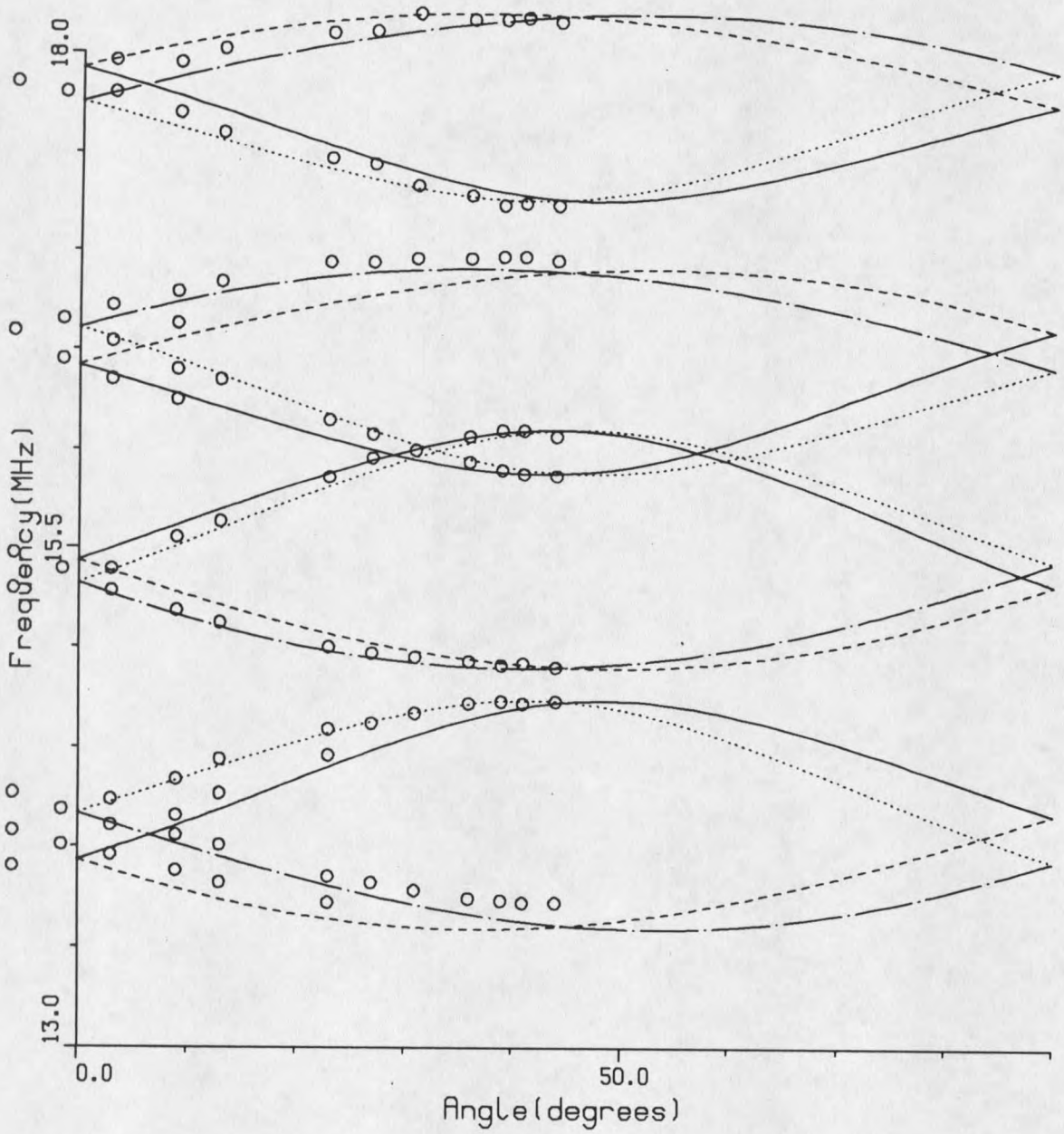

Figure 6.10 The ODNMR spectra with magnetic field in the *a*-*a'* plane for the same $EuVO_4$ transition as in Figure 6.9. Curves are the fit using the parameters obtained from the *c*-*a* plane data. The lack of perfect agreement is attributed to slight misalignment of the sample to the rotation axis.

than 1. Considering our discussions about the pseudoquadrupole effect of this site in section 5.5.3, most probably

$\alpha_x = 0.611$, $\alpha_y = 0.606$, and $\alpha_z = 1.415$,

and

$\alpha = 0^o$, $\beta = 28.2 \pm 0.5^o$, and $\gamma = 50 \pm 0.5^o$.

Earlier nuclear Zeeman holeburning studies of the $^5D_0$ state of this site (Cone *et al.* 1984) based on far less data yielded two fits for the direction of the crystal *c* axis in the defect coordinates. They are:

$\Theta = 83^o \pm 5^o$, $\Phi = 27^o \pm 5^o$

and

$\Theta = 66^o \pm 5^o$, $\Phi = 0^o \pm 5^o$

None of these agrees with the present fit for the $^7F_0$ state. Calculations using the present fit did not match the original $^5D_0$ data. It is not clear which fit should be correct for the $^5D_0$ state. Hansen's conclusion (1990) preferring the second fit should be regarded as false because of his incorrect assignment of the levels.

Line A (1.089220, 515868GHz)

This site has the strongest $^7F_0$ - $^5D_0$ transition line in all late growths. Its intensity is about ten times stronger than any other line in this region. Time-resolved fluorescence (TRF) showed a strong transfer of energy from this site to others. The TRF showed that the fluorescence lines from the acceptor sites gained intensity with time and reached maxima at about 50 μs. The fluorescence lines directly from the site being pumped had a lifetime of about 50 μs, indicating a simple transfer process between the two kind of sites. The three $^7F_1$ levels for line A were at 322, 389, and 391 cm^{-1}.

The $^5D_0$ - $^7F_2$ fluorescence was more complicated. Though we did see fast and slow lines, there were too many fast lines for a clear determination of the $^7F_2$ levels associated with this site.

The $^5D_0$ quadrupole splittings were studied by holeburning and found to be well fitted by P = 6.84, 17.5 MHz for the two isotopes and a single value of $\eta = 0.64$.

The $^7F_0$ ODNMR spectrum of this line showed clean resonance peaks at 13.53, 24.08, 34.76, 37.66, and 60.93 MHz. The last peak expected at 95.69 MHz was not observed probably due to the weak response of the RF coil in that frequency region. These numbers gave P = 6.135 MHz and $\eta = 0.315$ for ^{151}Eu, and P = 15.56 MHz and $\eta = 0.337$ for ^{153}Eu. The difference in the asymmetry parameter was evidence for the pseudoquadrupole effect. The ratio for the P's was 2.536, not far from the value given in the literature (2.550), implying that the pseudoquadrupole effects are small. The angular dependent Zeeman ODNMR results for the ^{151}Eu "1/2 to 3/2" transition are shown in Figure 6.11 and Figure 6.12 along with the fitted curves. Figure 6.11 gives the results with the magnetic field in the *c-a* plane. The angle θ denotes the angle between the magnetic field and the *c*-axis in this plane. Considering our discussion of the geometry consequences, there can be a maximum of 16 lines, whereas in this spectrum there are a maximum of 12 lines, implying that the coordinates must be tilted only in the *c-a* plane so that in our experimental geometry, two of the sites (four of the eight, more rigorously) are equivalent. Expressed in Euler angles, we have the defect coordinate system defined by $\alpha = 0$, $\beta = 10.7^o$, $\gamma = 0$.

An important feature of this spectrum is that around the *a*-axis, there are two groups of transitions. One group collapses around the center while the others are farther out in energy. This implies that considerable quenching of the nuclear magnetic moment occurred corresponding to the inner group. Nonlinear fitting gives the nuclear quenching factors as $\alpha_x = 0.96(2)$ or $1.04(2)$, $\alpha_y = 0.713(5)$, $\alpha_z = 0.700(5)$, the larger uncertainty

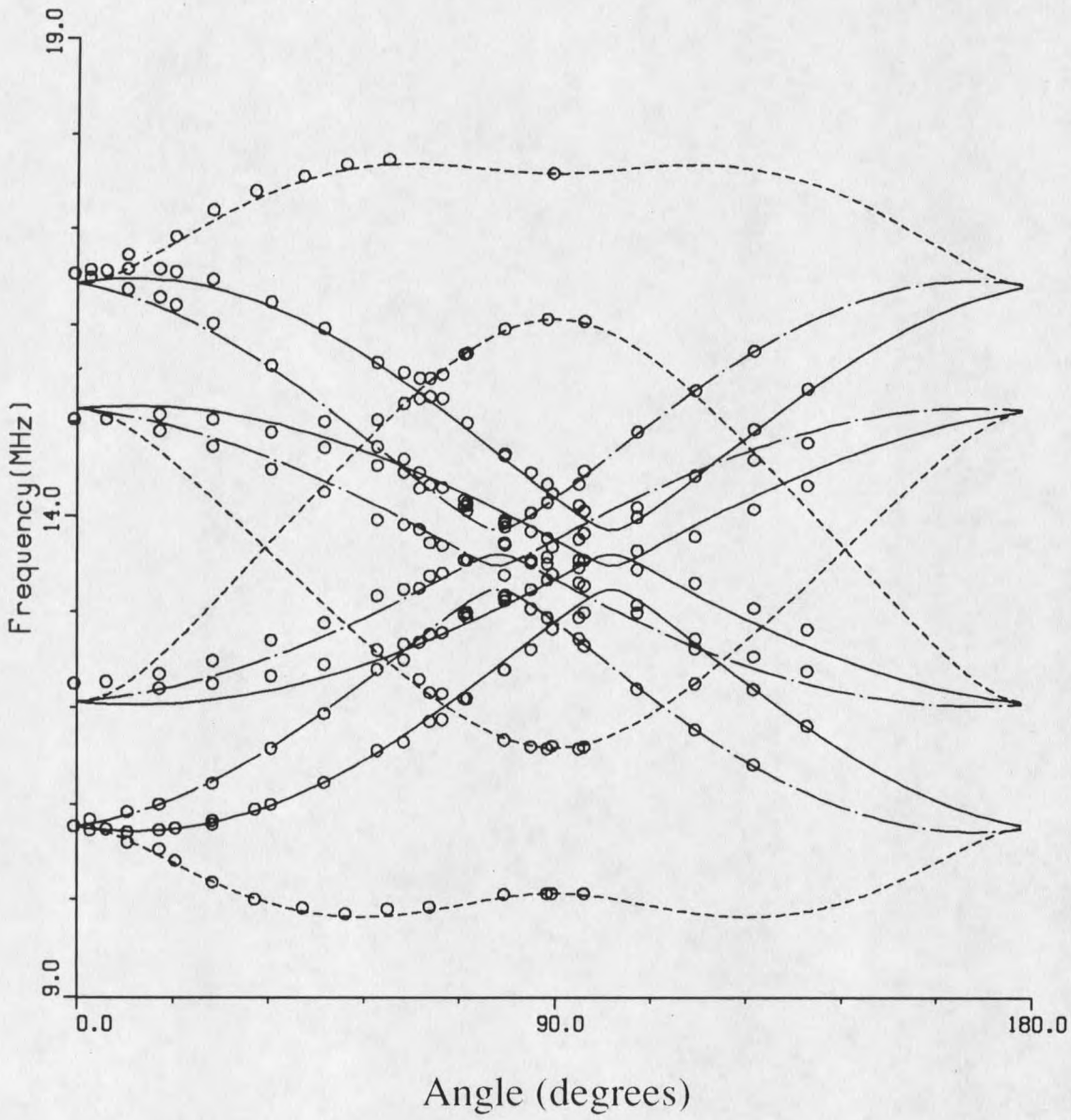

Figure 6.11 Constant field (H = 5.00 kG) ODNMR spectra as a function of the angle between the field and the *c*-axis in the *c*-*a* plane . The data are for the ^{151}Eu "1/2 - /3/2" transition for the defect line at 515868 GHz or 17207.50 cm^{-1} in $EuVO_4$.

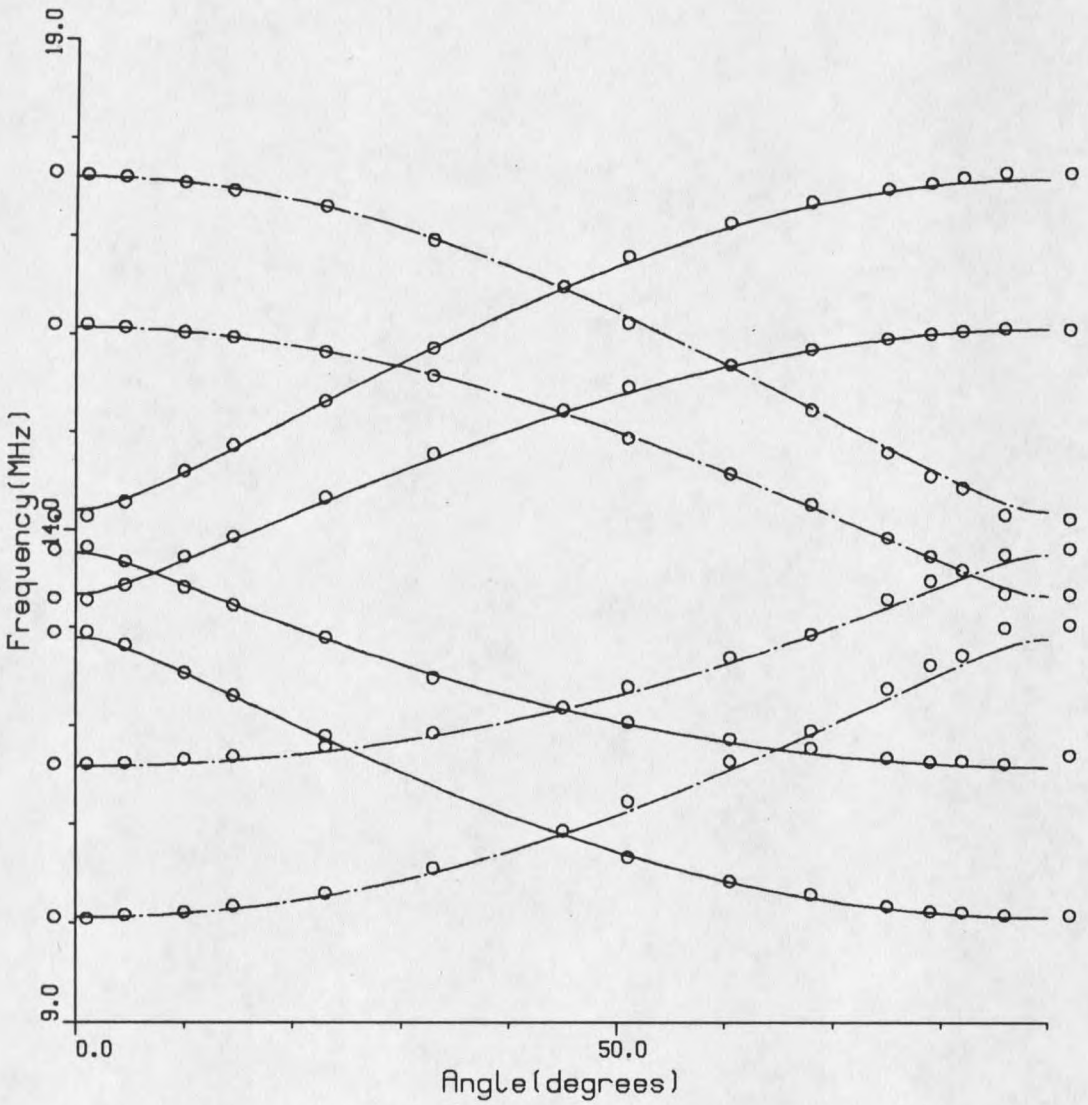

Figure 6.12. Constant field (H = 5.00 kG) ODNMR spectrum for the same $EuVO_4$ transiton as that shown in fig. 6.12, but with the field direction being rotated in the *a-a'* plane. The lines are the fit to the data based on the parameters obtained from fig. 6.12; no further adjustment of the paramaters was neccesary. This is a very special case that all the defect sites are equivalent along the 45° plane, so that only 4 lines are seen at 45°.

in the α_x fit being mainly due to the sensitivity of the data relative to the field direction in the *a*-axis region. The two values of α_x are again due to the problem of extracting α_x from the $|1-\alpha_x|$ value. Using 0.96 for α_x, the sum of the inverse of the shielding parameters is 3.87. Using 1.04 for α_x, it is 3.79. Changing the values of α_y and α_z will make this sum far from the value 4, so their values should be considered well determined.

From our TRF data, we can calculate the nuclear shielding factors. We cannot require this to give a perfect fit since it is possible that the nuclear quantization axes arenot exactly the same as the $^7F_1$ crystal field axes. If we use $\langle r^{-3} \rangle$ as 49.6 $Å^{-3}$, then we calculate α_i's to be 0.903, 0.745, and 0.741.

Line # 39 of Growth I

There are two strong high energy lines in the $^7F_0$ - $^5D_0$ defect spectra for the crystals grown with KF flux. These lines have been studied by time-resolved fluorescence (Cone and Leask, private communications), nuclear Zeeman holeburning (Lazzouni 1988 and Hansen 1990), and ODNMR (Hansen 1990). They are labeled as line #39 and line #41 of growth I and growth J. Line #39 is at 516389 GHz. A weaker line just above line #39 is called line #40. Line #41 is at 516635 GHz.

These lines are well separated from other defect lines and holeburn very readily. Lazzouni (1988) studied line #39 by nuclear Zeeman holeburning, and gave the direction of the nuclear quadrupole z axis at $\theta = 69.5^o$ and $\phi = 45^o$ in the crystal coordinate system. Hansen (1990) remeasured this line and obtained very similar spectra (figures 8.7 to 8.10), but his interpretation of the data led him to put this direction at $\theta = 45^o$, and $\phi = 45^o$ for the $^5D_0$ state. This large discrepancy is due to the assignment of the zero field holeburning lines. Lazzouni interpreted this spectrum with

$P = 11.1$ MHz $\quad \eta = 0.85 \quad$ for ^{151}Eu

$P = 30.0$ MHz $\quad \eta = 0.85 \quad$ for ^{153}Eu

while Hansen gave

$P = 19.6$ MHz $\quad \eta = 0.13 \quad$ for ^{151}Eu

$P = 48.4$ MHz $\quad \eta = 0.13 \quad$ for ^{153}Eu.

Angle-dependent ODNMR data were measured in this work on line #39 with H = 3.00 kG in the *c-a* plane. Data were taken for both the "1/2 -3/2" and the "3/2 - 5/2" transitions. Initial fitting was done on the "1/2 - 3/2" transition. Two sets of parameters were generated by the fitting program with comparable fitting quality. They are:

(1) ($\alpha = 0$, $\beta = 20\pm2^o$, $\gamma = 90^o$; $|1-\alpha_x| = 0.44$, $|1-\alpha_y| = 0.32$, and $|1-\alpha_z| = 0.71$)

(2) ($\alpha = 0$, $\beta = 70\pm2^o$, $\gamma = 90^o$; $|1-\alpha_x| = 0.437$, $|1-\alpha_y| = 0.46$, and $|1-\alpha_z| = 0.47$)

Using these parameters, we predicted the "3/2-5/2" transition spectrum. Predictions made from the first set of parameters did not match the data. Predictions made from the second set of parameters matched the data nicely. The spectra for the lower transition are shown in Figure 6.13. The spectra for the higher transition are shown in Figure 6.14. Since the quenched magnetic moment is quasi-isotropic and too large ($|1-\underline{\alpha}|$ is expected to be 0.2 for isotropic quenching), one of the α_i's must be larger than 1, but it is not at all clear which one it should be.

Though the $^7F_0$ ODNMR data for line # 39 are fitted nicely, we cannot use that fit to determine which interpretation of the $^5D_0$ spectra is correct, since the excited state and ground state quadrupole interaction may possibly have different principal axes.

The $\gamma = 90^o$ is important here, though at first glance this is equivalent to $\gamma = 0^o$, certainly when $\eta = 0$. But since $\eta \neq 0$ for this line, the quadrupole coupling constant is different in the x and y directions. From the convention of defining the axes, the z direction has the largest field gradient, the y direction has the intermediate field gradient but has the opposite sign, and x is the direction with the smallest field gradient. For this site, as for line A of growth A, the defect nuclear quadrupole coordinate system is tilted

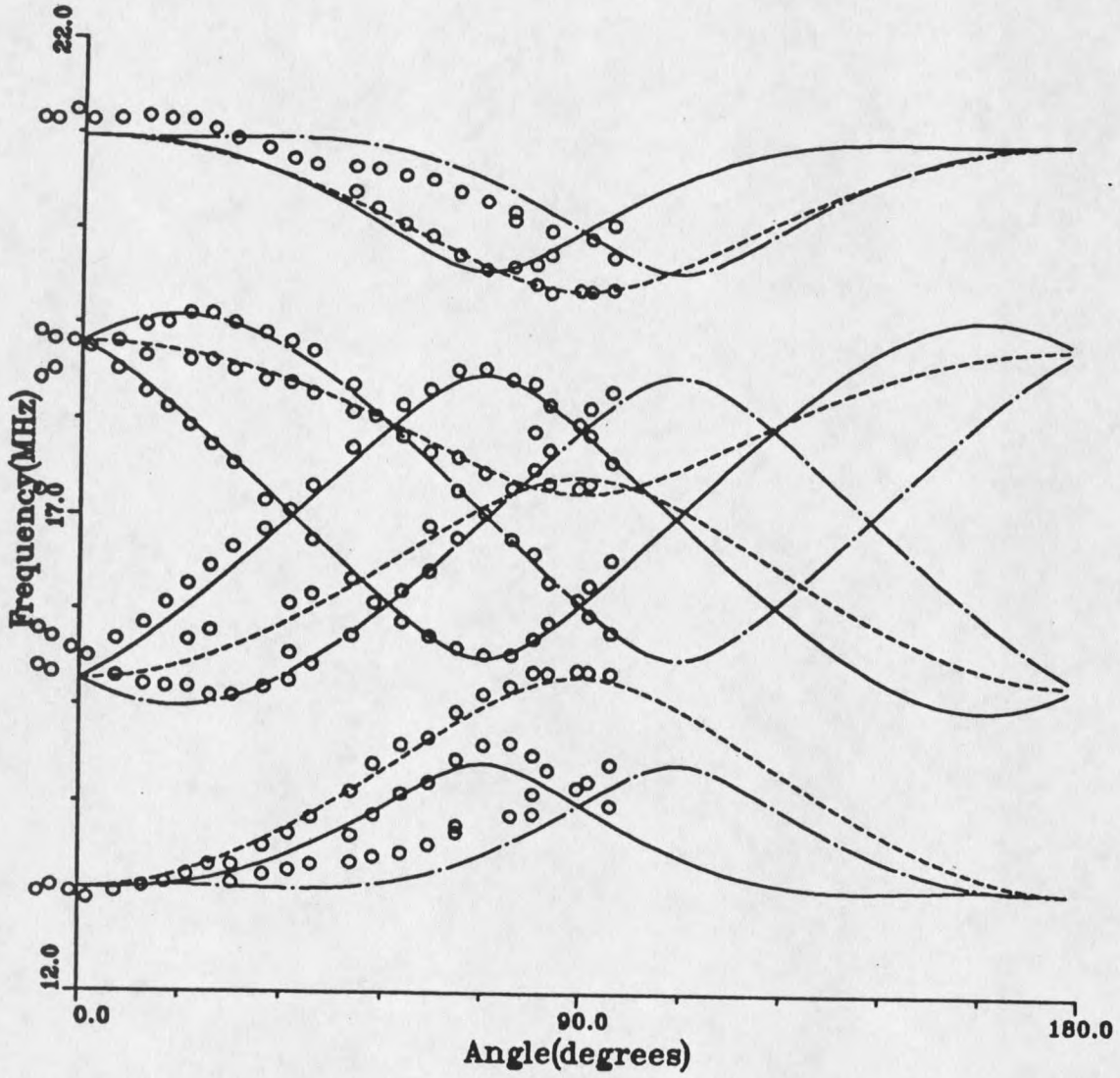

Figure 6.13 Constant field (H = 3.00 kG) angle-dependent ODNMR spectrum for line #39 of the growth I $EuVO_4$ Crystal. The field is in the *c-a* plane. Only the ^{151}Eu "1/2 - 3/2" transitions are shown.

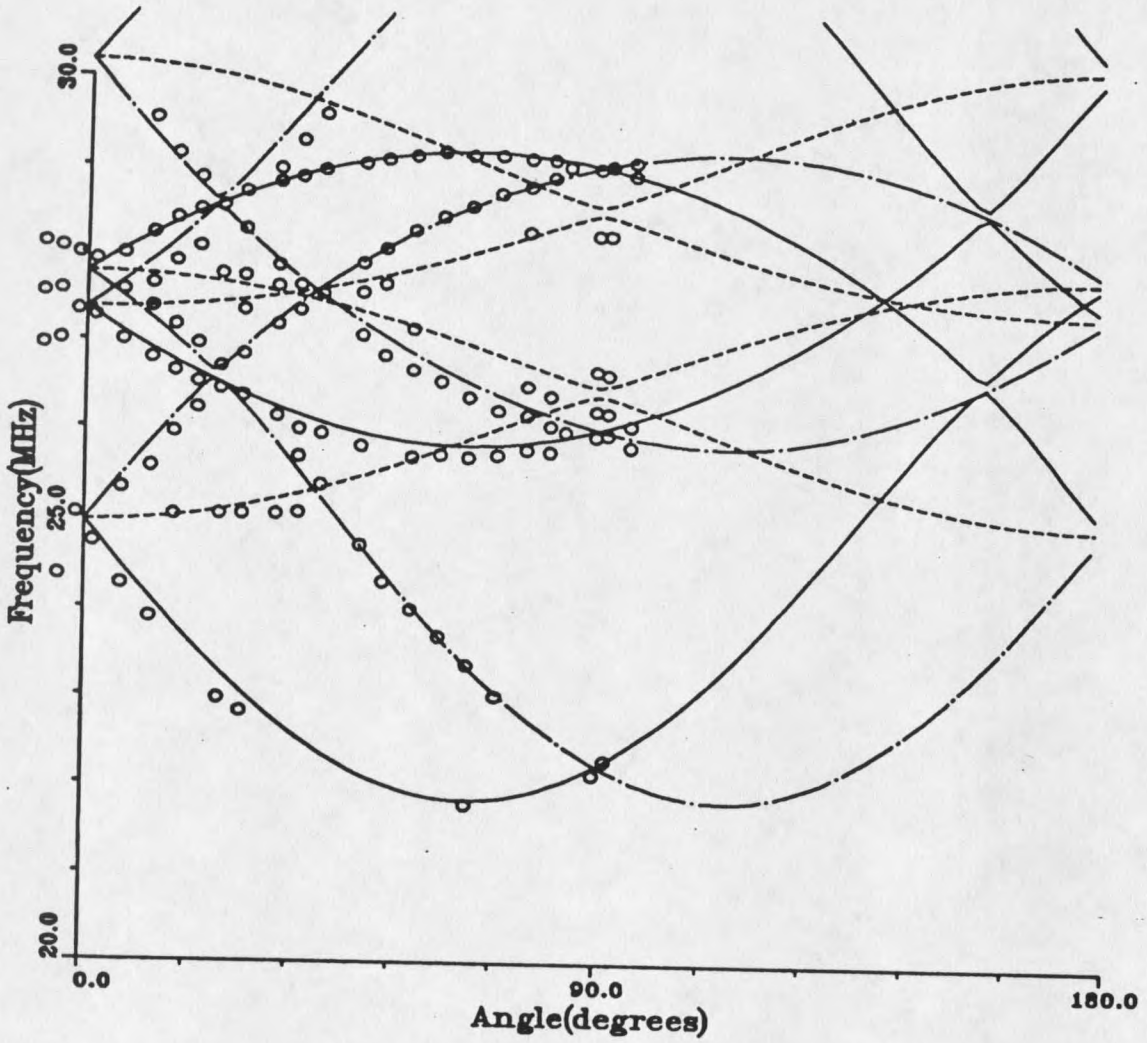

Figure 6.14 Constant field (H = 3.00 kG) angle-dependent ODNMR spectrum for line #39 of the growth I $EuVO_4$ Crystal. The field is in the *c-a* plane. Only the ^{151}Eu "3/2 - 5/2" transitions are shown.

only in the *c-a* plane. But, unlike line A. where the defect z-x plane overlaps the crystal *c-a* plane, the defect y-z plane overlaps the crystal *c-a* plane for line #39. This is equivalent to saying that the y axis is 20±2° away from the crystal *c* axis in the *c-a* plane, and the quadrupole x axis is along the *a*-axis.

Angle-dependent ODNMR has also been carried out on line #41. Due to the difficulty in determining whether $\eta = 0$. or $\eta = 1$ for that site, a reasonable fit has not been realized, but preliminary calculations with a uniform nuclear magnetic shielding factor of 0.42 and with $\Theta = 75°$, and $\Phi = 48°$ (Hansen's fit) do not fit the angle-dependent data.

Line E (1.089676, 516081 GHz)

This is the highest energy defect line in the $^7F_0$ - $^5D_0$ map for the growth A crystal. It holeburns most readily. Zero field ODNMR gave a very clean signal. Because this line is weaker overall than other lines we studied, the signal at a field was not very good. But reasonable data were taken with the magnetic field in the *c-a* plane and in the *a-a'* plane.

The signal corresponding to the nominally $\Delta I_z = \pm 2$ transitions was very weak. There were many missing points in the spectra. This presented a problem in the fitting because we could not be sure which transition belonged to which site. Further efforts must be taken to clarify the situation.

Lines F and G (515815, 515811 GHz)

These two sites have an energy difference of only about 4 GHz. They have similar intensities and always appear as a pair in the $EuVO_4$ crystals. They have very similar ODNMR patterns with similar P and η. The ODNMR spectra in a magnetic field are also very interesting. The Zeeman spectra of the "1/2 to 3/2" transition of ^{151}Eu show

very similar patterns for both lines, with similar splittings and similar ratio between the gaps. The linear Zeeman spectra with the magnetic field along both the *c* and *a* directions are shown in Figures 6.15 and 6.16. When the field is along the *c* direction, they are both almost linear. The spectra in the *a* direction are more interesting. They are already nonlinear at a field of 3 kG. There should be more peaks. Only the strongest peaks can be identified in a field due to the weak spectra. The spectrum for line F has two peaks around the center. Both of them curve up with the field. The spectrum for line G has only one strong line at the center. It is still very strong at a field of 4 kG. This may mean that it corresponds to the two central peaks of line F. The two stronger lines on both side are also similar for both line F and line G. Due to the weak signal, the angle-dependent data were not complete. But the magnetic moment was clearly anisotropic.

These two lines must have very similar local environments. They are probably due to the same defect. They also could be different neighbors of the same vacancy site or the neighbors of an off-center impurity or substitution.

Line O (515571 GHz)

This line has $\eta = 0$ for the ground state, corresponding to an axial case, but since ODNMR has been observed at zero field with the RF along the *c*-axis of the crystal, there must be a small departure from complete axial symmetry or else the axis is tilted. With a magnetic field in the *a* direction, the lowest transition splits into two peaks as would be expected for an axial system, since the $\Delta I_z = \pm 2$ transitions are not allowed. However, the upper branch shows very small splittings into several weak peaks at high fields. The splittings of these two peaks are not symmetric to the zero field position. The angle dependent study in the *a-a* plane shows that there are some changes in the

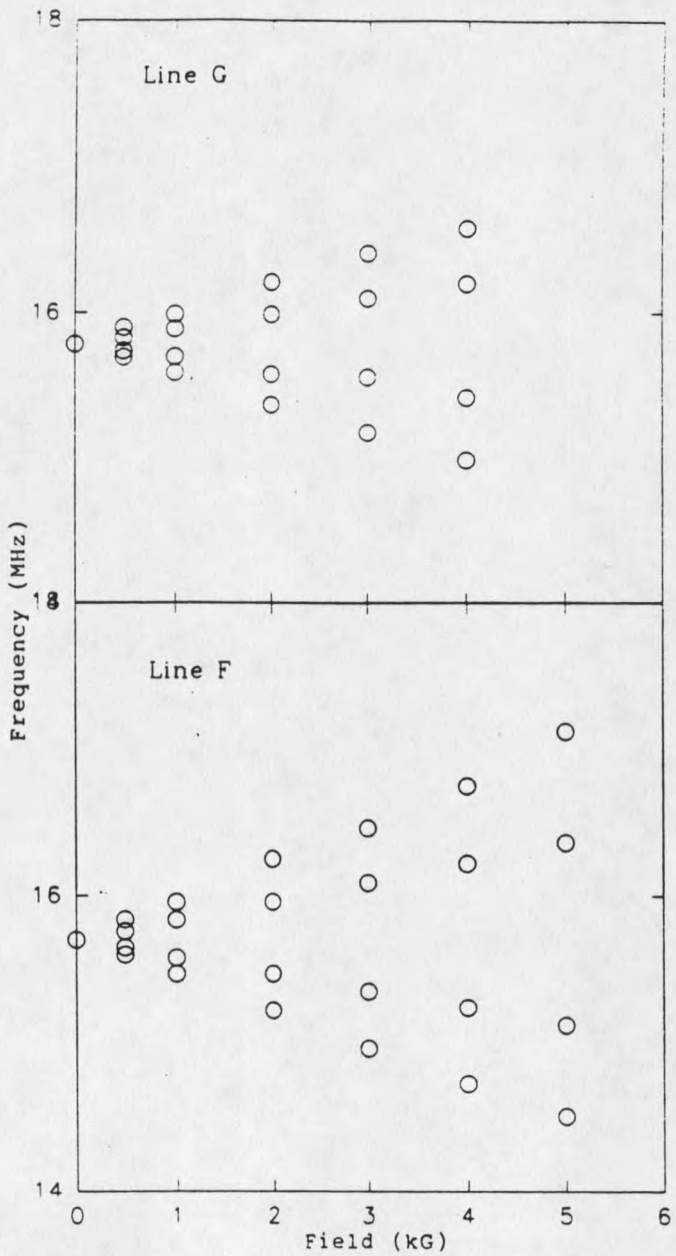

Figure 6.15 Zeeman effect of the ODNMR spectra of lines F and G with the magnetic field along the *c*-axis in $EuVO_4$.

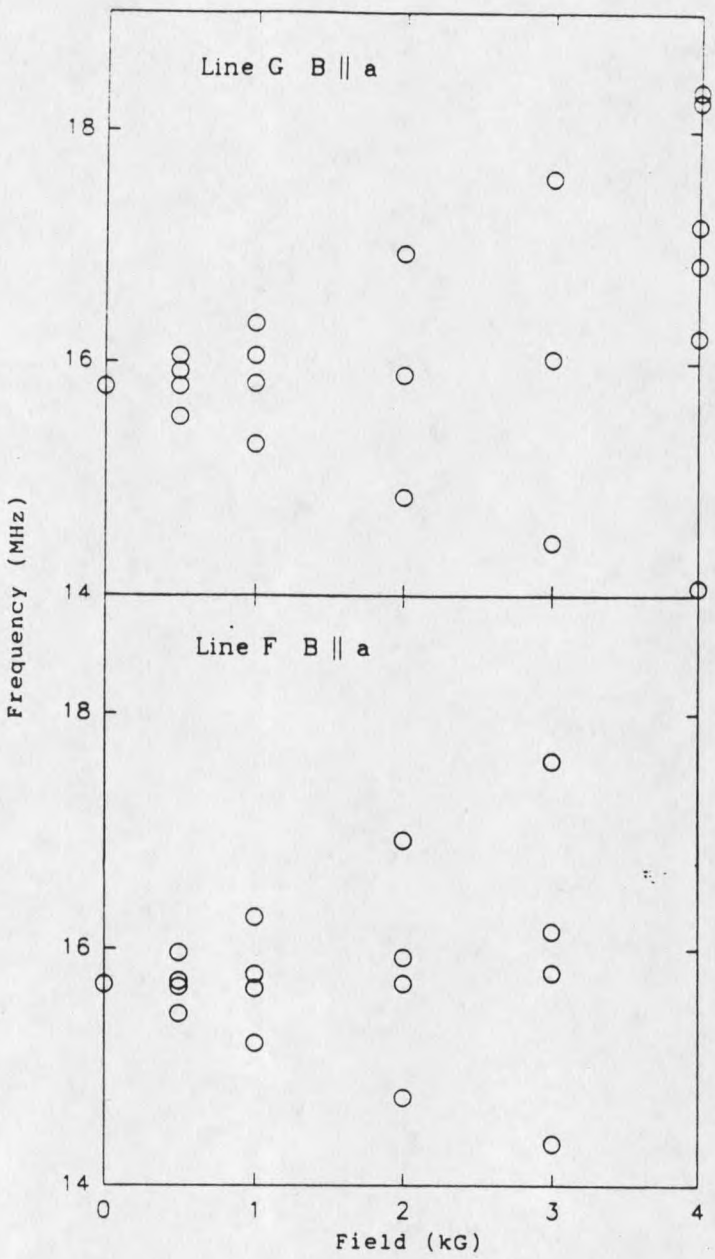

Figure 6.16 Zeeman effect of the ODNMR spectra of lines F and G with the magnetic field along the *a*-axis in $EuVO_4$.

positions of these peaks with angle, but these changes are very small. We have a near axial case in this line.

Other lines with $\eta = 0$ have better axial approximations. The line at 515520 GHz and 515554 both failed to show any ODNMR signal with the RF along the c direction. In the 515554 GHz line, the excited state quadrupole interaction has a non-zero value of η.

Possibility of ODNMR on the Intrinsic Site

It is difficult to carry out ODNMR on the field enhanced intrinsic transition because at too low a field, this transition may be comparable in intensity to the defect lines that are degenerate accidentally with the intrinsic line. At higher fields, on the other hand, the overall splittings will not be as sensitive to the quadrupole splittings as in the case of low fields used above. Although this should still be feasible, a better way to study the intrinsic site would perhaps be to use a green laser to excite the allowed $^7F_0$ to $^5D_1$ transitions.

The discussion at the end of the last chapter indicated that the intrinsic site could have very small quadrupole splittings. For example, the Eu^{3+} C_{4v} center in CaF_2 has a ground state quadrupole splitting described by P = 2.42 MHz; SrF_2 and BaF_2 have P = 0.89 MHz and 0.975 MHz, respectively (Silversmith and Macfarlane, 1992). The $^7F_1$ crystal field splittings in CaF_2, SrF_2 and BaF_2 are 147 cm^{-1}, 105 cm^{-1} and 67 cm^{-1}, respectively. If the relationship between $^7F_1$ splittings and the value of P (both determined at least in part by the value of B_{20}) is at all similar in the vanadates and arsenates, the small $^7F_1$ splittings in $EuVO_4$ (~10 cm^{-1}) make very small values of P (<0.5 MHz) seem likely. It may be feasible to drive the hyperfine levels to the high-field regime and record all the transitions in order to produce a satisfactory data analysis.

Conclusions

Using ODNMR, we have studied the defect sites of stoichiometric $EuVO_4$ for which we have no predetermined structural information. From the Zeeman ODNMR spectra, we were able to determine the principal directions of the nuclear quadrupole interaction for these sites, as well as the anisotropic nuclear magnetic moment of the ground state. This is the first time this kind of information has been determined unambiguously for an unknown low symmetry defect site.

Among the sites we have studied, two (line A and line #39) have one axis coincident with one of the crystal axes. For line A, the defect y axis and the crystal *a*-axis coincide. For line #39, the defect x axis coincides with the crystal *a*-axis. For line D, none of the interaction axes coincides with a crystal axis, but still, the z axis is in the *c*-*a* plane. This information about the quadrupole axes and the magnetic quenching should prove very useful in the study of unknown defect sites. Models based on this information may lead to the final determination of the lattice defects that cause these defect lines.

APPENDICES

APPENDIX I

CONVERSION OF WAVEMETER READINGS

This home-made wave meter is essentially a Michelson interferometer based on the design of Kowalski *et al.*. (1975).

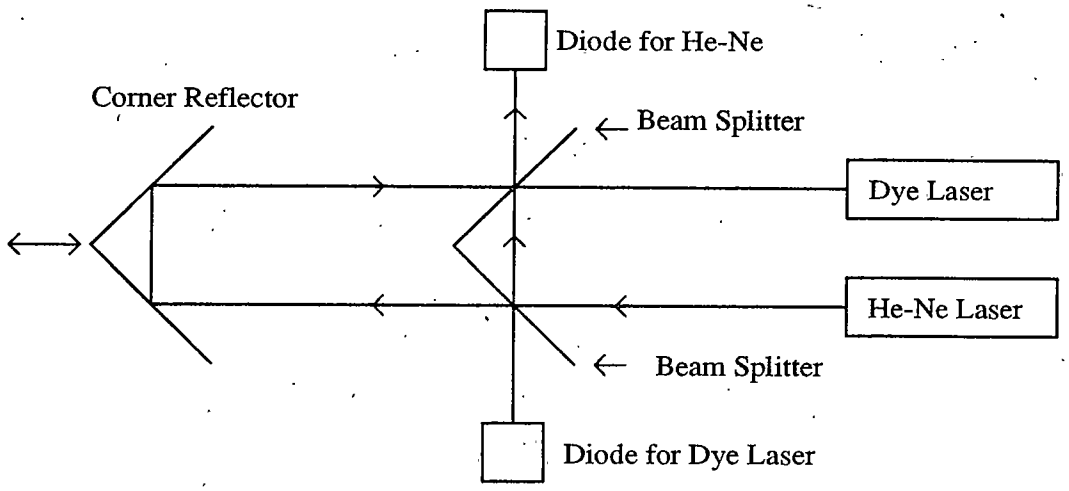

We have shown the light propagation direction only for the He-Ne. The Dye laser beam travels in the opposite direction. The corner reflector moves on a track that is parallel to the optical table. When the corner reflector moves a distance L, the He-Ne beam will go through $n_{HeNe}=2L/\lambda_{HeNe}$ fringes and the dye laser will go through $n_d=2L/\lambda_{dye}$ fringes. The ratio between the fringe numbers will be the inverse of the ratio of the wavelengths.

Conversion of this ratio to the dye wavelength is straight forward. From the wavelength in standard air (15°C, 760 mmHg), we can calculate the index of refraction by Edlen's formula.

$$n = 1 + 6432.8\times10^{-8} + \frac{2{,}949{,}810}{146\times10^{8}-\sigma^{2}} + \frac{25{,}540}{41\times10^{8}-\sigma^{2}} \qquad \text{for } \lambda>2000\text{Å}$$

Then, $\sigma=1/\lambda=1/n\lambda_{air}$ is the vaccum wavenumber.

There are additional corrections for the index of refraction in nonstandard air, but for most of our applications, the formula above is accurate enough.

A FORTRAN program was written to calculate the vaccum wavenumber and the index of refraction for a given wavelength in air. The pressure and temperature corrections were also included. Unfortunately, the original source code was deleted from the computer accidentally by somebody. There is only an executable version of the program left. Guangming Wang has written a new version in C language).

For our applications using the R6G dye, the wavelength is around 570-610 nm. The index of refraction in air changes from 1.0002774 to 1.0002768, so there is only a change in the 7th digit. If we take this number to be 1.0002771, and use 6328.1575 Å for the He-Ne wavelength, then

$$\sigma=1/\lambda=1/n\lambda_{air}=(\lambda_{He\text{-}Ne}/\lambda_{Dye})/1.0002771/6328.1575=15798.010\lambda_{He\text{-}Ne}/\lambda_{Dye}\ cm^{-1}$$

and

$$\nu=473612.43\ \lambda_{He\text{-}Ne}/\lambda_{Dye}\ GHz$$

APPENDIX II
OBSERVED AND CALCULATED ENERGY LEVELS

The $^5D_1$ and $^5D_2$ levels were determined from absorption. The $^5D_0$ levels were determined in a magnetic field via laser excitation and were measured by the wavemeter. The ^7F_J levels were determined from fluorescence originating from both the $^5D_0$ and $^5D_1$ levels. The conversions between the two popular systems of group theory labelings in D_{2d} symmetry are:
$\Gamma_1 = A_1, \Gamma_2 = A_2, \Gamma_3 = B_1, \Gamma_4 = B_2, \Gamma_5 = E$.
Levels labeled with * were not used in the crystal field calculations.

Energy levels of $EuVO_4$ (T=1.5 K)*

Europium vanadate has a tetragonal structure with cell dimensions a = 7.2373 Å, c = 6.3661 Å at room temperature. The rare earth sites have D_{2d} symmetry. Levels are labeled using D_{2d} representations.

Terms	Cf label	Energy (cm^{-1})	Calculated	$E_{obs} - E_{cal.}$
$^7F_0$	A_1	0	0.	
$^7F_1$	A_2	359.3	364.1	-4.9
	E	369.5	379.4	-9.9
$^7F_2$	B_2	936.8	941.2	-4.4
	A_1	994.	989.4	4.6
	E	1046.	1046.2	-0.2
	B_1	1117.	1120.8	-3.8
$^5D_0$	A_1	17196.7	17198.2	-1.55
$^5D_1$	A_2	18951.3	18954.5	-3.2
	E	18954.7	18955.2	-0.5
$^5D_2$	B_1	21379.8	21404.8	-25.
	E	21414.6	21421.	-6.4
	A_1	21435.7	21434.6	1.1
	B_2	21469.5	21446.8	22.7
$^5D_3$	B_1	24260.1	24273.1	-13.
	A_1	24271.8	24272.7	-0.9
	E	24271.9	24291.8	-19.8
	E	24312.4	24304.9	7.5
	B_2	24317.5	24300.4	17.1

* The $^5D_2$ B_1 and A_1 levels and all the $^5D_3$ levels are quoted from Hansen thesis.

From room temperature absorption experiments, we found the ^7F and ^5D energy levels for $J \leq 2$ were:

Terms	Cf label	Energy (cm^{-1})
$^7F_0$	A_1	0
$^7F_1$	A_2	364.8
	E	369.9
$^7F_2$	B_2	946.4
	A_1	1000.5
	E	1051.8
	B_1	1120.8
$^5D_0$	A_1	17203.0
$^5D_1$	A_2	18958.5
	E	18961.2
$^5D_2$	B_1	21388.0
	E	21421.8
	A_1	21443.1
	B_2	21475.8

Energy levels of Eu:YVO_4 (T=1.5 K)

Yttrium vanadate has a tetragonal structure with cell dimensions a = 7.2373 Å, c = 6.3661 Å at room temperature. The rare earth sites have D_{2d} symmetry. Levels are labeled using D_{2d} representations.

Terms	Cf label	Energy (cm^{-1})	Calculated	$E_{ob.} - E_{cal.}$
$^7F_0$	A_1	0	0	0
$^7F_1$	A_2	336.2	344.7	-8.5
	E	380.0	392.7	-12.7
$^7F_2$	B_2	937.6	935.0	-2.6
	A_1	986.1	979.2	6.9
	E	1042.3	1053.7	-11.4
	B_1	1189.*?	1165	/
$^7F_3$	B_2	1858.1	1843.6	14.5
	A_2	1878.1 ?	1865.7	12.4
	B_1	1904.8	1910.6	-5.8
	E	1907.8	1904.9	2.9
	E	1960.2	1959.3	0.9
$^7F_4$	B_1	2583.8*	2650.6	/
	E		2820.7	
	B_2	2872.6	2874.1	-1.5
	A_1	2873.0	2873.3	-0.3
	A_2		2908.5	
	E	2994.1	2985.4	8.6
	A_1	3044.7	3041.3	3.4
$^7F_5$	(not complete)			
	E	3870.3	3866.9	3.4
	B_2	3918.4	3914.8	3.6
	E	3958.5	3952.0	6.5
	E	4025.0	4028.6	-3.6
$^7F_6$	(not complete)			
	B_2	4876.1	4875.4	-0.7
	E	4921.5	4928.8	-7.3
	B_2	4949.4	4953.4	-4.0

$^5D_0$	A_1	17184.91	17177.2	7.9
$^5D_1$	A_2	18934.7	18934.0	0.7
	E	18944.7	18945.5	-0.8
$^5D_2$	B_1	21362.5 ??		
		(From $^5D_2$ fluorescence data)		
	E	21400.0	21414.0	-14.0
	A_1			
	B_2	21459.7	21451.1	8.6

We also determined some of the energy levels of Eu:YVO_4 at room temperature from the absorption spectra. They are:

$^7F_0$	A_1	0
$^7F_1$	A_2	343.9
	E	380.5
$^5D_0$	A_1	17192.0
$^5D_1$	A_2	18941.0
	E	18951.0
$^5D_2$	B_1	21370.6
	E	21406.9
	A_1	21424.6
	B_2	21465.1

Energy levels of Eu:$LuVO_4$ (T=1.5 K)

Lutetium vanadate has a tetragonal structure with cell dimensions a = 7.0263 Å, c = 6.2329 Å at room temperature. The rare earth sites have D_{2d} symmetry. Levels are labeled using D_{2d} representations.

Terms	Cf label	Energy (cm^{-1})	CF calculated	$E_{ob.} - E_{cal.}$
$^7F_0$	A_1	0	0	0
$^7F_1$	A_2	314.2	317.4	-3.2
	E	390.2	406.2	-16.0
$^7F_2$	B_2	940.3	934.9	5.4
	A_1	978.7	973.1	5.6
	E	1038.5	1040.7	-2.2
	B_1	1200.	1195.2	4.8
$^7F_3$	A_2	1851.0	1841.1	9.9
	B_2	1861.2	1848.6	12.6
	B_1	1895.9	1888.1	7.8
	E	1907.	1898.2	8.8
	E	1967.7	1968.7	-1.0
$^7F_4$	B_1	2577.4	2584.9	-7.5
	E	2830.	2830.2	-0.2
	B_2	2876.7	2877.3	-0.6
	A_1			
	A_2			
	E	3003.	3009.2	6.2
	A_1			
$^7F_5$	(not complete)			
		3868*		
		3953*		
$^7F_6$	(not complete)	4841.7*		
		4937.7*		
		4959.7*		
$^5D_0$	A_1	17176.71	17171.1	5.6
$^5D_1$	A_2	18920.9	18918.3	2.6
	E	18937.7	18939.7	-2.
$^5D_2$	B_1			
	E	21388.9	21402.0	-13.1
	A_1			
	B_2	21452.5	21439.6	12.9

Energy levels of Eu:YPO_4 (T = 1.5 K)

Yttrium orthophosphate has a tetragonal structure with cell dimensions a = 6.8840 Å, and c = 6.0202 Å at room temperature. The rare earth sites have D_{2d} symmetry. Levels are labeled using D_{2d} representations.

Terms	cf label	energy (cm^{-1})	Cf Calculated	$E_{ob.} - E_{cal.}$
$^7F_0$	A_1	0	0	0
$^7F_1$	E	340.8	347.1	-6.3
	A_2	432.0	440.9	-8.9
$^7F_2$	B_2	904.8	911.3	-6.5
	A_1	1059.8	1060.3	-0.5
	E	1061.0	1062.1	-1.1
	B_1	1086.3	1091.7	-5.4
$^7F_3$	B_2	1827.2	1824.5	2.7
	A_2	1866.3	1869.8	-3.5
	E	1873.5	1883.4	-9.9
	B_1	1937.7	1942.5	-4.8
	E	1954.5	1950.1	4.4
$^7F_4$	B_1	2686.9	2689.1	-2.2
	E	2804.9	2812.4	-7.5
	A_1		2818.2	/
	B_2	2844.2	2853.1	-8.9
	A_2			
	E			
	A_1	3017.3	3016.8	0.5
$^7F_5$		not observed		
$^7F_6$		not observed		
$^5D_0$	A_1	17201.20	17202.0	0.8
$^5D_1$	E	18951.5	18953.2	-1.7
	A_2	18970.5	18983.5	-13
$^5D_2$	B_1			
	E	21426.1	21438.4	-12.3
	A_1			
	B_2	21468.5	21459.7	8.8

Energy levels of Eu:$LuPO_4$ (T=1.5 K)

Lutetium orthophosphate has a tetragonal structure with cell dimensions a = 6.7937 Å, and c = 5.9582 Å at room temperature. The rare earth sites have D_{2d} symmetry. Levels are labeled using D_{2d} representations.

Terms	cf label	Energy (cm^{-1})	Cal.	E_{ob}-$E_{cal.}$
$^7F_0$	A_1	0	0	0
$^7F_1$	E	349.3	355.9	-6.6
	A_2	411.0	414.7	-3.7
$^7F_2$	B_2	906.2	910.0	-3.8
	A_1			
	E	1058.3	1056.7	1.6
	B_1	1101.5	1106.0	-4.5
$^7F_3$	B_2	1826.7	1820.0	6.7
	A_2	1858.0	1860.7	-2.7
	E	1879.1	1884.0	-4.9
	B_1	1920.8	1932.5	-11.7
	E	1950.1	1941.4	8.7
$^7F_4$	B_1**	2671.1	2667.3	3.8
	E	2802.1	2801.1	1.0
	A_1			
	B_2	2846.4	2848.6	-2.2
	A_2			
	E			
	A_1	3017.3	3015.3	2.0
$^7F_5$		not observed		
$^7F_6$		not observed		
$^5D_0$	A_1	17186.47	17184.0	2.5
$^5D_1$	E	18937.4	18934.1	3.3
	A_2	18950.8	18953.8	-3.0
$^5D_2$	B_1	21362.4	21385.1	-22.7
	E	21406.8	21408.1	-1.3
	A_1	21415.8	21424.0	-8.2
	B_2	21452.6	21435.0	17.2

** This level is surprisingly low lying in all the dilute crystals. It was not observed initially in the fluorescence experiments because it was out of the expected range for $^7F_4$. But crystal field calculations using other levels predicted this position for it. Later experiments confirmed this prediction. Interestingly, Eu:LaF_3 also has such a level according to Carnall *et al.* (1988).

APPENDIX III
COORDINATE TRANSFORMATION USING EULER ANGLES

First, define an arbitrary new coordinate system relative to an old system. The old system is described by (x,y,z) and the new system will be described by (x',y',z'). Initially, the two systems coincide. The transformation will be described by three Euler angles. There are two conventions to define them.

1.From p.146, H. Goldstein, Classical Mechanics, (2nd edition, Addison-Wesley, Reading, 1980)

ϕ around z-axis first

θ around intermediate x'-axis

ψ around intermediate and final z'-axis

2.From A.R. Edmonds, Angular Momentum in Q.M.

α around z-axis first

β around intermediate y'-axis

γ around intermediate and final z'-axis

So, for the first rotation, we have the transformation of

$$D = \begin{bmatrix} \cos\alpha & \sin\alpha & 0 \\ -\sin\alpha & \cos\alpha & 0 \\ 0 & 0 & 1 \end{bmatrix}$$

In this case, $\alpha=\phi$. So this transformation works for both conventions.
For the second rotation, we have either

$$C = \begin{bmatrix} 1 & 0 & 0 \\ 0 & \cos\theta & \sin\theta \\ 0 & -\sin\theta & \cos\theta \end{bmatrix}$$ for the Goldstein convention, or

$$C = \begin{bmatrix} \cos\beta & 0 & -\sin\beta \\ 0 & 1 & 0 \\ \sin\beta & 0 & \cos\beta \end{bmatrix}$$ for Edmonds' convention.

The last rotation will be the same for both conventions.

$$B = \begin{bmatrix} \cos\gamma & \sin\gamma & 0 \\ -\sin\gamma & \cos\gamma & 0 \\ 0 & 0 & 1 \end{bmatrix}$$

And the grand transformation *A* after all these rotations will be

$$A = \mathrm{BCD} = \begin{bmatrix} \cos\psi\cos\phi \\ -\cos\theta\sin\phi\sin\psi & \cos\psi\sin\phi \\ +\cos\theta\cos\phi\sin\psi & \sin\theta\sin\psi \\ -\sin\psi\cos\phi \\ -\cos\theta\sin\phi\cos\psi & -\sin\psi\sin\phi \\ +\cos\theta\cos\phi\cos\psi & \sin\theta\cos\psi \\ \sin\theta\sin\phi & -\sin\theta\cos\phi & \cos\theta \end{bmatrix}$$

For the Goldstein convention. For the Edmonds convention, we have

$$A = \begin{bmatrix} -\sin\alpha\sin\gamma \\ +\cos\alpha\cos\beta\cos\gamma & \cos\alpha\sin\gamma \\ +\sin\alpha\cos\beta\cos\gamma & -\sin\beta\cos\gamma \\ -\sin\alpha\cos\gamma \\ -\cos\alpha\cos\beta\sin\gamma & \cos\alpha\cos\gamma \\ -\sin\alpha\cos\beta\sin\gamma & \sin\beta\sin\gamma \\ \cos\alpha\sin\beta & \sin\alpha\sin\beta & \cos\beta \end{bmatrix}$$

We will use Edmonds' convention which is also known as the quantum mechanics convention.

APPENDIX IV
FITTING PROGRAMS

```
      PROGRAM angle_fit
c     this program need to link with the program fdf
c     a fitting program to get the directions of the nuclear quadrupole
c     axes from angular dependent odnr zeeman data
c     x,y represent the data pairs
c     a holds the parameters to be fitted
c     b is the zeeman field at input and used as the measure of the
c     splittings later on
c     sig records the standard deviations for individual data points
c     chisq tells how good is the fit. chi squared
c     fdf is the function to calculate the function fitting into y and its
c     jacobian.  See numerical recipes for the uses of the subroutines
c     typed in capital letters

      implicit none
      integer i,j,k,l,ma,lista(20),mfit,ndata(16)
      real x(16,100),y(16,100),xl,a(20),b,xxx
      real sig(16,100),covar(20,20),alpha(20,20),chisq,alamda
      real alp,beta,gamma
      character title*20
      external fdf
c     total 8 parameters dependent, 6 are to be fitted
      mfit=6
      ma=6
c     xl is the conversion factor between degree and radian, π/180
      xl=0.01745329
      write(*,*)'added angle?'
      read(*,*)xxx
c     initialize the list of the parameters to be fitted
      do 1001 i=1,mfit
      lista(i)=i
1001  continue
c     input of the data
c     a fake deviation of each data point.
c     Better if we have them and read them in
c     namelist.dat is the file that contains all the filenames of the
c     different lines in the spectrum
      open(unit=2,status='old',file='namelist.dat')
      do 1111 i=1,16
      read(2,1112)title
                  if (title .eq. 'none')
                  then ndata(i)=0
                 goto 1111
                  end if
      open(unit=3,status='old',file=title)
```

```
      do 1113 k=1,100
      read(3,1114,end=1115)x(i,k),y(i,k)
      x(i,k)=(x(i,k)-xxx)*xl
1113  continue
1115  ndata(i)=k-1
      close(unit=3)
1111  continue
1112  format(a20)
1114  format(2f13.6)
      close(unit=2)
      do 3001 j=1,16
      do 3002 k=1,100
      sig(j,k)=0.04
3002  continue
3001  continue
c     input of initial known and guessed parameters
c     write(*,*)'what is the zeeman field?'
c     read(*,*)b
c     In the followibng case, the field is 3 kG
      b=3.*1.0559
c     1.0559 MHz/KG for 151Eu nuclei.
      write(*,*)'initial guess for the parameters'
      write(*,*)'input of the angles(degree):alp,beta,gamma'
      read(*,*)a(1),a(2),a(3)
      a(1)=a(1)*xl
      a(2)=a(2)*xl
      a(3)=a(3)*xl
      write(*,*)'input of the shielding parameters:Kx,Ky,Kz'
      read(*,*)a(4),a(5),a(6)
      a(4)=(1.-a(4))*b
      a(5)=(1.-a(5))*b
      a(6)=(1.-a(6))*b
c     a(4-6) correspond to betas now
c     required alamda <0 to initialize the program
      alamda=-0.1
      do 1002 j=1,100
      call mrqmin(x,y,sig,ndata,a,ma,lista,mfit,
     &          covar,alpha,mfit,chisq,fdf,alamda)
c     converting back to what we like to see
      write(*,*)a(1)/xl,a(2)/xl,a(3)/xl
      write(*,*)(1.-a(4)/b),(1.-a(5)/b),(1.-a(6)/b)
      write(*,*) chisq
      write(*,*)'give a one digit number to continue, 2 digit to stop'
      read(*,*)k
      if(k .gt. 9) then
```

```
      alamda=0.
      call mrqmin(x,y,sig,ndata,a,ma,lista,mfit,
     &     covar,alpha,mfit,chisq,fdf,alamda)
      write(*,*)a(1)/xl,a(2)/xl,a(3)/xl
      write(*,*)(1.-a(4)/b),(1.-a(5)/b),(1.-a(6)/b)
      write(*,*)chisq
      write(*,*)'done'
      goto 1014
      end if
1002  continue
1014  stop
      end

c     These routines are copied from Numerical recipes
      SUBROUTINE MRQMIN(x,y,SIG,NDATA,A,MA,LISTA,MFIT,
     *  COVAR,ALPHA,NCA,CHISQ,FUNCS,ALAMDA)
      PARAMETER (MMAX=20)
      DIMENSION X(16,100),Y(16,100),SIG(16,100),A(MA),LISTA(MA),
     * COVAR(NCA,NCA),ALPHA(NCA,NCA),ATRY(MMAX),
     * BETA(MMAX), DA(MMAX)
      DIMENSION NDATA(16)
      IF(ALAMDA.LT.0.)THEN
        KK=MFIT+1
        DO 12 J=1,MA
          IHIT=0
          DO 11 K=1,MFIT
            IF(LISTA(K).EQ.J)IHIT=IHIT+1
11        CONTINUE
          IF (IHIT.EQ.0) THEN
            LISTA(KK)=J
            KK=KK+1
          ELSE IF (IHIT.GT.1) THEN
            PAUSE 'Improper permutation in LISTA'
          ENDIF
12      CONTINUE
        IF (KK.NE.(MA+1)) PAUSE 'Improper permutation in LISTA'
        ALAMDA=0.001
      CALL MRQCOF(X,Y,SIG,NDATA,A,MA,LISTA,MFIT,ALPHA,BETA,
     * NCA, CHISQ, FUNCS)
        OCHISQ=CHISQ
        DO 13 J=1,MA
          ATRY(J)=A(J)
13      CONTINUE
      ENDIF
      DO 15 J=1,MFIT
```

```
          DO 14 K=1,MFIT
          COVAR(J,K)=ALPHA(J,K)
14        CONTINUE
          COVAR(J,J)=ALPHA(J,J)*(1.+
          ALAMDA) DA(J)=BETA(J)
15      CONTINUE
        CALL GAUSSJ(COVAR,MFIT,NCA,DA,1,1)
        IF(ALAMDA.EQ.0.)THEN
          CALL COVSRT(COVAR,NCA,MA,LISTA,MFIT)
          RETURN
        ENDIF
        DO 16 J=1,MFIT
          ATRY(LISTA(J))=A(LISTA(J))+DA(J)
16      CONTINUE
        CALL MRQCOF(X,Y,SIG,NDATA,ATRY,MA,LISTA,MFIT,COVAR,DA,
     *  NCA,CHISQ,FUNCS)
        IF(CHISQ.LT.OCHISQ)THEN
          ALAMDA=0.1*ALAMDA
          OCHISQ=CHISQ
          DO 18 J=1,MFIT
            DO 17 K=1,MFIT
              ALPHA(J,K)=COVAR(J,K)
17          CONTINUE
            BETA(J)=DA(J)
            A(LISTA(J))=ATRY(LISTA(J))
18        CONTINUE
        ELSE
          ALAMDA=10.*ALAMDA
          CHISQ=OCHISQ
        ENDIF
        RETURN
        END


c         called by mrqmin
        SUBROUTINE
        MRQCOF(X,Y,SIG,ndata,A,MA,LISTA,MFIT,ALPHA,BETA,
     * NALP,CHISQ,FUNCS)
        PARAMETER (MMAX=20)
        DIMENSION X(16,100),Y(16,100),SIG(16,100),ALPHA(NALP,NALP),
     *  BETA(MA),DYDA(MMAX),LISTA(MFIT),A(MA),ndata(16)
        DO 12 J=1,MFIT
          DO 11 K=1,J
            ALPHA(J,K)=0.
11        CONTINUE
```

```
          BETA(J)=0.
12        CONTINUE
          CHISQ=0.
          DO 151 JJ=1,16
            IF(NDATA(JJ) .LE. 1) GOTO 151
          DO 15 I=1,NDATA(JJ)
          CALL FUNCS(X(JJ,I),A,YMOD,DYDA,MA,JJ)
          SIG2I=1./(SIG(JJ,I)*SIG(JJ,I))
          DY=Y(JJ,I)-YMOD
            DO 14 J=1,MFIT
              WT=DYDA(LISTA(J))*SIG2I
              DO 13 K=1,J
          ALPHA(J,K)=ALPHA(J,K)+WT*DYDA(LISTA(K))
13            CONTINUE
              BETA(J)=BETA(J)+DY*WT
14          CONTINUE
            CHISQ=CHISQ+DY*DY*SIG2I
15        CONTINUE
151         CONTINUE
          DO 17 J=2,MFIT
            DO 16 K=1,J-1
              ALPHA(K,J)=ALPHA(J,K)
16          CONTINUE
17        CONTINUE
          RETURN
          END

c         called by Mrqmin
          SUBROUTINE COVSRT(COVAR,NCVM,MA,LISTA,MFIT)
          DIMENSION COVAR(NCVM,NCVM),LISTA(MFIT)
          DO 12 J=1,MA-1
            DO 11 I=J+1,MA
              COVAR(I,J)=0.
11          CONTINUE
12        CONTINUE
          DO 14 I=1,MFIT-1
            DO 13 J=I+1,MFIT
                IF(LISTA(J).GT.LISTA(I)) THEN
                COVAR(LISTA(J),LISTA(I))=COVAR(I,J)
              ELSE
                COVAR(LISTA(I),LISTA(J))=COVAR(I,J)
              ENDIF
13          CONTINUE
14        CONTINUE
          SWAP=COVAR(1,1)
```

```
      DO 15 J=1,MA
        COVAR(1,J)=COVAR(J,J)
        COVAR(J,J)=0.
15    CONTINUE
  COVAR(LISTA(1),LISTA(1))=SWAP
      DO 16 J=2,MFIT
      COVAR(LISTA(J),LISTA(J))=COVAR(1,J)
16    CONTINUE
      DO 18 J=2,MA
        DO 17 I=1,J-1
          COVAR(I,J)=COVAR(J,I)
17      CONTINUE
18    CONTINUE
      RETURN
      END

c       called by mrqcof
      SUBROUTINE GAUSSJ(A,N,NP,B,M,MP)
      PARAMETER (NMAX=50)
      DIMENSION A(NP,NP),B(NP,MP),IPIV(NMAX),INDXR(NMAX),
     * INDXC(NMAX)
        DO 11 J=1,N
        IPIV(J)=0
11    CONTINUE
      DO 22 I=1,N
        BIG=0.
        DO 13 J=1,N
          IF(IPIV(J).NE.1)THEN
            DO 12 K=1,N
              IF (IPIV(K).EQ.0) THEN
            IF (ABS(A(J,K)).GE.BIG)THEN
            BIG=ABS(A(J,K))
            IROW=J
            ICOL=K
                  ENDIF
                  ELSE IF (IPIV(K).GT.1) THEN
                  PAUSE 'Singular matrix'
                ENDIF
12            CONTINUE
            ENDIF
13        CONTINUE
      IPIV(ICOL)=IPIV(ICOL)+1
      IF (IROW.NE.ICOL) THEN
          DO 14 L=1,N
            DUM=A(IROW,L)
```

```
      A(IROW,L)=A(ICOL,L)
        A(ICOL,L)=DUM
14          CONTINUE
            DO 15 L=1,M
        DUM=B(IROW,L)
      B(IROW,L)=B(ICOL,L)
        B(ICOL,L)=DUM
15          CONTINUE
          ENDIF
          INDXR(I)=IROW
          INDXC(I)=ICOL
          IF (A(ICOL,ICOL).EQ.0.) PAUSE 'Singular matrix.'
          PIVINV=1./A(ICOL,ICOL)
          A(ICOL,ICOL)=1.
          DO 16 L=1,N
            A(ICOL,L)=A(ICOL,L)*PIVINV
16        CONTINUE
          DO 17 L=1,M
            B(ICOL,L)=B(ICOL,L)*PIVINV
17        CONTINUE
          DO 21 LL=1,N
            IF(LL.NE.ICOL)THEN
              DUM=A(LL,ICOL)
              A(LL,ICOL)=0.
              DO 18 L=1,N
                A(LL,L)=A(LL,L)-A(ICOL,L)*DUM
18            CONTINUE
              DO 19 L=1,M
              B(LL,L)=B(LL,L)-B(ICOL,L)*DUM
19            CONTINUE
            ENDIF
21        CONTINUE
22      CONTINUE
        DO 24 L=N,1,-1
          IF(INDXR(L).NE.INDXC(L))
          THEN
            DO 23 K=1,N
       DUM=A(K,INDXR(L))
              A(K,INDXR(L))=A(K,INDXC(L))
              A(K,INDXC(L))=DUM
23          CONTINUE
          ENDIF
24      CONTINUE
        RETURN
        END
```

```
c       the following is a subroutine to be used by the angle_fit program
c       it calculates eigenvalues of the nuclear quadruple hamiltonian and
c       the difference between certain two sets of the eigenvalue.
c       At the same time, it will calculate the jacobian relative to the
c       parameters
c       x is the angle data and y is the frequency data
c       a in the order of alpha,beta,gamma,bx,by,bz

        subroutine fdf(x,a,y,dyda,na,label)
        dimension a(na),dyda(na),b(6)
        y=f(a,x,label)
        do 11 i=1,na
        b(i)=a(i)+0.0001
        dyda(i)=(f(b,x,label)-y)/0.0001
        b(i)=a(i)
11      continue
        return
        end

c       depending which curve we are fitting to,the arguments of d should be
c       changed lup is the upper level
c       llo is the lower level of the transition
c       lal tells where we are looking
c       1----closest to the c-a plane
c       2 and 3 looking through ca' plane
c       4---- farthest
        function f(para,x,label)
        real para(7),x,a(12,12),d(12),v(12,12),p,eta,dir(3),eul(3,3),hpi,phi
        integer nrot,n,np,label,upper,lower
        external jacobi
        n=12
        np=12
        p=6.102
        eta=0.3869
        hpi=1.5707963
        pp=para(1)
        if (label .eq. 1) then
        upper=7
        lower=9
        else if(label .eq. 2) then
        pp=pp-hpi
        upper=7
        lower=9
        else if(label .eq. 3) then
```

```
pp=pp+hpi
upper=7
lower=9
else if(label .eq. 4) then
pp=pp+2.*hpi
upper=7
lower=9
else if(label .eq. 5) then
upper=7
lower=11
else if(label .eq. 6) then
pp=pp-hpi
upper=7
lower=11
else if(label .eq. 7) then
pp=pp+hpi
upper=7
lower=11
else if(label .eq. 8) then
pp=pp+2.*hpi
upper=7
lower=11
else if(label .eq. 9) then
upper=5
lower=9
else if(label .eq. 10) then
pp=pp-hpi
upper=5
lower=9
else if(label .eq. 11) then
pp=pp+hpi
upper=5
lower=9
else if(label .eq. 12) then
pp=pp+2.*hpi
upper=5
lower=9
else if(label .eq. 13) then
upper=5
lower=11
else if(label .eq. 14) then
pp=pp-hpi
upper=5
lower=11
else if(label .eq. 15) then
```

```
            pp=pp+hpi
            upper=5
            lower=11
            else
            pp=pp+2.*hpi
            upper=5
            lower=11
            end if
            dir(1)=sin(x)
            dir(2)=0.
            dir(3)=cos(x)
            call euler(pp,para(2),para(3),eul)
            call trans(eul,dir)
            call matrix(a,p,eta,dir,para)
            call jacobi(a,n,np,d,v,nrot)
            call eigsrt(d,v,n,np)
            f=d(upper)-d(lower)
            return
            end
c     c
            subroutine matrix(a,p,eta,dir,para)
            dimension a(12,12),a1(6,6),b(6,6),para(6)
            real eta,dir(3),p,bx,by,bz,x,y,z,xi,xi0
            integer i,j,k
c           this is to create a hamiltonian matrix for nuclear quadruple and
c           nuclear zeeman interaction, according to p.8.5 of Hansen thesis
c           real part of the matrix,symmetric
            bx=para(4)
            by=para(5)
            bz=para(6)
            do 1100 i=1,12
            do 1200 j=1,12
            a(i,j)=0.
1200        continue
1100        continue

            do 10 i=1,6
            do 20 j=1,i
            a1(i,j)=0.
20          continue
10          continue
            x=dir(3)*bz
            y=dir(1)*bx
            a1(1,1)=10.*p/3.+2.5*x
            a1(2,1)=sqrt(5.)/2.*y
```

```
      a1(3,1)=sqrt(10.)*eta*p/3.
      a1(2,2)=-2.*p/3.+1.5*x
      a1(3,2)=sqrt(2.)*y
      a1(4,2)=sqrt(2.)*eta*p
      a1(3,3)=-8.*p/3.+x/2.
      a1(4,3)=1.5*y
      a1(5,3)=a1(4,2)
      a1(4,4)=-8./3.*p-x/2.
      a1(5,4)=a1(3,2)
      a1(6,4)=a1(3,1)
      a1(5,5)=-2.*p/3.-1.5*x
      a1(6,5)=a1(2,1)
      a1(6,6)=10.*p/3.-2.5*x
      do 30 i=1,6
      do 40 j=i,6
      a1(i,j)=a1(j,i)
40    continue
30    continue

cc    imaginary part, b(i,j)=-b(j,i)
c     only three independent quatities
      x=by*dir(2)
      y=sqrt(2.)*x
      z=1.5*x
      x=sqrt(5.)/2.*x
      do 50 i=1,6
      do 60 j=1,i
      b(i,j)=0.
60    continue
50    continue
      b(2,1)=x
      b(3,2)=y
      b(4,3)=z
      b(5,4)=y
      b(6,5)=x
      do 70 i=1,6
      do 80 j=i,6
      b(i,j)=-b(j,i)
80    continue
70    continue

cc    completed
cc    need to put these two together
cc    |a1  -b|
cc    |b   a1|
```

```
c       this is a symmetric matrix
        do 110  i=1,6
        do 100  j=1,6
        a(i,j)=a1(i,j)
100     continue
110     continue
        do 130  i=1,6
        do 120  j=7,12
        a(i,j)=-b(i,j-6)
120     continue
130     continue
        do 150 i=7,12
        do 140 j=1,6
        a(i,j)=b(i-6,j)
140     continue
150     continue
        do 170 i=7,12
        do 160 j=7,12
        a(i,j)=a1(i-6,j-6)
160     continue
170     continue
        return
        end

c       the following gives the transformation matrix by euler angles
c       make sure the input for angles are in radians
        subroutine  euler(alp,bet,gam,eul)
        real alp,bet,gam,eul(3,3)
        eul(1,1)=-sin(alp)*sin(gam)+cos(alp)*cos(bet)*cos(gam)
        eul(1,2)=cos(alp)*sin(gam)+sin(alp)*cos(bet)*cos(gam)
        eul(1,3)=-sin(bet)*cos(gam)
        eul(2,1)=-sin(alp)*cos(gam)-cos(alp)*cos(bet)*sin(gam)
        eul(2,2)=cos(alp)*cos(gam)-sin(alp)*cos(bet)*sin(gam)
        eul(2,3)=sin(bet)*sin(gam)
        eul(3,1)=cos(alp)*sin(bet)
        eul(3,2)=sin(alp)*sin(bet)
        eul(3,3)=cos(bet)
        return
        end

        subroutine trans(eul,dir)
c       thos routine transforms the lab coordinates into the local
c       coordinates for the defects
        real eul(3,3),dir(3),x,y
        x=eul(1,1)*dir(1)+eul(1,2)*dir(2)+eul(1,3)*dir(3)
```

```
      y=eul(2,1)*dir(1)+eul(2,2)*dir(2)+eul(2,3)*dir(3)
      dir(3)=eul(3,1)*dir(1)+eul(3,2)*dir(2)+eul(3,3)*dir(3)
      dir(1)=x
      dir(2)=y
      return
      end


c     copied from numerical recipes, eigsrt puts eigenvalues in order
c        according to the magnitude
      SUBROUTINE EIGSRT(D,V,N,NP)
      DIMENSION D(NP),V(NP,NP)
      DO 13 I=1,N-1
         K=I
         P=D(I)
         DO 11 J=I+1,N
            IF(D(J).GE.P)THEN
               K=J
               P=D(J)
            ENDIF
11       CONTINUE
         IF(K.NE.I)THEN
            D(K)=D(I)
            D(I)=P
            DO 12 J=1,N
               P=V(J,I)
               V(J,I)=V(J,K)
               V(J,K)=P
12          CONTINUE
         ENDIF
13    CONTINUE
      RETURN
      END

c        Jacobi method to find the eigenvalues of a matrix
      SUBROUTINE JACOBI(A,N,NP,D,V,NROT)
      PARAMETER (NMAX=100)
      DIMENSION A(NP,NP),D(NP),V(NP,NP),B(NMAX),Z(NMAX)
      DO 12 IP=1,N
         DO 11 IQ=1,N
            V(IP,IQ)=0.
11       CONTINUE
         V(IP,IP)=1.
12    CONTINUE
```

```
      DO 13 IP=1,N
         B(IP)=A(IP,IP)
         D(IP)=B(IP)
         Z(IP)=0.
13    CONTINUE
      NROT=0
      DO 24 I=1,50
         SM=0.
         DO 15 IP=1,N-1
            DO 14 IQ=IP+1,N
               SM=SM+ABS(A(IP,IQ))
14          CONTINUE
15       CONTINUE
         IF(SM.EQ.0.)RETURN
         IF(I.LT.4)THEN
            TRESH=0.2*SM/N**2
         ELSE
            TRESH=0.
         ENDIF
         DO 22 IP=1,N-1
            DO 21 IQ=IP+1,N
               G=100.*ABS(A(IP,IQ))
               IF((I.GT.4).AND.(ABS(D(IP))+G.EQ.ABS(D(IP)))
     *          .AND.(ABS(D(IQ))+G.EQ.ABS(D(IQ))))THEN
               A(IP,IQ)=0.
               ELSE IF(ABS(A(IP,IQ)).GT.TRESH)THEN
               H=D(IQ)-D(IP)
               IF(ABS(H)+G.EQ.ABS(H))THEN
                     T=A(IP,IQ)/H
                  ELSE
                     THETA=0.5*H/A(IP,IQ)
                     T=1./(ABS(THETA)+SQRT(1.+THETA**2))
                     IF(THETA .LT. 0.)T=-T
                  ENDIF
                  C=1./SQRT(1+T**2)
                  S=T*C
                  TAU=S/(1.+C)
                  H=T*A(IP,IQ)
                  Z(IP)=Z(IP)-H
                  Z(IQ)=Z(IQ)+H
                  D(IP)=D(IP)-H
                  D(IQ)=D(IQ)+H
                  A(IP,IQ)=0.
                  DO 16 J=1,IP-1
                     G=A(J,IP)
```

```
                H=A(J,IQ)
            A(J,IP)=G-S*(H+G*TAU)
            A(J,IQ)=H+S*(G-H*TAU)
16              CONTINUE
                DO 17 J=IP+1,IQ-1
                  G=A(IP,J)
                  H=A(J,IQ)
            A(IP,J)=G-S*(H+G*TAU)
            A(J,IQ)=H+S*(G-H*TAU)
17              CONTINUE
                DO 18 J=IQ+1,N
                  G=A(IP,J)
                  H=A(IQ,J)
            A(IP,J)=G-S*(H+G*TAU)
            A(IQ,J)=H+S*(G-H*TAU)
18              CONTINUE
                DO 19 J=1,N
                  G=V(J,IP)
                  H=V(J,IQ)
            V(J,IP)=G-S*(H+G*TAU)
            V(J,IQ)=H+S*(G-H*TAU)
19              CONTINUE
                NROT=NROT+1
              ENDIF
21          CONTINUE
22        CONTINUE
          DO 23 IP=1,N
            B(IP)=B(IP)+Z(IP)
            D(IP)=B(IP)
            Z(IP)=0.
23        CONTINUE
24      CONTINUE
        PAUSE '50 iterations should never happen'
        RETURN
        END
```

REFERENCES CITED

Abraham A. and Bleaney B., *EPR of Transition Ions* (Clarendon Press, Oxford, 1970)

Alfred A.T., Acta Cryst. **B40**, 569 (1984).

Aminov L.K., 1981, Sov. Phys. Solid State, **23**, 1266 (1981).

Baker J.M. and Bleaney B., Proc. R. Soc. London **A245**, 156 (1958).

Baker J.M. and Williams , Proc. R. Soc. London, **A267**, 283 (1962).

Barnes R.G., Phys. Rev. **136** A175 (1964)

Battison J.E., Kasten A., Leask M.J.M., and Lowry J.B., J. Phys. C, **10**, 323 (1977).

Baumert R., Pelzl J., and Hüfner S., Solid State Commun. **16**, 345 (1975).

Blok J. and Shirley D.A., Phys. Rev. **143**, 276 (1966).

Boger J.K., M.S. Thesis (Montana State University, 1987)

Bouazaoui M., Doctoral Thesis (l'Universite Claude Bernard LYON I, 1991).

Boyd E.L., Phys. Rev. **145**, 174 (1966).

Brecher C., Samelson H., Lempicki A., Riley R. and Peters T., Phys. Rev. **155**, 178 (1967).

Brecher C., Samelson H., Riley R. and Lempicki A., J. Chem. Phys. **49**, 3303 (1968).

Carnall W.T., Goodman G.L., Rajnak K., and Rana R.S., *A Systematic Analysis of the Spectra the Lanthanides Doped into Single Crystal LaF_3*, Argonne National Laboratory Report, ANL-88-8 (1988)

Chen H.T. and Meltzer R.S., Phys. Rev. Lett. **44**, 599 (1980).

Chen G., Stump N.A., Haire R.G., Peterson J.R., and Abraham M.M., J. Phys. Chem. Solids **53**, 1253 (1992), Solid State Comm. **84**, 313 (1992).

Cone R.L., J. Chem. Phys. **57**, 4893 (1972).

Cone R.L. unpublished (1986).

Cone R.L., Harley R.T., and Leask M.J.M., J. Phys. C **17**, 3101 (1984).

Cone R.L., Leask M.J.M., Robinson M.G., and Watts B.E., J. Phys. C **21**, 3361 (1988).

Cone R.L., Hansen P.C., and Leask M.J.M., J. Opt. Soc. Am. B, **9**, 779 (1992).

Cone R.L., Hansen P.C., Leask M.J.M., and Wanklyn B.M., J. Phys: Condens. Matter **5**, 573 (1993)

Cone R.L. and Faulhaber R., J. Chem. Phys. **55** 5198 (1971).

Cone R.L. and Meltzer R.S., Chapter 8 in *Spectroscopy of Solids Containing Rare Earth Ions*, ed. by Kaplyanskii A.A. and MacFarlane R.M. (North-Holland, Amsterdam, 1987)

Cone R.L. and Meltzer R.S., J. Chem. Phys. **62**, 3575 (1975).

Dahl M. and Schaack G., J. Lumin. **31-32**, 84 (1984), Phys. Rec. Letters **56**,232 (1986).

Edmonds A.R., Angular Momentum in Quantum Mechanics (Princeton University Press, Princeton, N.J., 1957)

Edmonds D.T., Phys. Rev. Letters **10**, 129 (1963).

Elliott R.J., 1957, Proc. R. Soc. London. **B 70**, 119 (1957).

Elliott R.J., Harley R.T., Hayes W., and Smith S.R.P., Proc. R. Soc. London, **A328**, 217 (1972)

Ergun H.B., Gehring K.A., and Gehring G.A., J. Phys. C **9**, 1101 (1976).

Erickson L.E., Opt. Commun. **21**, 147 (1977a).

Erickson L.E., Phys. Rev. B **16**, 4731 (1977b).

Erickson L.E., Phys. Rev. B **19**, 4412 (1979).

Erickson L.E., Phys. Rev. B**34**, 36 (1986).

Erickson L.E. and Sharma K.K., Phys. Rev. B **24**, 3697 (1981).

Evans L., Sanders P.G.H., and Woodgate G.K., Proc. R. Soc. London **A289**, 114 (1965).

Gehring G.A. and Gehring K.A., Rep. Prog. Phys. **38**, 1 (1975).

Goldstein H., *Classical Mechanics*, second edition (Addison-Wesley, Reading, 1980)

Grenet G., Kibler M., Linarès C., Louat A., and Gaume F., Chem. Phys. Lett. **51**, 160 (1977).

Ham F.S., 1965, Phys. Rev. A**138**, 1727.

Ham F.S., 1968, Phys. Rev. **166**, 307

Ham F.S.,.Chap. 1 in *Electron Paramagnetic Resonance*, ed. by S. Geschwind. (Plenum Press, New York, 1972)

Hansen P.C., D. Phil. dissertation (University of Oxford, Oxford, 1990).

Hayes W. and Loudon R., Scattering of Light by Crystals. (John Wiley & Sons, 1978).

Hougen J.T., 1964, J. Mol. Spectry. **13**, 149.

Hüfner S., *Optical Spectra of Transparent Rare Earth Compounds* (Academic Press, New York, 1978).

Jahn H.A. and Teller E., Proc. R. Soc. A**161**, 220 (1937).

Judd B.D., Lovejoy C.A., and Shirley D.A., Phys. Rev. **128**, 1733 (1962).

Karayianis N., Morrison C.A., and Wortman D.E., Harry Diamond Laboratories Report TR-1776 (NTIS#030849) (1976).

Krebs K. and Winkler R. Naturwissenschaffen **47**, 490 (1960).

Lazzouni M., D. Phil. dissertation (University of Oxford, Oxford,1988).

Liu G.K. Ph. D. Thesis (Montana State University, Bozeman, 1988).

Jayaraman A., Kourouklis A., Espinosa G.P., Cooper A.S., and Van Uitert L.G., J. Phys. Chem. Solids **48**, 755 (1987).

Jørgensen C.K., *Orbitals in Atoms and Molecules* (Academic Press, New York, 1962).

Jørgensen C.K., *Modern Aspects of Ligand Field Theory* (North-Holland, Amsterdam, 1971)

Kawalski F.V., Hawkins R.T., and Schawlow A.L., J. Opt. Soc. Am. **66**, 965 (1976).

Koster G.F., Dimmock J.O., Wheeler R.G., and Statz H., *Properties of the 32 Point Groups* (M.I.T. Press, Cambridge,1963)

Martin J.P.D., Boonyarith T., Manson N.B., and Hasan Z., J. Phys. Condens. Matter **4**, L411 (1992).

Macfarlane R.M. and Shelby R.M., Opt. Lett. **6**, 96 (1981)

Macfarlane R.M. and Shelby R. M., Chapter 2 in *Spectroscopy of Solids Containing Rare Earth Ions*, ed. by Kaplyanski A.A. and Macfarlane R.M. (Northern Holland, Amsterdam, 1987).

Macfarlane R.M., Shelby R.M., and Barum D.P., Opt. Lett. **6**, 593 (1981)

Manson N.B., Hasan Z., Fisk P.T.H., Reeves R.J., and Jones G.D., J. Phys: Condens. Matter **4**, 5591 (1992)

Meltzer R.S. and Moos H.W., Phys. Rev. B **6**, 264 (1972).

Mitsunaga M., Kintzer E.S., and Brewer R.G., Phys. Rev. B **31**, 6947 (1985)

Morrison C.A., Mason D.R., and Kikuchi C., Phys. Lett. **A24**, 607 (1967).

Morrison C.A. and Leavitt R.P., Chap. 46 in *Handbook of the Physics and Chemistry of Rare Earths* Vol. 5, ed. by Gschneider K.A. Jr. and Eyring L. (North-Holland, Amsterdam, 1982).

Muller W., Stendel A., and Walther H., Z. Phys. **183**, 303 (1965).

Newman D.J., J. Phys. Chem. Solids, **134**, 541 (1973).

Otteson M.S., Ph.D Dissertation (Montana State University, 1984).

Press W.H., Flannery B.P., Teukolky S.A., and Vetterling W.T., *Numerical Recipes* (Cambridge University Press, Cambridge, 1986)

Robinson M.G., D.Phil. Dissertation. (University of Oxford, Oxford, 1986).

Sanders G.H. and Woodgate G.K., Proc. R. Soc. London **A257**, 269 (1960).

Schwiesow R.L., Ph.D Thesis. (Johns Hopkins University, 1968).

Scott P.D., Ph.D Dissertation. (Yale University, 1970).

Sharma K.K. and Erickson L.E., Phys. Rev. Lett. **45**, 294 (1980)

Sharma K.K. and Erickson L.E., J. Phys. C: Solid State Phys. **18**, 2935 (1985).

Shelby R.M. and Macfarlane R.M. Phys. Rev. Lett. **47**, 1172 (1981).

Shelby R.M., Tropper A.C., Harley R.T., and Macfarlane R.M., Opt. Lett. **8**, 304 (1983).

Shelby R.M., Barum D.P., and Macfarlane R.M., Opt. Commun. **52**, 283(1984).

Silversmith A.J. and Macfarlane R.M., Phys. Rev. B **45**, 5811 (1992).

Silversmith A.J. and Manson N.B., J. Phys. C **17**, L97 (1984).

Silversmith A.J. and Manson N.B., Phys. Rev. B **34**, 4854 (1986).

Silversmith A.J. and Radlinski A.P., and Manson N.B., Phys. Rev. B **34**, 7554 (1986).

Teplov M.A., Zh. Eksp. & Teor. Fiz **53**, 1510 [Sov. Phys. - JETP **26**, 872] (1968).

Tinkham M., *Group Theory and Quantum Mechanics* (McGraw-Hill, New York, 1964).

Venikouas G.E. and Powell R.C., Phys. Rev. B **17**, 3456 (1978).

Wyckoff R.W.G., *Crystal Structures* (John-Wiley and Sons, New York, 1963)

Yano R., Mitsunaga M., and Uesugi N., Optics Letters **23**, 1884 (1991)